

박 사 학 위 논 문  
Ph.D. Dissertation

극한강우를 고려한 토석류 재해평가에 관한  
순차적 선별 및 분석범위 축소 기반 접근

A sequential sifting and scale reduction based  
approach to hazard assessment for extreme  
rainfall-induced debris flow

2016

니킬 네뎀팔릴 바수 (Nikhil Nedumpallile Vasu)

한 국 과 학 기 술 원

Korea Advanced Institute of Science and Technology

박 사 학 위 논 문

극한강우를 고려한 토석류 재해평가에 관한  
순차적 선별 및 분석범위 축소 기반 접근

2016

니킴 네뚌팔릴 바수

한 국 과 학 기 술 원

건설 및 환경공학과

DICE  
20115554

니킬 네둠팔릴 바수 . 극한강우를 고려한 토석류 재해평가에  
관한 순차적 선별 및 분석범위 축소 기반 접근. 2016 년.  
156+vii 쪽. 지도교수: 이승래. (영문 논문)

Nikhil Nedumpallile Vasu. A sequential sifting and scale reduction  
based approach to hazard assessment for extreme rainfall-induced  
debris flow. Department of Civil and Environmental Engineering.  
2016. 154+ix pages Advisor: Lee, Seung-Rae. (Text in English)

## 초 록

최근 들어 한국의 증가하는 추세의 극한강우 사상은 중력으로 인한 지표 이동 위험에 대한 증가된 노출을 초래하였다. 극한강우로 유발된 토석류는 주거지, 도로 및 그 외 사회기반시설들에 막대한 피해를 야기시키므로, 이에 대해 예측 정확성 및 신뢰성과 반비례 관계가 있는 여러 분석 스케일에서의 위험도 평가가 요구된다. 본 연구에서는, 극한강우로 유발된 산사태 위험도 평가를 위한 광역 지역에서부터 국부 지역에 이르는 스케일에서의 접근법을 제시하였다. 광역 스케일에서는, 산사태 민감도와 ERI 모델을 개발하여 공간적 및 시간적 확률 요소를 결합함으로써 산사태 위험도 평가가 수행된다. 산사태에 대한 매우 높은 민감성을 가지고 있는 대상 지역은 토석류로의 전이 여부에 대해 추가로 시험되며, 이어서 수문학적 평가를 통해 선별된 사면 단위의 국부지역으로 스케일이 전환된다. 국부적인 사면 스케일에서 토석류 위험도 요소들인 속도와 최종 부피는 DAN3D로 명명된 SPH 기반의 유동 모의 모델을 사용하여 평가된다. 토석류에 대한 예측 모델링은 세 가지 주요 입력 인자인 초기 부피, 유동(rheology) 모델, 연행 증가율에 대한 데이터베이스 개발을 위한 체계를 구축함으로써 수행되었다. 입력 인자들은 다음과 같은 방법을 이용하여 추정하였다. 초기 부피는 3-D 수리역학 연계 모델을 이용하여 추정하였고, 유동 모델은 유효응력 기반의 마찰 유동 모델로 채택되었으며 마찰각의 경우 인공신경망 모델을 이용하여 추정하였다. 마지막으로, 연행 증가율은 초기 부피와 토심 지도를 이용하여 결정하였다. 제시된 토석류 위험도 평가 방안은 2011년 7월경 서울에 위치한 우면산에서 발생한 극한강우 재해 사례에 적용되었다. 우면산을 대상으로 Extreme Learning Machine 기반 하이브리드 모델을 적용한 결과 13 개의 인자가 영향을 미치는 것으로 판단되었고, 85%와 89%의 높은 성공률 및 예측율을 각각 나타냈다. 지반 요소와 강우 요소를 고려하는 ERI를 이용하여 시간적 요소를 추정하기 위한 새로운 접근법이 개발되었으며, 이는 DHI를 이용한 위험도 평가를 위한 하이브리드 모델과 연계되었다. 2011년 7월경 서울에 위치한 우면산에서 발생한 극한강우 사례에 대한 ERI와 DHI의 적용 결과 DHI의 기준 값을 0.5로 하였을 때, 모든 산사태를 예측하였다. 그러므로, 기준값 0.5는 제시된 평가 체계에서 임계기준으로 사용할 수 있다. 산사태 발생 예상 지역들에서 토석류로 전이 가능한 영역은 4가지 인자인 사면경사, 종단 곡률, SPI 및 고도를 이용하는 전이기준을 사용하여 선별되었으며, 각 인자들의 하한 임계값은  $24^{\circ}$ , -4 to +4, 4.0, 60 m 로 설정되었다.

본 전이규준은 유역 분석과 결합되어 우면산에서 총 45개 사면 단위들을 선별하였으며, 토석류 위험도 예측 평가는 래미안 사면을 대상으로 국부 스케일에서 수행되었다. 3-D 기반의 침투 및 한계평형법 해석을 수행한 결과 23.5시간 이후 지하수 상승에 의한 불안정( $FOS=0.907$ )을 예측하였으며, 초기부피는  $2626.5 m^3$ 로 계산되었다. ANN 기반의 모델은 마찰각을 완전히 유동화된 흐름을 의미하는  $0^\circ$ 로 추정하였다. 추정된 입력인자들을 사용한 토석류 유동 모델링은 최종부피  $52642.6 m^3$ , 속도  $27 m/s$ , 그리고 래미안 아파트 근처에 집중된 약 5m 토사 두께를 예측하였으며, 이는 현장에서 관측 및 기록된 수치들과 일치하였다.

핵심 낱말 : ELM; ERI; DHI; 산사태 위험도; 극한 강우; 한계 평형법; 토석류 모델링

### Abstract

An increasing trend of extreme rainfall event contribution to annual precipitation during recent times in South Korea has resulted in higher exposure to dangerous gravity induced surface processes. Extreme rainfall induced landslides are one of the most dangerous gravity-induced surface processes causing severe damage to dwellings, roads and other lifelines and therefore requires hazard assessment at different scales with accuracy and reliability being inversely related to the scale. In this study, an approach for extreme rainfall induced landslide hazard assessment from large to detailed (site-specific) scale has been proposed. At large scale, the landslide hazard assessment is conducted by combining the spatial and temporal component through development of a landslide susceptibility and ERI model. The areas delineated as highly susceptible to landslides under extreme rainfall event are further tested for mobilization into debris flow using a criterion and are transitioned to detailed scale using slope units developed through hydrological assessment. The debris flow hazard components, velocity and final volume, at detailed slope scale are assessed using a SPH based runout model called DAN-3D. The predictive modelling of the debris flow was conducted by establishing a framework to develop the database for three major input factors: initial volume, rheological model, and growth rate. The input factors were estimated as follows: the initial volume was estimated using a 3-D coupled hydro-mechanical model; an effective stress based frictional rheological model was adopted and the bulk frictional angle for the same was estimated using a ANN based model; growth rate was determined from the initial volume and soil depth map. The proposed hazard assessment scheme was applied to Mt. Woomyeon, Seoul for the catastrophic extreme rainfall event in July 2011.

Application of the ELM based hybrid model to Mt. Woomyeon selected 13 influential factors and gave a high success and prediction rate AUC of 85% and 89%, respectively. A new approach to estimate the temporal component was developed using ERI explicitly considering soil and rainfall factors and was coupled to the hybrid model for hazard assessment using DHI. Application of ERI and DHI to Mt. Woomyeon for July 2011 extreme event indicates DHI of 0.5 can predict all landslides and thus, 0.5 is used as threshold in the proposed framework. The sifting of debris flows from landslides probable regions was performed using the mobilization criterion considering four factors; Slope angle, profile curvature, SPI, and elevation with lower threshold values of  $24^\circ$ , -4 to +4, 4.0, and 60 m, respectively. The criterion combined with watershed analysis delineated the Mt. Woomyeon into 45 slope units and the predictive debris flow hazard assessment is conducted at a site-specific scale on the, Raemein slope unit.



The 3-D based seepage and limit equilibrium method analysis predicted instability to occur at 23.5 hrs (FOS=.907) due to the progression of ground water table and gave an initial volume of 2626.5 m<sup>3</sup>. The ANN based model estimated a bulk frictional angle of 00 indicating a completely fluidized flow. The debris flow runout modelling using the estimated parameters predicted a final volume of 52642.6 m<sup>3</sup>, a velocity of 27 m/s and about 5 m debris thickness concentrated near the Raemian apartment, and is in agreement with that observed in the field.

Keywords: ELM; ERI; DHI; landslide hazard; extreme rainfall; limit equilibrium method; debris flow modelling

# Table of Contents

<b>Abstract</b> .....	i
<b>Table of contents</b> .....	iv
<b>List of Tables</b> .....	vi
<b>List of Figures</b> .....	vii
 <b>Chapter 1. Introduction</b>	
1.1 Research background .....	1
1.2 Research scope and layout .....	4
 <b>Chapter 2. A feedback-loop-based hybrid algorithm using ELM: Methodology for spatial assessment of extreme rainfall induced landslide assessment at large scale</b>	
2.1 Introduction .....	6
2.2 Study area and database development	
2.2.1 Landslide inventory .....	8
2.2.2 Database for landslide explanatory variables .....	10
2.3 Methodology	
2.3.1 Factor selection using filter method .....	18
2.3.2 Extreme machine learning method .....	19
2.3.3 Logistic regression .....	20
2.3.4 Hybrid model algorithm .....	20
2.4 Hybrid model implementation	
2.4.1 Preparation of training and validation data.....	23
2.4.2 Selection of best predictor .....	24
2.5 Discussion .....	35
2.6 Conclusion .....	42
 <b>Chapter 3. Extreme rainfall index and Dynamic hazard index: Approach for temporal and hazard assessment for extreme rainfall induced landslide at large scale</b>	
3.1 Introduction .....	43
3.2 Study area and database development	
3.2.1 Database for temporal assessment .....	46
3.2.2 Database for landslide susceptibility model .....	51
3.3 Methodology	
3.3.1 Temporal assessment using ERI .....	56
3.3.2 Spatial assessment of landslides .....	57

3.4 Results and discussion	
3.4.1 Extreme rainfall index .....	58
3.4.2 Landslide spatial assessment .....	61
3.4.3 Landslide hazard assessment using DHI .....	66
3.5 Conclusions .....	71
<b>Chapter 4. A transition scheme for site-specific scale reduction and initial volume estimation for landslide induced debris flow hazard assessment</b>	
4.1 Introduction .....	73
4.2 Debris flow mobilization scheme for sorting debris flows from slides	
4.2.1 Existing empirical mobilization criteria .....	76
4.2.2 Study area and data .....	78
4.2.3 Debris flow initiation factors .....	79
4.2.4 Methodology .....	81
4.2.5 Discussion and conclusion .....	82
4.3 Methodology for slope selection at site-specific scale	
4.3.1 GIS based database .....	86
4.3.2 Methodology .....	86
4.3.3 Application .....	87
<b>Chapter 5. Predictive debris flow runout assessment at site-specific scale using DAN-3D</b>	
5.1 Introduction .....	89
5.2 Framework for database development	
5.2.1 Site-specific initial volume estimation .....	91
5.2.2 Rheological model and parameters estimation.....	97
5.2.3 Growth rate estimation methodology.....	106
5.3 3-D based post-failure hazard assessment model for debris flow using DAN-3D .....	107
5.4 Application to Raemein slope unit, Mt. Woomyeon, Seoul	
5.4.1 Site-specific 3D based failure assessment .....	110
5.4.2 Post-failure hazard assessment .....	133
<b>Chapter 6. Conclusion and recommendations .....</b>	<b>137</b>

## List of Tables

Table 2.1: Database characteristics for susceptibility map development in Mt. Woomyeon .....	10
Table 2.2: Correlation of explanatory variables with landslide index.....	25
Table 2.3: Final number of hidden neurons selected for each group.....	31
Table 2.4: Algorithm phase and selection of optimal conditioning factors.....	32
Table 2.5: ELM output weights and bias.....	32
Table 2.6: (a) Coefficients of the selected landslide susceptibility model using logistic regression in SPSS; (b) Test for factor significance and goodness-of-fit.....	40
Table 3.1: Correlation analysis for antecedent factors.....	49
Table 3.2: Database for susceptibility map development in Deokjeok-ri Creek.....	52
Table 3.3: (a) Coefficients of the selected ERI model using logistic regression in SPSS; (b) Test for factor significance and goodness-of fit.....	59
Table 3.4: Correlation of explanatory factors with landslide index.....	61
Table 3.5. (a) Model coefficients and (b) Reliability test.....	63
Table 3.6: Percentage of area classified under each hazard level for different rainfall conditions.....	67
Table 4.1: Database characteristics for debris flow initiation criterion development.....	80
Table 4.2: Correlation among the debris flow initiation factors.....	83
Table 5.1: Summary of 3D limit equilibrium methods.....	93
Table 5.2: Fitted parameters to field observations (Lee, 2016).....	100
Table 5.3: Database of factors influencing bulk friction angle (Park,2015; Lee, 2016).....	102
Table 5.4: Soil hydraulic and strength characteristics.....	112
Table 5.5. Predicted input factors for DAN-3D.....	133
Table 5.6. Debris flow intensity parameters predicted using the model.....	136

## List of Figures

Fig. 1.1. Proposed framework for the debris flow hazard level assessment.....	3
Fig. 2.1. Scheme for ELM-based susceptibility modeling.....	8
Fig. 2.2. (A) Study area: Mt. Woomyeon; (B) Hourly and total rainfall distribution on 25–27 July 2011 at Namhyun and Seocho stations (Park et al., 2013).....	10
Fig. 2.3. Landslide conditioning factors: (A) Elevation; (B) Aspect; (C) Profile curvature; (D) Plan curvature; (E) Total curvature; (F) Slope; (G) TRI; (H) SRR; (I) Topography; (J) SEI; (K) TWI; (L) Humidity; (M) SPI; (N) STI; (O) Distance from stream; (P) Geology; (Q) Weathering; (R) Drainage; (S) Soil type; (T) Soil texture; (U) Soil density; (V) Forest density; (W) Soil depth.....	18
Fig. 2.4. Algorithm for feature selection using the filter and the learning scheme (ELM).....	22
Fig. 2.5. Sampling of unstable and stable points.....	24
Fig. 2.6. Satellite imagery and overlay with landslide locations (Training and testing dataset).....	24
Fig. 2.7. Variation of RMSE versus number of neurons for training and validation data to select the optimal hidden neurons for the groups.....	28
Fig. 2.8. Final landslide susceptibility model: (A) Success rate and prediction rate curve; (B) Relative importance of the final conditioning factors.....	33
Fig. 2.9. Landslide susceptibility of Mt. Woomyeon: (A) Histogram; (B) Landslide susceptibility weight; (C) Landslide susceptibility levels.....	35
Fig. 2.10. Area percentage of susceptibility classes.....	37
Fig. 2.11. Landslides on Mt. Woomyeon: (A) Landslide scarp; (B) Debris flow gully (entrainment); (C) Ground water table underlying the removed colluvium; (D) Deposition zone (Korean Geotechnical Society, 2011).....	38
Fig. 2.12. (A) Logistic regression-based susceptibility map; (B) Validation curve for the logistic regression-based susceptibility map.....	41
Fig. 3.1. Study area for ERI estimation and rainfall gauge distribution (Gangwon Province).....	45
Fig. 3.2. Study area for spatial assessment (Gangwon Province).....	45
Fig. 3.3. Continuous rainfall resulting in landslides during 1995-2013 in Gangwon.....	46
Fig. 3.4. Average monthly rainfall during 1990-2012 in Gangwon.....	47
Fig. 3.5. Continuous rainfall versus maximum hourly intensity for landslide events.....	48

Fig.3.6. General framework and database development method for ERI.....	51
Fig.3.7. Landslide conditioning factors: (a) Elevation; (b) Aspect; (c) Total curvature; (d) Slope; (e) IR; (f) TWI; (g) SPI; (h) STI; (i) Distance to drainage; (j) Drainage density; (k) Forest type (Pradhan and Kim, 2014).....	55
Fig. 3.8. Accuracy assessment using AUC of the cumulative gains chart.....	60
Fig. 3.9. Distribution of ERI values for making probability levels.....	60
Fig.3.10. Models and corresponding AUC for training datasets.....	62
Fig.3.11. (a) Landslide susceptibility weights for Deokjeok-ri Creek and (b) Landslide susceptibility class for Deokjeok- ri Creek.....	65
Fig.3.12. Training and validation curves for accuracy assessment.....	65
Fig.3.13. Extreme rainfall event in July 2006 in Deokjeok-ri.....	67
Fig.3.14. ERI map for July 2006 extreme rainfall event in Deokjeok-ri: (a) the day before the rainfall event, (b) rainfall event day 1, (c) rainfall event day 2, (d) rainfall event day 3 and (e) rainfall event day 4.....	68
Fig.3.15. Landslide hazard map for July 2006 extreme rainfall event in Deokjeok-ri: (a) the day before the rainfall event, (b) rainfall event day 1, (c) rainfall event day 2, (d) rainfall event day 3 and (e) rainfall event day 4.....	69
Fig.3.16. ERI map for July 2011 extreme rainfall event in Mt. Woomyeon: (a) rainfall event day 1, (b) rainfall event day 2, (c) rainfall event day 3, and (d) rainfall event day 4.....	70
Fig.3.17. Landslide hazard map for July 2011 extreme rainfall event in Mt. Woomyeon: (a) rainfall event day 1, (b) rainfall event day 2, (c) rainfall event day 3, and (d) rainfall event day 4.....	71
Fig 4.1. Influence of initial stress state on the stress path to mobilization.....	74
Fig 4.2. AMI criterion for debris flow mobilization (Fleming et al., 1989).....	75
Fig 4.3. Slope-upslope criterion for debris flow initiation (Rickenmann and Zimmermann, 1993).....	77
Fig 4.4. Debris flow inventory in Woomyeon mountain.....	78
Fig. 4.5. Application of mobilization criterion to Mt. Woomyeon.....	84
Fig. 4.6. Evolution of debris flow points for 2011 extreme rainfall event: (a) Day 3; (b) Day 4.....	85
Fig 4.7. (a) Original DEM; (b) Reverse DEM.....	86
Fig 4.8. (a) Flow directions for DEM; (b) Flow directions for combined DEM.....	87
Fig 4.9. Slope units for Mt. Woomyeon.....	88
Fig. 5.1. Framework for database establishment for predictive hazard assessment of debris flow runout.....	90
Fig 5.2. Forces acting on the column considered in a 3D slope stability scheme.....	92
Fig 5.3. Data sampling locations of debris flow events.....	97

Fig 5.4. Methodology for optimizing the rheological parameters (Aaron et al., 2015).....	99
Fig 5.5. Histogram for independent factors used for making the ANN model.....	103
Fig 5.6. RMSE for training, testing and validation dataset.....	105
Fig.5.7. (a) Error histogram with 20 bins; (b) Training stoppage for best validation performance .....	106
Fig 5.8. Watershed selection for initial volume analysis.....	110
Fig 5.9. (a) Sampling locations, and (b) cross-section showing soil layers (KSCE report).....	111
Fig 5.10. (a) Hydraulic conductivity for colluvium and weathered rock; (b) SWCC.....	111
Fig 5.11. Rainfall pattern for initial volume estimation in Raemein slope.....	112
Fig 5.12. Numerical model used for initial volume estimation.....	113
Fig. 5.13. (a) Bottom surface; (b) Downstream boundary; (c) Left boundary sidewall; (d) Right boundary sidewall; (e) Upstream boundary.....	114
Fig 5.14. Pore-water pressure distribution corresponding to section Y=68m for time t=0 to 30 hr.....	120
Fig 5.15. Spatial distribution of pwp on surface 1 (top of bedrock): (a) 0 hr ; (b) 7 hr ; (c) 12 hr ; (e) 15 hr; (d) 18 hr; (f) 21 hr; (g) 23 hr; (h) 25 hr; (i) 28 hr; (j) 30 hr.....	125
Fig 5.16. Spatial distribution of pwp on surface 2 (layer between colluvium and weathered rock): (a) 0 hr ; (b) 7 hr ; (c) 12 hr ; (e) 15 hr; (d) 18 hr; (f) 21 hr; (g) 23 hr; (h) 25 hr; (i) 28 hr; (j) 30 hr.....	130
Fig 5.17. Spatial distribution of pwp on surface 3 (Top of colluvium layer) at time= 23 hr.....	132
Fig 5.18. Critical slip surface at time t=23 hr.....	132
Fig 5.19. Yield strength and viscosity for different water content in Raemein slope (Lee, 2016).....	134
Fig 5.20. Debris flow thickness and impact area.....	135
Fig 5.21. Debris flow impact on buildings (Jang Seung-Yoon/ Getty images, Truth Leem/ Reuters).....	135

# Chapter 1. Introduction

*“Nature’s imagination is so much greater than man’s, she is never going to let us relax” ~Richard Feynman*

## 1.1 Research background

Extreme rainfall events in South Korea show an increasing trend in contribution to the annual precipitation (Choi, 2004). The annual precipitation during the period of 1973-2005 mainly occurred during summer season and was characterised by an increase in the frequency and intensity of extreme precipitation (Jung et al., 2011). Extreme rainfall induced landslides are one of the most dangerous gravity-induced surface processes causing severe damage to dwellings, roads and other lifelines. Destructive debris flows mobilized from shallow landslides are generally the most common and widespread. About 70 % of the Korean peninsula is covered with mountains composed of soils formed from the in situ weathering of granite and gneiss. Shallow landslides are typically 1-3 m deep and often occur at boundaries between the colluvium and the underlying more solid parent rock (Salciarini et al., 2008). In most parts of Korea, shallow landslides are characterized by shallow failure surfaces of 2-3 m depth that develop parallel to the original slope (Kim et al., 2004). Due to the mountainous terrain with a shallow layer of colluvium, landslides have proven a hazard across most of the country. The socio-economic impact, moreover, has become much higher than before because of the current population levels in the hazardous zones. Hence risk mitigation through structural counter-measures or through alternative cost effective means like early warning systems (EWS) are viable especially in areas where slope stabilization is not a solution. The United Nations International Strategy for Disaster Reduction defines EWS as “the set of capacities needed to generate and disseminate timely and meaningful warning information to enable individuals, communities and organizations threatened by a hazard to prepare and to act appropriately and in sufficient time to reduce the possibility of harm or loss” (UNISDR, 2009). There are several other definitions for the EWS given by different researchers (Medina-Cetina and Nadim, 2008; Dikau and Weichselgartner, 2005). Irrespective of the definitions, it is generally accepted that EWS work towards zero casualty in areas of risk anticipating an imminent collapse, thus, operating as a risk mitigation tool (Intrieri et al., 2012). Therefore, any EWS for being considered efficient should comprise of the following qualities: 1) Monitoring and data acquisition capability along with maintenance of the devices; 2) Systems incorporating hazard and risk models to provide information on potentially hazardous events; 3) Alarm systems based on thresholds, either empirical or deterministically derived, can give warning on exceedance monitored using real-time systems; 4) Warning dissemination and appropriate response capability.



The development of near real-time EWS involves several key elements like meteorological systems, monitoring systems, hazard and risk assessment, and distribution of information and response procedures.

In designing the EWS, hazard assessment is one of the most vital component needed to identify or locate the areas along with the intensity of the event for the warning need to be issued. The warning system can be developed at different scales like national, regional or local and for a general or specific landslide types. The type developed depends on the data availability, model complexity and the area under consideration.

There are several existing statistical, empirical or deterministic models for assessing the hazard due to landslides or debris flow at different scales. The accuracy and reliability of the estimation has an inverse relationship with scale i.e., the larger the scale of the area under consideration, the lower the accuracy and reliability of the hazard assessment. Hence, for EWS we have applied a scale reduction framework from large (regional/ local) to site specific (watershed/ massif) scale. Thus, the current methods for hazard assessment of debris flow from a prediction perspective are limited by scale. Though modelling at site-specific scale can be performed with high reliability but it is difficult to predict which slope is susceptible to debris flow when the area under considering is quite large. A simple solution to this problem is to develop a statistical debris flow model considering geomorphological and rainfall factors and use the result from the model to delineate the potential slopes for site-specific analysis. However, this is difficult owing to the lack of complete debris flow inventory and rainfall data causing these events. In Korea, there is well established database for temporal (consisting of all landslide types and no clear distinction between them) and spatial information of landslides (clear distinction among the slides and debris flows inventories). Hence, though the spatial probability for the debris flow susceptibility can be established but creating a temporal database which triggers only the debris flow events is difficult. Hence, there is a need to develop a simple and reliable methodology which utilizes the well-defined spatial database at large scale (regional/ local) and the incomplete temporal database (in this study incomplete database means there is no information regarding type of landslide) identify the triggering areas under extreme rainfall and smoothly transition to a site-specific scale with the objective of predictive hazard modelling.

Thus, motivation for this research is to develop a framework and related methods for the hazard component of the debris flow early warning system through systematic scale reduction and delineation of debris flow events from other landslide types due to extreme rainfall. The extreme rainfall induced debris flow hazard can then be combined with vulnerability assessment to make the decision on whether or not warning ought to be given in the specific location of the region. The proposed framework for the debris flow hazard level assessment is as shown in Fig.1.

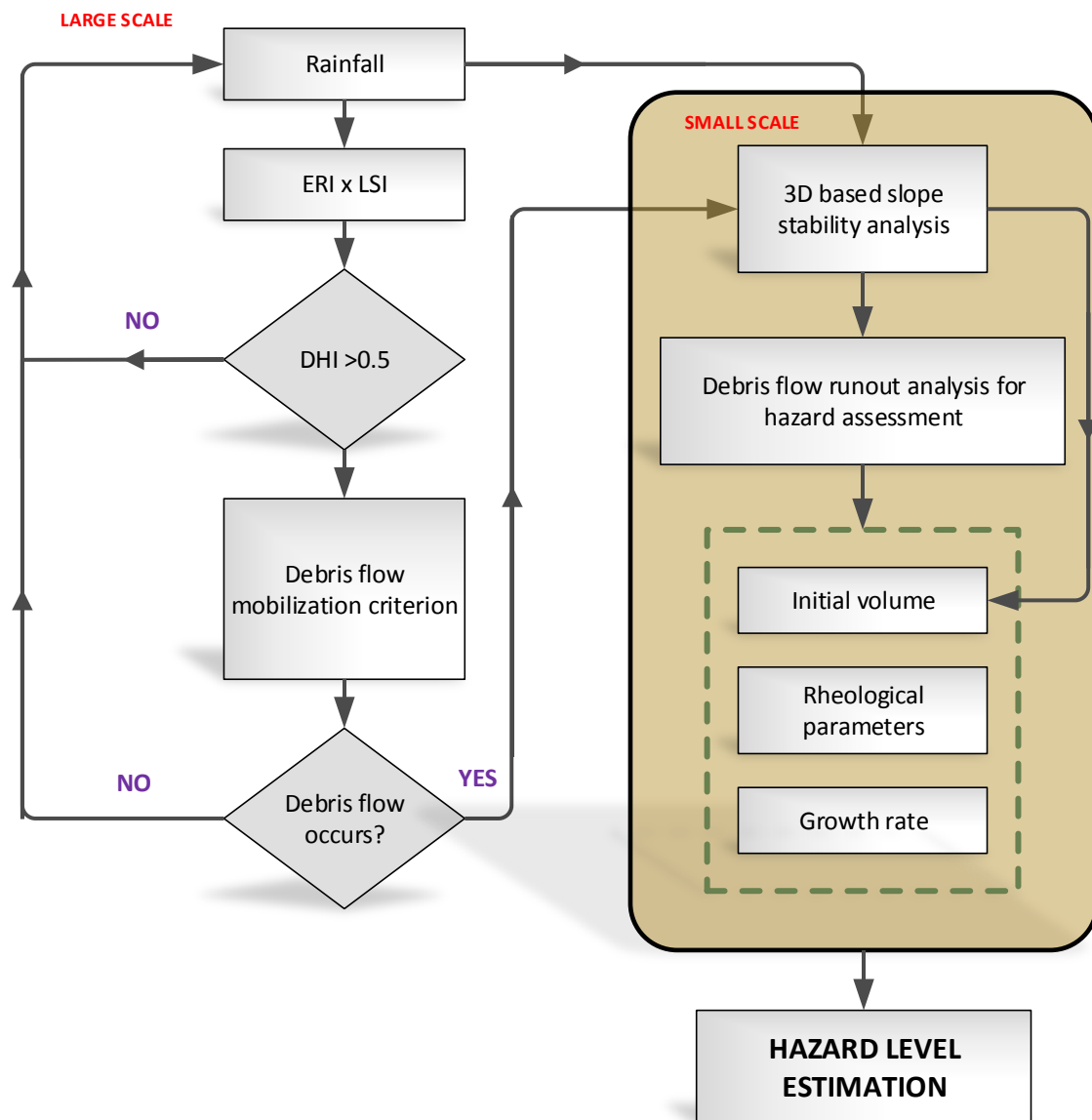


Fig.1.1: Proposed framework for the debris flow hazard level assessment

## 1.2 Research scope and layout

Objective of the study is to identify the spatial variability of debris flow with real-time extreme rainfall data and to conduct hazard assessment for early warning system in order to send out warning alerts to near-by population against the catastrophic event. Therefore, there is a need to develop a framework for using the real-time rainfall information in a particular region (large scale e.g. mountain) and identifying locations on the mountain where the debris flow might occur and predict the intensity of the event.

In order to do that development of new core technologies are needed which can fit in the prediction framework and also, development of database establishment methodologies for existing state of the art technologies is a necessity.

In order to achieve the above, the following work has been done in this thesis:

- 1) Proposed a new framework for hazard assessment which, in association with vulnerability assessment, can be adopted in EWS.
- 2) Developed three new core technologies for the hazard component in the EWS.
- 3) Advanced the database establishment technique for DAN-3D at site-specific scale through the use of 3-D coupled slope stability analysis and a predictive model for the rheological parameter.

Thus, the scope of this thesis can be summed up as: *“to develop and apply a sequential landslide discernment and scale reduction based approach for hazard analysis of debris flow mobilized from shallow landslides under extreme rainfall, to be used in a landslide early warning system”*.

The main objective thus has been realized in this research and is as described in the following chapters:

Chapter 2 proposes a ELM based feedback controlled hybrid model with the objective to create a high performance landslide susceptibility model by addressing the issue of feature selection for supervised learning techniques.

Chapter 3 introduces a novel scheme to consider the temporal component using ERI, which in combination with spatial probability model can be used to assess the landslide susceptibility. An index termed DHI is also suggested to describe the variation in susceptible zones considering the real-time rainfall condition.

Chapter 4 presents a transition scheme for scale reduction from large to site-specific using an index based mobilization criterion and establishment of slope units through the combination of hydrological assessment and the mobilization criterion.

Chapter 5 finally focusses on the database estimation methodology for the site-specific debris flow run-out hazard assessment. A deterministic analysis using 3D seepage and 3D limit equilibrium analysis is conducted to estimate the initial volume that mobilizes into debris flow. The most appropriate rheological model for Korean condition is identified and a ANN based model is developed with the objective of predictive modelling. The hazard components comprising of final volume and velocity for the mobilized mass are finally calculated using SPH based 3D model called DAN-3D. Chapter 6 summaries the conclusion from the study and recommendations for further study.

## **Chapter 2. A feedback-loop-based hybrid algorithm using ELM: Methodology for spatial assessment of extreme rainfall induced landslide assessment at large scale**

### **2.1. Introduction**

Extreme rainfall events in South Korea have exhibited an increasing trend in contribution to the annual precipitation (Choi, 2004). Annual precipitation during the period 1973 to 2005 primarily occurred during the summer season and was characterized by an increase in the frequency and intensity of extreme precipitation (Jung et al., 2011). Landslides induced by extreme rainfall caused by climate change (Kim et al., 2008) are one of the most dangerous gravity-driven surface processes causing severe damage to dwellings, roads, and other lifelines. Among such events, destructive debris flows mobilized from shallow landslides are generally the most common and widespread. Approximately 70% of the Korean peninsula is covered by mountains with shallow soil layers formed from in-situ weathering of granite and gneiss. Shallow landslides typically are 1-3 m deep and often occur at boundaries between the colluvium and the underlying more solid parent rock (Salciarini et al., 2008). In most parts of Korea, shallow landslides are characterized by failure surfaces 2-3 m deep that develop parallel to the original slope (Kim et al., 2004). The socioeconomic impact has become much higher than before because of the current population levels in hazardous zones. Hence, risk mitigation through structural countermeasures or alternative cost-effective means, such as early warning systems, are viable especially in areas where slope stabilization is not a solution. In order for the above solutions to be implemented, landslide susceptibility maps need to be developed displaying the zones with varying spatial distributions of landslides according to morphological, hydrological, geotechnical, and geological types of conditioning factors. A detailed literature review indicates presence of a large number of landslide instability factors. However, consideration of all factors can not only result in overfitting but also affect the model generalization (Kotsiantis, 2011) owing to the issue of dimensionality (Hughes, 1968). Hence feature selection for dimensionality reduction through identification of relevant features is an imperative process in preparation of high quality landslide susceptibility maps. Many of the studies focusing on objective conditioning factor selection for optimal landslide susceptibility model design have mainly been conducted using either filtering (e.g., univariate correlation statistics, Akaike Information Criterion and genetic algorithms; Ercanoglu and Gokceoglu, 2001; Roth and Lange, 2003; Yu et al., 2004; Boutsidis et al., 2009; Kavzoglu et al., 2015), or wrapper techniques through

supervised learning algorithms (such as logistic regression, support vector machines, artificial neural network, Random Forest, and AdaBoost; Guzzetti et al., 1999; Ermini et al., 2005; Castellanos and Van Westen, 2007; Yao et al., 2008; Pradhan et al., 2010; Yeon et al., 2010; Yilmaz, 2010; Marjanovic et al., 2011; Oh and Pradhan, 2011; Sezer et al., 2011; Althuwaynee et al., 2012; Ballabio and Sterlacchini, 2012; Devkota et al., 2012; Lee et al., 2012; Pourghasemi et al., 2012a; 2012b; Zare et al., 2012; Tien Bui et al., 2012; Xu et al., 2012; Zhu et al., 2014, Dou et al., 2015). However, both of these methods have the disadvantage of not considering classifier bias and of being computationally expensive. This motivated the development of a hybrid model combining both of the above techniques by using filter methods for preprocessing (initial screening) and wrapper methods on the created subsets for further fine tuning leading to the final optimized factor subset.

A study by Costanzo et al. (2012) utilized a hybrid framework for susceptibility map development using univariate correlation statistics and the matrix method. In this research, the selection of factors and its importance were assessed using correlation indices, i.e., the linear and contingency correlation coefficient (R), and Goodman-Kruskal's gamma (G-K); and the optimal combinations made using ranking-based progressive addition were chosen according to the matrix method. They showed that the best model could be obtained using the parameters identified utilizing the R and G-K statistics and therefore concluded that statistical univariate correlation index-based filter models are sufficient to identify the optimal factors and to make geologically meaningful susceptibility maps. However, studies (Micheletti et al., 2014; Goetz et al., 2015) have shown that the selection of factors and the importance of those factors is a function of the nominated supervised learning algorithm, and thus relying only on a filter model will not suffice. Additionally, this hybrid approach strongly depends on the quality of input data because of the use of a statistical correlation-based filter model and a statistical wrapper model and also lacks a quantitative method to estimate factor importance.

Hence, the objective of this paper is to address the issue of feature selection for supervised learning techniques by providing a simple general framework to create systematic subsets for  $2^n$  combinations of factors (where n is number of conditioning factors) in pursuit of a high performance landslide susceptibility model by proposing a two-stage approach based on a hybrid method through feedback control. Fig. 2.1 shows the general framework of the method implemented to develop the susceptibility map.

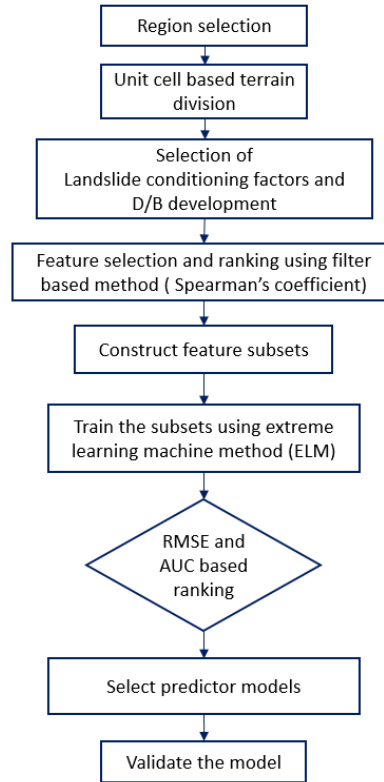


Fig. 2.1. Scheme for ELM-based susceptibility modeling.

## 2.2 Study Area and Data

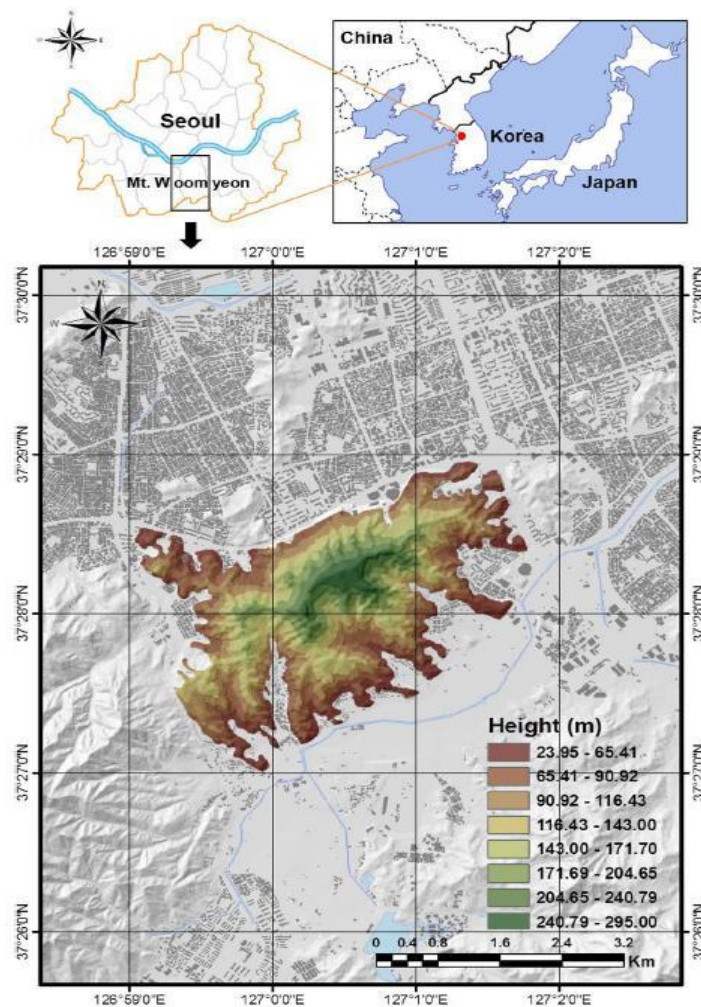
A susceptibility map was developed for Mt. Woomyeon, located in the Seocho district of Seoul, South Korea (Fig. 2.2A). The 5,104,162 m<sup>2</sup> area under consideration extends between 37°27'00"–37°28'55"N latitude and 126°59'02"–127°01'41"E longitude, with the highest point 293 m above sea level. The average annual precipitation is in the range of 1100 to 1500 mm. The mountain has moderate to dense vegetation cover, predominately consisting of Mongolian oak trees (*Quercus mongolica*), Dales Acacia (*Acacia catechu*), Sawthorn oak trees (*Quercus Acutissima-Carruth*), black birch (*Betula davurica*) and other types of pine trees. A soil profile of the mountain exhibits three main layers: a colluvium layer consisting of a poorly sorted sand and gravel mixture in a silty matrix up to 3 m thickness, a dark-brown clay layer with a thickness of 0.2 to 0.5 m, and a subsoil of stiff weathered bedrock of low permeability.

### 2.2.1 Landslide inventory

An extreme rainfall event from 26 to 27 July 2011 (470 mm in 16 h) in the Mt. Woomyeon area caused several shallow landslides, with many mobilized into debris flows, resulting in 16 casualties and damage to 10 buildings. Rainfall in July 2011 was significantly higher than the average, with Mt. Woomyeon receiving 55% of its total annual precipitation of 2039 mm. The maximum hourly rainfall measured at the two rainfall stations, Namhyun and Seocho, were 114 mm/h,

with a return period of 120 years, and 87 mm/h, with a return period of 20 years, respectively (Park et al., 2013). Fig.2.2B shows the hourly rainfall from both stations.

Approximately 163 landslide inventory points consisting of debris flows and slides were mapped for Mt. Woomyeon using satellite images, high resolution aerial photographs, and field reconnaissance. High-resolution photographs of 25-cm resolution were procured from the National Geographic Information Institute (NGII), and satellite images were obtained from Google Earth and Bing maps. These images were orthorectified via ground control points in ArcGIS 10.1, and landslide locations were detected through visual interpretation.





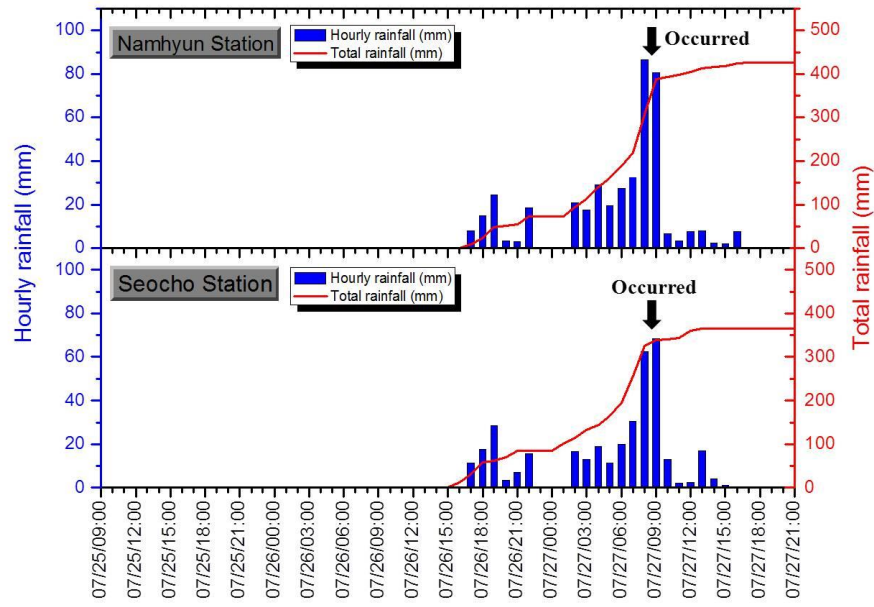


Fig. 2.2. (A) Study area: Mt. Woomyeon; (B) Hourly and total rainfall distribution on 25–27 July 2011 at Namhyun and Seocho stations (Park et al., 2013).

### 2.2.2 Database for landslide explanatory variables

Based on a detailed literature review, we selected 23 explanatory variables and grouped them into five types, as seen in Table 2.1: morphological, hydrological, geotechnical, geological, and forest. To reduce the subjectivity in selection and to identify the most significant variables affecting the landslide occurrence, bivariate correlation analysis was conducted, a detailed explanation of which is presented in section 2.3.

Table 2.1: Database characteristics for susceptibility map development in Mt. Woomyeon

Type	Factor	Source	Scale (Resolution)	Organization
Morphological	Aspect	DEM	10 x 10 m	NGII
	Elevation			
	Slope			
	Plan curvature			
	Profile curvature			
	TRI			
	SRR			
	SEI			

		Forestry map	1:25000	KFS
	Total curvature			
	Topography	DEM		NGII
Hydrological	Distance from stream	DEM	10 x 10 m	NGII
	TWI			
	Drainage	Forestry map	1:25000	KFS
	Humidity			
	STI	DEM	10 x 10 m	NGII
	SPI			
Geotechnical	Soil depth	Forestry map	1:25000	KFS
	Soil density			
	Soil texture			
	Soil type			
Forestry	Forest density	Forestry map	1:25000	KFS
Geological	Geology	Geology map	1:25000	KFS
	Weathering			
Landslide inventory		Field investigation report		Korean Society of Civil Engineers
		High resolution images	25 x 25 cm	NGII
		Satellite images		Bing maps Google Earth

#### 2.2.2.1 Morphological types

Many studies conducted around the world have shown that landslides are influenced by geomorphological features, such as elevation, slope, aspect, profile curvature, plan curvature, total curvature, TRI, SSR, SEI and topography. Elevation has been used as a conditioning factor in several studies, and higher values are generally related to higher susceptibility caused by variation in rainfall, vegetation, and potential energy availability (Pachauri and Pant, 1992; Ercanoglu et al., 2004). Elevation was positively correlated with landslide occurrence (Table 2.2) and was divided into six classes, with a maximum value of 293 m (Fig. 2.3A). Aspect is also considered as an important variable (Carrara et al., 1991; Maharaj 1993; Jakob, 2000), inducing landslides through exposure of the surface to wind and rainfall. Figure 2.3B shows aspect dividing the entire area into nine classes of flat (-1), north (337.5-360 and 0-22.5), northeast (22.5-67.5), east (67.5-112.5), southeast (112.5-157.5), south (157.5-202.5), southwest (202.5-247.5), west (247.5-292.5), and northwest (292.5-337.5). Slope, defined as steepness of a surface, and its second-order derivative curvature, helps in understanding the characteristics of a basin for runoff and erosion processes.

In this study, three types of curvature are considered: (i) profile curvature is defined along the line of maximum slope (Fig. 3C); (ii) plan curvature is defined along the line of intersection between the surface and XY plan (Moore et al., 1993; Figs. 2.3D); (iii) total curvature is a general curvature of the surface rather than curvature along some line (Wilson and Gallant, 2000; Fig. 2.3E). Curvature can affect landslide susceptibility through acceleration or deceleration and through convergence or divergence of flow (Kimerling et al., 2011), depending on if it is convex, planar, or concave. In addition, steeper slope angles are related to higher shear stress, and Fig. 2.3F shows the five classes of the raster, with second class (12.95-25.92) and third class (25.92-38.87) occupying 61.76% and 24.72% of the total area, respectively.

Morphological indices related to surface roughness, such as the topographic roughness index (TRI) and surface relief ratio (SRR), also contribute to landslide susceptibility. Studies have shown that topography inside the landslide is rougher and more distinct from that of the smoother unfailed portion of the landscape. Riley (1999) classified TRI values as level, nearly level, slightly rugged, intermediately rugged, moderately rugged, highly rugged and extremely rugged. In Fig. 2.3G, TRI values in the study area are classified into four classes; slightly rugged, moderately rugged, highly rugged, and extremely rugged. The index is given by Eq. (2.1)

$$TRI = \gamma [\sum (x_{ij} - x_{00})^2]^{1/2} \quad (2.1)$$

where  $x_{ij}$  is the elevation of each neighbor cell to cell (0,0).

SRR also gives information regarding the rugosity in addition to the potential energy for mass wasting and is divided into five classes in this study, as shown in Fig. 3H. Pike and Wilson (1971) described the equation as

$$SRR = \frac{z(mean) - z(min)}{z(max) - z(min)} \quad (2.2)$$

where  $z(mean)$ ,  $z(max)$ , and  $z(min)$  are the mean, maximum, and minimum elevations, respectively.

Spatial variability owing to topographic effects can have significant influence on landslide initiation from exposure to varying climatic conditions and cause variation in hydrological conditions, such as soil moisture and groundwater flow (Park and Lee, 2014). In this study, the topography conditioning factor, which depends on the general slope and drainage characteristics of the region, has been divided into five types (Fig. 2.3I): flatland, low hilly areas, piedmont slope, valley and alluvial fan, and hilly and mountainous area. The transitions between different regimes, that significantly affect the morphology through gravitational stresses; and erosion processes, are primarily influenced by climate, tectonic characteristics, rock strength, and the history of the fluvial system (Tarolli and Fontana, 2009).

The site exposure index (SEI) rescales the aspect to a north/south axis, and weighs it by steepness of slope, creating a data set indicating the coolest to warmest locations (Davies et al., 2010), and thus providing insight into the spatial moisture variability. The SEI values were classified into five levels in this study area, with -50.08 and 53.47 respectively indicating the coolest and warmest spots, (Fig. 2.3J) and are calculated using the following equation:

$$SEI = slope \times \cos ine \left( \pi \frac{aspect - 180}{180} \right) \quad (2.3)$$

#### 2.2.2.2. Hydrological types

TWI, based on assumptions of uniform soil properties and steady state conditions (Conforti et al., 2014), can be used to describe the distribution pattern of moisture for potential infiltration volumes according to five classes (Fig.2.3K), with higher values in natural drainage channels and lower values along ridges and alluvial fans. The factor is calculated using Eq. (4) (Moore et al., 1991):

$$TWI = \ln \left( \frac{A_s}{\tan \beta} \right) \quad (2.4)$$

where  $A_s$  is the specific catchment areas, and  $\beta$  is the local slope gradient measured in degrees.

Additionally, the humidity factor provides information regarding the variation of soil wetness across the mountain and is extracted from the forestry map. Figure 2.3L shows the mountain is mainly classified into high and low humidity classes. SPI, which measures the erosive power of the flow, increases with the surge because of a larger upslope area and slope (Florinsky, 2012). Figure 2.3M shows higher erosive values existing along the drainage channels. It is given by (Moore et al., 1991)

$$SPI = A_s \times \beta \quad (2.5)$$

Another index called STI, a dimensionless term, is associated with sedimentation transport capacity, and it is a nonlinear function of slope angle and specific catchment area (in turn, affecting the discharge). Areas with high STI values correspond to greater susceptibility of the soil to erosive effects of overland flow, thus contribute to landslides. STI values of Mt. Woomyeon in Fig.2.3N are divided into five classes, with lower values occurring along ridges and flat areas. The equation is given using a combined slope factor, and can be calculated as (Moore and Burch, 1996)

$$STI = \left( \frac{A_s}{22.13} \right)^{0.6} \left( \frac{\sin \beta}{0.0896} \right)^{1.3} \quad (2.6)$$

In the hillslope domain, the presence of a slope close to drainage divides and stream networks (Fig.2.3O) can cause instability through erosion or saturation (Gokceoglu and Aksoy, 1996) and, hence, is considered as a hydrological factor. The distance from streams in the region was determined using the Euclidean distance tool in ArcGIS 10.1 and classified into five classes: < 5, 5-10, 10-15, 15-20, and > 20 m.

#### *2.2.2.3. Geological types*

Lithology plays a significant role in landslide susceptibility owing to varying characteristics, such as strength, composition, and structure (Carrara et al., 1991; Kincal et al., 2009; Chauhan et al., 2010). Figure 2.3P shows that approximately 73.55% of the area is covered by metamorphic rocks, whereas only 22.64% and 3.8% is covered by sedimentary and igneous rocks, respectively. The level of weathering, as shown in Fig. 2.3Q, will have an effect on shallow heterogeneities, such as fractures and weak zones in a slope (Bachmann et al., 2004), which can affect the susceptibility to landslides. The entire study area under consideration is exposed to only two levels of weathering: high weathering is concentrated along the ridges and piedmont slope, and moderate high weathering occurs in the valley and alluvial fans.

#### *2.2.2.4. Geotechnical types*

The landslide occurrence in Korea mainly is a result of wetting depth progression caused by infiltration of rainfall (Kim et al., 2004). The infiltration rate is affected by particle distribution, initial void ratio, and forest density, and can be represented using drainage, soil type, soil texture, soil density, soil depth, and forest density factors, as shown in Table 2.1.

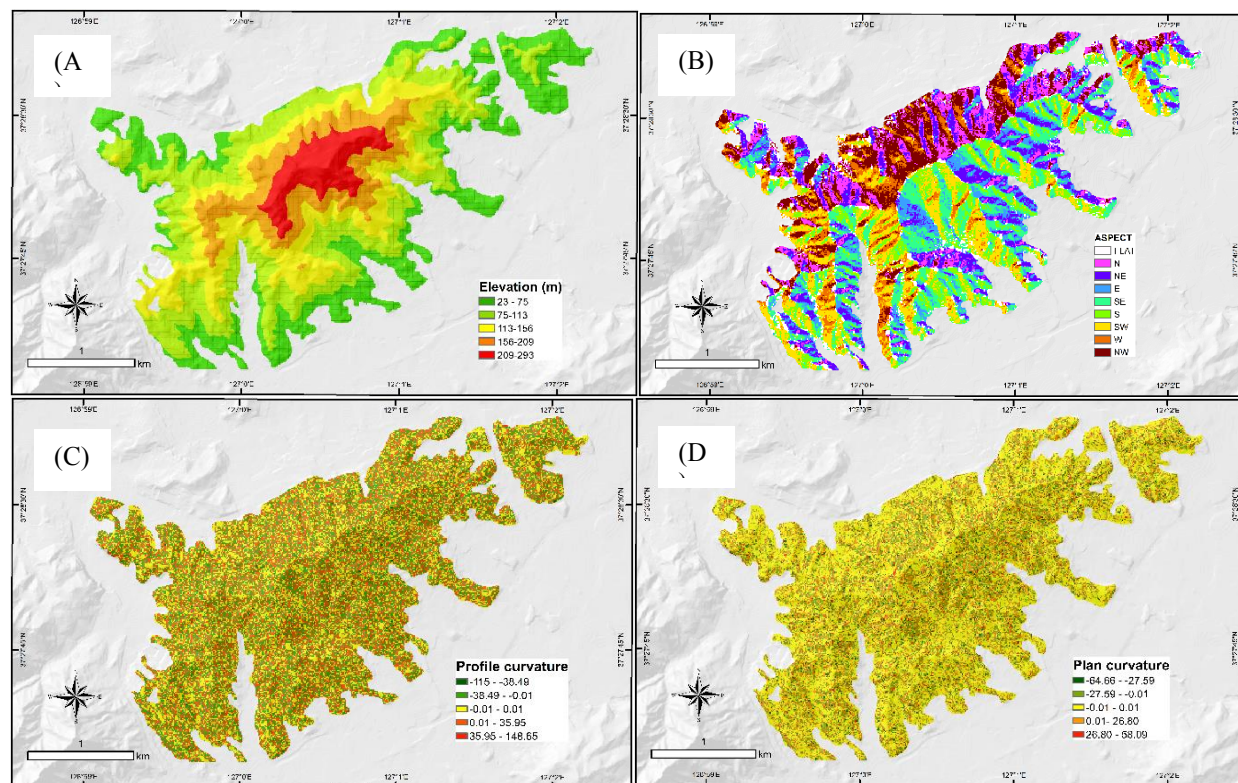
Drainage, a function of the soil water characteristic curve, indicates the relative ease of water movement through the soil. In the current study region, as seen from Fig. 2.3R, it is classified into three classes of moderate, good, and high, with increasing landslide probability. Soil type (Fig. 2.3S) and texture (Fig. 2.3T) also affect landslide susceptibility because the particle distribution governs the shape of the soil water characteristics curve and hence, the soil hydro-mechanical behavior (Lee and Min, 2001). Figures 2.3S and 2.3T show the area to have three soil types: namely, dry brown forest soil, slightly brown forest soil, and moderately moist brown forest soil, and three types of soil textures: namely, sandy loam, loam and silty loam. Several studies have been conducted to determine the effect of the void ratio or stress history on soil water characteristics in terms of influencing the initiation and failure modes of landslides (Iverson, 1997; McKenna et al., 2011).

Loose, unconsolidated soils mainly evolve into slides or debris flow, because of either high hydraulic conductivity values, which allow rapid infiltration of rainfall, or substantial entrainment under high velocity impacts of water streams, called the fire-hose effect (Johnson and Rodine, 1984), or both.

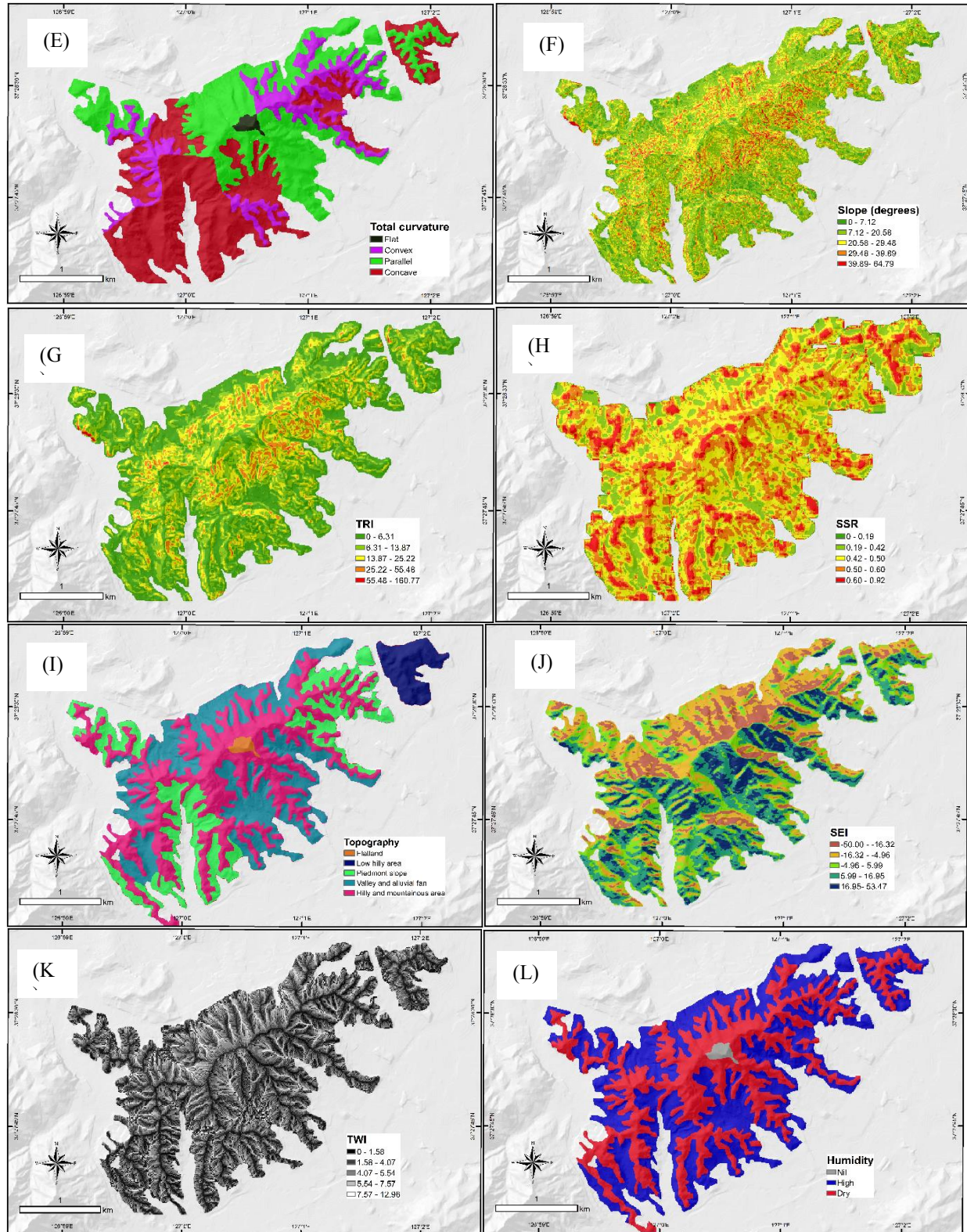
However, though dense soils may evolve into a slide or debris flow from initial slope instability from a perched water table, ground water table rise or surface runoff, the probability in comparison to the former initial stress condition is significantly lower. Figure 2.3U shows the study area to be divided into no soil (0.8%), very loose soil (10.11%), loose soil (78.35%), and medium density soil (10.76%).

#### 2.2.2.5. Forest types

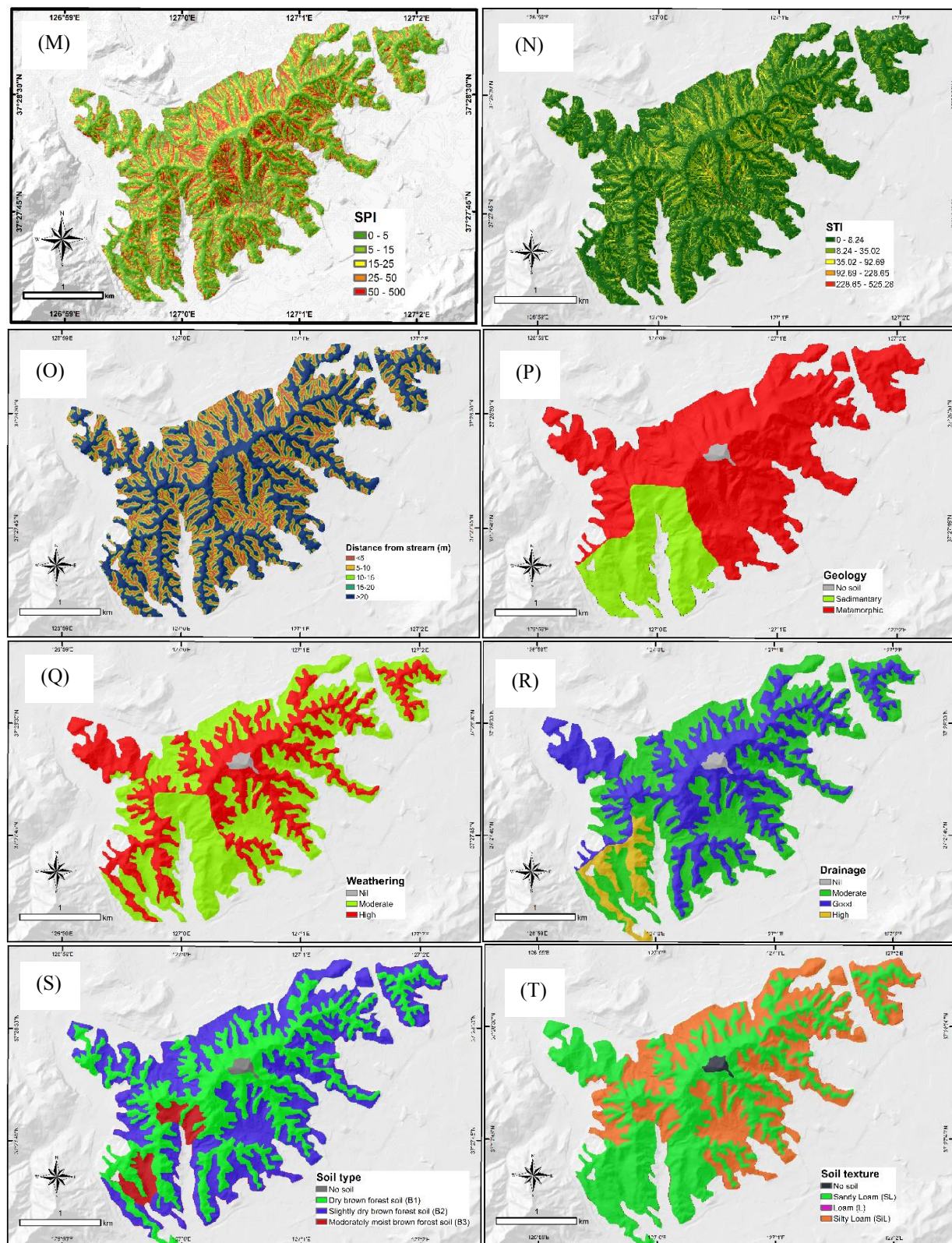
Forest density characteristics can also influence the spatial variability in landslide susceptibility through root reinforcements and reduction of soil erosion owing to surface runoff, or increase the driving stress from the additional weight of the trees. The region under study, as shown in Fig. 2.3V, consists of three forest density classes: low (0.8%), dense (18.5%), and moderate (80.7%). Soil depth (Fig. 2.3W), resulting from parent material erosion, also plays a dominant role in landslide initiation by affecting the water storage capacity and determining if the presence of vegetation favors or prevents slope instability (Dietrich et al., 1995). Figure 2.3W shows five classes of soil depth ranging from 0 to 0.88 m, indicating its spatial variability, which is the lowest at ridges and increases downslope. Additionally, the highest soil depth class (0.75-0.88) is mainly observed in the southwest part of the mountain.













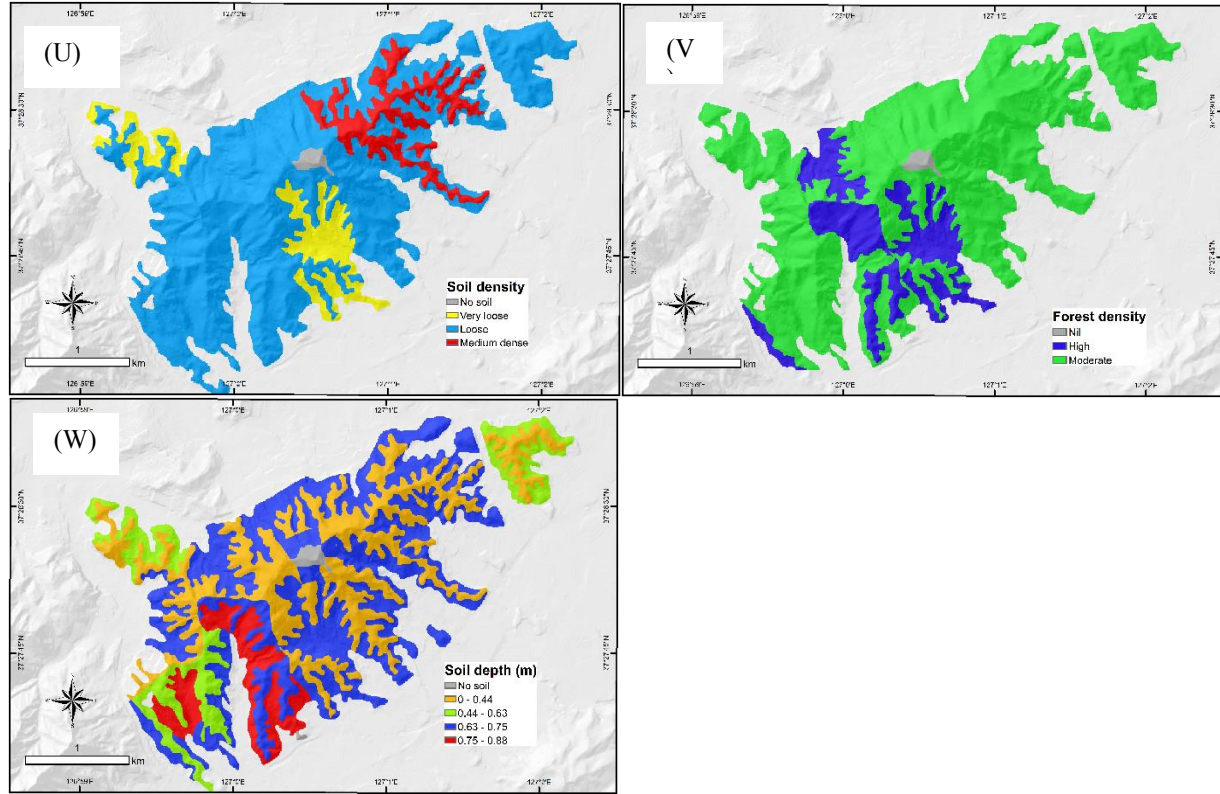


Fig. 2.3. Landslide conditioning factors: (A) Elevation; (B) Aspect; (C) Profile curvature; (D) Plan curvature; (E) Total curvature; (F) Slope; (G) TRI; (H) SRR; (I) Topography; (J) SEI; (K) TWI; (L) Humidity; (M) SPI; (N) STI; (O) Distance from stream; (P) Geology; (Q) Weathering; (R) Drainage; (S) Soil type; (T) Soil texture; (U) Soil density; (V) Forest density; (W) Soil depth.

## 2.3 Methodology

Conditioning factor selection is an important step in determining the best generalized model that can be used for landslide susceptibility mapping, and studies have been conducted to evaluate landslide factor selection methods (Santacana et al., 2013; Costanzo et al., 2012). In this study, we used a filter-based approach to make two groups, i.e., relevant and irrelevant groups, and then screened the factors in each group using the feedback loop via ELM.

### 2.3.1. Factor selection using filter method

Filter models have the advantage of not being dependent on the learning method; i.e., there is no relation between the bias of the learning algorithm and the bias of the feature selection algorithm (Tang et al., 2014). The group set of ranked factors obtained from the filter model based on correlation, distance or consistency is used to identify the best predictor model through the forward sequential scheme.

The ranking of factors is performed using a bivariate non-parametric correlation analysis called Spearman's coefficient, which evaluates the statistically significant correlation of each factor with the landslide index (LI).

For ranks  $a_i$ ,  $b_i$  calculated from raw scores  $A_i$ ,  $B_i$ , of sample size  $n$ , the correlation coefficient is calculated as follows:

$$\rho = 1 - \frac{6 \sum d_i^2}{n(n^2 - 1)} \quad (2.7)$$

where  $d_i = a_i - b_i$  is the difference between ranks.

A factor is considered significant only if its significance level is below 0.05 and the coefficient values exist between 1 (perfectly positive correlation) and -1 (perfectly negative correlation).

### 2.3.2 Extreme machine learning

The ELM was proposed by Huang et al. (2006), and is implemented as a single-layer, feed-forward network (SLFN) having  $N$  hidden neurons and arbitrarily chosen input weights and hidden layer biases. In this scheme, a better performance generalization can be obtained with a learning speed thousands of times faster than traditional learning algorithms, such as back propagation (Huang et al., 2006). This method overcomes the difficulty of tuning all parameters in traditional learning algorithms, and the problem with gradient descent based methods converging to local minima and iterative steps for better performance.

For a given training set  $\mathcal{S} = \{(x_i, t_i) \mid x_i \in R^n, t_i \in R^m, i = 1 \dots N\}$ , the learning algorithm is executed in three steps. Initially, the input weight  $w_i$  and bias  $b_i$  are randomly assigned with the size of the matrix depending on the chosen number of hidden neurons and the number of variables. The randomized weight and bias together with a user-selected activation function are used to construct a hidden output matrix  $H$ , and finally, the output weight is determined as the smallest norm least square solution  $\hat{\beta}$  given by

$$\hat{\beta} = H^\dagger T \quad (2.8)$$

where  $H^\dagger$  is the Moore-Penrose generalized inverse of the hidden layer output matrix:

$$H = \begin{bmatrix} g(w_1 \cdot x_1 + b_1) & \cdot & \cdot & \cdot & g(w_N \cdot x_1 + b_N) \\ \cdot & & & & \cdot \\ \cdot & \cdot & \cdot & \cdot & \cdot \\ \cdot & & & & \cdot \\ g(w_1 \cdot x_N + b_1) & \cdot & \cdot & \cdot & g(w_N \cdot x_N + b_N) \end{bmatrix}_{\tilde{N} \times m}, \text{ and } T \text{ is the output vector given as } \begin{bmatrix} t_1^T \\ \cdot \\ \cdot \\ \cdot \\ t_N^T \end{bmatrix}_{N \times m} \quad (2.9)$$

where  $g(x)$  is the activation function, and  $\tilde{N}$  is the hidden neuron number.

### 2.3.3 Logistic regression

Logistic regression has been widely used to estimate the relationship between landslide occurrence or non-occurrence and a set of conditioning factors (Ayalew and Yamagishi, 2005; Yesilnacar and Topal, 2005; Van Den Eeckhaut et al., 2006). This relationship is determined using the log (odds) change of the dichotomous dependent variable, and the resulting probability will always lie between 0 and 1. Though no assumption regarding the normal distribution or homoscedasticity is needed, a linear relationship is assumed between the log odds and independent variables. This linear combination is expressed as

$$Y = \beta_0 + \beta_1 A_1 + \beta_2 A_2 + \beta_3 A_3 + \dots + \beta_n A_n \quad (2.10)$$

where  $Y$  is the logit or log (odds), and  $(\beta_0, \beta_1, \beta_2, \beta_3, \dots, \beta_n)$  are the coefficients indicating the influence of independent factors  $(A_1, A_2, A_3, \dots, A_n)$  on the logit  $Y$ .

The coefficients are determined using the maximum likelihood criterion, derived from a probability density function of the dependent factor. The critical points of the log likelihood function and its maximization is conducted by taking the first and second derivative and solving the resulting non-linear set of equations iteratively. Finally, the probability of the landslide occurrence ( $P_{LC}$ ) in terms of the calculated logit is given by

$$P_{LC} = \frac{1}{1 + e^{-Y}} \quad (2.11)$$

The importance of the factors cannot be directly determined using the coefficients from SPSS because these are unstandardized values. Hence, the importance of the factors are calculated as follows:

$$\beta_s = \beta \times S_E \quad (2.12)$$

where  $\beta_s$  is the standardized coefficient,  $\beta$  is the unstandardized coefficient, and  $S_E$  is the standard error.

### 2.3.4 Hybrid model algorithm

The entire process of optimum conditioning factor selection for susceptibility mapping (Fig.2.4) is performed using the training dataset. The first stage of the scheme involves filter based screening of the entire twenty-three conditioning factors into two groups, i.e., relevant and irrelevant groups, where the factors are sorted according to correlation coefficient values in descending order. In the second stage, the hybrid algorithm conducts further factor assortment through two phases: In phase one, the backward selection based feedback loop of statistically relevant factors is used, and in phase two, the factor subset from phase one and the forward selection based feedback loop of irrelevant factors are used.

In this scheme, phase two, which involves irrelevant factors, is considered because of the following conditions: (1) the possibility of omitting indiscernible but relevant features (Kira and Rendell, 1992); (2) a feature that appears to be useless alone can contribute to significant model performance improvement when considered in combination with others (Guyon and Elisseeff, 2003; Xu et al., 2010); (3) the learning algorithm should not depend on biases in the selection of the optimal factor subset (Tang et al., 2014). In the initial step, all the factors considered in the relevant group are trained using ELM, and its performance is determined by calculating the AUC. In the subsequent steps, each of the lowest ranked factors are removed, and the performance of the new model is checked against the model built in the previous step. If the AUC value of the new model is higher than that of the previous one, then the new model is adopted, and the factor is removed; otherwise the factor is retained, indicating the importance of the factor. This process continues until all the factors in the relevant group are tested. Once the selection of best performing landslide conditioning factors are complete in the relevant group, phase two of the algorithm is set into motion. In phase two, a detailed study is performed to analyze whether adding irrelevant factors will improve the performance of the model. In this stage, the irrelevant factors are added in the forward direction, with utmost priority to the top ranked factors. The difference between the former and the latter phases is based the direction of consideration of the factors in the feedback loop for model building and the relative importance ranking of the factors.

Therefore, in this phase, the models are constructed by sequential addition of top-ranked factors and simultaneous performance control of the criteria, either the initial AUC (obtained from phase one) or those in previous step (if  $(AUC)_{previous} > (AUC)_{initial}$ ). Consequently, if the performance of the model increases by the addition of the irrelevant factor, it is then retained; otherwise, the successively ranked factor is considered. The final susceptibility model selected at the end of the second phase is then validated using the testing dataset through the prediction rate curve (Chung and Fabbri, 2003, 2005; Guzzetti et al., 2005; 2006).

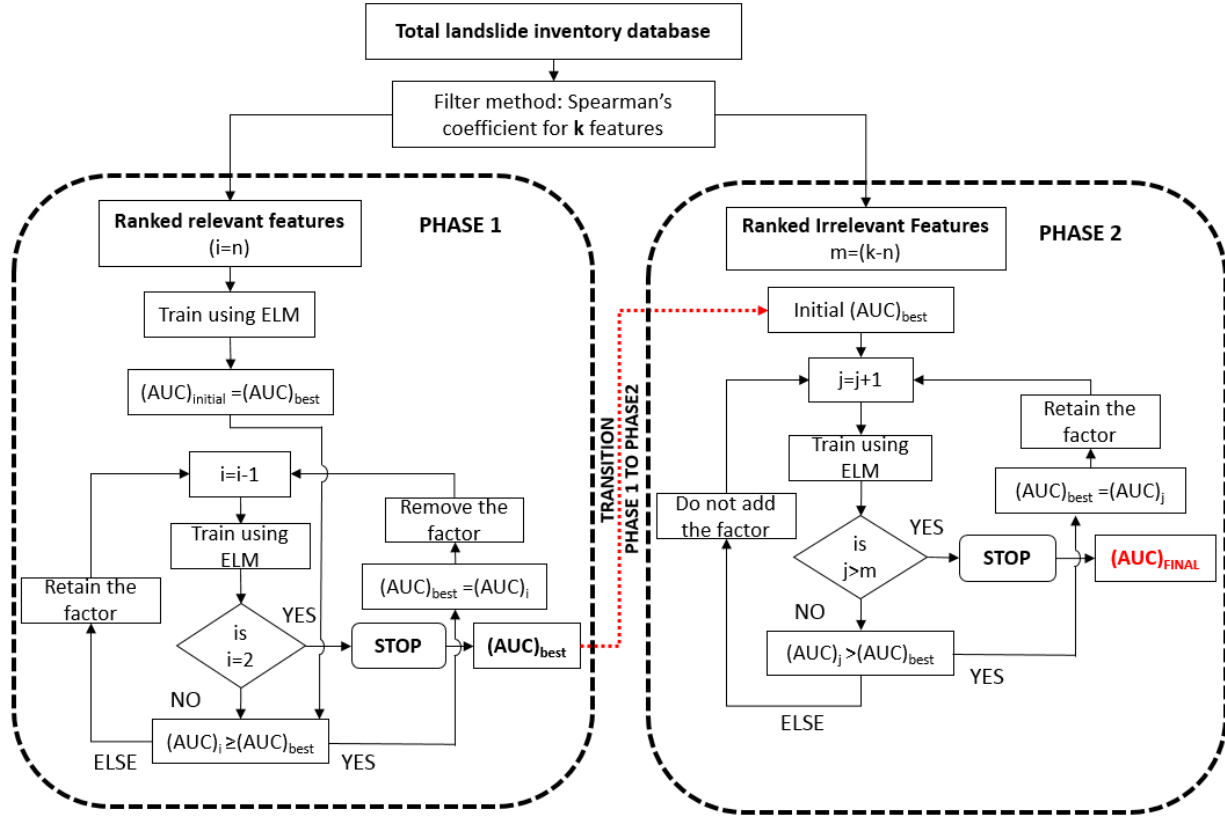


Fig. 2.4. Algorithm for feature selection using the filter and the learning scheme (ELM).

The connection weight matrices of input neurons to hidden neurons and hidden neurons to output neurons can be used to study the relative importance (RI) of the conditioning factors selected at the end of the second phase. The RI is estimated using Eq. (2.13) (Garson, 1991) to eliminate the random effect owing to randomly generated assignment to the hidden layer by normalizing the input-hidden layer weights. The relative importance is given as

$$RI_i = \frac{\sum_{j=1}^n \left( \left( |W_{ij}^{IH}| / \sum_{l=1}^m |W_{lj}^{IH}| \right) \cdot |W_j^{HO}| \right)}{\sum_{l=1}^m \left\{ \sum_{j=1}^n \left( \left( |W_{ij}^{IH}| / \sum_{l=1}^m |W_{lj}^{IH}| \right) \cdot |W_j^{HO}| \right) \right\}} \quad (2.13)$$

where  $RI_i$  is the relative importance of the input conditioning factors  $i$  for the output,  $n$  is the number of hidden neurons,  $m$  is the number of input neurons,  $W^{IH}$  is the synaptic weight matrix between the input and hidden layers, and  $W^{HO}$  is the synaptic weight matrix between the hidden and output layers.

## 2.4 Hybrid Model Implementation

### 2.4.1 Preparation of training and validation datasets

Conditioning factors, such as elevation, aspect, slope, profile curvature, plan curvature, TWI, distance from streams, SPI, STI, SEI, SRR, and TRI, were extracted from digital elevation models at 10-m resolution in ArcGIS 10.1. Additionally, other explanatory factors, such as soil type, geology, soil depth, soil density, humidity, topography, total curvature, and drainage, were extracted from a forestry map developed by the Korea Forest Service (KFS) at a scale of 1:25,000. The study area was divided into 367,856 grid cells considering a 10-m resolution in ArcGIS 10.1, and the dimensions of the raster dataset were 664 rows by 554 columns. The landslide inventory primarily consists of two main typologies: (i) flow type landslides, which are rapid moving masses through first- and second-order downhill drainages, and (ii) slides, which mainly occur on open hill-slopes with short travel distances. The landslide and stable locations were mapped as points in single grid cells to avoid issues related to the assumption of independence of factors in multivariate models because of spatial autocorrelation and errors from landslide boundary mapping (Van Den Eeckhaut et al., 2009). To avoid the class imbalance and sampling bias caused by a large area of negative samples (stable areas) in comparison to positive samples (landslide/unstable areas), an equal number of samples in both classes were considered. The negative samples or stable points were extracted by creating a buffer zone of 50 m around the landslide-affected area, as seen in Fig.2.5 (Dai and Lee, 2002; Yesilnacar and Topal, 2005), and then stable data points outside these buffer zones were selected at random. Thus, 163 stable and unstable points were selected respectively, with 87% of the total dataset being used for training and 13% being used for validation of the trained susceptibility model. The whole mountain was divided into training and validation zones, as shown in Fig.2.6, from which the training and testing datasets were extracted (Chung and Fabbri, 2003). The continuous and discrete conditioning factor datasets, respectively corresponding to the selected landslide and non-landslide points, were extracted to a csv format using the spatial analyst tool in ArcGIS 10.1, and normalized between -1 and 1 to account for the difference in scales of the conditioning factors.



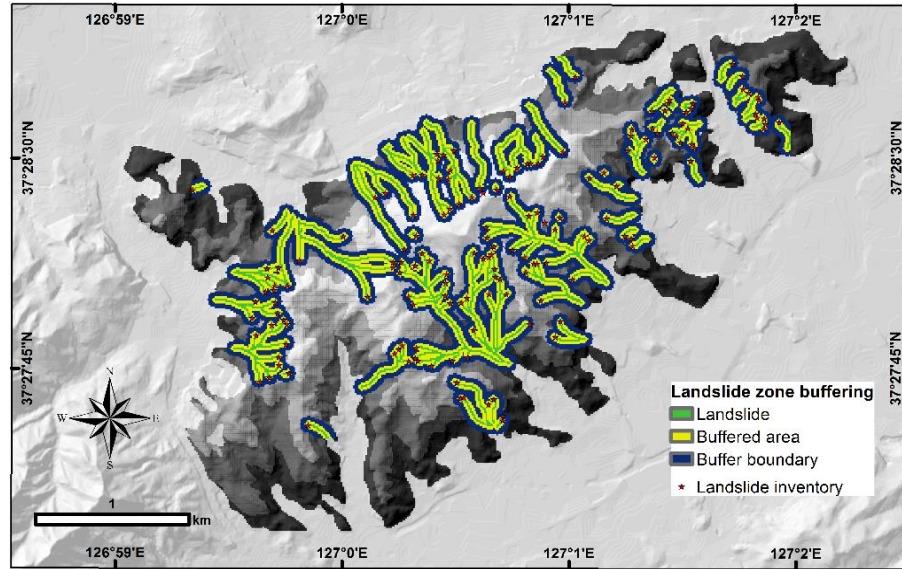


Fig.2.5. Sampling of unstable and stable points.

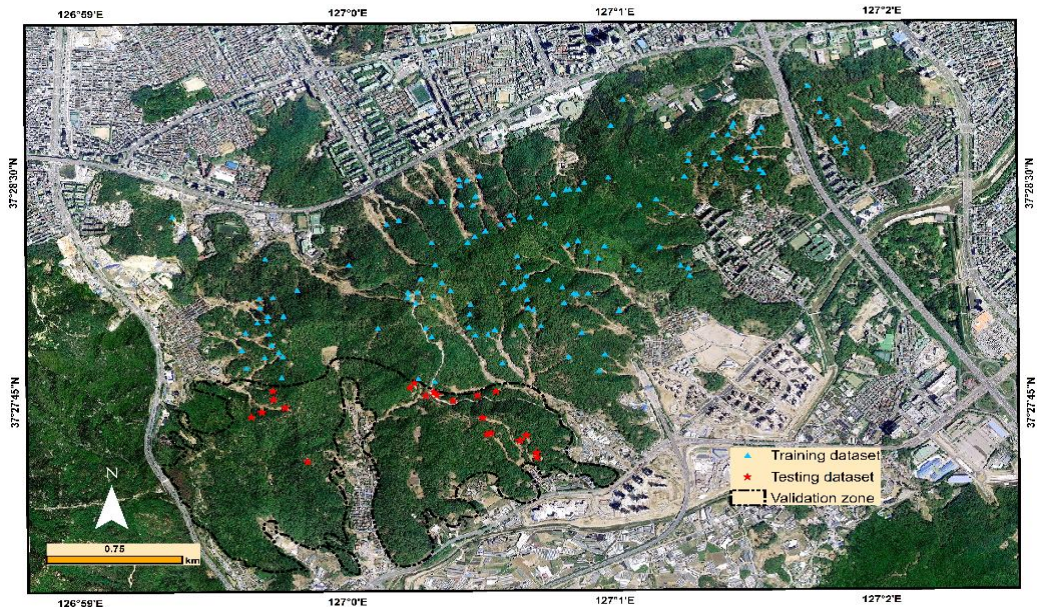


Fig.2.6. Satellite imagery and overlay with landslide locations (Training and testing dataset).

#### 2.4.2 Selection of the best predictor model

As discussed in section 2.2, initially 23 conditioning factors assumed to have significant influence on landslide initiation were selected from the literature. The correlation analysis was conducted using IBM SPSS Statistics 23, a statistical software package with several built-in statistical techniques for analytic processes, from data preparation to exploring relationship among variables, trend identification and forecasting.

Table 2.2 shows the Spearman's correlation values and their significance, indicating that only eleven factors, namely, elevation, total curvature, soil depth, geology, TRI, distance from stream, STI, SPI, slope, plan curvature, and soil density, are considered statistically significant ( $p < 0.05$ ) and, hence, relevant. The selected factors were sorted and ranked from high to low based on their correlation coefficient values. Elevation is the most influential conditioning factor, with a coefficient of 0.401, followed by total curvature (0.274), and soil depth (-0.214). The negative correlation for the soil depth and soil density indicates that areas with shallow soil depth and loose soils are highly susceptible to landslides.

Table 2.2: Correlation of explanatory variables with landslide index

<b>Factors</b>	<b>Mann-Whitney U (<math>\chi^2</math>)</b>	<b>Sig. (2-tailed)</b>	<b>Correlation Coefficient</b>	<b>Significance level</b>
Elevation	5336.0	0	0.401	0
Total curvature	6954.5	0	0.274	0
Soil depth	7515.0	0	-0.214	0
Geology	8302.0	0.001	0.191	0.001
TRI	7759.0	0.001	0.190	0.001
Distance from stream	8003.5	0.003	-0.178	0.003
STI	8013.0	0.005	0.168	0.005
SPI	8030.5	0.005	0.167	0.005
Slope	8209.5	0.011	0.151	0.011
Plan curvature	8585.0	0.033	0.127	0.033
Soil density	8837.0	0.043	-0.121	0.043
TWI	8842.0	0.108	0.091	0.108
Topography	9326.0	0.321	0.059	0.322
Aspect	9324.0	0.353	0.055	0.354
Drainage	9388.5	0.365	-0.054	0.366
Soil texture	9459.0	0.403	-0.050	0.404
Soil type	9512.0	0.481	-0.042	0.482
SRR	9467.0	0.490	0.041	0.431
Profile curvature	9516.0	0.524	-0.038	0.525
Forest density	9653.0	0.563	-0.035	0.564

Table 2.2  
(continued)

<b>Factors</b>	<b>Mann-Whitney U (<math>\chi^2</math>)</b>	<b>Sig. (2-tailed)</b>	<b>Correlation Coefficient</b>	<b>Significance level</b>
Weathering	9887.5	0.930	0.005	0.330
SEI	9926.0	0.983	0.001	0.383



Once subsets of features were developed using the methodology previously described (section 2.3), extreme learning machine is used to construct models. The selection of the best predictor model is performed by considering the AUC through plotting the landslide distribution percentage against the landslide susceptibility class of the training data. The input used in model development using ELM is the training data, testing data, number of hidden neurons and the type of activation function (sigmoid, sine, or hard limit). The selection of the optimal number of hidden neurons was conducted by setting up a group of neurons in the range of 5 to 150 and examining the RMSEs of both the training and testing data. Figure 2.7 illustrates that the RMSE values for training data decreases with the increasing number of neurons; the RMSE of the testing data is initially very close to that the training data, but starts diverging rapidly after 20 (Figs.2.7A to 2.7J) and 30 (Figs.2.7K to 2.7L), indicating overfitting. Consequently, the search for an optimal number of neurons was conducted between the minimum number of neurons and maximum threshold of 20 or 30, and finally the one with the least RMSE for both training and testing data was selected.

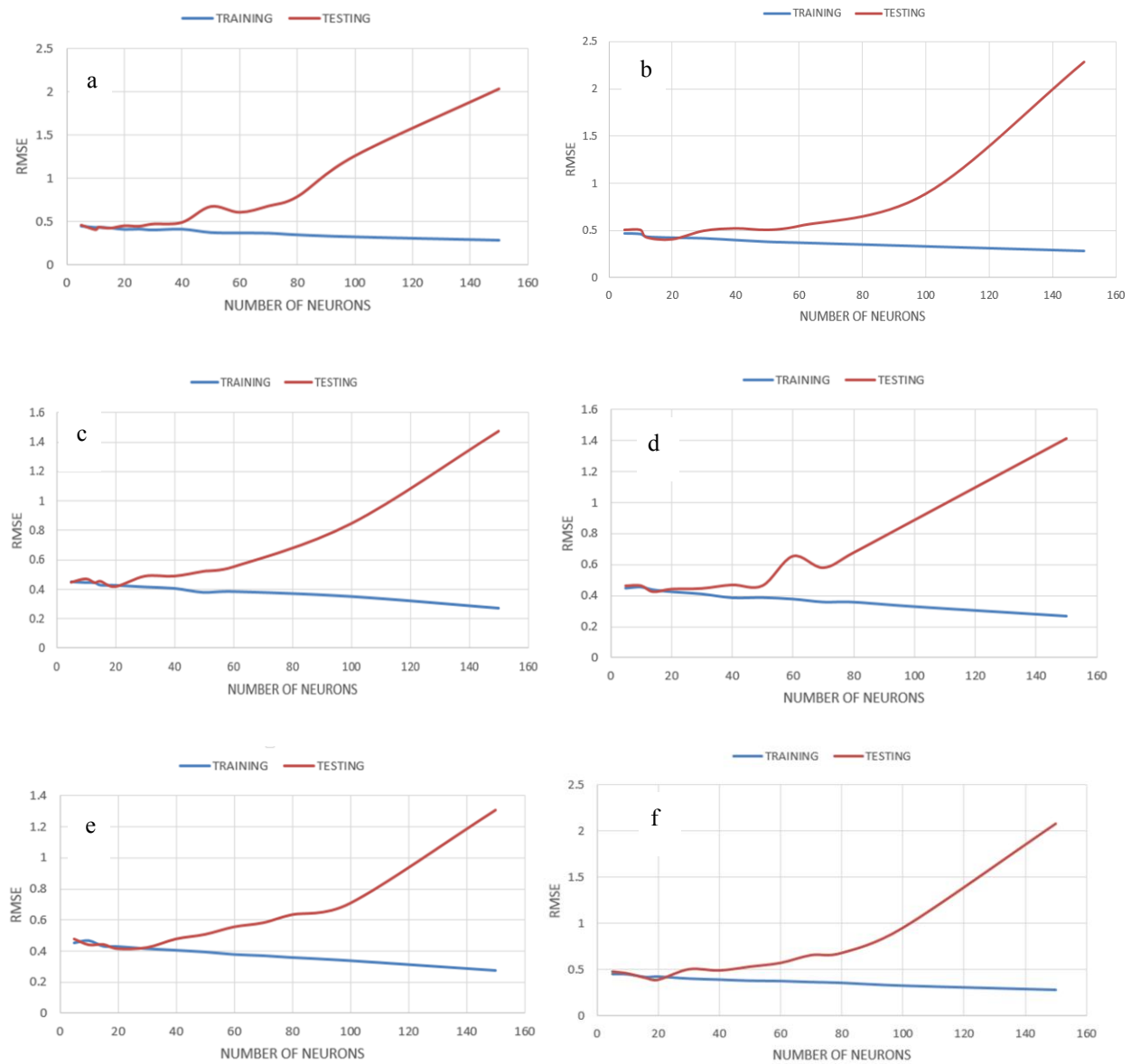


Fig. 2.7. Variation of RMSE versus number of neurons for training and validation data to select the optimal hidden neurons for the groups (Cont.)

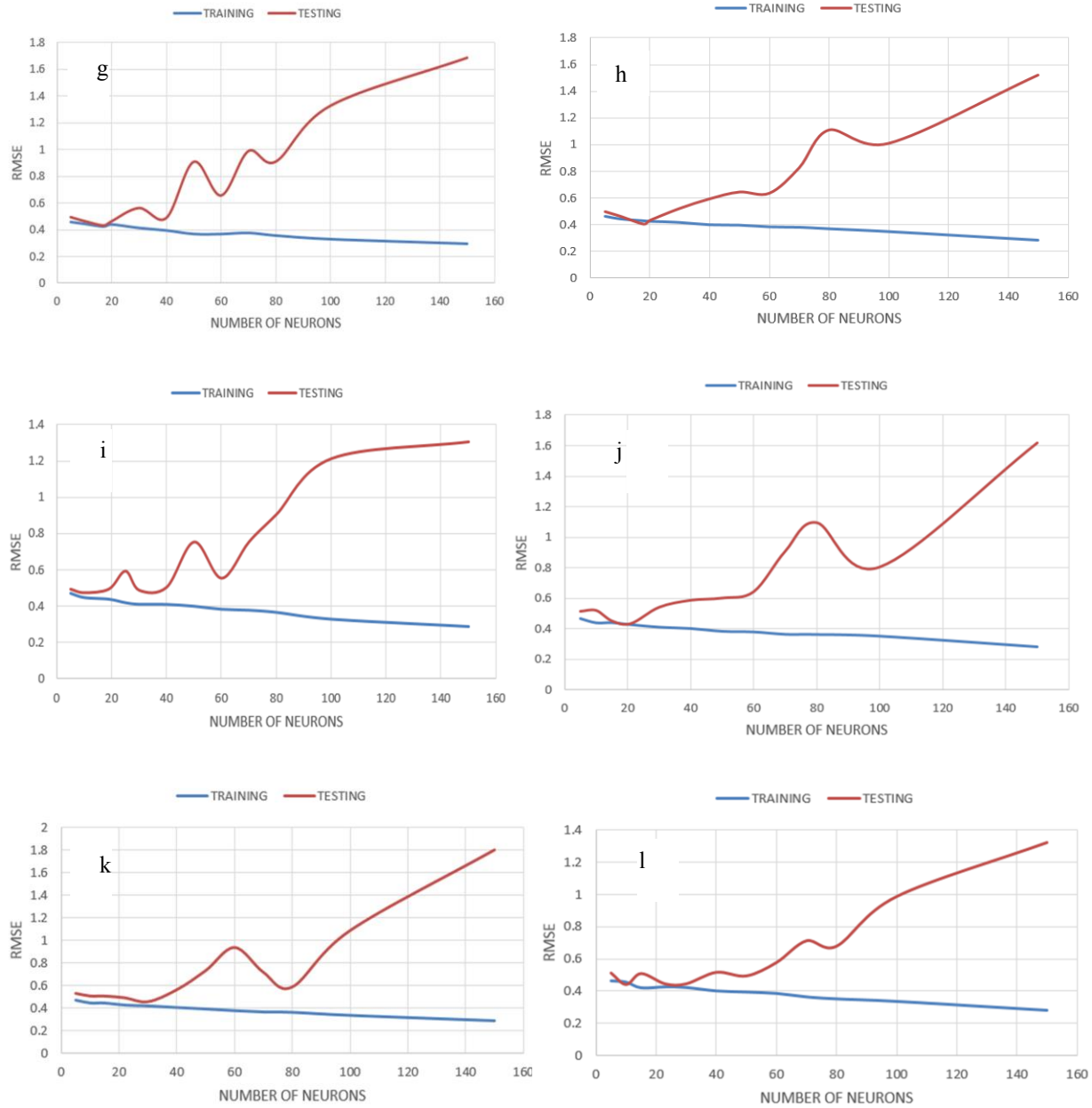


Fig. 2.7. Variation of RMSE versus number of neurons for training and validation data to select the optimal hidden neurons for the groups.

Table 2.3 shows the optimal number of neurons contributing to the lowest values of training as well as testing RMSE for the two phases. In phase one, the algorithm initially considers all eleven significant factors, and uses ELM to train and identify the optimal fifteen hidden neurons that minimize the training and testing error to 0.4308 and 0.4203, respectively, and the performance index  $AUC_{initial}$  is set to 68.3%. In the next step, the exclusion of the conditioning factor of soil density ( $-0.121, p=0.011$ ) increases both the training RMSE (0.4532) and testing RMSE (0.4436), and thus decreases the AUC obtained from the success rate curve to 68%, as seen in Table 2.4. A comparison of new and

initial AUC by the feedback loop shows a decrease in performance, prompting the factor to be retained, and the performance criterion is not updated. In steps 5 and 10, the exclusion of SPI and soil depth shows a modest increase in the performance relative to the preceding steps by 3.56% and 0.25%, respectively, but the performance is still lower than that of  $AUC_{initial}$ , leading to the inclusion of the factors. Thus, in phase one, a general trend of performance decrease is observed owing to successive removal of relevant factors in all of the 11 steps. Hence, all relevant factors are considered during the transition to phase two along with the performance criterion AUC value of 68.3%. Additionally, though Group 1 uses only the statistically important variables that are related to the dependent variables, it still gives a very low training performance of 68.30%, suggesting the possible contribution of factors classified as irrelevant to increasing the model prediction performance.

In the second phase, low-ranked, statistically non-significant factors are added one by one using a forward search scheme. However, the selection of a model only based on the RMSE value can be misleading, and the same is noted for the application of AUC in Table 2.4. It is evident from Table 2.4 that Group 2 and Group 3 in phase two, though not showing the lowest training or testing RMSEs, yield the best performances. Similarly, Groups 7, 11 and 12 and Groups 6 and 8, with the lowest training and testing RMSEs, respectively, have lower AUC values in comparison to Groups 2 and 3. For Group 2, the addition of TWI increases the performance of the model by 9.3%; thus, by retaining the parameter, the AUC criterion in the algorithm increased to 77.6%. In the next step, topography is added to the Group 3 model and is trained using ELM with a hidden layer of 20 optimal neurons, giving an AUC value of 85%. Therefore, the algorithm retains the factor and updates the AUC criterion, yielding the best predictor model, with thirteen conditioning factors. A further assessment demonstrates a drastic decrease in the performance, signifying the irrelevance of the following factors: aspect, drainage, soil texture, soil type, SSR, profile curvature, forest density, humidity, weathering and SEI. Therefore, to develop a susceptibility model for Mt. Woomyeon, the conditioning factors in subset Group 3 of the second phase are used. The weight and bias between the hidden and output layers obtained after the training of the Group 3 predictor model are shown in Table 2.5.

Validation of the selected model is performed using the prediction rate curve, which has a high AUC of 0.89, as seen in Fig. 2.8A. The figure also shows the success rate curve with a high AUC of 0.85, which along with RMSE was concurrently used in the hybrid feedback scheme.

Many researchers have divided the susceptibility map histogram into different categories based on expert opinions or using automated classification systems, such as quantiles, natural breaks, equal intervals and standard deviations

(Guzzetti et al., 1999; Lee and Min, 2001; Dai and Lee, 2002; Ayalew and Yamagishi 2005). For a given histogram of susceptibility weight, the following classification schemes can be used in ArcGIS 10.1: (i) the equal interval scheme, which divides the data into equal classes, with the probability of some classes being zero; (ii) the quantile scheme, which distributes an equal number of features to each class, leading to some classes having a wide range of values and the same values falling into different classes; (iii) the standard deviation scheme, which creates classes by using the standard deviation from mean values under the Gaussian distribution constraint; (iv) the natural breaks scheme, which creates classes by grouping similar values and selecting boundaries with large jumps in data values.

The histogram in Fig. 2.9A shows the distribution of landslide susceptibility values with its mean and standard deviation. However, the non-normal distribution of the susceptibility data, tested using the Kolmogorov-Smirnov (K-S) test, renders only the natural breaks (jenks) as the best scheme for classification. The landslide susceptibility weight map illustrated in Fig. 2.9B was reclassified using the jumps in data values at -0.0319, 0.2272 and 0.5004 into four hazard classes of low, moderate, high, and very high, as in Fig. 2.9C.

Table 2.3: Final number of hidden neurons selected for each group

Group	Number of variables	Activation function	Optimal number of neurons	Training RMSE	Testing RMSE
PHASE1					
1	11	Sigmoid	15	0.4308	0.4203
2	10	Sigmoid	10	0.4532	0.4436
3	10	Sigmoid	10	0.4985	0.4936
4	10	Sigmoid	15	0.4863	0.4789
5	10	Sigmoid	15	0.4798	0.4769
6	10	Sigmoid	20	0.4621	0.4532
7	10	Sigmoid	20	0.4652	0.4551
8	10	Sigmoid	20	0.4852	0.4462
9	10	Sigmoid	15	0.4513	0.4510
10	10	Sigmoid	20	0.4766	0.4701
11	10	Sigmoid	20	0.4666	0.4585
12	10	Sigmoid	20	0.5239	0.4965
PHASE2					
1	11	Sigmoid	15	0.4308	0.4203
2	12	Sigmoid	20	0.4251	0.4100
3	13	Sigmoid	20	0.4286	0.4210
4	14	Sigmoid	14	0.4414	0.4278
5	14	Sigmoid	20	0.4292	0.4131
6	14	Sigmoid	20	0.4272	0.3896
7	14	Sigmoid	14	0.4244	0.4291
8	14	Sigmoid	15	0.4276	0.4043
9	14	Sigmoid	15	0.4458	0.4747
10	14	Sigmoid	20	0.4278	0.4355
11	14	Sigmoid	30	0.4170	0.4521
12	14	Sigmoid	30	0.4222	0.4476
13	14	Sigmoid	30	0.5901	0.4877

Table 2.4: Algorithm phase and selection of optimal conditioning factors

Phase	Group	Variables	Removed/ added	Training model based AUC (%)
<b>1st phase Backward Elimination scheme</b>	Group 1	All(significant)		68.30
	Group 2	Soil density	No	68.00
	Group 3	Plan curvature	No	62.00
	Group 4	Slope	No	61.80
	Group 5	SPI	No	64.00
	Group 6	STI	No	63.50
	Group 7	Distance from stream	No	61.30
	Group 8	TRI	No	61.54
	Group 9	Geology	No	60.85
	Group 10	Soil depth	No	61.00
	Group 11	Total curvature	No	60.96
	Group 12	Elevation	No	60.12
<b>2nd phase Forward search scheme</b>	Group 1	All (significant)		68.30
	Group 2	TWI	Yes	77.60
	Group 3	Topography	Yes	85.00
	Group 4	Aspect	No	53.37
	Group 5	Drainage	No	49.78
	Group 6	Soil texture	No	55.68
	Group 7	Soil type	No	52.56
	Group 8	SRR	No	56.37
	Group 9	Profile curvature	No	54.26
	Group 10	Forest density	No	59.65
	Group 11	Humidity	No	53.20
	Group 12	Weathering	No	56.05
	Group 13	SEI	No	51.00

Table 2.5: ELM output weights and bias

Weight	0.5584	-0.2714	0.0241	-0.7014	1.2635	0.6771	-0.434	-0.3253	-1.032	-0.4348	0.6661
Bias	0.4517	0.6098	0.0594	0.3158	0.7727	0.6964	0.1253	0.1301	0.0923	0.0078	0.4231

Weight	0.8303	-1.2799	1.8021	-2.4232	0.3641	-0.0329	-1.6116	1.89	0.796
Bias	0.6555	0.7229	0.5312	0.1088	0.6317	0.1265	0.1343	0.0985	0.142

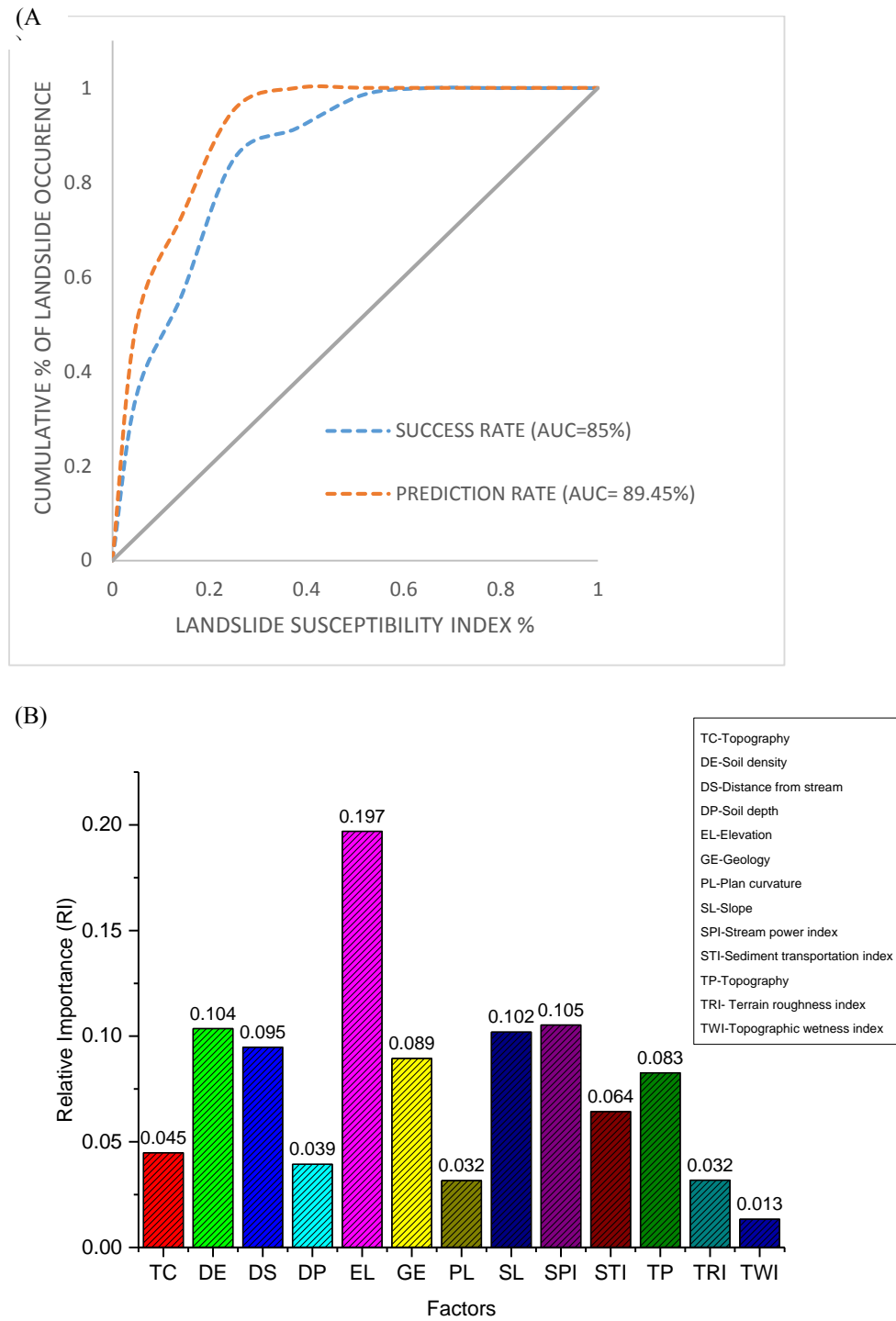
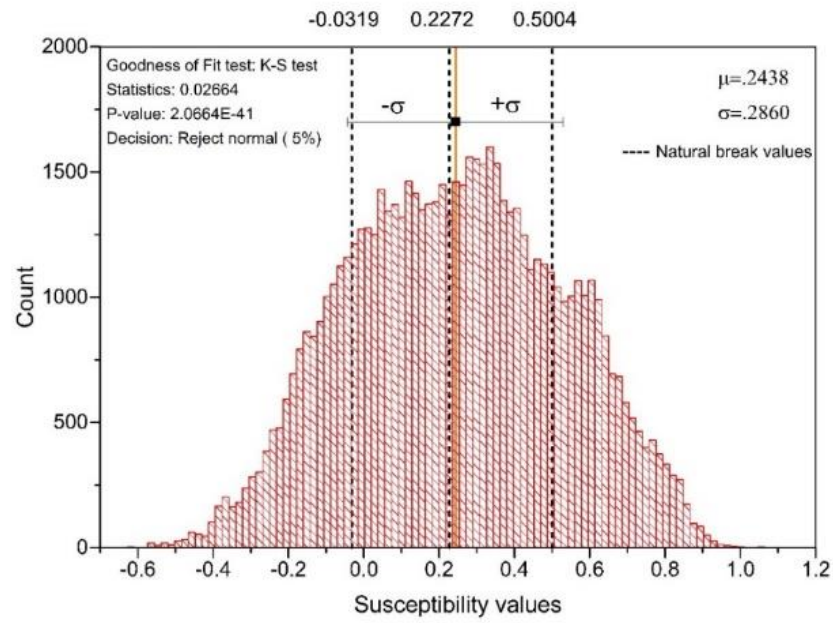


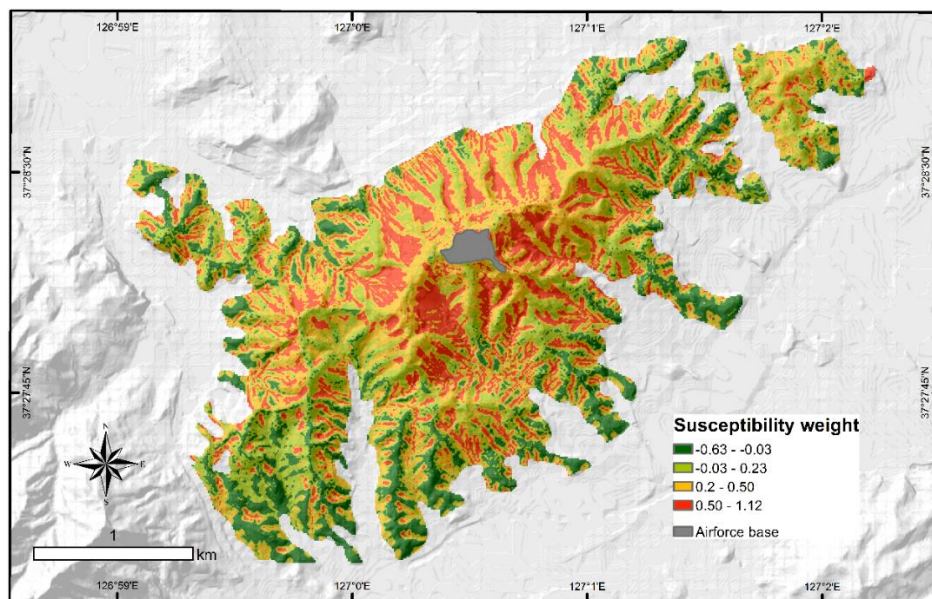
Fig. 2.8. Final landslide susceptibility model: (A) Success rate and prediction rate curve; (B) Relative importance of the final conditioning factors.



(A)



(B)



(C)

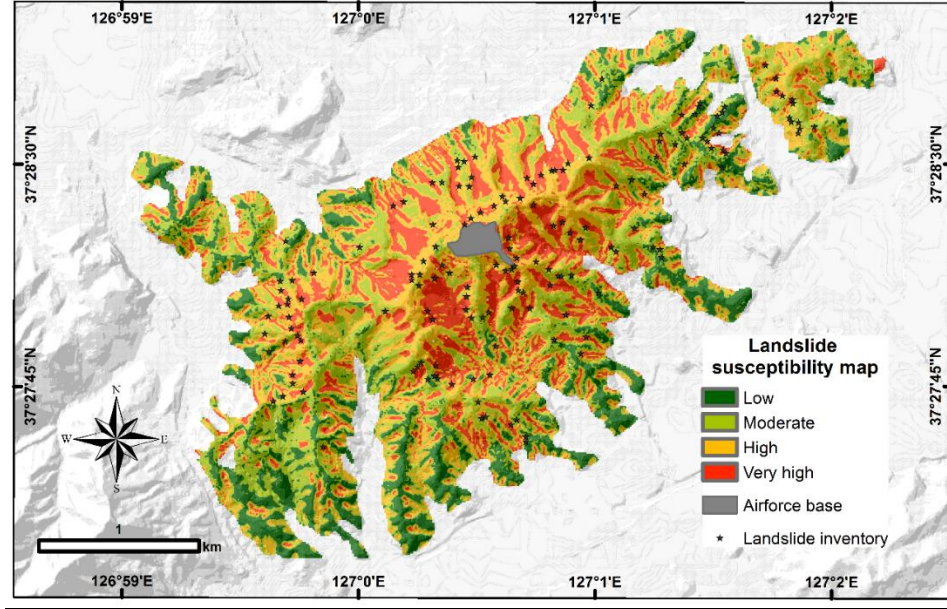


Fig. 2.9. Landslide susceptibility of Mt. Woomyeon: (A) Histogram; (B) Landslide susceptibility weight; (C) Landslide susceptibility levels.

## 2.5 Discussion

In this study, high values of AUC for the success and prediction rate curves point towards the high predictability of the developed susceptibility model. The susceptibility map predicts the following percentage of areas in each susceptibility class, as shown in Fig. 2.10: low (19.3%), moderate (29.2%), high (30.9%), and very high (20.6%).

The percentages of training and testing data distributed in the susceptibility classes of the model are also shown in Fig. 2.10. Approximately 98.68% of the total training landslides were distributed among the very high (70.92%) and high (27.66%) susceptibility classes, whereas only 1.42% fell within the moderate class. However, 86.36% of the total testing landslide data were classified within the very high susceptibility class, and the remaining 13.64% were grouped into the high susceptibility class.

Using a two stage-hybrid model algorithm, thirteen factors, namely, soil density, plan curvature, slope, SPI, STI, distance from stream, TRI, geology, soil depth, total curvature, elevation, TWI, and topography, were selected as the most relevant factors in the study area. Adoption of this method helped in identification of the significant factors, some of which were initially classified as irrelevant for developing an optimized susceptibility map. The susceptibility model, consisting of eleven conditioning factors with high correlation values at the end of phase one, gave a low success rate curve AUC of 68.3%; in other words, there were conditioning factors that might have been unaccounted

for in the model, and misclassified into the irrelevant subset. Thus, in the second phase, the addition of TWI and topography, with correlation values less than 0.1 (significance level,  $p > 0.05$ ), increased the success rate of the susceptibility map by 24.5%. In GIS-based landslide susceptibility research, the selection of conditioning factors depends on the correlation with landslide occurrence, study area representation, spatial variation and relevance (no double consequence effect in the final result) (Yalsin, 2008). Table 2.2 shows the chi-square values and their significance calculated using the Mann-Whitney U test for analyzing if a significant difference exists between the landslide and non-landslide sets of the landslide conditioning factors. The test suggests that a significant difference exists between the median of the sets for the following factors: elevation, total curvature, soil depth, geology, TRI, distance from stream, STI, SPI, slope, plan curvature, and soil density. The test result in Table 2 also shows no difference between the medians of the landslide and non-landslide sets for all of the factors in the irrelevant group because of insignificant chi-square values, and hence, these factors are not significantly correlated to the LI. The landslide susceptibility conditioning factors of aspect, profile curvature, SSR, SEI, drainage, humidity, soil texture, soil type, weathering, and forest density were classified as irrelevant and removed in the hybrid scheme because the factors as shown in Table 2.2 exhibited non-significant Chi-square values, suggesting that no median difference exists between the landslide and non-landslide sets, and they are correlated to the relevant conditioning factors. However, the irrelevant group contributes two factors, TWI and topography, to the final susceptibility model, with RIs of 8.3% and 1.3%, respectively. This behavior can be attributed to the fact that both topography and TWI are correlated to other relevant factors used in the final model. This unconditional independence yet conditional dependence between the explanatory and dependent factors can be explained using the suppression concept (MacKinnon et al., 2010). The two irrelevant factors, though not significantly related to the target, act as suppressors to increase the predictability of the overall model because their correlations to other relevant factors are statistically significant. The relevant hydrological factors used in the model, i.e., SPI and STI, are primarily related to the erosive effects of streams or the sediment transportation capability of a channel and are not used to assess the spatial variability of the moisture pattern influencing infiltration. The presence of a higher proportion of landslides in convex (31.21%) and parallel (46.81%) types of curvatures strongly implies that the matric suction reduction because of infiltration or an increase in groundwater table are likely reasons for these observed instabilities in addition to the erosion caused by runoff. The field monitoring of the matric suction adjacent to debris flow gullies shows a rapid decrease of suction in the colluvium during rainfall events, especially at a shallow depth of 30 cm, and slightly delayed effect at a depth of 1.3 m, indicating

favorable conditions for slope failure at shallow depths (Korean Society of Civil Engineers, 2012). Another phenomenon resulting in slope instability and thus, debris flow mobilization, is the influence of groundwater table variation, typically controlled by the topographic characteristics of the region. A field investigation after a debris flow event showed the exfiltration of groundwater from the bedrock underlying the initiated zone (Jeong et al., 2015), implying the effect of the groundwater table in the failure of the above colluvium layer and its liquefaction under rapid undrained conditions. Though, it can be argued that relevant factors statistically correlated to TWI or topography can also be used to indirectly consider these effects, the success rate curve AUC for the susceptibility model considering only relevant factors at the end of phase one suggests otherwise (Table 2.4). Hence, TWI and topography, which can be used to assess the spatial distribution pattern of moisture caused by rainfall, are thus considered analogous to the volume of water likely to infiltrate, and the groundwater table variation, respectively, and therefore, are assimilated with the hydro-morphological characteristics controlling the landslide initiating phenomenon in the region.

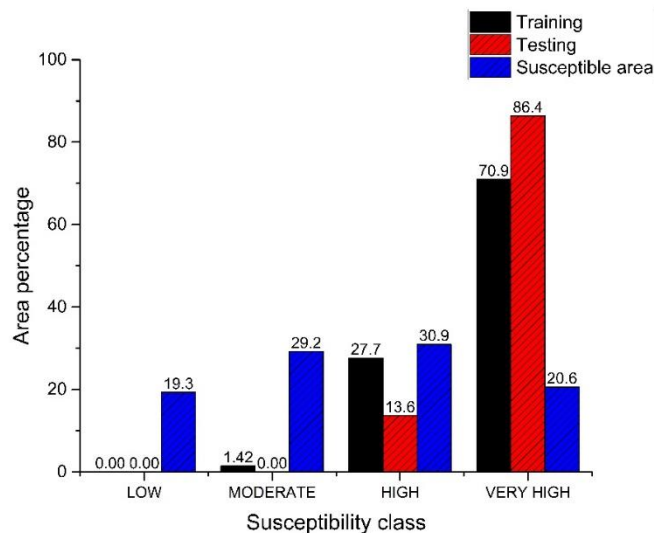


Fig. 2.10. Area percentage of susceptibility classes.





Fig. 2.11. Landslides on Mt. Woomyeon: (A) Landslide scarp; (B) Debris flow gully (entrainment); (C) Ground water table underlying the removed colluvium; (D) Deposition zone (Korean Geotechnical Society, 2011).

Figure 2.8B shows the relative importance (RI) of the thirteen factors with respect to landslide susceptibility in the Woomyeon area calculated using equation (2.12).

The chart suggests that the most important topographic control is elevation with an RI of 21.24% followed by SPI, soil density, and slope, with RIs of 10.53%, 10.36% and 10.19%, respectively, indicating that the areas with geomorphological characteristics of large upslope areas and steep slopes at high altitude covered by loose, colluvium have significantly high probability for landslide (debris flows/slides) occurrence under heavy rainfall. The hourly and cumulative rainfall, shown in Fig.2.2B, was measured at the meteorological stations located at 87.1 m a.s.l and 35.5 m a.s.l, respectively (Park et al., 2013), indicating that the actual rainfall was most likely higher from the development of convective systems caused by the orographic effect (Park and Lee, 2007). This orographic effect results in localized torrential rainfall, thereby controlling the spatial distribution of landslides. Elevation, with the highest RI in comparison to the other relevant factors, can also capture the localization effect in the rainfall distribution. The landslide susceptibility map in Fig. 2.9C therefore illustrates the considerable number of slopes closer to the peak of the mountain in all directions that are classified as high and very high susceptible zones. Additionally, the classification

of grid cells in the drainage channels and valleys as highly susceptible to landslides can be ascribed to the selection of four influential hydrological parameters, SPI, distance from stream, STI and TWI. These hydrological factors can primarily be used to identify the grid cells with predisposition to erosion risk, either at the channel head or along streams, with those at higher elevations having higher susceptibility to flow type landslides owing to intensified inertial and kinematic stresses. This result is consistent with that observed in the field after the 2011 event (Fig. 2.11B), wherein intense entrainment was observed in the channels under high erosion energy, instigating the debris flows. In comparison, a higher percentage of slopes in the southwestern, northwestern and far northeastern areas of the mountain show low to moderate susceptibility, which under the effect of heavy rainfall can be reach high or very high susceptibility levels with increased instability.

The wrapper method utilizing the logistic regression was conducted for the selection of landslide conditioning factors, providing an optimized susceptibility map for comparison with the hybrid model. This analysis was performed using the same training and testing datasets in IBM SPSS Statistics 23 through binary logistic regression with the factor selection based on maximum changes in the likelihood ratio. The reliability test for the selected model with a set of fifteen conditioning parameters was performed using the Omnibus and Hosmer and Lemeshow goodness-of-fit statistics test by calculating the Chi-square value and its significance (Table 2.6B). The Omnibus test gives the model Chi-square value of 138.588, with a significance of  $< 0.05$ , suggesting that the relationship between the dependent variable and the subset of conditioning factors is significant. The Hosmer and Lemeshow goodness-of-fit statistic, a measure of the correspondence between the actual and predicted values of the dependent factors, gives a Chi-square value of 10.077 and a significance of 0.260. Thus, a goodness-of-fit statistic with a value  $> 0.05$  indicates a close correspondence between the predicted landslide susceptibility weight and the actual landslide susceptibility weight, i.e., a good model fit. Additionally, a check for numerical problems in the model was conducted by checking if the standard error (S.E.) was  $> 2$  or had unusually large B coefficients. Table 2.6A shows that all the conditioning factors have S.E.  $< 2$ , and no inherent numerical errors in the model existed.

Using the coefficient values of the fifteen factors, a landslide susceptibility map was developed, as shown in Fig. 2.12A, and the validation was performed using the AUC of the success rate and prediction rate curves. Figure 2.12B demonstrates the success and prediction rate curves and the corresponding AUC values. Although a classification accuracy of 79.4% is obtained, considering 0.50 as the cutoff, the success rate curve gives an AUC of only 69.19%, and an even lower AUC value of 56.19% for the prediction rate curve. The backward conditional feature selection

method selected six factors, namely, forest density, humidity, profile curvature, SEI, soil texture, and weathering, all of which are deemed as irrelevant using the hybrid algorithm implemented in this study. Though the same dataset was used in both methods, different subsets of conditioning factors were selected, indicating the importance of the factor selection methodology in terms of the predictive quality of a susceptibility map. Thus, a hybrid scheme using a filter and wrapper model as a coupled system, similar to the method implemented in this study, helps in objective selection of conditioning factors, leading to superior landslide susceptibility determination.

Table 2.6: (a) Coefficients of the selected landslide susceptibility model using logistic regression in SPSS

<b>Coefficients</b>	<b>B</b>	<b>Standard error</b>	<b>Coefficients</b>	<b>B</b>	<b>Standard error</b>
Total curvature	-0.947	0.385	Profile curvature	0.020	0.012
Soil density	-1.798	0.485	SEI	0.019	0.010
Distance from stream	-0.390	0.129	Slope	0.030	0.018
Elevation	0.017	0.004	Soil texture	0.969	0.831
Forest density	0.957	0.675	STI	-0.009	0.016
Geology	1.528	0.616	Topography	-0.777	0.524
Humidity	2.138	0.714	Weathering	-3.731	1.225
Plan curvature	0.031	0.014	Constant	1.343	2.777

(b) Test for factor significance and goodness-of-fit

<b>Type</b>	<b><math>\chi^2</math></b>	<b>Significance level</b>
Omnibus test	138.588	.000
Hosmer and Lemeshow test	10.077	.260

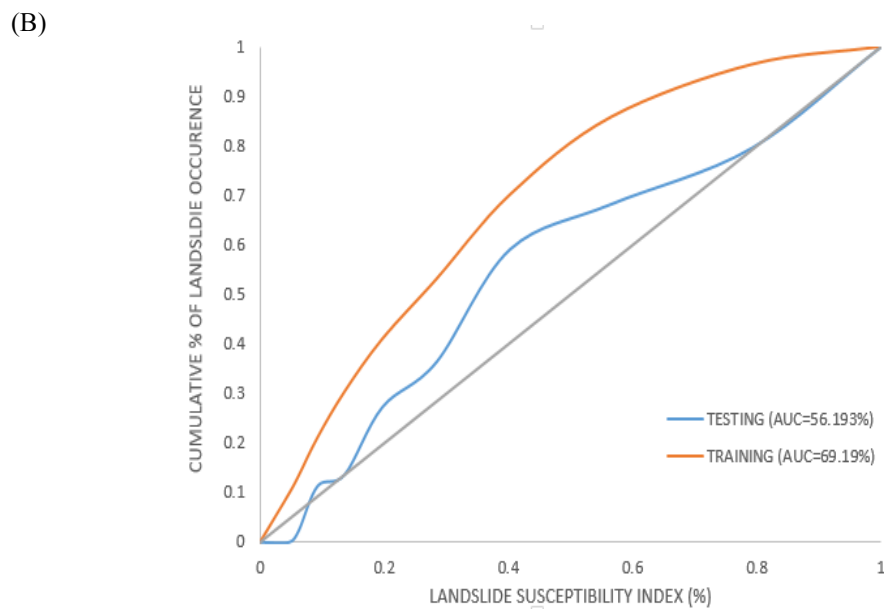
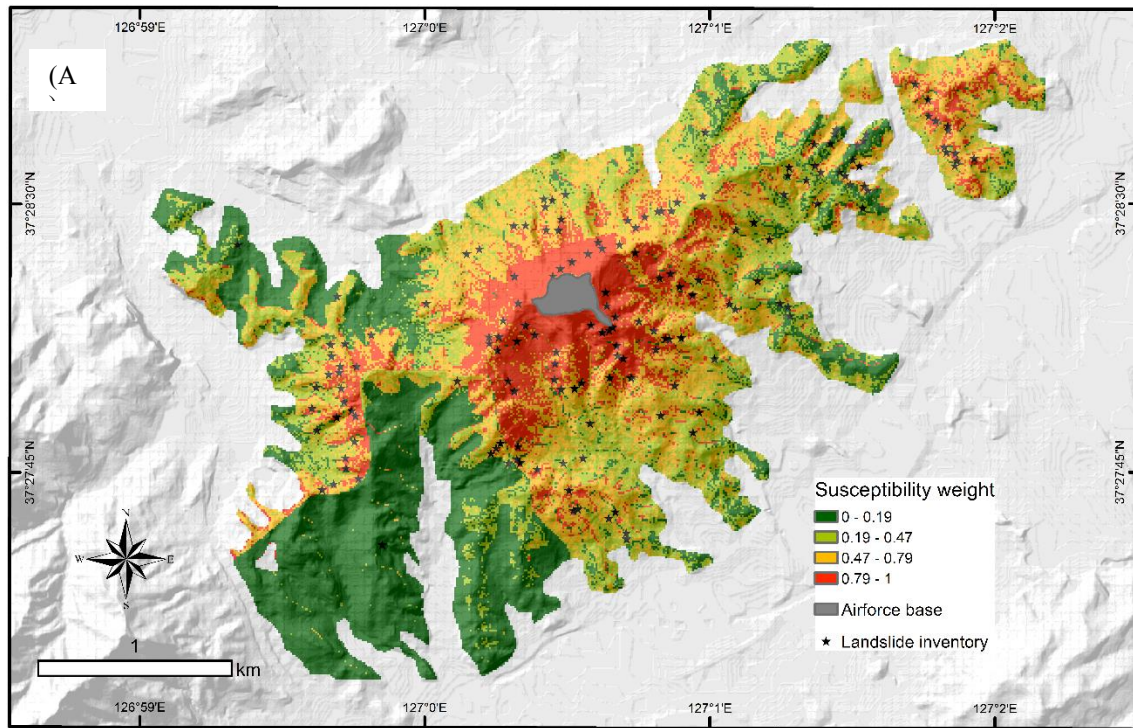


Fig. 2.12. (A) Logistic regression-based susceptibility map; (B) Validation curve for the logistic regression-based susceptibility map.



## 2.6 Conclusions

Many previous studies have focused on either using different supervised learning schemes with a fixed set of factors and selecting the best performance model or using filter models to generate a subset of relevant factors. When using the same dataset for creating a landslide susceptibility model through different learning algorithms or filter models, diverse factors will be selected each time, as observed from the comparison of the hybrid and logistic regression models, thereby indicating the importance of the methodology under consideration. In addition, it is shown in this study that only using the set of relevant factors selected through initial screening does not always provide the best susceptibility model, and the selection of factor subsets to train among  $2^n$  number of subset combinations (more than eight million combinations considering twenty-three factors) or choosing to train all the possible combinations is not economically or computationally efficient. This research is an attempt to shed light on the determination of the best subset of factors from numerous possible combinations using an objective general hybrid framework. A two-stage hybrid algorithm was devised to select the optimal subset by first implementing a filter approach, using the Spearman's correlation, for the initial partitioning into relevant and irrelevant factors. The feedback-controlled scheme is further developed in two phases, the first of which is conducted to check for redundancy among the relevant subsets through backward substitution, and the latter is conducted through a forward search scheme, effectively screening for relevant features among the initially categorized irrelevant factors. The results showed that thirteen factors, namely, soil density, plan curvature, slope, SPI, STI, distance from stream, TRI, geology, soil depth, total curvature, elevation, TWI, and topography, are the most relevant factors for Mt. Woomyeon. TWI and topography, though considered irrelevant, were used in the model as suppressors, and can explain the effect of infiltration and groundwater table characteristics inducing slope instabilities, which may mobilize debris flows. The landslide susceptibility map developed using the hybrid model in comparison to that developed by the wrapper model gave the best performance, using a lower number of factors with a success rate and prediction rate AUC of 85% and 89%, respectively. The implemented scheme therefore provides a systematic approach to rank and select the relevant conditioning factor subsets, and the resulting high performing landslide susceptibility map can be used for hazard assessment by linking it with the temporal probability.

## **Chapter 3. Extreme rainfall index and Dynamic hazard index: Approach for temporal and hazard assessment for extreme rainfall induced landslide at large scale**

### **3.1 Introduction**

Extreme rainfall events have become an increasing component of the annual precipitation in South Korea (Choi, 2004). The annual precipitation during the period of 1973–2005 mainly occurred during summer (monsoon season) and was characterised by an increase in the frequency and intensity of extreme precipitation (Jung et al., 2011). Extreme-rainfall-induced landslides are one of the most dangerous gravity-induced surface processes, and they cause severe damage to dwellings, roads, and other lifelines. Destructive debris flows mobilized from shallow landslides are generally the most common and widespread. About 70% of the Korean peninsula is covered with mountains with soils formed from in situ weathering of granite and gneiss. Shallow landslides are typically 1–3 m deep and often occur at boundaries between the colluvium and the solid underlying parent rock (Salciarini et al., 2008). In most parts of Korea, shallow landslides are characterized by shallow failure surfaces of 2–3 m depth that develop parallel to the original slope (Kim et al., 2004). Due to the mountainous terrain with a shallow layer of colluvium and increased annual precipitation, landslides have proven a hazard across most of the country. The socio-economic impact, moreover, has become much higher than before because of the increased population levels in the hazardous zones. Hence, there is a pressing need for risk mitigation through structural counter-measures, or through alternative cost-effective means like early warning systems, especially in areas where slope stabilization is not possible. The implementation of an early warning system over a large area requires a landslide hazard technique able to distinguish landslide and non-landslide areas when they are subjected to extreme rainfall. Moreover, they must use parameters that are easy to obtain, and that also allow quantification of the uncertainties involved.

Assessment of landslide hazard is usually stated as the probability of a landslide in a specified period of time and in a given area (Varnes, 1984; Van Westen et al., 2006). Thus the estimation of hazard usually needs a spatial probability definition of “where” it occurs using predisposition factors, and a temporal probability definition for “when” or how frequently it occurs, considering the trigger factors. While predisposition or preparatory factors are assumed not to evolve with time, but to be spatially variable, the trigger factors can vary both temporally and spatially. However, due to the difficulty in capturing the spatial variability of the trigger factor, rainfall in this case, owing to the low resolution

of the rain gauge grid (too few locations), only its temporal variability is considered. In the literature, temporal probability was estimated by considering the annual probability of rainfall events that would exceed the rainfall threshold known to cause landslides. The regional variability of the thresholds was also considered during preparation of a different threshold for each region. Thus, the effect of soil properties on surface water infiltration behavior was considered implicitly. However, it is difficult to obtain sufficient spatially distributed landslide occurrence data in each region to establish the thresholds. While the use of a physically based approach in identifying the critical rainfall through infiltration models are the most desirable, the difficulty in estimating a large number of soil parameters, and their validation, makes this approach impractical for real, large-scale applications. Therefore, a simple statistical model called “Extreme Rainfall Index” (hereafter, ERI) was developed to overcome the above mentioned difficulties through explicit consideration of soil properties, storage capacity, and permeability; along with the rainfall parameters, for the assessment of temporal probability. The index which gives the temporal probability can thus be further combined with the spatial probability for hazard assessment. Thus, the resulting hazard, which evolves with temporal variation leading to spatial distribution of landslides, is quantified using an index termed the Dynamic Hazard Index (DHI). This index in conjunction with real-time rainfall data could be used in an early warning system on a regional scale.

### **3.2 Study area and database development**

The ERI was developed using data obtained from Gangwon Province, which is located in middle-eastern part of the Korean peninsula. It covers an area of 20,569 km<sup>2</sup> (37°02′ – 38°37′ N and 127°05′ – 129°22′ E). The Taebaek Mountains, which occupy a high percentage of the area, have gentle slopes on their east side, but steep slopes on their west side. While the eastern regions receive annual rainfall of 2058 mm, the western regions receive about 1690 mm. Elevations greater than 500 m above sea level occur in about 51.1% of the total area. The major geological features in this province are Archean to Proterozoic age metamorphic rocks, and foliated granite from the Jurassic age.

Another study area, the Deokjeok-ri Creek located in the northeastern part of Korea (Inje County, Gangwon Province) was selected for development of the susceptibility and hazard map. The study area (38°04′07″ – 38°05′42″ N and 128°11′11″ – 128°18′00″ E) is surrounded by steep mountains and occupies 33.4 km<sup>2</sup>. The area was subjected to extreme rainfall in July 2006 (Fig.2.13), resulting in numerous landslides and debris flows that resulted in the deaths of 17 people. The geology in the area consists of gneisses from the Precambrian era and granites from the Mesozoic era (Pradhan and Kim, 2014).

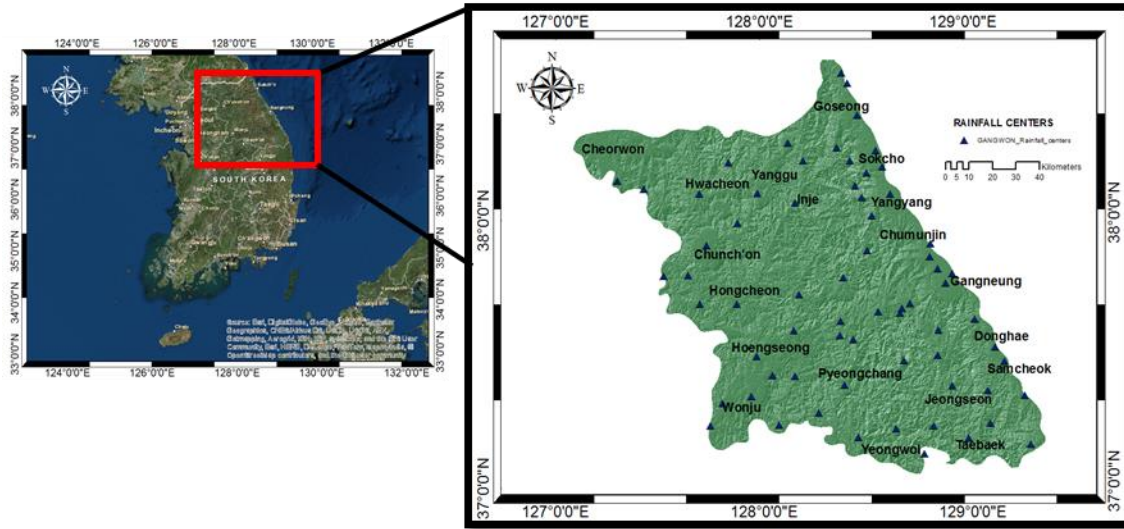


Fig. 3.1. Study area for ERI estimation and rainfall gauge distribution (Gangwon Province).

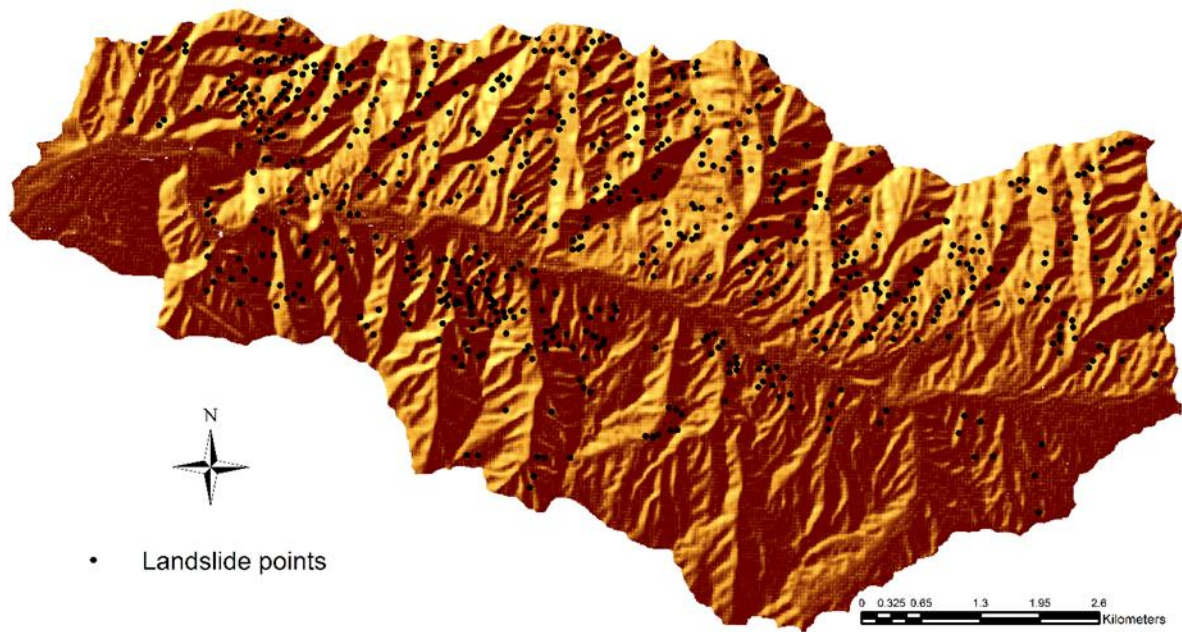


Fig. 3.2. Study area for spatial assessment (Gangwon Province).

### 3.2.1 Database for temporal assessment

#### 3.2.1.1 Database for ERI model development

The database for the temporal assessment model was developed using landslide data from Gangwon Province. The temporal landslide, and corresponding geotechnical soil data, were obtained from literature review of case studies in journals and reports. A total of 132 cases for both landslides and non-landslides were collected and 10% of the total data was used for validation of the model. The landslide inventory for Gangwon Province covered the interval 1995–2013. For the study area, the hourly rainfall data were collected from rainfall gauges in the landslide occurrence area. The automated rainfall gauges were installed and operated by the Korean Meteorological Center, with rainfall data after 2006 available for free from the organization website (<http://www.kma.go.kr>), and the data before 2006 purchased from the organization. Figure 3.1 shows the location of rainfall gauges throughout Gangwon Province.

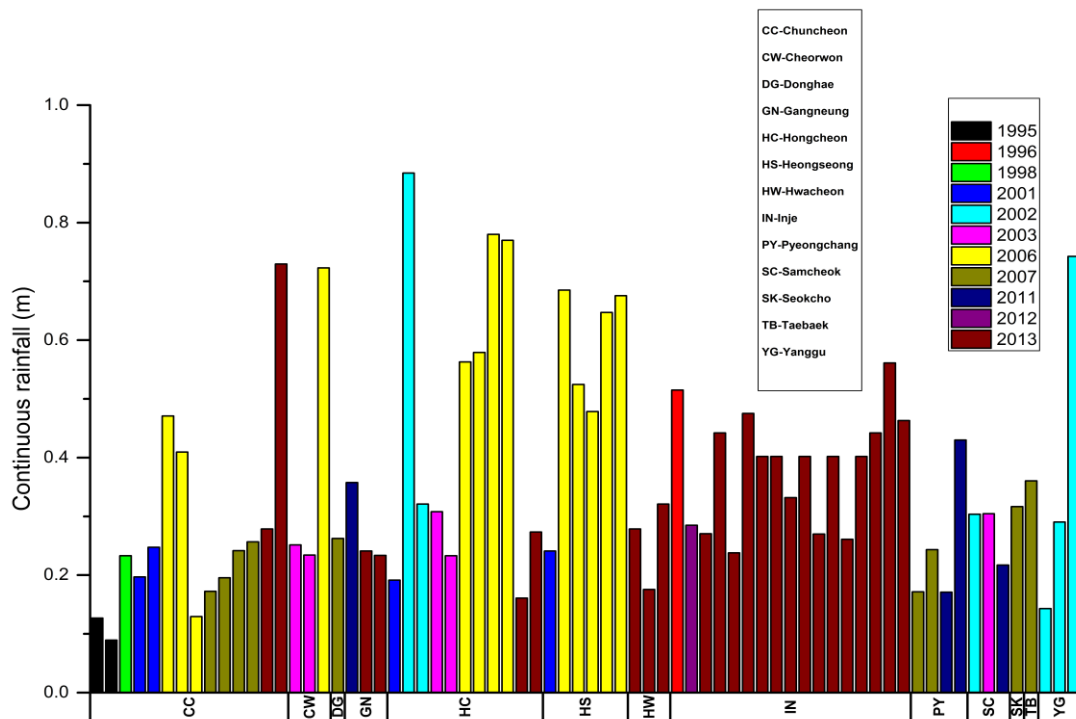


Fig. 3.3. Continuous rainfall resulting in landslides during 1995-2013 in Gangwon

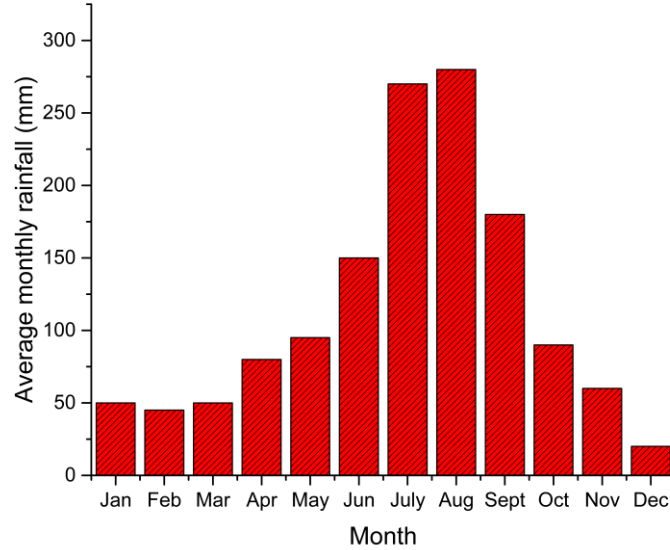


Fig. 3.4: Average monthly rainfall during 1990-2012 in Gangwon

Most of the landslides occurred between July and August during or after continuous rainfall greater than 150 mm (Fig. 3.3). This is evident from Fig. 3.4, which shows the highest average monthly rainfall in July and August for the years 1990–2012.

Different rainfall factors, like daily rainfall, maximum hourly intensity, continuous rainfall or antecedent rainfall have been considered by researchers. The selection of rainfall factor type for temporal assessment prior to the landslide hazard estimation, depended on the availability of rainfall data and on the influential failure mechanism being considered. Although landslide initiation in Korea is mainly the result of wetting-depth progression due to infiltration of rainfall (Kim et al., 2004), there is also evidence of other contributing mechanisms like the rise of groundwater, or erosion due to surface runoff. In this work, the model for landslide temporal evaluation considered rainfall factors including maximum hourly intensity, continuous rainfall, and antecedent rainfall (the prior 3, 5, 10, 15, 20, 25, and 30 days).

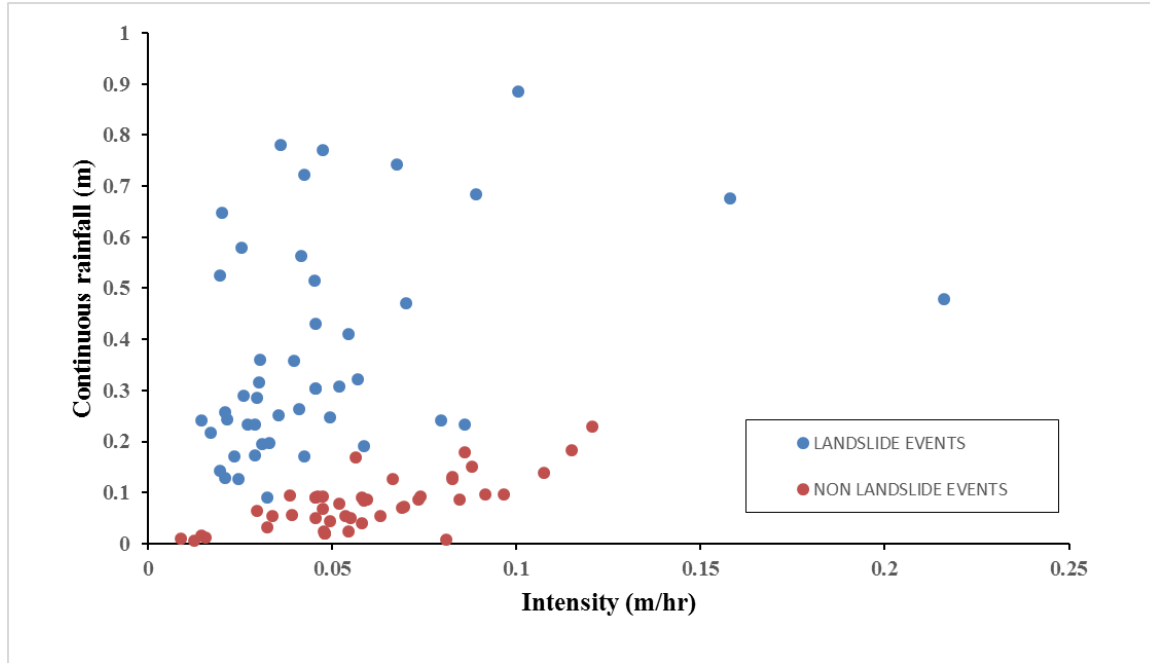


Fig. 3.5: Continuous rainfall versus maximum hourly intensity for landslide events

Figure 3.5 plots the maximum hourly intensity versus the continuous rainfall for the landslide and non-landslide events in Gangwon Province. As shown in the figure, the continuous rainfall factor can discriminate between non-landslide and landslide-causing rainfall, unlike the intensity factor, which lacks sufficient delineation ability and thus leading to the drop of the latter as an independent factor for the temporal assessment. Another rainfall factor, the antecedent rainfall, plays an important role in triggering landslides by decreasing soil suction and influencing the ground water levels (Guzzetti et al., 2007). Studies conducted by Govi et al. (1985), Kim et al. (1991), Crozier (1999), De Vita (2000), Chleborad (2003), Heyerdahl et al. (2003), Aleotti (2004), Cardinali et al. (2006), and Tien Bui et al. (2013) suggested the significance of 60 days, 3 days, 10 days, 1 to 19 days, 18 days, 4 days, 7 10 and 15 days, 3-month or 4-month and 15 days, respectively. This difference in number of days selected can be attributed to the regional variability of geotechnical, climatic, and morphological characteristics along with the incompleteness of the landslide inventory (Tien Bui et al., 2013; Guzzetti et al., 2007). In order to determine the appropriate number of days among the six antecedent rainfall intervals mentioned earlier, correlation analysis using Pearson's correlation analysis in IBM SPSS statistics 23 was carried out among the landslide and non-landslide events, as shown in Table 3.1 (Zezere et al., 2005). From the analysis, it was observed that the antecedent rainfall over 10 and 15 days had the highest correlation values (0.856 and 0.855, respectively). However, using each of the six antecedent rainfall factors for model development

through logistic regression indicated that only 5 and 20 days prior rainfall gave a reliable model (standard error  $< \pm 2$ ). Therefore, the final ERI model used the antecedent rainfall of 20 days since it provided the higher classification accuracy (better than 5 days).

Table 3.1: Correlation analysis for antecedent factors

Antecedent rainfall types	ERI
3 days	0.581**
5 days	0.790**
10 days	0.815**
15 days	0.812**
20 days	0.694**
25 days	0.796**
30 days	0.772**

It has been shown through experiments that development of the in-situ pore pressure due to infiltration is affected by the rainfall, soil, and morphological characteristics (Lim et al., 1996). The infiltration mechanism is controlled by the hydraulic properties, such as soil water characteristic curve (SWCC) and hydraulic conductivity (Cho and Lee, 2002). The SWCC expressing the relationship between the volumetric water content and matric suction is non-unique and varies spatially due to its dependence on the pore size and stress history (Fredlund and Xing, 1994). Storage capacity indicates the water content availability after the infiltrated water volume drains under the effect of gravity. The factor is determined by:

$$S_c = F_c \times d \quad (3.1)$$

where  $S_c$  is the storage capacity (mm),  $F_c$  is the field capacity defined as the volumetric water content at a matric suction of 30 kPa ( $\text{mm}^3/\text{mm}^3$ ), and  $d$  is the soil depth (mm).

In areas of high storage capacity, the antecedent rainfall will have a significant effect due to the presence of substantial infiltrated water, which drains slowly relative to a soil with lower storage capacity. Thus, the existence of a greater amount of water provides a favorable condition for landslide initiation with a lower increase in the supply of additional water by future rainfall. The storage capacity of a soil is influenced by the SWCC and soil depth.

Meanwhile, the saturated hydraulic conductivity is an important factor influencing infiltration, and thus the stability of a slope. The saturated hydraulic conductivity, defined as the ease with which water passes through a medium, varies depending on the soil type and stress history (McKenna et al., 2011). Loose, unconsolidated soils mainly evolve into



slides or debris flows due to either high hydraulic conductivity that allows rapid infiltration of rainfall, or substantial entrainment under high velocity impacts of water streams called ‘the fire-hose effect’ (Johnson and Rodine, 1984), or both. However, although dense soils may evolve into slides or debris flows from initial slope instability due to a perched water table, to rise in the ground water table, or to surface runoff, the probability is significantly lower, in comparison to the former initial stress condition. Thus, the factors storage capacity and hydraulic conductivity were selected to incorporate the spatial variability of infiltration characteristics during an extreme rainfall event, on a regional scale.

### 3.2.1.2 Database development method for ERI application for landslide hazard estimation in Deokjeok-ri

As the first step to estimate the ERI for a given rainfall condition, the region under consideration could be divided using geological units obtained from a geology map, and any existing relationship between geology and the soil texture could be used. However, for this research the soil-type information in the study area was available. The soil properties used to calculate the ERI was estimated as follows:

- (i) Soil depth: The data for soil depth in the region was obtained from the National Academy of Agriculture Sciences and is as shown in Fig. 3.7. The soil depth in the area is shown to vary.
- (ii) Volumetric water content at  $-30$  kPa: The volumetric water content at matric suction of 30 kPa was estimated by determining the SWCC using an ANN model developed for Korean soils using density, void ratio, and porosity, to develop the database (Lee et al., 2003).
- (iii) Permeability: Database development for permeability was done using a multivariate regression model developed for Korean soils using void ratio, sand percentage, and clay percentage as input parameters (Seok et al., 2015).
- (iv) Continuous and antecedent rainfall for the extreme rainfall event on July 2006 was obtained from the Korean Meteorological Center.

The described process is shown in Fig. 3.6 using a flow chart.

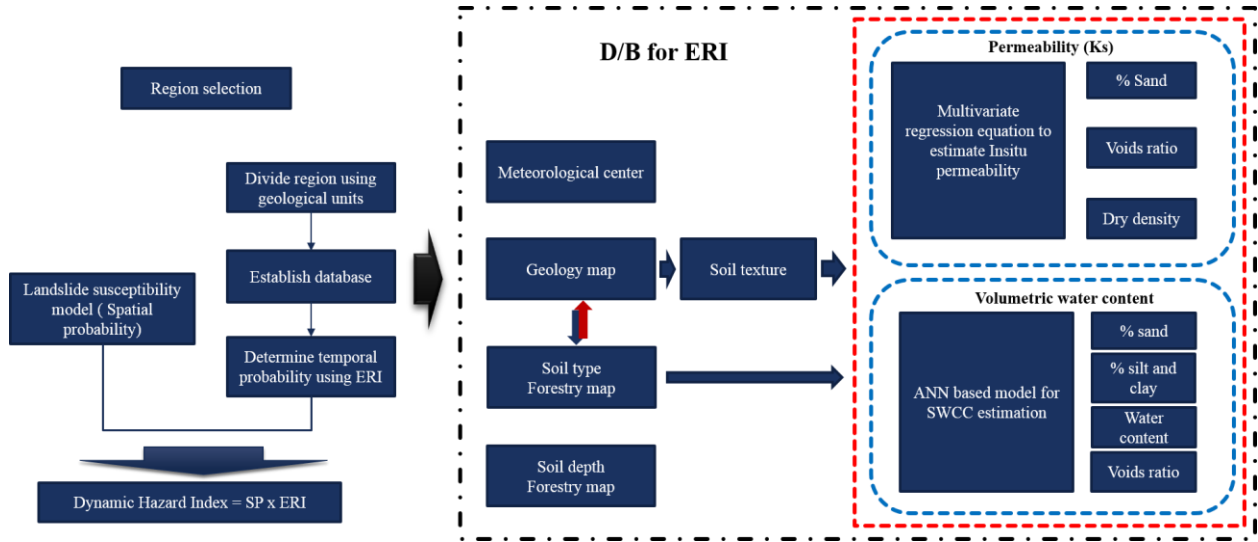


Fig.3.6: General framework and database development method for ERI

### 3.2.2 Database for landslide susceptibility model

Based on a detailed literature review, we selected 11 explanatory variables and grouped them into three types, as seen in Table 3.2; i.e., morphological, hydrological, and forestry.

The factors such as elevation, aspect, slope, total curvature, Topographic Wetness Index (TWI), Stream Power Index (SPI), Sediment Transportation Index (STI), internal relief (IR), distance to drainage, and drainage density were extracted from digital elevation models (DEM) at 10 m resolution in ArcGIS 10.1. The explanatory factor for forest type considered in this study was extracted from a forestry map (1:25,000) developed by Korea Forest Service. The study area was divided into 558,080 grid cells with 10 m resolution in ArcGIS 10.1, and the dimension of the raster dataset was 545 rows by 1024 columns. The landslide and stable locations were mapped as points in single grid cells to avoid issues related to the assumption of the independence of factors in multivariate models due to spatial autocorrelation, and of errors due to landslide boundary mapping (Van Den Eeckhaut et al., 2009). To avoid the class imbalance and sampling bias caused by a large area of negative samples (stable areas) in comparison to the positive samples (landslide/unstable areas), an equal number of samples in both classes were considered. Thus, 748 unstable

and stable points were selected, with 90% of the total dataset used for training and 10% used for validation of the trained susceptibility model. Because there were many cells with stable areas, several sets of non-landslide points were made and the best model was selected considering the ROC value.

Table 3.2: Database for susceptibility map development in Deokjeok-ri Creek (Pradhan and Kim, 2014)

Factor type	Conditioning factors	Scale	Source
Morphological	Slope	1:10000	NGII
	Curvature		
	Aspect		
	Elevation		
	Internal relief		
Hydrological	TWI	1:10000	
	Distance to drainage	1:10000	
	SPI		
	STI		
	Drainage density		
Forestry	Forest type	1:25000	Korea Forest Service

### 3.2.2.1 Morphological type

Many studies conducted over the world have shown that landslides are influenced by geomorphological features such as elevation, slope, aspect, total curvature, and internal relief. Elevation has been used as a conditioning factor in several studies and usually higher values are related to higher susceptibility due to variation in rainfall, vegetation, and potential energy (Pachauri and Pant, 1992; Ercanoglu et al., 2004). The factor was divided into six classes with maximum value of 1225 m (Fig.3.7a). Aspect is also considered an important variable (Carrara et al., 1991; Maharaj, 1993; Jakob, 2000) because induction of landslides can be affected by exposure of the surface to wind and rainfall. Fig.3.7b shows aspect dividing the entire area into nine classes of flat (−1), north (337.5–360 and 0–22.5), northeast (22.5–67.5), east (67.5–112.5), southeast (112.5–157.5), south (157.5–202.5), southwest (202.5–247.5), west (247.5–292.5), and northwest (292.5–337.5). Slope, defined as steepness of a surface, and its second-order derivative curvature, helps in understanding the characteristics of a basin for runoff and erosion processes. Curvature (convex, planar, or concave), by its effects on acceleration/deceleration and convergence/divergence of flow, can affect the susceptibility of a location to landslides (Kimerling et al., 2011). Thus, this study considers total curvature, which is a

general curvature of the surface rather than curvature along a line (Wilson and Gallant, 2000) (Fig. 3.7c). On the other hand, steeper slope angles are related to higher shear stress and Fig.3.7d shows the five classes of the raster, with third class (25–35) and fourth class (35–45), occupying 32.8 and 30.6% of the total area, respectively.

IR also contributes to the landslide susceptibility and gives information regarding the potential energy for mass wasting. The factor was divided into four classes in this study as shown in Fig.3.7e. The conditioning factor can be calculated as

$$IR = \frac{1}{m} \sum_j Z_{\max} - Z_{\min} \quad (3.2)$$

where  $Z_{\max}$ ,  $Z_{\min}$  and  $m$  are the maximum elevation, minimum elevation, and number of pixels in the catchment, respectively.

### 3.2.2.2 Hydrological

TWI defined based on assumptions of uniform soil properties and steady state condition (Conforti et al., 2014) can be used to describe the distribution pattern of moisture for potential infiltration volumes using three classes (Fig.3.7f) with higher values in natural drainage channels and the lowest values along the ridge and alluvial fans. The hydrological factor is calculated using Eq. 3.3 (Moore et al., 1991).

$$TWI = \ln \left( \frac{A_s}{\tan \beta} \right) \quad (3.3)$$

where  $A_s$  is the specific catchment area and  $\beta$  is the local slope gradient measured in degrees.

SPI, measuring the erosive power of the flow, increases with the surge in amount of water due to larger upslope area and slope (Florinsky, 2012). Fig. 3.7g shows higher erosive values existing along the drainage channels. It is given by (Moore et al., 1991), as

$$SPI = A_s \times \beta \quad (3.4)$$

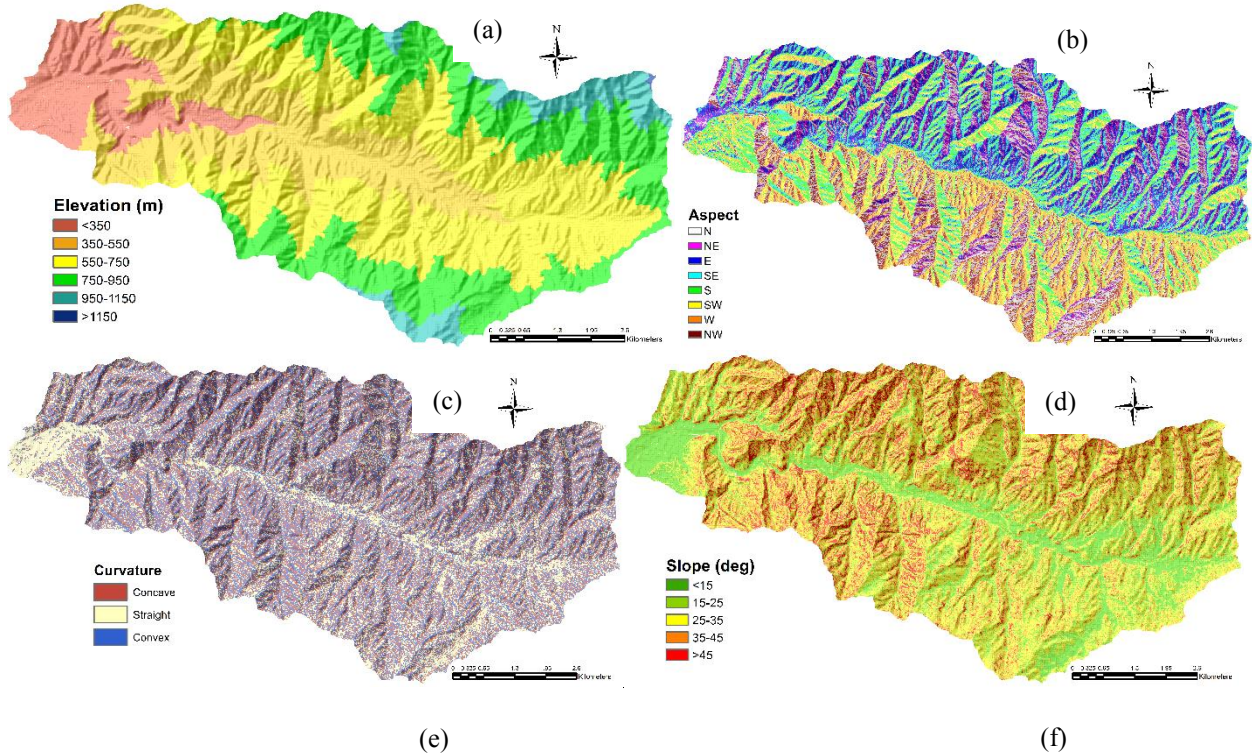
Another index called STI, a dimensionless term, is associated with sedimentation transport capacity and it is a nonlinear function of slope angle and specific catchment area (in turn affecting the discharge). Areas with high STI values correspond to greater susceptibility of the soil to erosive effects of overland flow, and thus contribute to landslides. STI values for Deokjeok-ri Creek shown in Fig. 3.7h are divided into four classes with lower values existing along ridges and flat areas. The equation is given using a combined slope factor and can be calculated as (Moore and Burch, 1986)

$$STI = \left( \frac{A_s}{22.13} \right)^{0.6} \left( \frac{\sin \beta}{0.0896} \right)^{1.3} \quad (3.5)$$

In the hill slope domain, the presence of a slope close to drainage divides and stream networks (Fig. 3.7i) can cause instability through erosion or saturation (Gokceoglu and Aksoy, 1996); hence, hill slope was considered a hydrological factor. The distance to drainage in the region was determined using the Euclidean distance tool in ArcGIS 10.1, and classified into five ranges (< 25 m, 25–50 m, 50–75 m, 75–100 m, and > 100 m). The susceptibility is also affected by the drainage density or streams, which can positively contribute to surface erosion (Pradhan and Kim, 2014). Figure 3.7j shows the drainage density in four classes (< 5 m/m<sup>2</sup>, 5–10 m/m<sup>2</sup>, 10–15 m/m<sup>2</sup>, and > 15 m/m<sup>2</sup>).

### 3.2.2.3 Forestry

The characteristics of forest could also influence the spatial variability in landslide susceptibility through root reinforcements, reduction of soil erosion due to surface runoff, or increase in the driving stress from the additional weight of trees. The region under study is shown in Fig. 3.7k, and consists of six types of forests: cultivated (0.8%), Japanese larch (18.5%), Japanese red pine, Korean pine, Mongolian pine, and soil deposit (80.7%).





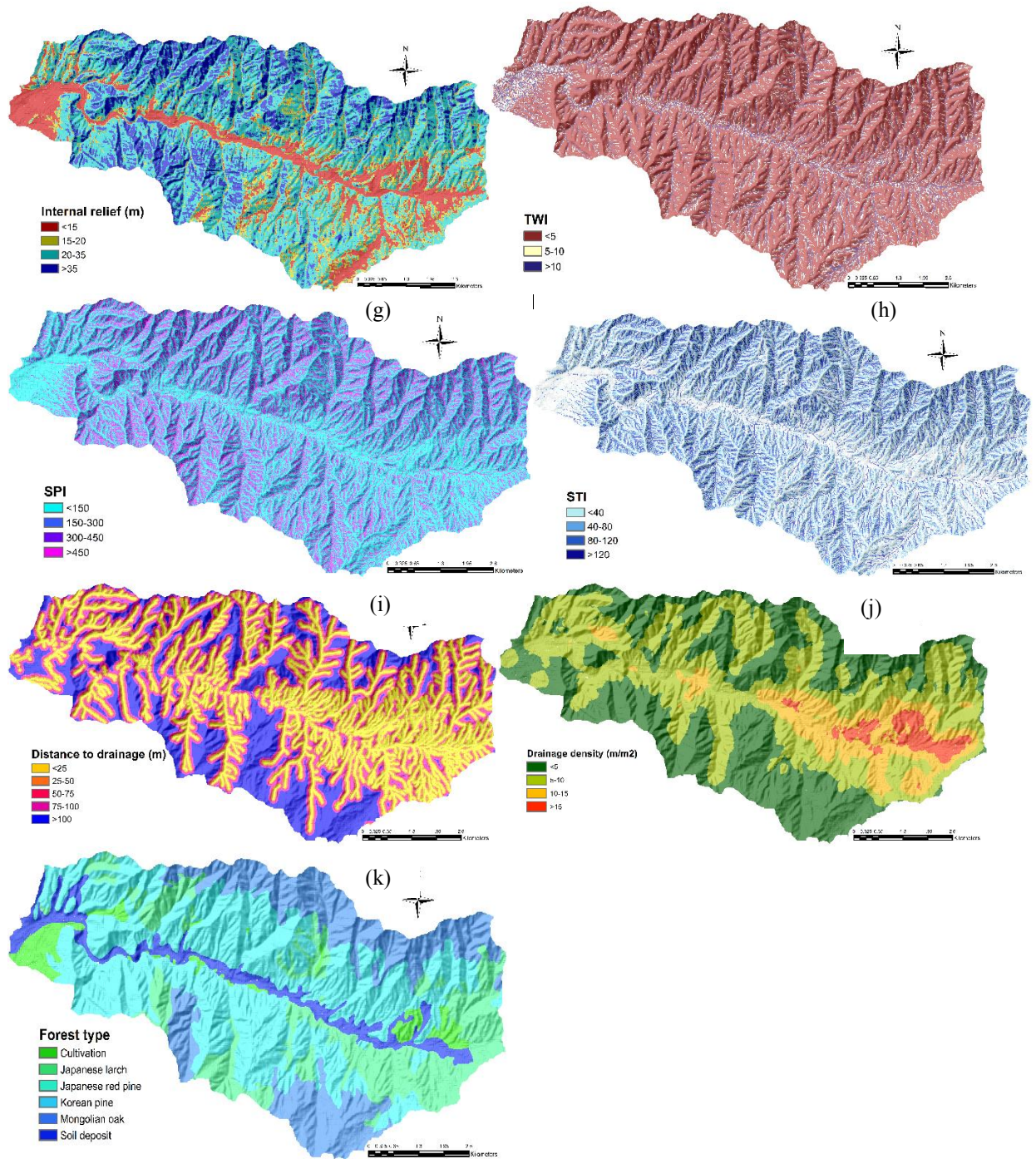


Fig.3.7: Landslide conditioning factors: (a) Elevation; (b) Aspect; (c) Total curvature; (d) Slope; (e) IR; (f) TWI; (g) SPI; (h) STI; (i) Distance to drainage; (j) Drainage density; (k) Forest type ( Pradhan and Kim, 2014)

### 3.3. Methodology

#### 3.3.1 Temporal assessment using ERI

The proposed index to estimate a probability is assumed to be valid under the following two conditions. First is that, considering the principle of uniformitarianism, factors that triggered landslides in the past will also trigger landslides in the future, given the same conditions. Second, is that all landslides are considered as independent events.

In this study, it was our intention to find a method to incorporate the rainfall effect in the identification of landslide hazard regions for the first stage in an early warning system. While the spatial probability is used to identify regions with high potential or likelihood for failure characterized by a given set of parameters, it does not represent the probability that a landslide may occur by the rainfall. Hence, ERI has been defined and used to estimate the probability of landslide occurrence under an extreme rainfall condition.

In contrast to estimation of spatial probability, there has been less research into rainfall incorporation as an independent variable giving a probabilistic estimate. Most common approach has been through calculation of temporal frequency of landslide events (Keaton et al., 1988; Lips and Wieczorek, 1990; Coe et al., 2000; Crovelli, 2000; Guzzetti et al., 2002; Jaiswal and van Westen, 2009; Ghosh et al., 2012). Most of these models attempt to predict “when” a landslide will occur by establishing the probability that landslide occurrence would exceed a rainfall threshold, because they are imperfect predictors of landslides (Chleborad, 2006). The incompleteness of landslide inventory prevents the direct calculation of temporal probability. Thus instead, a link between the landslide occurrence day and the rainfall is used to establish this probability. While some researchers used discriminant analysis to classify the landslide-causing rainfall (Ghosh et al., 2012) others used daily and antecedent rainfall in a bivariate linear relationship (Chleborad et al., 2006; Jaiswal and Van Westen, 2009). In the following methods, the temporal probability is obtained by using a Poisson’s distribution model during a period ‘t’ as shown below:

$$p[N_L(t) \geq 1] = 1 - p[N_L(t) = 0] = 1 - e^{-t/\mu} \quad (3.6)$$

where,  $p[N_L(t) \geq 1]$  is the exceedence probability of one or more landslides during a time t and  $\mu$  is the mean recurrence interval.

Furthermore, researchers have developed I-D rainfall thresholds using logistic regression and a Bayesian approach. These thresholds using statistical approaches are objective and reproducible, while being able to quantify the uncertainties related to the quality of the rainfall data. However, none of these studies have considered the soil

properties in calculating the temporal probability, due to the difficulty in its estimation. Moreover, uncertainties will always remain in the prediction of landslide occurrence only using rainfall inventory, because there is no acceptable limit on the size of inventory to be collected or surety regarding the completeness of the inventory. Moreover, when using real-time rainfall data to assess the variation of hazard areas, the above stated methods are not warranted. Thus, in this study a probabilistic index was used to estimate the hazard related to varying rainfall, through consideration of soil properties that were estimated by a novel approach of database development for these soil properties.

In this study a logistic regression model is used to estimate the conditional probability that the rainfall of a particular return period, for given soil characteristics in a region, could initiate a landslide. The logistic equation can be expressed as:

$$\log \left( \frac{P(L_e / R, S)}{1 - P(L_e / R, S)} \right) = f(S, R) + e \quad (3.7)$$

where  $L_e$  is the landslide occurrence and,  $R$  and  $S$  are the rainfall and other spatial factors.

$$P(L_e / R, S) = \frac{\exp(\beta_0 + \beta_1 \times R + \beta_2 \times S)}{1 + \exp(\beta_0 + \beta_1 \times R + \beta_2 \times S)} \quad (3.8)$$

where  $(\beta_0, \beta_1, \beta_2)$  are the coefficients indicating the influence of independent factors on the probability of landslide occurrence.

### 3.3.2 Spatial assessment of landslides

Logistic regression has been widely used to estimate the relationship between landslide occurrence or non-occurrence, and a set of conditioning factors (Ayalew and Yamagishi, 2005; Yesilnacar and Topal, 2005; Van Den Eeckhaut et al., 2006). This relationship is determined using change in the log (odds) of the dichotomous dependent variable, and the resulting probability will always lie between '0' and '1'. Although no assumption regarding normal distribution or homoscedasticity is needed, a linear relationship is assumed between the log odds and independent variables. This linear combination is expressed as

$$Y = \beta_0 + \beta_1 A_1 + \beta_2 A_2 + \beta_3 A_3 + \dots + \beta_n A_n \quad (3.9)$$

where  $Y$  is the logit or log (odds), and  $(\beta_0, \beta_1, \beta_2, \beta_3, \dots, \beta_n)$  are the coefficients indicating the influence of independent factors  $(A_1, A_2, A_3, \dots, A_n)$  on the logit  $Y$ .



The coefficients are determined using the maximum likelihood criterion, derived from the probability density function of the dependent factor. The critical points of the log likelihood function and its maximization are determined by taking the first and second derivative, and then solving the resulting non-linear set of equations iteratively. Finally, the probability of the landslide occurrence ( $P_{LC}$ ), in terms of the calculated logit, is given by

$$P_{LC} = \frac{I}{I + e^{-Y}} \quad (3.10)$$

### 3.4. Results and Discussion

#### 3.4.1 Extreme Rainfall Index

The logistic regression analysis was performed on the training dataset using IBM SPSS Statistics 23. Table 3.3a shows the model descriptive values obtained from the logistic analysis. The reliability test for the selected model was performed using the Omnibus and Hosmer and Lemeshow goodness-of-fit statistics tests by calculating a Chi-square value and its significance (Table 3.3b). The Omnibus test gives the model Chi-square value of 103.095 with a significance of  $< 0.05$ , suggesting that the relationship between the dependent and the subset of conditioning factors is not by chance. The Hosmer and Lemeshow goodness-of-fit statistic, a measure of the correspondence between actual and predicted values of the dependent factors, gives a Chi-square value of 4.622 and a significance of 0.797. Thus, a significance of  $> 0.05$  for this goodness-of-fit statistic indicates a close correspondence between the predicted landslide susceptibility weight and the actual landslide susceptibility weights, and therefore, a good model fit. Also, a check for numerical problems in the model was conducted by checking if the standard error (S.E.) was  $> \pm 2$  or if there were unusually large, odd ratio coefficients. Table 3.3a shows that all the conditioning factors had S.E.  $< \pm 2$ ; thus there were no inherent numerical errors in the model. Finally, the ERI is expressed as,

$$ERI = \frac{E \times p(.02 \times CR + .008 \times AR_{20} + .002 \times SC - .002 \times K_s - 4.209)}{1 + E \times p(.02 \times CR + .008 \times AR_{20} + .002 \times SC - .002 \times K_s - 4.209)} \quad (3.11)$$

where CR is the continuous rainfall (mm),  $AR_{20}$  is the 20-day antecedent rainfall (mm), SC is the storage capacity (mm), and  $K_s$  is the permeability (mm/hr).

The classification accuracy of the selected model calculated by the statistical software was 88.8%, considering a cut-off value at 0.5.

However, the possibility of attaining different accuracy values over various cut-off values motivated the need to identify an optimal cut-off value either using methods such as cost benefit or Youden's index; or by using ranking and lift-chart-based analysis. For evaluating the accuracy of both the training and testing datasets in this study, we used lift analysis, wherein the true positive values (landslide occurrence) were assigned to 10 bins with value between '0' and '1'. Thus, instead of actually assessing if a certain ERI value is above or below an optimal threshold, the lift analysis method assigns a probability indicating the likelihood in which the predicted value belongs to the true positive class (Youden, 1950; Miha and Curk, 2006). Figure 8 shows the AUC value of 0.89 and 0.97 from the cumulative gains chart for the training and testing dataset respectively, implying that the model was robust and reliable with high predictive power. The histogram of the ERI values used for training and validation (Fig. 3.9) can be used to make ERI classes between '0' and '1' using the natural breaks method.

Table 3.3: (a) Coefficients of the selected ERI model using logistic regression in SPSS;  
(b) Test for factor significance and goodness-of-fit

<b>Coefficients</b>	<b>B</b>	<b>Standard error</b>
Continuous rainfall	0.020	.005
20 day antecedent rainfall	0.008	.008
Storage capacity	0.002	.003
Permeability	-0.002	.004
<b>Type</b>	<b>X<sup>2</sup></b>	<b>Significance level</b>
Omnibus test	103.095	.000
Hosmer and Lemeshow test	4.622	.797

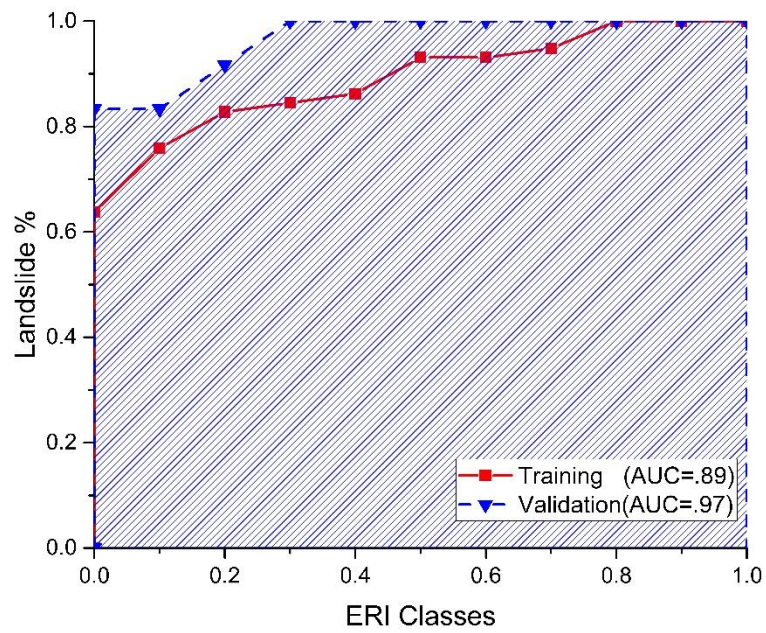


Fig. 3.8: Accuracy assessment using AUC of the cumulative gains chart

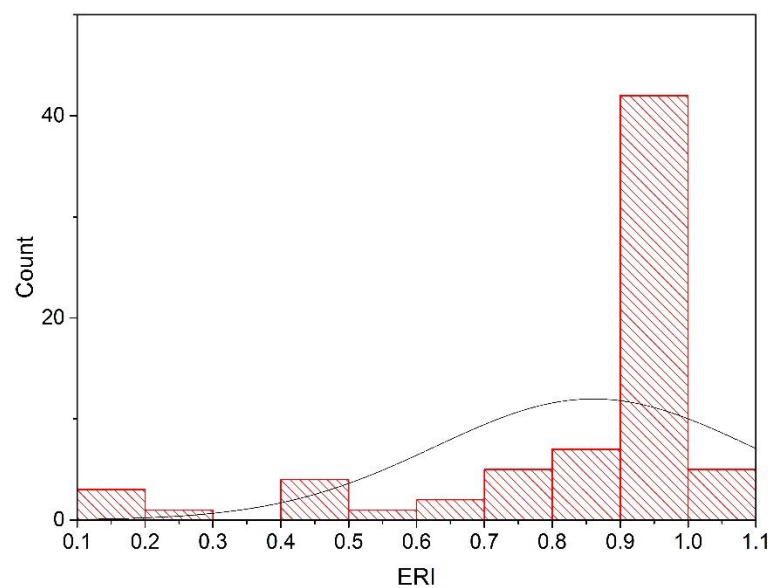


Fig. 3.9: Distribution of ERI values for making probability levels

### 3.4.2 Landslide spatial assessment

Another major component of the landslide hazard analysis, the spatial probability assessment, was determined by developing a landslide susceptibility model based on a logistic regression. As discussed in Section 3.2, initially 23 conditioning factors assumed to have significant influence on landslide initiation were selected from the literature. A correlation analysis was conducted using IBM SPSS Statistics 23, a statistical software package with several built-in statistical techniques for analytic processes, from data preparation to exploring relationships among variables, trend identification, and forecasting.

Table 3.4 shows the Spearman's correlation value and its significance, indicating that 11 factors such as elevation, aspect, total curvature, distance to drainage, STI, SPI, slope, TWI, IR, drainage density, and forest type that were statistically significant ( $p < 0.05$ ). These were also strongly correlated to the landslide index and, hence, relevant. It is also seen from the correlation analysis that elevation and IR are strongly correlated; hence, one of the two parameters could be excluded during the model building exercise.

Table 3.4: Correlation of explanatory factors with landslide index

Conditioning factor	Landslide index	
	Correlation coefficient	Sig.
Elevation	-0.701**	.000
Aspect	-0.091**	.001
Total curvature	0.045**	.005
Slope	0.586**	.000
TWI	-0.137**	.000
STI	0.250**	.000
SPI	0.250**	.000
Internal relief	0.670**	.000
Distance to drainage	-0.727**	.000
Drainage density	0.696**	.000
Forest type	-0.434**	.000

\*\*Correlation is the significant at the 0.01 level (2-tailed).

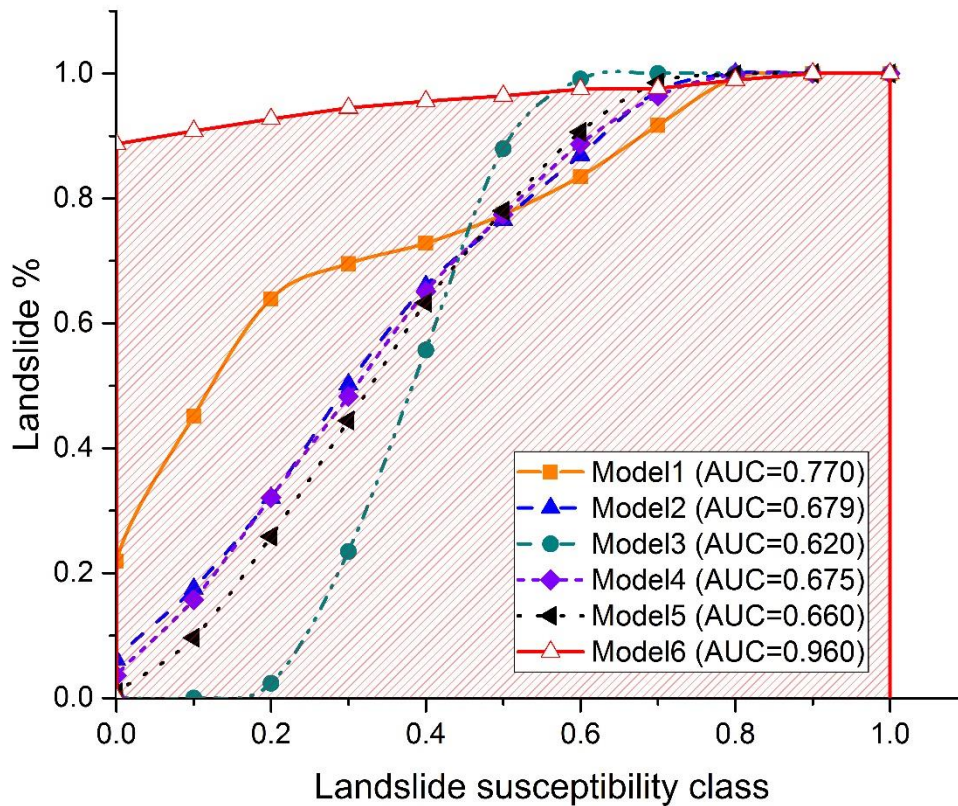


Fig.3.10: Models and corresponding AUC for training datasets

The identification of the optimal susceptibility map in the region was conducted using six models, with the first five models initially considering all eleven of the significant conditioning factors, and the last model considering only nine factors. All six of the models used different sets of non-landslide samples, selected at random.

Figure 3.10 shows the variation of training accuracy using AUC values for six different models developed using the maximum likelihood ratio based on stepwise logistic regression. Models 2, 3, 4, and 5 were found to have very low AUC values, indicating poor fit to the training datasets. However, Model 1, with ten conditioning factors excluding SPI, showed sufficiently good fit, with S.E.  $< \pm 2$  and a significant Chi-square value. However, the validation using lift analysis gave an AUC of about 66.13% inferring the predictive quality of the susceptibility model to be quite low. The susceptibility map development using Model 6 was carried out by neglecting the elevation factor due to its correlation with the internal relief. During its initial run through all the steps, this model gave a classification accuracy greater than 95%. However, upon closer examination of the coefficient values for the conditioning factors, it was

evident that the drainage density factor had an unusually high value of standard error ( $\sim \pm 1308.2$ ) and a coefficient value of 20.12. Hence, this conditioning factor was also discarded and a model with seven explanatory factors with extremely high training subset AUC (95.8) was chosen. Table 3.5-a shows the model descriptive values obtained from the logistic analysis. A reliability test for the selected model was performed using Omnibus and Hosmer and Lemeshow goodness-of-fit statistics tests by calculating Chi-square value and its significance (Table 3.5b). The Omnibus test gave the model a Chi-square value of 1283.897 with significance  $< 0.05$ , suggesting that the relationship between dependent and the subset of conditioning factors was significant, and thus not by chance. The Hosmer and Lemeshow goodness-of-fit statistic, which measures the correspondence between actual and predicted values of the dependent factors, gave a Chi-square value of 13.465 and significance of 0.097. Thus, the significance  $> 0.05$  for this goodness-of-fit statistic, indicated a close correspondence between the predicted landslide susceptibility weight and the actual landslide susceptibility weights, indicating a good model fit. Moreover, Table 3.5a shows that all the conditioning factors had S.E.  $< \pm 2$  and thus, no inherent numerical errors existed in the model. The selected model weights were then used to make the susceptibility map of Deokjeok-ri (Fig. 3.11a), and the susceptibility classes visualized in Fig. 3.11b were decided using the *Natural breaks* classification scheme in ArcGIS 10.1. Figure 3.12 shows the high values of AUC (96 and 94%), obtained for the cumulative gain chart plotted using the training and validation datasets, respectively. Thus, a high performance susceptibility model including seven relevant conditioning factors was developed for Deokjeok-ri Creek (Inje).

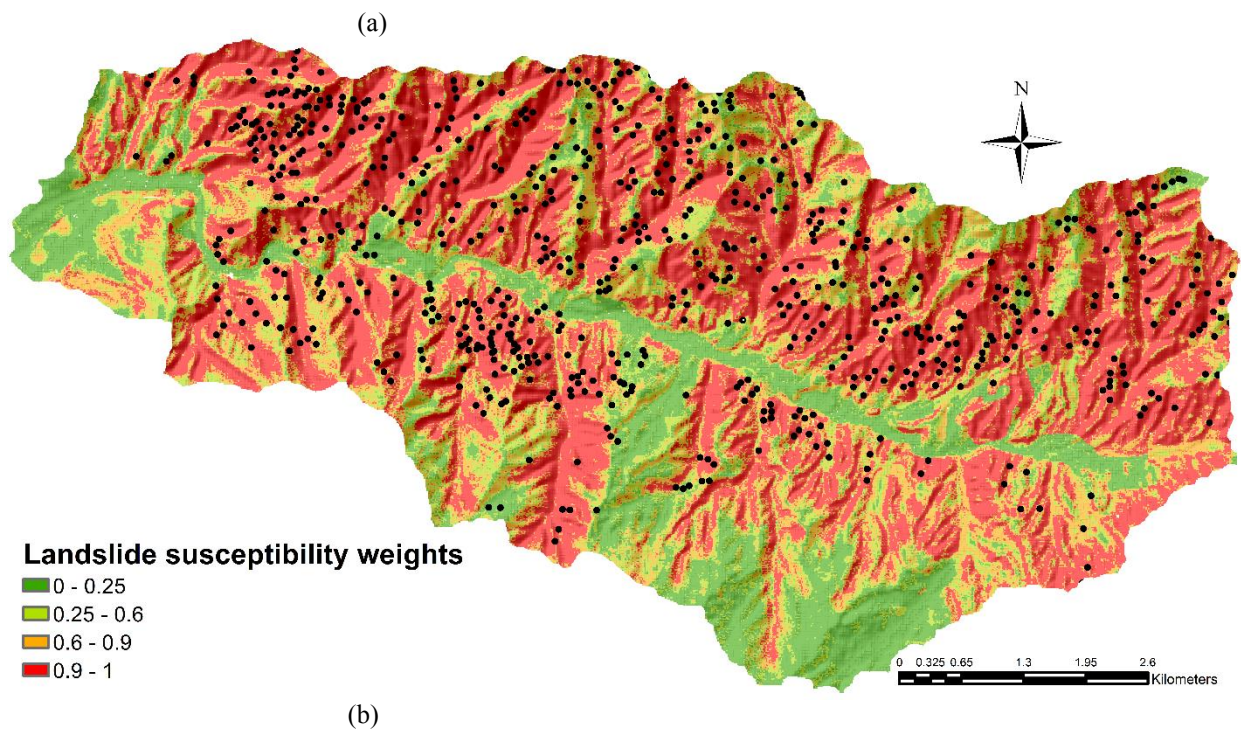
Table 3.5. (a) Model coefficients and (b) Reliability test

<b>Coefficients</b>	<b>B</b>	<b>Standard error</b>	<b>Wald's significance</b>
Aspect	-0.277	.047	.000
Total curvature	-0.134	.130	.004
Slope	0.402	.128	.002
STI	0.237	.109	.029
Internal relief	1.570	.171	.000
Distance from drainage	-1.129	.077	.000
Forest type	-0.801	.097	.000
Constant	3.217		.000



(b) Test for factor significance and goodness-of-fit

Type	X <sup>2</sup>	Significance level
Omnibus test	1283.897	.000
Hosmer and Lemeshow test	13.465	.097



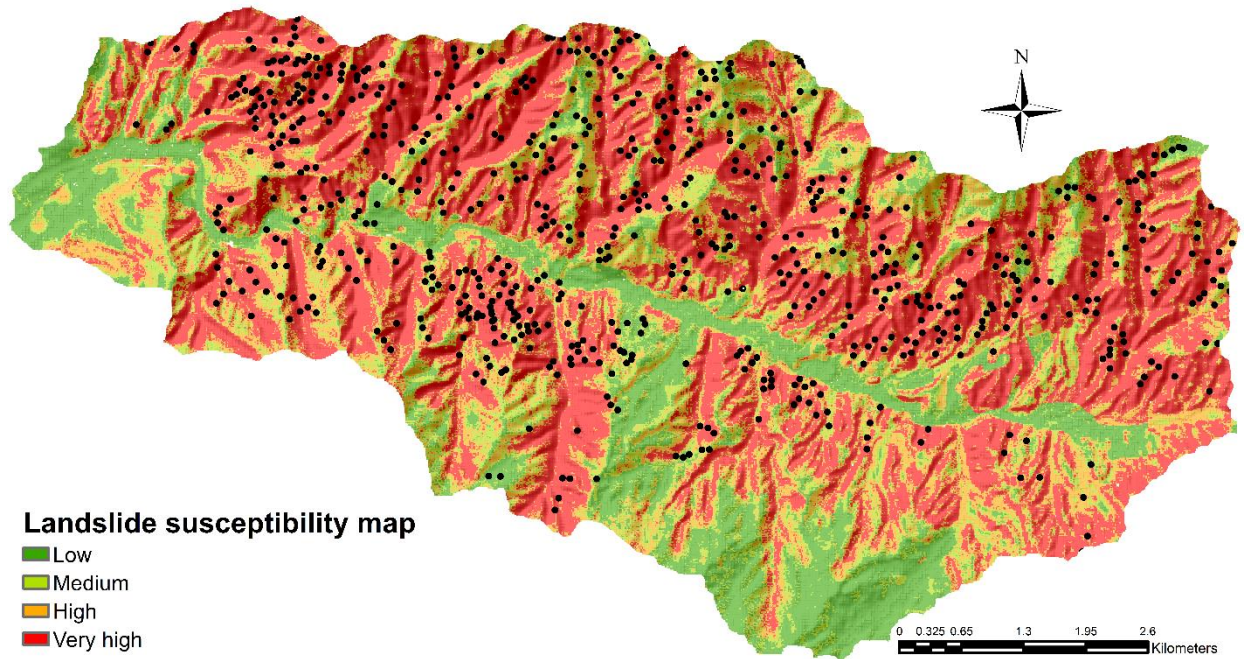


Fig.3.11 (a) Landslide susceptibility weights for Deokjeok-ri Creek and (b) Landslide susceptibility class for Deokjeok-ri Creek

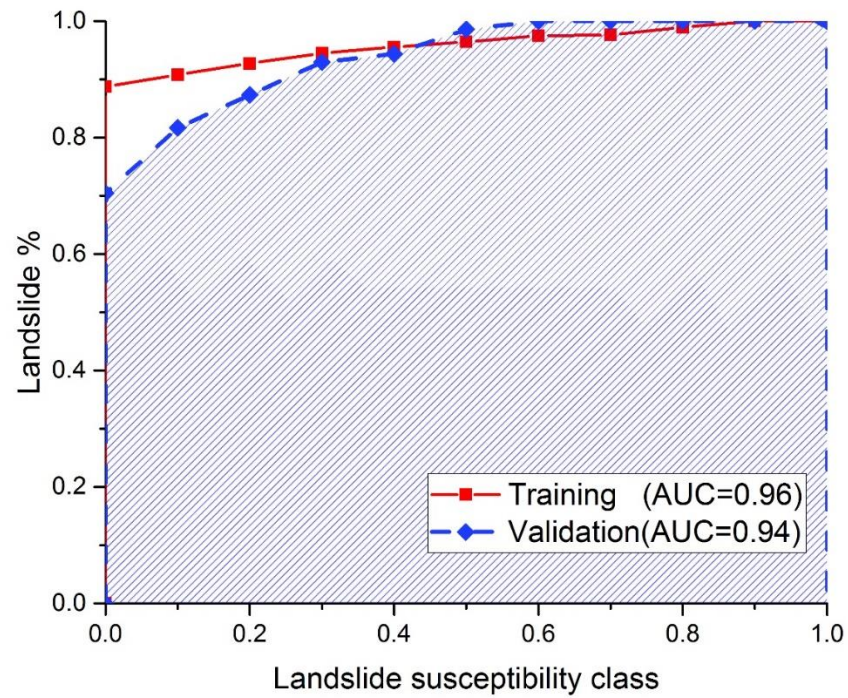


Fig.3.12: Training and validation curves for accuracy assessment



### 3.4.3 Landslide hazard assessment using DHI

A landslide hazard assessment was performed for the Deokjeok-ri region corresponding to the 2006 extreme rainfall event that occurred between 12 and 15 July 2006 using DHI. The permeability and storage capacity database for the Deokjeok-ri Creek region used in the temporal probability model was developed as described in Section 3.2.1.2. Figure 3.13 shows the daily rainfall data of Deokjeok-ri Creek, for July 2006. The temporal probability (using the ERI) was calculated for five days i.e., 11<sup>th</sup>, 12<sup>th</sup>, 13<sup>th</sup>, 14<sup>th</sup> and 15<sup>th</sup> July. Through the consideration of the rainfall pattern over five days, it was the objective of the study to show that the ERI could be used to study the real-time spatial evolution of landslides. On the 11<sup>th</sup> July, with no continuous rainfall and antecedent rainfall of 160 mm, the ERI had values between 0.04 and 0.05. The distribution of ERI across the study area is mainly due to the spatial variability of  $K_s$  and storage capacity. Therefore, combining the ERI with the spatial probability shows the entire region to be classified at a very low DHI value between 0 and 0.25 as in Fig. 3.14a, due to the zero continuous rainfall. The commencement of rainfall event with continuous rainfall of 175 mm resulted in significant jump of the ERI value from 0.04–0.05 to 0.65–0.7 (Fig. 3.14b), thereby increasing the % of area from very low (0–0.25) to high (0.65–0.9) level of DHI (Fig. 3.15b). The rainfall on 12<sup>th</sup> July resulted in about 38.11% of the total area being classified to a high hazard level (0.65–0.90), while about 42.44% as medium hazard, and 19.45% as low hazard level as seen in Table 3.6. It can also be observed from the figure that the ERI is highest at few isolated downslope areas in the north and south of the region (represented in yellow) and decreases towards the ridge at the upslope. This can be attributed to the permeability variation due to presence of sandy loam (low ERI), rocky loam and silty clay loam (high ERI) type of soils. However, under different rainfall conditions the pixels in that region has low DHI owing to the geomorphological conditioning factors, considered analogous to the soil strength characteristics. Frequency analysis of the top four influential conditioning factors identified in this study illustrates the following conditions for maximum number of landslides;  $IR > 20$ , distance to drainage  $< 75$  m, slope  $> 25^\circ$  and  $STI < 80$ . Thus, the low DHI in the above mentioned area can be explained by the presence of, low value of IR, large distance from the drainage and low slope angles. The rainfall series advancing to the second day (13<sup>th</sup> July) drastically decreased to 15 mm, however increasing the ERI slightly by 8.6% as shown in Fig. 14c. This small amount of rainfall transformed about 3.8% of area existing in both low and medium DHI levels to high (Fig. 3.15c). Third day of the extreme rainfall event brought in 75 mm of rainfall resulting in 32.84% of the area previously existing under high DHI level to be reclassified into very high failure probability. The regions, shown in red (Fig. 3.15d, Fig. 3.15e), indicates the very high (0.90–1.0) DHI level at which the slope

failure is imminent. A very high daily rainfall of 202 mm as the storm progressed into the fourth day, propelled the ERI to attain a value close to '1' (Fig. 3.14e), and subsequently driving the areas with lower DHI values to higher. The extreme rainfall of 15 July 2006 resulted in the model classifying about 48.86% of the region with DHI values in the range of 0.90-1.0 as very high (Fig. 3.15e).

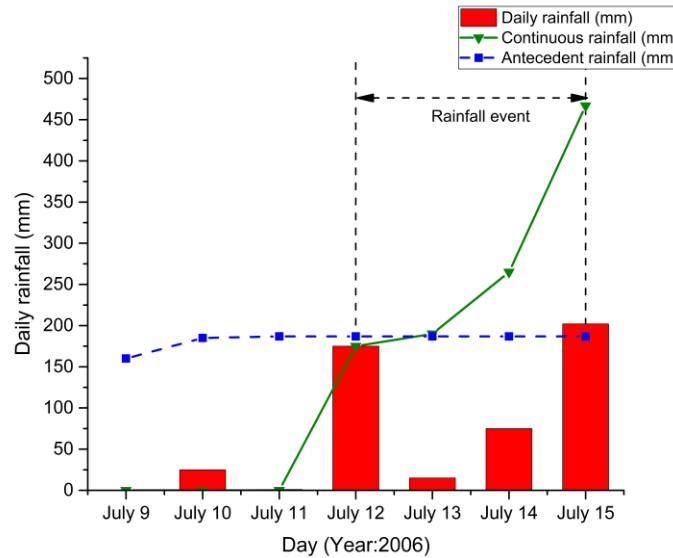


Fig.3.13: Extreme rainfall event in July 2006 in Deokjeok-ri

Table 3.6: Percentage of area classified under each hazard level for different rainfall conditions.

DHI level	% Landslide area				
	Before event	Rainfall event			
		Day 1	Day 2	Day 3	Day 4
<b>Low (0-0.25)</b>	100	19.45	18.34	16.04	15.31
<b>Medium (0.25-0.65)</b>	0	42.44	29.09	17.78	15.62
<b>High (0.65-0.90)</b>	0	38.11	52.57	33.34	20.21
<b>Very high (0.90-1.0)</b>	0	0	0	32.84	48.86

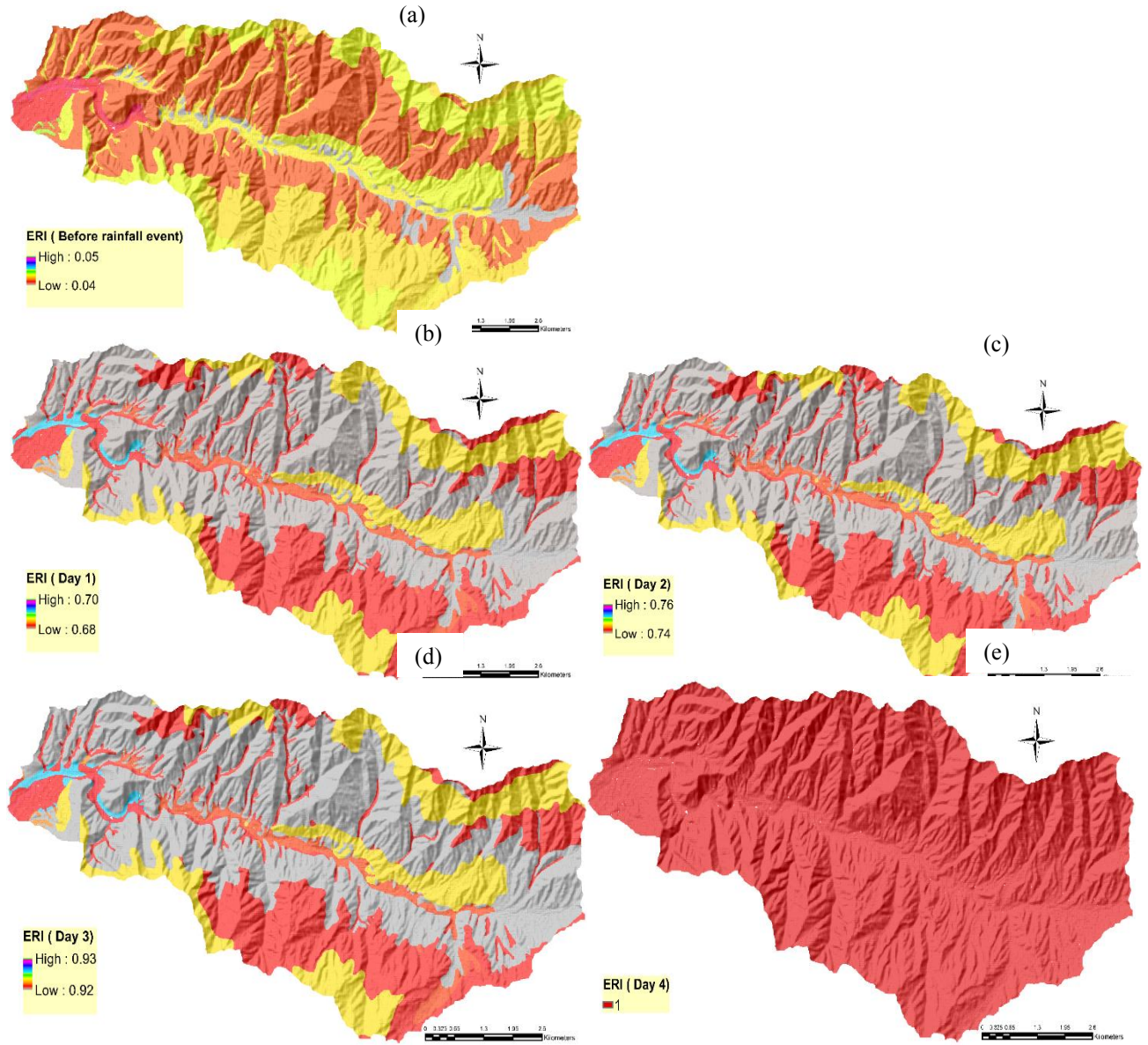


Fig.3.14: ERI map for July 2006 extreme rainfall event in Deokjeok-ri: (a) the day before the rainfall event, (b) rainfall event day 1, (c) rainfall event day 2, (d) rainfall event day 3 and (e) rainfall event day 4

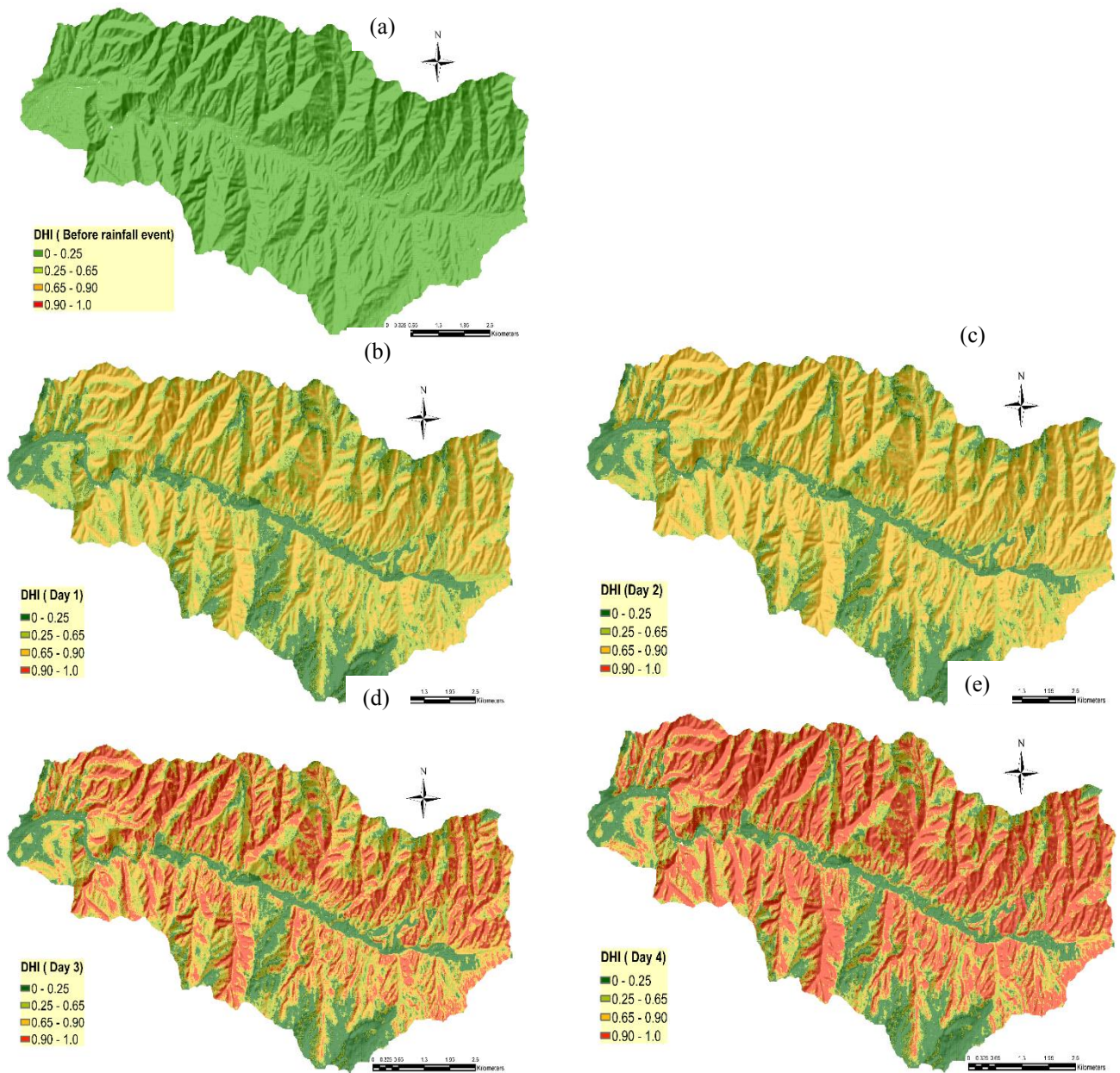


Fig.3.15: Landslide hazard map for July 2006 extreme rainfall event in Deokjeok-ri: (a) the day before the rainfall event, (b) rainfall event day 1, (c) rainfall event day 2, (d) rainfall event day 3 and (e) rainfall event day 4



The temporal assessment using ERI was applied to Mt. Woomyeon for the extreme rainfall event of July 2011 (Fig.2.2b) using 20-day antecedent rainfall (AR<sub>20</sub>) of 346.3 mm and continuous rainfall (CR) of 3 mm, 4.5mm, 77.5 mm and 435.5 mm corresponding to day 1, day 2, day 3, and day 4 rainfall, respectively. It can be observed that at extremely low continuous rainfall on day 1 and day 2 the ERI values are quite low (Fig 3.16a and Fig. 3.16b) and thus none of the cells lies under the high or very high landslide hazard classes as seen from the corresponding DHI maps (Fig 3.17a and Fig. 3.17b). As the event progresses to day 3 for ERI values jump to .57~.62 (Fig. 3.16c), and cells in the upper southeast and northeast near to air force base evolves to high hazard (Fig. 3.17c). On day 4 due to extremely heavy rainfall, the ERI approaches almost 1 (Fig. 3.16d) and a significant portion of the area is classified into very high hazard class (Fig. 3.17d). The high hazard class established at 0.5 cutoff as seen is able to predict all the landslides and hence can be used as a threshold in the proposed hazard framework (Fig. 1).

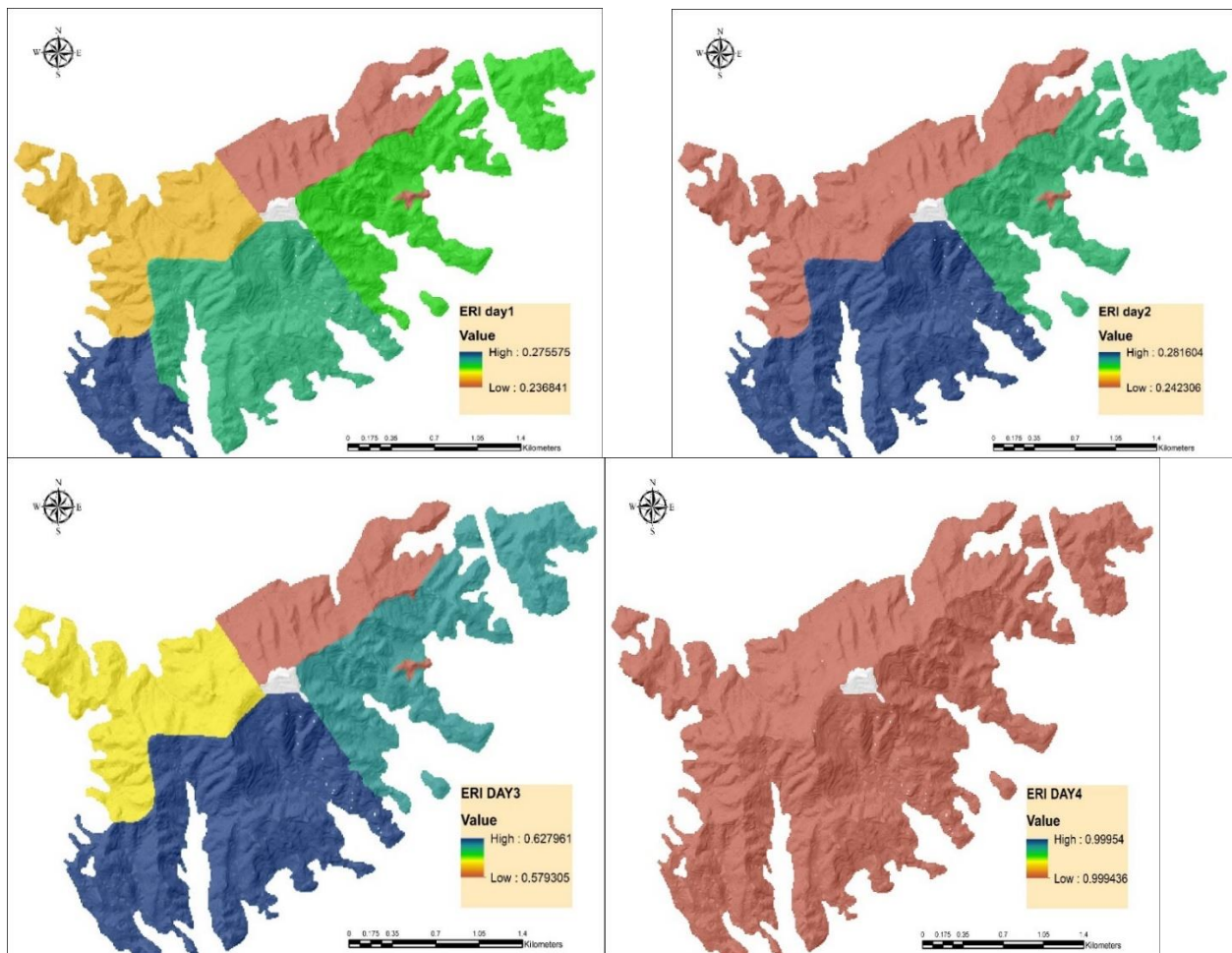


Fig.3.16: ERI map for July 2011 extreme rainfall event in Mt. Woomyeon: (a) rainfall event day 1, (b) rainfall event day 2, (c) rainfall event day 3 and (d) rainfall event day 4

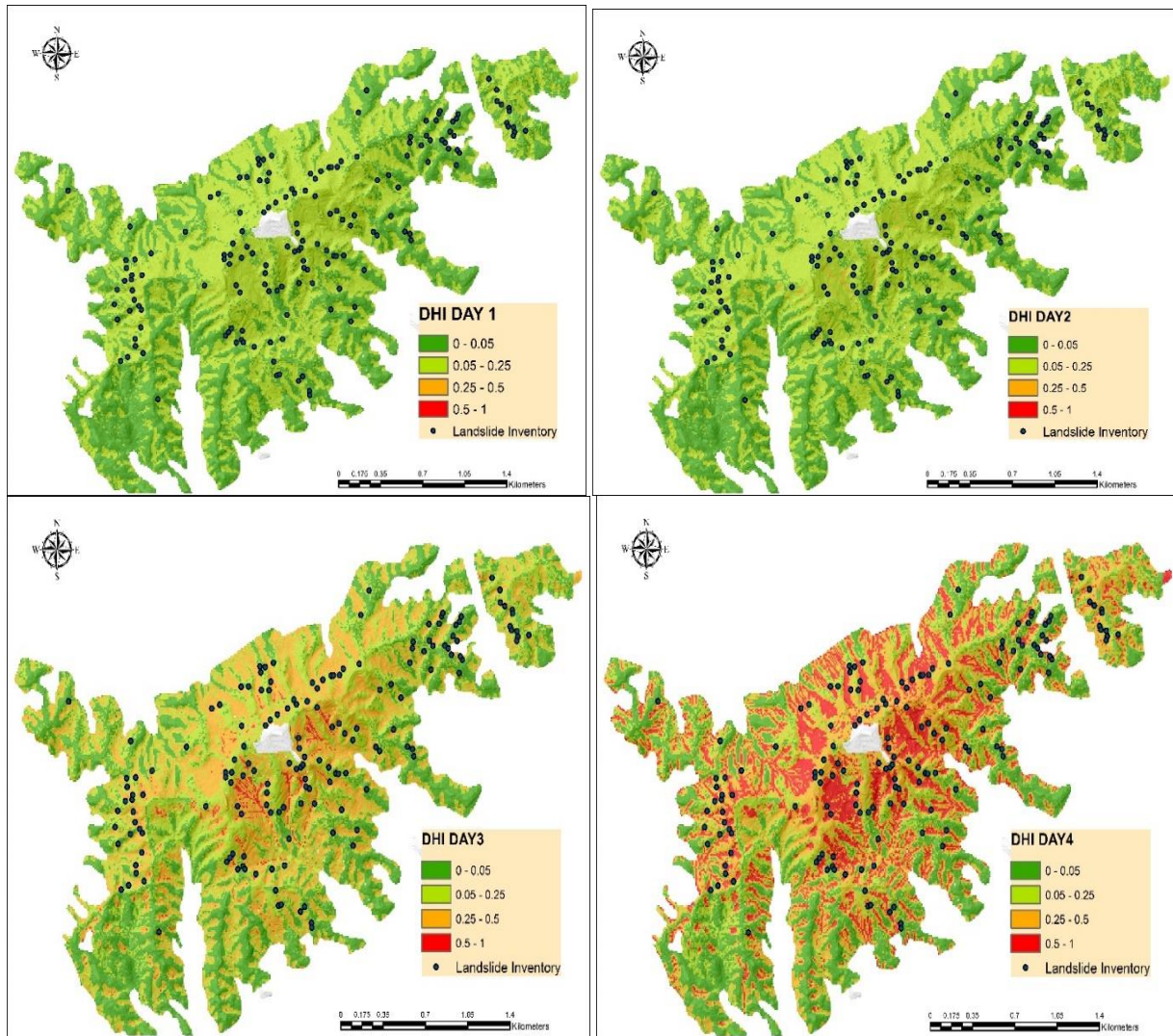


Fig.3.17: Landslide hazard map for: (a) rainfall event day 1, (b) rainfall event day 2, (c) rainfall event day 3 and (d) rainfall event day 4

### 3.5. Conclusions

Most of the existing landslide temporal component assessment computes a threshold exceedance-based temporal probability corresponding to the regional characteristics. However, this method does not serve well in situations where the spatial variation of landslides induced by extreme rainfall is observed due to the variability of soil properties. Therefore, the evolution of hazard levels in an area, needs to be studied. This is especially critical when using real-time-based early warning systems, and when the landslide-hazard-level information is utilized at different tiers of

decision-making. Thus, an attempt has been made through this research to develop a simple statistical index coupling the rainfall and geotechnical factors to study evolution of the landslide hazard due to temporal variation of factors that trigger landslides. The extreme rainfall index (ERI) was developed using four factors (continuous rainfall, 20-day antecedent rainfall, permeability, and storage capacity). The developed model was assessed for accuracy using a cumulative gains chart, by plotting the percentage of landslides in each class. The high AUC values (89 and 97%, respectively) obtained for the training and validation curves, indicate the good performance of the statistical index. Moreover, a spatial probabilistic assessment using logistic regression analysis, was conducted in Deokjeok-ri Creek (located in Inje), resulting in development of a susceptibility map. The final susceptibility model had high training and validation AUC values of 96 and 94%, respectively. The model identified seven relevant conditioning factors (i.e., aspect, internal relief, total curvature, slope, distance to drainage, STI, and forest type). Thus, both of the well validated models were used to study the landslide hazard in Deokjeok-ri Creek for the extreme rainfall-induced landslide events in July 2006 using DHI. It was seen that the ERI values were quite low for the rainfall events prior to the extreme rainfall events starting on 11 July 2006, but increased almost 14-fold during the continuous rainfall (175 mm) on 12 July 2006, and reached the maximum value (0.99) for a CR of 467 mm on 15 July 2006. The entire study area prior to 12 July had very low DHI and was classified as low hazard. However, the extreme rainfall from 12 to 15 July reduced the percentage of cells in the low DHI level to 15.31%. About 48.86% of the cells in the region were reclassified as being under high hazard of landslides after the extreme rainfall of 202 mm on 15 July (formerly 20.59%), and an incremental trend towards transformation to instability was observed. This change in hazard areas accompanying the temporal variation of extreme rainfall, quantified using DHI, is useful in taking decisions with regard to dissemination of the early warning and thus the mitigation of the risk.

## **Chapter 4. A transition scheme for site-specific scale reduction and initial volume estimation for landslide induced debris flow hazard assessment**

### **4.1 Introduction**

The increase in extreme rainfall occurrences is responsible for debris flow related hazards in mountains across South Korea. The Korea Forest Research Institute (2014) has attributed debris flow to cause greater damage in comparison to slides, which moves a certain distance and stops along the path. The identification of factors involved requires a detailed study of the mechanism leading to the initiation. There are several mechanisms which has been hypothesized and studied by researchers for mobilization of debris flow from landslides (Gabet and Mudd, 2006; Iverson 1997; Anderson 1991; Sassa 1984) depending on the initial stress state or the drainage condition. Seed et al. (1988) assigned the mechanism leading to flow-type failure to undrained loading where there is an excess pore water pressure generation during the initial loading and at later stage the soil undergoes strain without any additional loading. Also, for loose sand several studies were conducted pertaining to instability and liquefaction under undrained condition (Leong et al. 2000; Sasitharan et al. 1993; Lade 1993). It was shown by Eckersley (1991) that slopes can undergo drained instability and the subsequent pore pressure generation is the result of flow-type failure. In Korea, most of the mountains are overlain by weathered soil at shallow depth and thus, a drained failure instability mechanism preceding the mobilization is the most suited and an effective stress based analysis will be undertaken for the same. Though the initial instability is a result of drained loading, however, depending on the soil stress state the initiation mechanism may vary. A soil with voids ratio above the critical-state porosity i.e., contractive or loose, will undergo contraction leading to generation of excess pore water pressure and thereby flow liquefaction. But if the initial voids ratio is below the critical-state porosity, i.e., dilative condition, the explanation for flow type failure occurrence is a bit tricky and has been the focus of few studies. Flow-failure in some of the well documented studies like the Fort Peck Dam case and Nerlerk berm failure case (Been et al. 1988; Torrey and Weaver 1984), was shown to occur for dilative sands that lies above the steady state and ruled out undrained mechanism as the probable cause.



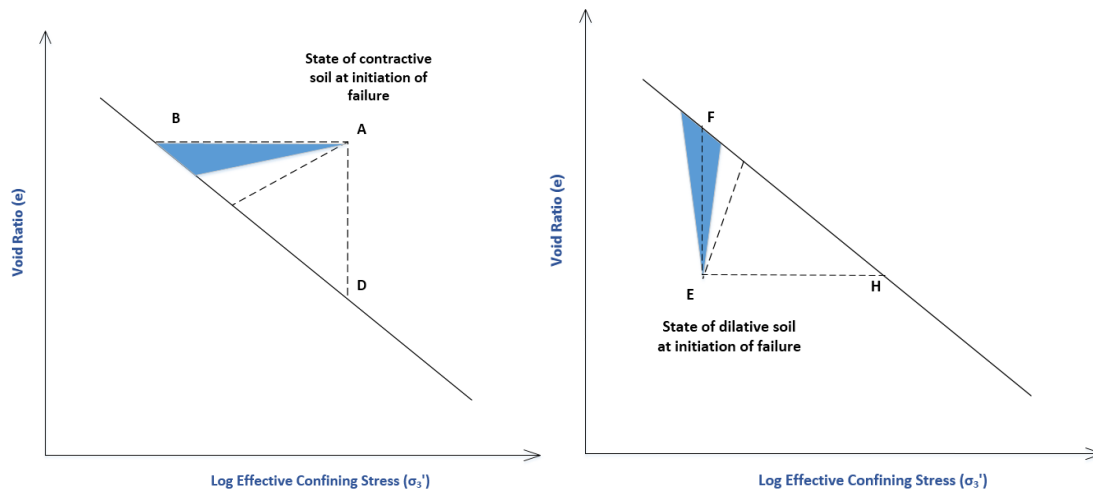


Fig 4.1. Influence of initial stress state on the stress path to mobilization

Chu et al (1993) and Chu and Leong (2001) established that dilative soils cannot undergo plastic strain under undrained conditions. A slope under infiltration follows a stress path where, a dilative soil at initial stress state, reaches the critical state line (CSL) under a constant shear stress through an effective stress decrease. The contention for emphasizing the importance of this stress path is that the actual increase in shear stress due to change in moist unit weight is small and only a change in seepage characteristics can cause the deviation from a horizontal stress path. Also, under drained condition the reduction of mean effective stress would not generate any negative pore pressure thus, preventing the soil from stabilizing thereby transitioning into a contractive phase and the presence of a favorable geomorphological characteristics like a channel, will further the large straining and remolding or void redistribution leading to a flow-type failure (USGS video recordings). In another scenario, the dilative soil failed under drained condition, through some undrained stress path mechanism transforms and forms a slump, then only additional supply of water (e.g. rainfall or ponding at upstream) can provide the necessary pore-water pressure for mobilizing (Gabet and Mudd, 2006; Harp et al., 2004; Fleming et al., 1989). From the above it can be seen that the mobilization of landslides into debris flow is quite a complicated process involving the initial stress state, hydraulic conductivity and geomorphological characteristics. Few attempts have been made to develop the mobilization criterion for dilative soils like the one proposed by Gabet and Mudd (2006) which however, requires extensive testing to determine the critical voids ratio, dilation angle or the shear zone thickness. A 1-D model for debris flow mobilized from landslide was proposed by Takahashi (2001), in which a deep seated cohesive landslide mass propagates downwards through undrained mechanism and the liquefied shear

zone cannibalizes the upper saturated body. This mechanism and model however is not applicable to events observed in Korean mountains since the weathered soil undergoes complete destruction of the void rich structure during its mobilization into debris flow. Another criterion, approximate mobility index defined as the ratio of the in-situ saturated water content to its liquid limit (Ellen and Fleming 1987), though simple but cannot be applied to soil with abundant coarse fraction and also, there is the issue with sampling and lab testing when a large region is involved.

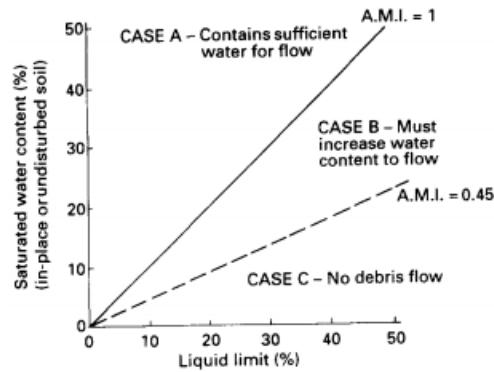


Fig 4.2: AMI criterion for debris flow mobilization (Fleming et al., 1989)

It is therefore difficult to explicitly adopt the above mechanisms for landslide induced debris flow in EWS through analytical models or their analogous simplified criteria based on geotechnical factors. Hence, currently only empirical based methods are the way forward which though having the drawback of being data dependent and non-transferable to other regions, can implicitly accommodate all of the above mechanisms and be incorporated inexpensively into the EWS for spatial based sifting of debris flows from slides or other landslide types.

## 4.2 Debris flow mobilization scheme for sifting debris flows from landslides

### 4.2.1 Existing empirical mobilization criteria

Data driven methods are usually adopted when the mechanism involved are too complicated and expensive in terms of modelling, data collection and validation. In several instances like the landslide susceptibility modelling over a large scale or debris flow hazard assessment (runout velocity, volume or spreading), the empirical methods are preferred due to their relative easiness and accessibility to quality real event database.

In this study, the main objective of the mobilization criterion is to discriminate the locations where debris flows will initiate from the non-debris flow events. In literature there are two main methods to achieve this objective: (a) developing mobilization criterion using debris flow occurrence events and either non-occurrence (which includes non-landslide points and non-debris flow events) or the non-debris flow events; (b) developing initiation criterion through an index based approach using only the debris flow events.

The empirical statistical model developed by Cui (1992) through experimental results of debris flow initiation. The model considered fine grain content  $C$  ( $< 1$  mm), the soil saturation  $S_r$ , and the bed slope  $\theta$  are the main factors in the regression equation given as:

$$\theta - 8.0062S_r - 2.4859S_r^2 - \frac{3.4896}{C - 0.0996} + 7.0195 = 0 \quad (4.1)$$

The above equation gives a curved surface, on which if any point which is a function of the above parameters exists at a critical state.

Another GIS based initiation criterion using an empirical method is implemented in a distributed model called Flow-R. The model though mainly used for run-out susceptibility modelling but also has methodology for identifying the initial source areas. The source area delineation is based on an index-based approach in which a grid cells are classified as favorable or excluded or ignored. Three debris flow initiation parameters, slope, flow accumulation, and plan curvature were selected based on three criteria's (Rickenmann and Zimmermann, 1993; Takahashi, 1981): slope, water supply, and material availability. A value of  $15^\circ$  for the slope was selected as the lower threshold for debris flow occurrence based on case studies from Alps and Japan. The upslope contribution value was selected through a

combined work of Rickenmann and Zimmermann (1993) and of Heinimann (1998) by plotting a curve for the extreme events between terrain slope and the upslope area as shown in Fig 4.3. The threshold fitted using the data as in the figure is given as:

$$\begin{aligned} \tan \beta_{thresh} &= 0.32 S_{uca}^{-0.2} & \text{if } S_{uca} < 2.5 \text{ km}^2 \\ \tan \beta_{thresh} &= 0.26 & \text{if } S_{uca} \geq 2.5 \text{ km}^2 \end{aligned} \quad (4.2)$$

The grid cells in a region is selected as susceptible to debris flow if a cell is at least once selected as favorable and never excluded.

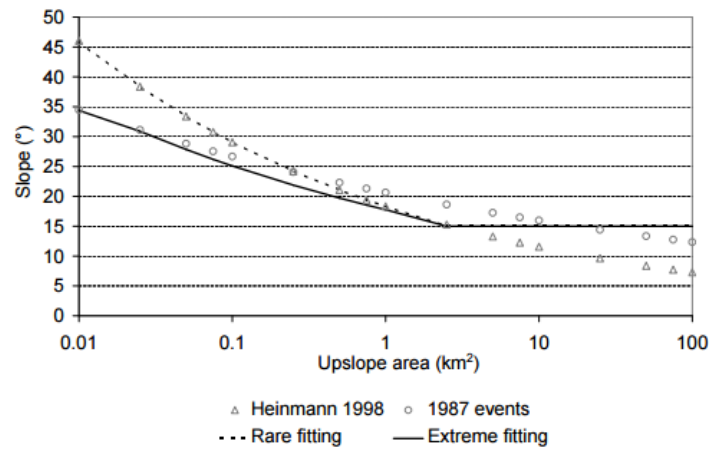


Fig 4.3: Slope-upslope criterion for debris flow initiation (Rickenmann and Zimmermann, 1993)

Flow-initiation source areas were determined in the LAHARZ program (Griswold and Iverson, 1998) using the morphometric parameters, slope and upslope contributing area. The slope criterion and upslope contributing factors had a minimum threshold of  $30^\circ$  and  $10^3 \text{ m}^2$  respectively. The threshold criterion was implemented in the program using the rule for the area around the centered prospective initiation cell as: steep slopes with 95 % of grid cells exceeding  $30^\circ$  in a  $100 \text{ m}^2$  area. Blahut et al. (2010) analyzed areas susceptible to landslide induced debris flow using the debris flow susceptibility map. The model was developed through the Weight-of-Evidence technique on medium scales (1:25,000 to 1: 50,000) for Valtellina Valley in Central Italian Alps. The national database for landslide inventory GeoIFFI, consisting of 1478 landslide scarps mapped using points, lines, and polygons were classified as debris flow, earth flows, shallow landslides, and deep seated landslides. The assessment of debris flow initiation was conducted using five factors, namely, slope, land use, geology, internal relief, and planar curvature. A relationship based on

regression equation was derived by Chen and Yu (2011) using debris flow events in 11 river basins to study the debris flow initiation areas in Taiwan. The debris flows initiated at slope values between  $30^{\circ}$  and  $42^{\circ}$  and the relationship between TWI and slope was established through regression as:

$$TWI = -.04S_R + 6.34 \quad r^2 = 0.95 \quad (4.3)$$

#### 4.2.2 Study area and data

The criterion for assessing the spatial information of landslide induced debris flows was developed for Mt. Woomyeon, Seoul, South Korea. The geologic, soil, and vegetation related information has been described in detail in Chapter 2 of the thesis.

Mt. Woomyeon in Seoul was subjected to extreme rainfall event of 460 mm in 16h from 26 to 27 July 2011 resulting in several catastrophic debris flows.

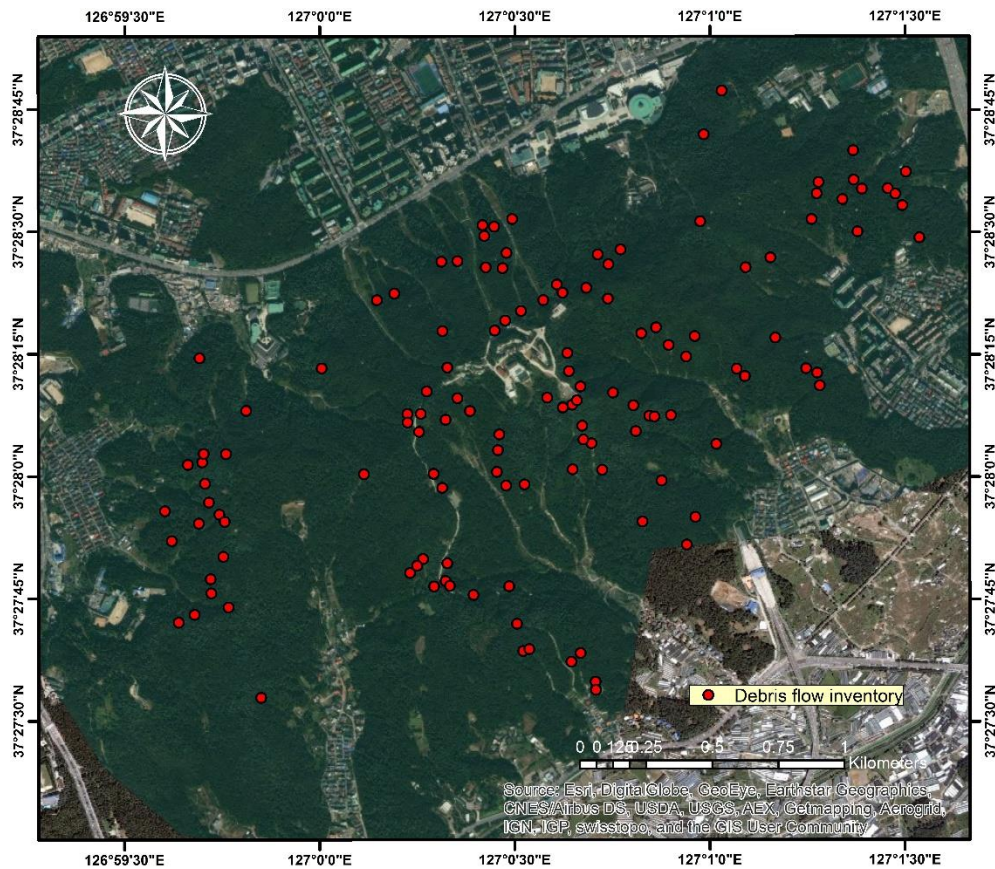


Fig 4.4: Debris flow inventory in Woomyeon mountain.

Out of total 163 landslide inventory points mapped, about 141 were debris flow induced from landslides as is seen in Fig.4.1. The debris flow points were mapped using satellite images using satellite images, high resolution aerial

photographs, and field reconnaissance. High-resolution photographs of 25-cm resolution were procured from the National Geographic Information Institute (NGII), and satellite images were obtained from Google Earth and Bing maps. These images were orthorectified via ground control points in ArcGIS 10.1, and landslide locations were detected through visual interpretation.

#### 4.2.3 Debris flow initiation factors

Through a detailed literature review seven geomorphological factors which can influence the debris flow initiation were selected and classified into two types as seen in Table 4.1: morphological and hydrological. The factors selection was performed through a consideration of four criteria's suggested by Rickenmann and Zimmermann (1993) and Takahashi (1981): potential energy, water supply, material availability and presence of channel.

##### 4.2.3.1 Morphological types

Elevation has been used as a conditioning factor in several studies, and higher values are generally related to higher susceptibility caused by variation in rainfall, vegetation, and potential energy availability (Pachauri and Pant, 1992; Ercanoglu et al., 2004). Elevation was positively correlated with landslide occurrence and was divided into six classes, with a maximum value of 293 m (Fig. 4.2.3A).

Slope, defined as steepness of a surface, and its second-order derivative curvature, helps in understanding the characteristics of a basin for runoff and erosion processes. In this study, three types of curvature are considered: (i) profile curvature is defined along the line of maximum slope (Fig. 4.2.3C); (ii) plan curvature is defined along the line of intersection between the surface and XY plan (Moore et al., 1993; Figs. 4.2.3D). Curvature can affect landslide susceptibility through acceleration or deceleration and through convergence or divergence of flow (Kimerling et al., 2011), depending on if it is convex, planar, or concave. In addition, steeper slope angles are related to higher shear stress, and Fig. 4.2.3F shows the five classes of the raster, with second class (12.95-25.92) and third class (25.92-38.87) occupying 61.76% and 24.72% of the total area, respectively.

##### 4.2.3.2 Hydrological types

Flow accumulation is a fundamental hydrological attribute and indicates the area that has the potential to produce runoff to a cell under consideration (Erskine et al., 2006).

TWI, based on assumptions of uniform soil properties and steady state conditions (Conforti et al., 2014), can be used to describe the distribution pattern of moisture for potential infiltration volumes according to five classes (Fig. 2-3K),

with higher values in natural drainage channels and lower values along ridges and alluvial fans. The factor is calculated using Eq. (4) (Moore et al., 1991):

$$TWI = \ln \left( \frac{A_s}{\tan \beta} \right) \quad (4.4)$$

where  $A_s$  is the specific catchment areas, and  $\beta$  is the local slope gradient measured in degrees.

SPI, which measures the erosive power of the flow, increases with the surge because of a larger upslope area and slope (Florinsky, 2012). Figure 4.2.3M shows higher erosive values existing along the drainage channels. It is given by (Moore et al., 1991)

$$SPI = A_s \times \beta \quad (4.5)$$

Table 4.1: Database characteristics for debris flow initiation criterion development

Type	Factor	Source	Scale (Resolution)	Organization
Morphological	Elevation	DEM	10 x 10 m	NGII
	Slope			
	Plan curvature			
	Profile curvature			
Hydrological	Flow accumulation	DEM	10 x 10 m	NGII
	TWI			
	SPI			
Landslide inventory		Field investigation report		Korean Society of Civil Engineers
		High resolution images	25 x 25 cm	NGII
		Satellite images		Bing maps Google Earth

#### 4.2.4 Methodology

As described in section 4.2.3 there are two ways to develop debris flow initiation criterion depending on the database availability. The criterion developed by Blahut et al. (2010) and Cui et al. (1992) used the first method owing to the availability of database which clearly distinguished between the different landslide types. However, LAHARZ, Chen and Yu and Flow-R use the index-based approach of debris flow mobilization since the database is limited to only debris flow type of landslides. In this study, the debris flow mobilization criterion was established through an index based approach by setting up a lower threshold for the factors at which debris flow would initiate. The new criterion developed in this study is different from the other index-based previously discussed because of the rule used to classify the potential cell as susceptible to debris flow, which is stated as follows: *“a pixel is classified as a potential debris flow source, if and only if all the four conditions are satisfied”*. The main reason for adoption of this approach is not only the availability of reliable database for debris flow type landslides but also the lack of database to conduct a temporal assessment of the landslide induced debris flow which combined with the spatial component gives an indication of hazard to the catastrophic event at large scale. Thus, the development of ERI and ELM based hybrid model for landslide susceptibility considering all the types of landslides necessitated the use of a mobilization criterion incorporating only the debris flow events. Though, a criterion based on regression or ANN could be made through the consideration of both debris flow and slide events, but the lack of a benchmark for distinct discrimination between the two types of landslides during the mapping process will compromise the integrity of the final model. The use of a simple classification scheme based on distance and mapped based on visualizations on aerial photos can be misleading. Many a times owing to considerable time between the events, vegetation may cover a debris flow path and can deceive the researcher into mapping the point as a slide. On occasions, landslides occurring at lower elevations and have shorter run-out path lengths may get classified as a slide or debris flow. In such cases, it is of utmost importance that a site investigation be conducted and the soil sample analyzed to check if it is susceptible to liquefaction or if the soil at the deposition zone has liquefied to classify it as a debris flow. Hence, owing to so many uncertainties and to preserve the quality of database established, it was decided to adopt only the debris flow occurrence based (index-based approach) database for the criterion development.

The seven debris flow mobilizing conditioning factors were extracted from the DEM at 10-m resolution in ArcGIS 10.2. A filter based method was used to screen the relevant factors by conducting correlation analysis. The bivariate parametric analysis called Pearson's coefficient is used to study the correlation between the initiation conditioning



factors. All the debris flow events were divided as two sets: 95 % of the data was used for the criterion establishment and 5% was used for validation. The accuracy assessment of the criterion was carried out by evaluating if the cells classified as susceptible lies within the real debris flow path. This type of simple validation technique was adopted since the cells identified as susceptible are used only for transitioning into the detailed scale and not to estimate the initial volume of landslide that mobilizes into debris flow, therefore, is explicitly not part of the quantitative run-out hazard assessment carried out at the site-specific scale.

#### 4.2.5 Discussion and conclusion

Table 4.2 indicates the correlation among the morphometric and hydrological types of debris flow mobilization factors. It can be observed that SPI has significant relationship with TWI and plan curvature, while slope is also significantly correlated to TWI. On the other hand, TWI is also substantially related to upslope area. Profile curvature has significant correlation only with plan curvature, and elevation among all the seven is not related to any of the factors. Thus, in light of this relationship, four factors mainly, elevation, profile curvature, slope and SPI are selected for the mobilization criterion development. Thus, the debris flow criterion was applied to the Woomyeon mountain using the four factors; slope angle, profile curvature, SPI, and elevation having lower threshold values of  $24^\circ$ , -4 to +4, 4.0, and 60 m, respectively.

Fig. 4.5 shows the result from application of the debris flow criterion to the entire Woomyeon mountain in Seoul. A quick glance at the figure shows majority of potential areas to be mainly located at the higher elevation around the air force base, which has seen several debris flow events and also, along the stream channels. The criterion developed using only the debris flow cases and not considering any other landslide types gives a conservative estimate. The debris flow criterion can be coupled with temporal data to determine the locations where debris flow will mobilize for a given rainfall event. The DHI map developed for rainfall event in Chapter 3 can be coupled with the criterion (Fig. 4.5) and the result is as seen in Fig. 4.6. Day 1 and Day 2 were not considered since no cells were classified into the very high hazard classes ( $DHI \geq 0.5$ ). From the figure for day 3 it can be seen that few cells in southeast and one cell in north at top of the mountain mobilize into debris flow (Fig 4.6a). On the other hand, for extreme rainfall on day 4 (Fig 4.6b) a significant number of debris flow points can be seen and many of them correspond to the real event location.

Table 4.2: Correlation among the debris flow initiation factors

		SPI	Slope	TWI	Upslope	Profile	Elevation	Plan
SPI	Pearson Correlation	1	.194	.872**	.206	.018	.041	-.474**
	Sig.(2-tailed)		.080	.000	.063	.872	.715	.000
Slope	Pearson Correlation	.194	1	-.302**	-.032	-.001	.124	-.015
	Sig.(2-tailed)	.08		.006	.773	.996	.268	.896
TWI	Pearson Correlation	.872**	-.302**	1	.209*	.026	-.004	-.450**
	Sig.(2-tailed)	.000	.006		.048	.814	.971	.000
Upslope	Pearson Correlation	.206	-.032	.219*	1	-.209	.061	.022
	Sig.(2-tailed)	.063	.773	.048		.060	.586	.848
Profile	Pearson Correlation	.018	-.001	.026	-.209	1	-.09	-.449**
	Sig.(2-tailed)	.872	.996	.814	.060		.423	.000
Elevation	Pearson Correlation	.041	.124	-.004	-.061	-.090	1	.212
	Sig.(2-tailed)	.715	.268	.971	.586	.423		.055
Plan	Pearson Correlation	-.474**	-.015	-.450**	.022	-.449**	.212	1
	Sig.(2-tailed)	.000	.896	.000	.848	.000	.055	

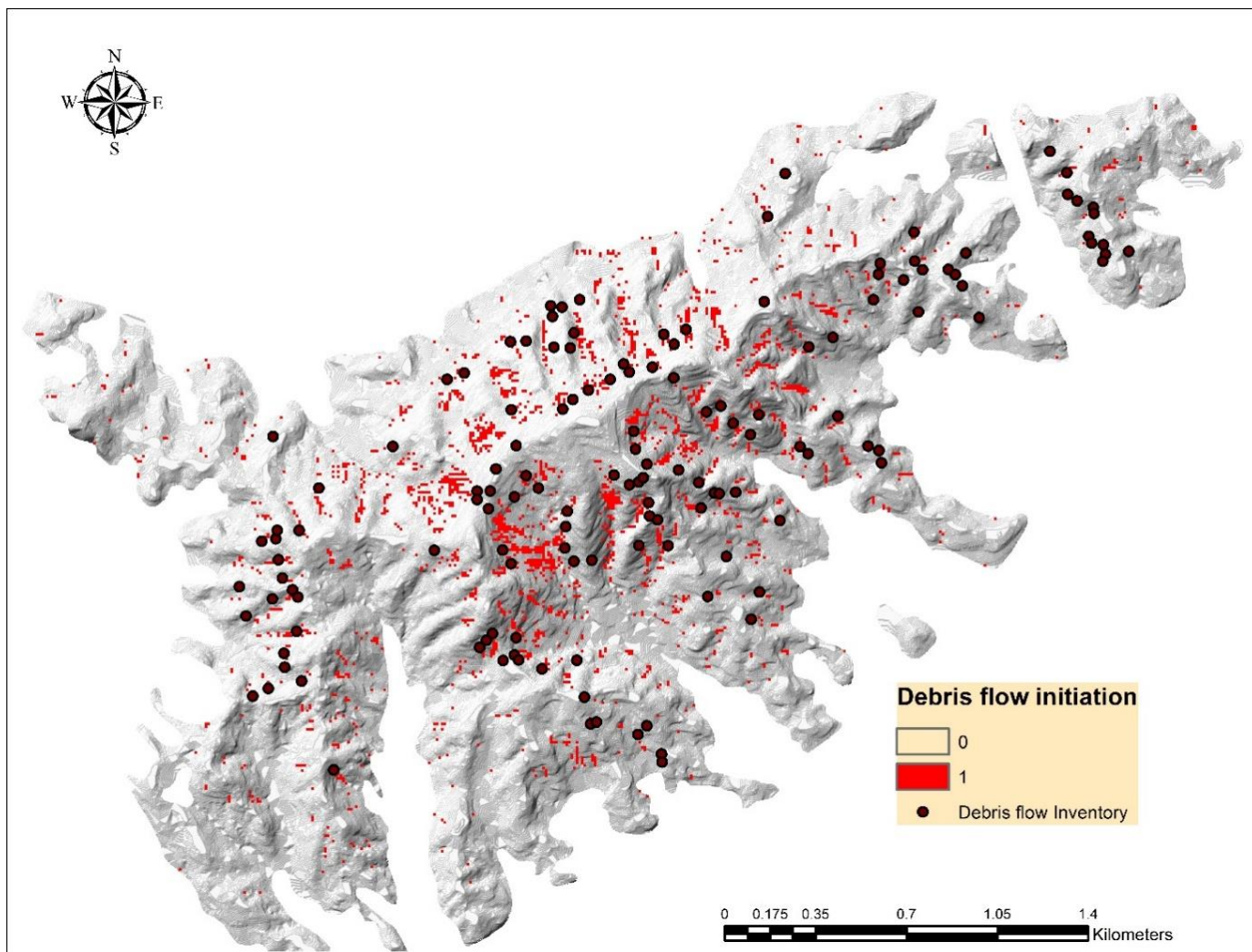


Fig. 4.5: Application of mobilization criterion to Mt. Woomyeon

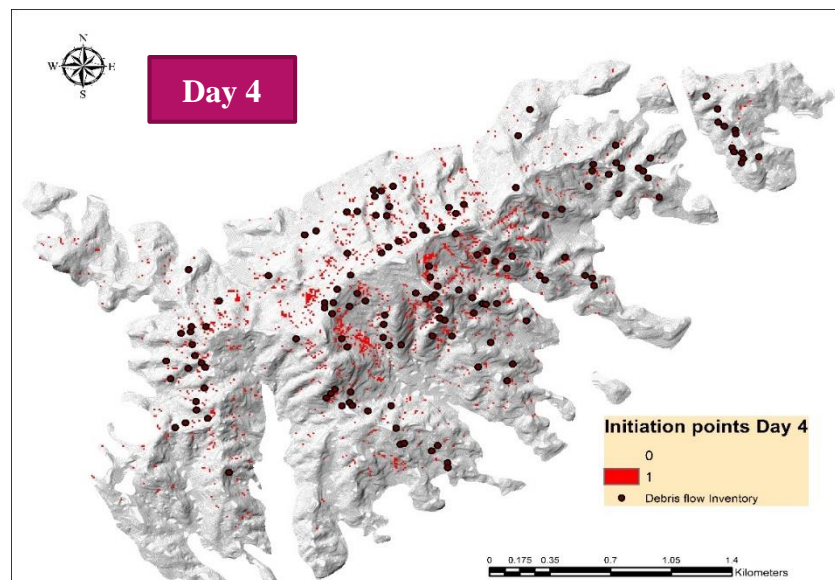
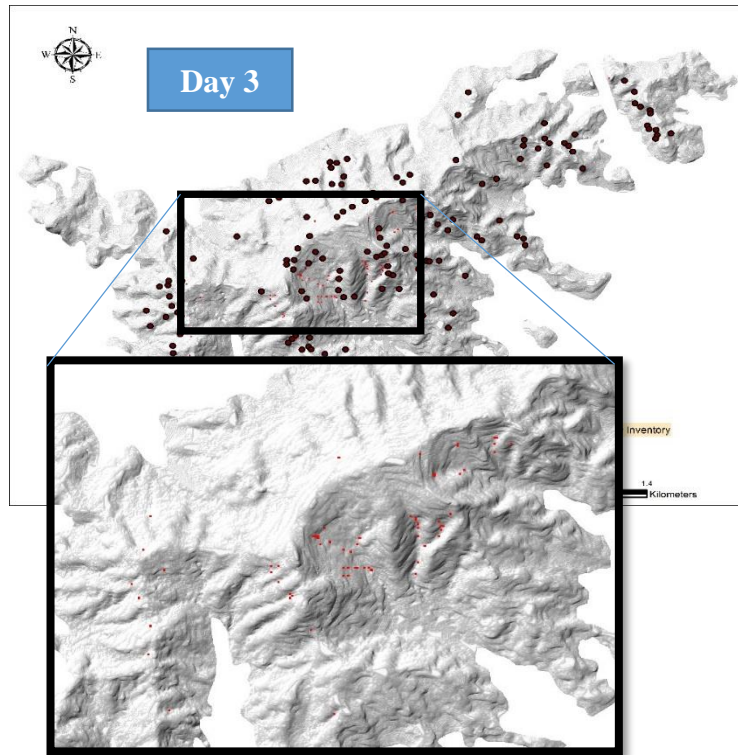


Fig. 4.6: Evolution of debris flow points for 2011 extreme rainfall event: (a) Day 3; (b) Day 4

### 4.3 Methodology for slope selection at site-specific scale

#### 4.3.1 GIS based database

The scale reduction from large to site specific involves establishing slope units incorporating the debris flow mobilization criterion. The study area for the application of this scheme is Mt. Woomyeon, Seoul.

For application of the scheme, DEM and reverse DEM at 10-m resolution are obtained as seen in Fig 4.7a and Fig 4.7b. Also, the mobilization criterion developed in the study area, shown in Fig 4.5, is also used.

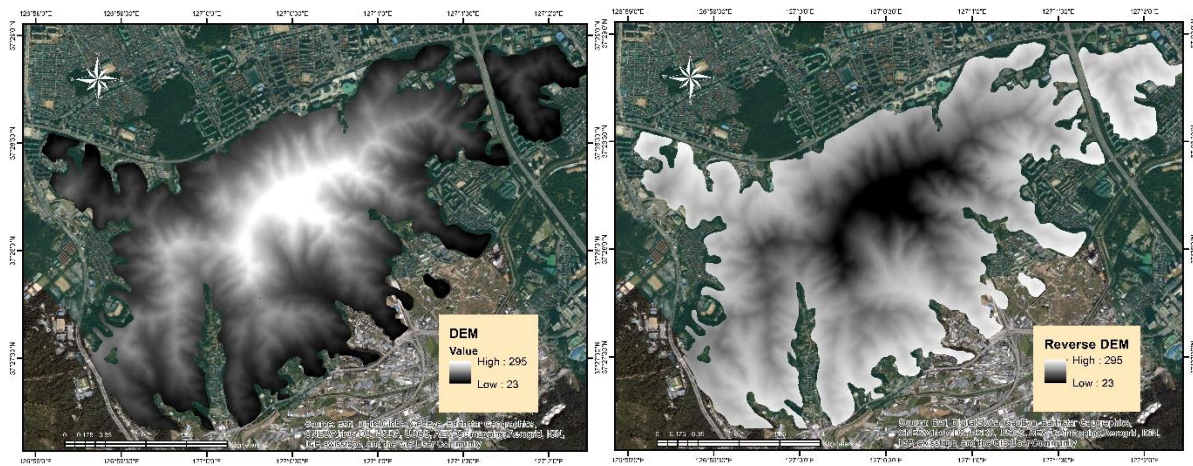


Fig 4.7. (a) Original DEM; (b) Reverse DEM

#### 4.3.2 Methodology

In the previous section, debris flow mobilization criterion and their application to Woomyeon mountain, Seoul was discussed. The application of debris flow mobilization criterion shows the spatial locations where the landslide has very high probability to mobilize into a debris flow. Thus, among the large spatial distribution of landslides at regional scale it was possible to sift the potential debris flow mobilizing ones for further analysis in EWS.

The slope for detailed debris flow run-out assessment was selected using the watershed management tools in ArcGIS 10.1. The following procedure was adopted for same:

- a) Initially, the DEM of the desired assessment region is checked for errors due to sinks using the Fill tool.
- b) The stream flow directions are calculated using the D8 algorithm through flow direction tool which is used to determine the actual river lines through flow accumulation tool.



- c) The debris flow mobilization criterion is applied in the region and the points overlaying the landslide points determined from the susceptibility map are selected.
- d) The selected potential debris flow points are combined with the stream flow directions and the lowest value along the stream flow is carefully chosen as the outlet point of the watershed. Finally, the chosen pour points are inputted in the watershed tool to create the automated watersheds.
- e) Instead of step (d), another method through inversion of DEM can be used to create the watersheds (Xie et al., 2003). The reverse DEM transforms the previous valleys as ridges and thus on combining with the original DEM it is possible to get the left and right part of slope units. Finally, polygons can be created only for the regions where debris flow criterion and landslide occurrence points overlap each other.

### 4.3.3 Application

The stream flow directions using the hydrologically corrected 10-m DEM of Mt. Woomyeon is as shown in Fig 4.8a and the calculated flow direction is used to determine the stream flow channels for an upslope area threshold of 250 m<sup>2</sup>. It can be seen that the southeast side of the mountain has channels of higher order in comparison to those at the northeast side.

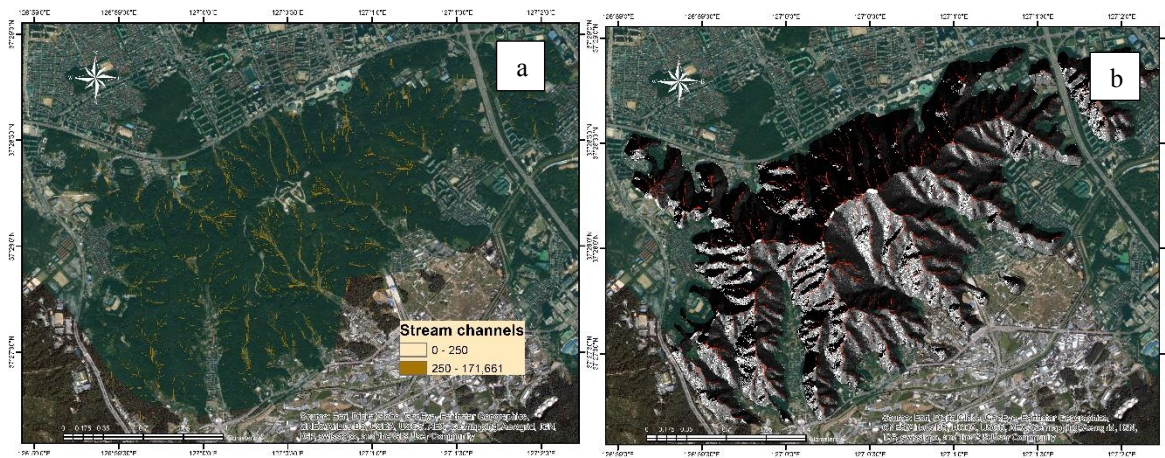


Fig 4.8. (a) Flow directions for DEM; (b) Flow directions for combined DEM

In this study, the reverse DEM method is applied onward to get the watersheds in the region. Fig 4.8b shows the delineation of the ridges and valleys obtained through flow accumulation tools in ArcGIS 10.1 using the DEM obtained from combination of original and reverse. The redlines seen in the figure represents the ridges.

The final slope unit distribution for Mt. Woomyeon developed in combination with the mobilization criterion is shown in Fig.4.9. Mt. Woomyeon has been divided into 45 slope units based on drainage channels and the debris flow mobilization criterion. The watershed area is smaller in the northeast side of the mountain in comparison to the southeast side because of the presence of drainage channels of lower order.

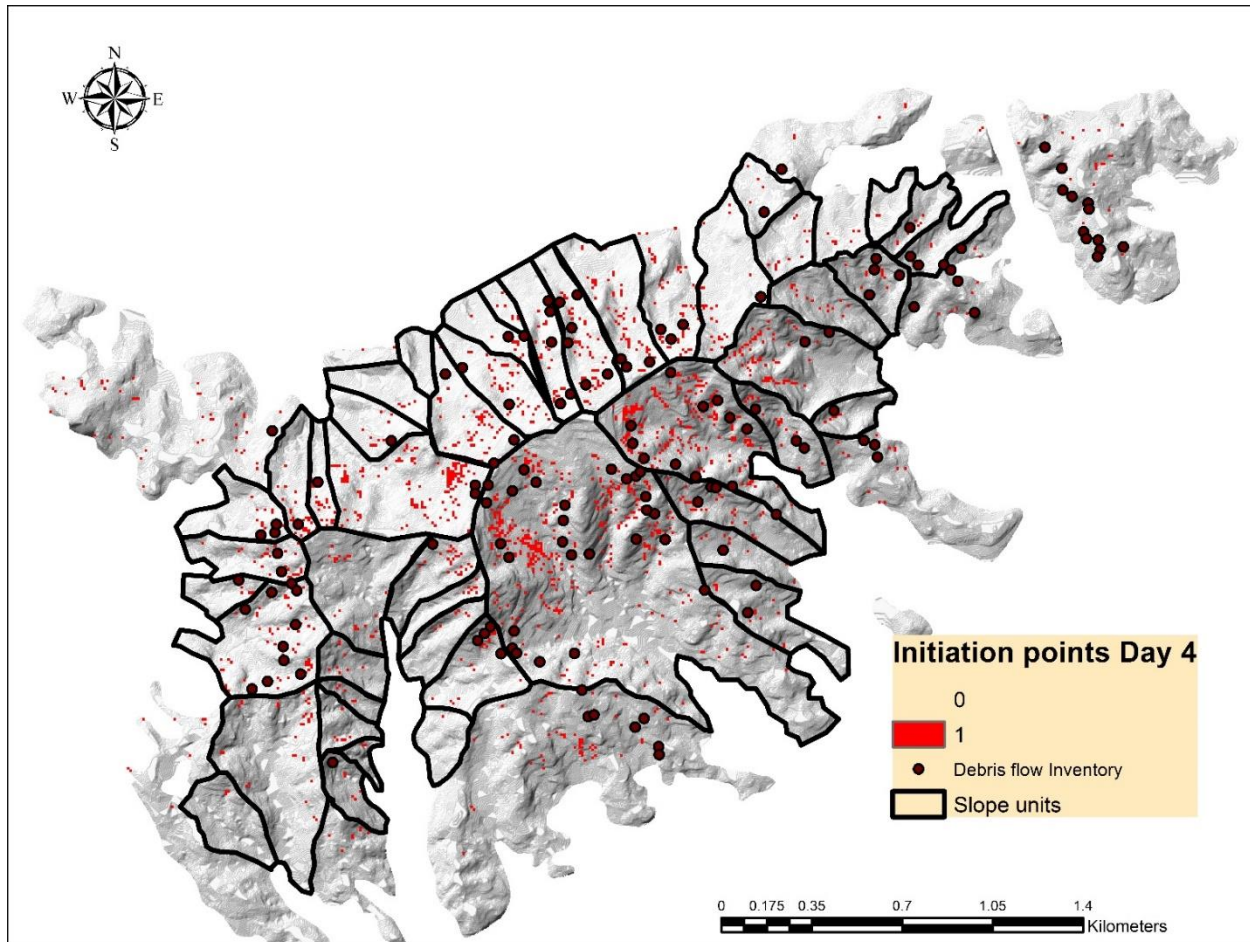


Fig 4.9: Slope units for Mt. Woomyeon

## **Chapter 5. Predictive debris flow runout assessment methodology at a site-specific scale using a quasi-3-D model**

### **5.1 Introduction**

The most catastrophic landslide events in Korea are the debris flow mobilized from landslides due to extreme rainfall. These rapid to extremely rapid processes are characterized by completely liquefied materials comprising of coarse and fine particles matrix with varying level of water saturation. The hazard evaluation as a component of EWS would require the evaluation of the debris flow intensity and magnitude factors like velocity, volume or the flow depth. There are several existing approaches to estimate the flow type run out which vary with respect to the type of landslide, the scale of analysis, availability of data and the extent of outputs. The run out models for debris flow simulation can be broadly classified into two types i.e., empirical and physical. The models developed using empirical methods are used to estimate the travel distances or the final volume rather than other quantitative factors like velocity, thickness, flow direction, etc. (Pastor et al., 2014). These type of models, established using past event database though simple and easy to implement, have the major limitation of systematic collection of large database for model building and verification and not being transferable to other regions.

There are two main concepts used to physically model the flow type landslides in the literature and can be classified as discontinuum methods like discrete, molecular dynamics, or statistical mechanics (Campbell and Brennen, 1985; Campbell, 1990; Cundall and Strack, 1979), and continuum methods (Hungr, 1984; Denlinger and Iverson, 2004; Pastor et al., 2014). Discontinuum based methods are mainly used to model rock falls, rock avalanches, granular flows with particle-fluid coupling, or flows with significant boulders. The application of discrete models to flow type landslides especially granular flows are considered since many researchers believe the solid to show discrete characteristics, with particle collisions and interstitial fluid altering the flow properties along the flow path. The solid particles in this method can be represented in spherical or non-spherical shapes and interactions are modelled using force-displacement law and Newton's second law of motion (Teufelsbauer et al., 2011). However, these methods are still at infant stage in application towards geohazard problems of the flow type landslides which will involve modelling different grain sizes (sand, silt, clay or boulders) involved and also owing to large computational resources requirements. On the other hand, continuum models are the most popular and widely used by researchers for modelling



most of the flow-type landslides. This method is based on the concept that particles can be modelled as continuous mass rather than discrete for analyzing their mechanical and kinematic behavior. The lumped mass models using the work-energy theory and assuming the displacement of the landslide as a single point are the simplest continuum models (Perla et al., 1980; Hutchinson, 1986). In these models the internal deformation and energy dissipations are neglected but provides a reasonable approximation of the center of gravity motion of the debris flow (Hung, 1995). However, these models cannot be used for hazard analysis owing to the failure to simulate the flow front.

## 5.2 Framework for database development

In this section, a methodology for database establishment with the objective of debris flow runout hazard assessment is presented. Fig.5.1 shows the methodology adopted for the same.

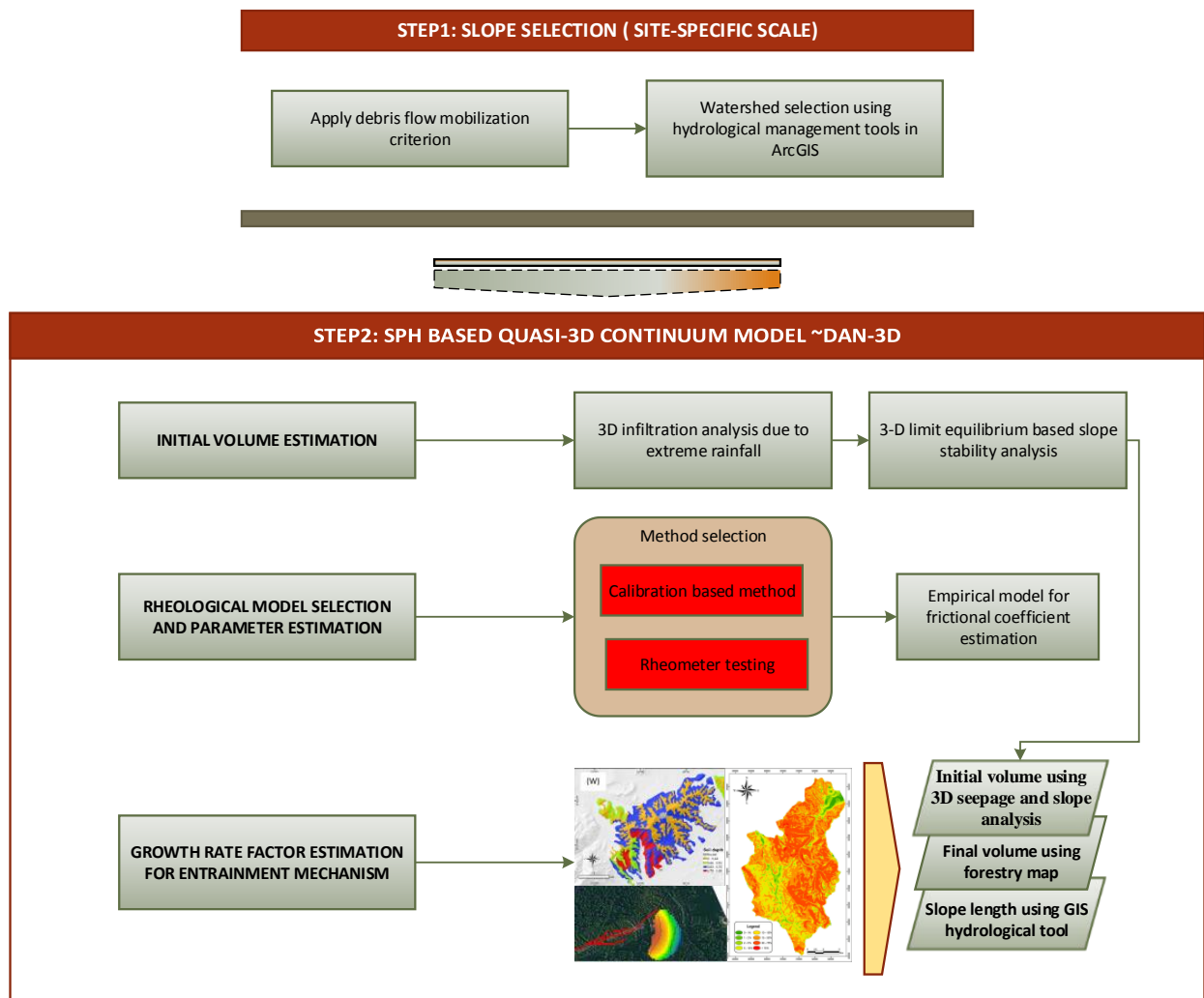


Fig. 5.1. Framework for database establishment for predictive hazard assessment of debris flow runout

### 5.2.1 Site-specific initial volume estimation

Initial volume is analogous to the potential energy that will be transformed into bulk translational kinetic energy. As mentioned in introduction (Chapter 1) there are several models for landslide initiation volume estimation and its accuracy varies depends on the scale of application. In this research we have used coupled 3D hydro-mechanical model for assessment of initial volume that will mobilize into debris flow at a slope scale.

#### 5.2.1.1 State-of-art 3D slope stability methods

Slope stability methods can generally be classified into, (i) limit formulation which provides a theoretical understanding through upper and lower bound solutions, (ii) displacement formulation such as finite element method (Fredlund, 1984). Limit equilibrium analysis technique is an example of the upper bound type of solutions which considers the slope behavior at verge of failure under static condition and does not analyze the stress-strain relationship or the corresponding deformation within the soil body. Consequently, assumptions are needed with respect to slip surface, defining the sliding body, and also the interslice forces. The following principles are mutual in the framework of all the limit equilibrium methods:

- a. A kinematically feasible sliding surface is assumed to define the mechanism of failure.
- b. Available shearing strength along the assumed slip surface is obtained by using the application of static principles. Two applied static principles are the assumption of plastic behavior for soil mass and validity of Mohr-coulomb failure criterion.
- c. Satisfying the equilibrium conditions (three forces and three moments in 3D)
- d. The comparison of available shear strength and required shear resistance to bring the equilibrium into limiting condition is made in terms of FOS.
- e. The satisfying value of FOS is determined through an iterative process.

Two-dimensional limit equilibrium methods are the most popular and widely used in practice owing to its simplicity and being on the conservative side. 2-D models are based on the assumption of infinite width of the failure surface such that 3D effects are negligible, which is not the case in the real scenario. Several models integrate the GIS with 1-D or 2-D slope stability methods either through a DEM cell by cell basis (Montgomery and Dietrich, 1994; Wu and

Sidle, 1995; Pack et al., 1998; Baum et al., 2010) or by extracting a cross-section (Miller, 1995; Miller and Sias, 1998). The real topography has 3D characteristics and can integrate the effects of strength, morphology and pore pressure over potential areas larger than a single pixel in the DEM. the assumption of infinite width and neglecting the lateral variations of these properties results in lower dimensional stability analysis inaccurate (Hung, 1987; Stark and Eid 1998; Bromhead et al., 2002). The use of 3D based LEM can give the direct estimate of potential failure volumes which serves as input to landslide run-out models for hazard assessments. The 3D methods are an extension of the 2D through the use of columns instead of slices and depending on the type of method the assumptions related to the interslice forces change. Fig 4.9 shows the column considered for a 3D analysis along with all the actual forces acting on it. Thus, recently several 3D LEM based slope stability has been conducted by incorporating 3D column based methods in to GIS framework (Xie et al., 2006; Mergili et al., 2014; Reid et al., 2015). Table 4.3 gives a brief summary of existing 3D based methods.

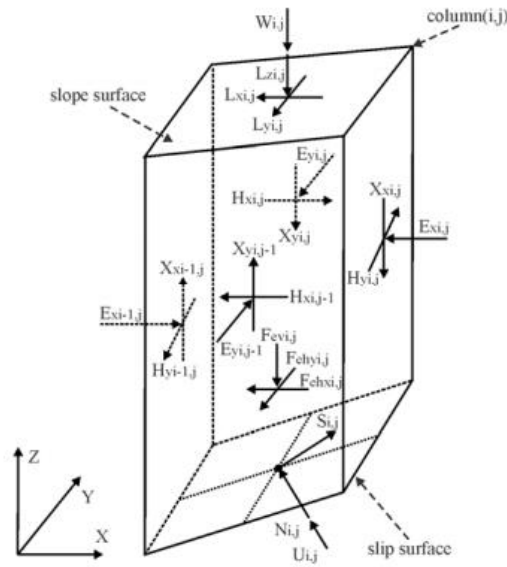


Fig 5.2: Forces acting on the column considered in a 3D slope stability scheme.

Though significant research has been done into the 3D slope stability methods, however many of the methods does not incorporate transient pore-pressure variability considering the 3D topographic characteristics which can affect the final volume of the landslide to be used for further hazard assessments. Hence, in this research, a commercial code called SVOFFICE 5 considering a coupled 3D seepage and limit equilibrium based stability method has been used.

Table 5.1: Summary of 3D limit equilibrium methods

Name	Based method	Direction of sliding	Slip surface	Optimization method for critical surface
Anagosti (1969)	Morgenstern-price	Assumed	Generalized	No
Hovland (1977)	Fellenius method	Assumed	Cone/ wedged shape	No
Hungr (1987)	Bishop's modified method	Assumed	Rotational with circular central section	No
Hungr et al. (1989)	Simplified Bishop and Janbu's method	Assumed	Symmetrical rotational	No
Lam and Fredlund (1993)	Generalized limit equilibrium	Assumed	Generalized rotational surfaces	No
Cheng and Yip (2007)	Bishop's, Janbu and Morgenstern-price	Calculated	Spherical	No
Xie et al. (2006)	Hovland	Assumed		Probabilistic Monte-Carlo method
Mergili et al. (2014)	Hovland	Assumed	Ellipsoidal	Monte-Carlo method on variability of shear strength and depth
Scoops-3D (2015)	Ordinary/ Simplified Bishop's	Assumed	Spherical ( rotational slip)	Search lattice

### 5.2.1.2 Methodology

#### 5.2.1.2.1 Transient 3-D seepage analysis

The transient 3D seepage analysis is carried using the commercial code SVFLUX. Before detailing the governing equations and the flow laws, it is necessary to understand the assumptions governing the pde derivation for seepage modelling:

- 1) Soil phases can be described using the continuum mechanics approach,
- 2) Atmospheric pressure gradients are negligible.
- 3) The factors involved are continuous and valid from a macroscopic and phenomenological standpoint.

A representative element is assumed based on continuum mechanics concept to derive the governing equation for conservation of mass of water for saturated and unsaturated seepage.

The continuity equation is considered by taking into consideration the flow rates in and out of the REV and equating the difference to the rate of change of mass to storage within REV with time. A three dimensional flow condition is used to derive the following differential equation in Cartesian coordinates:

$$-\frac{\partial q_x^w}{\partial x} - \frac{\partial q_y^w}{\partial y} - \frac{\partial q_z^w}{\partial z} = \frac{1}{V_o} \frac{\partial M_w}{\partial t} \quad (5.1)$$

where:

$q_w^i$  = total water flow rate in the i-direction across a unit area of the soil, kg/m<sup>2</sup>-s

$\rho$  = density of water, 1000 kg/m<sup>3</sup>,

$v_i^w$ = water flow rate in the i-direction across a unit area of the soil m/s (specific discharge),

$V_o$ = referential volume,  $V_o=dx dy dz$ , m<sup>3</sup>

$M_w$ =mass of water within the representative elemental volume, kg,

$t$ = time, s.

The amount of water stored in the soil pores is usually written in terms of volume of water with respect to the overall total volume. The change in volume of water stored in the soil pores is expressed as a coefficient of water storage  $m_2^w$  and is given as follows:

$$\frac{dV_w}{V_0} = m_2^w d(u_a - u_w) \quad (5.2)$$

where

$$m_2^w = \frac{d(V_w/V_0)}{d(u_a - u_w)} = \frac{e}{1+e} \frac{dS}{d(u_a - u_w)}$$

$V_w/V_0$ = volumetric water content,

$E$ = voids ratio

$S$ =degree of saturation

$(u_a - u_w)$  =matric suction

The above equation indicates that the changes in volume of water stored in the soil pores are a function of matric suction and are independent of changes in total stress. The coefficient of water storage can be obtained from taking derivatives of the slope of soil-water characteristics curve (SWCC).

This approach is essential to providing a smooth transition between the saturated and unsaturated conditions. As the degree of saturation increases in the soil, the changes in soil suction and effective stress becomes equal and the changes in volume can be referenced to changes in voids ratio.

#### 5.2.1.2.2 Coupled 3-D limit equilibrium analysis

The general limit equilibrium method (GLE) was developed as the 2D method of slices (Lam and Fredlund, 1993). The formulation assumes that a slip mechanism has the direction of movement in one plane and that the FOS due to cohesion and frictional component is the same. The method of columns is indeterminate and to reduce the same some assumptions are additionally considered:

- (a) Normal force acts through the center of the base area
- (b) Intercolumn force functions are used to relate the normal force with intercolumn shear forces acting on each face.

Summing the forces on each column in the y direction, the normal force N acting perpendicular to the base of a column can be expressed as

$$N = \frac{W - (X_L - X_R) - (V_L - V_R)}{m_\alpha} - \frac{\frac{A'_c \sin \alpha_x}{F} + \frac{U \tan \phi' \sin \alpha_x}{F}}{m_\alpha} \quad (5.3)$$

where,

$$m_\alpha = \cos \theta_y + \frac{\tan \phi' \sin \alpha_x}{F}$$

W is the weight of the column of the soil,

$X_L, X_R, V_L, V_R$  is the intercolumn shear force,

$\theta$  is the angle between the horizontal and the shear force at the base of the slice

C is the effective cohesion

$\phi'$  is the effective angle of shear friction

A is the area of the column base

U is the pore water pressure acting at base of column

The factor of safety with respect to moment equilibrium, can be derived by summing the moment of all the forces over the entire failed mass about an axis of rotation as

$$F_m = \frac{\sum (A'_c + N \tan \phi' - U \tan \phi') (\cos \alpha_x d_y + \sin \alpha_x d_x)}{\sum N \cos \theta_x d_y + N \cos \theta_y d_x + W d_x} \quad (5.4)$$

$$F_f = \frac{\sum (A'_c + N \tan \phi' - U \tan \phi') \cos \alpha_x}{\sum N \cos \theta_x d_y} \quad (5.5)$$

### 5.2.2 Rheological model and parameters estimation

The selection of appropriate rheological model and growth rate estimation for predictive assessment of debris flow runout has been conducted by collecting suitable debris flow related data from 3 district located in Gyeonggi province, South Korea: Yongin, Seoul and Yeosu. The database thus developed will be used to achieve the following objectives: (a) selection of rheological model with emphasis on representation of the mechanism under consideration, easiness of acquirement, and apt for predictive hazard assessment; (b) ANN based model development for the selected rheology parameter; and (c) last but not the least, to recreate a real event and comment on predictability using the proposed approach.

For achieving the above stated objectives, 35 debris flow cases were collected from the previously mentioned areas as; 23 events from Yongin, 10 events from Woomyeon mountain in Seoul, and 2 from Yeosu. However, 4 of the event flow paths did not have curvature and hence could not estimate the velocity for fitting. The locations of the area and the events are as shown in Fig. 5.3.

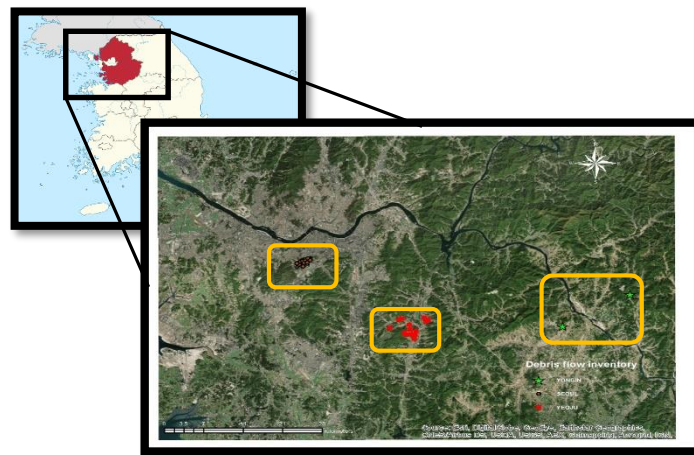


Fig. 5.3. Data sampling locations of debris flow events

#### 5.2.2.2 Selection of rheological model

Debris flow, a sediment-water mixture, mostly moves downslope as unsteady and non-uniform surges. These surges at debris flow head have pore pressure close to zero, however the flow body behind has pore pressure almost balancing the total normal stress thus, liquefying the mass. Also, the flow appears to be undrained since no pore fluid escapes from the surge heads during the rapid motion (Iverson, 1997). Many laboratory tests on the rheological characteristics of debris flow indicate the mixtures to behave as non-Newtonian fluids and they are influenced by factors like



aggregate formation (shape, size, and size distribution of particles), solid volume concentration and particle forces (Vander Waals, thermal, and electrical) (Major and Pierson, 1992).

There are five rheological models that are implemented in the rheological kernel of Dan-3D. However, for debris flow mainly, Bingham, frictional, or Voellmy models are suitable.

In order to identify the suitable rheological model for predictive debris flow modelling for events observed in Korea using two methods; calibration and rheometer testing for debris flow events in Korean peninsula. Calibration of the rheological parameters were done by running the model several trials to get a good match of the landslide footprint, final volume and velocity. For debris flow channels with curvature, the velocity at curvature were determined using the forced vortex equation and the back calculation of the rheological factors were done using an optimization code (Aaron, 2015). The parameters for the Bingham rheology were determined using rheometer test with a parallel plate rheometer, with distance between the plates set at 2 mm and the soil finer than .075 mm was used.

Many researchers tried to model the debris flows mobilized from landslides owing to liquefaction using the Bingham model by defining the yield strength and viscosity. The mobilization of the flow-type landslides was characterized based on if the strength of the failed rigid landslide mass was higher or lower than the yield strength. However, the model is oversimplified for capturing the overall flow behavior (Iverson, 1997; Jeong, 2011).

In order to assess the suitability of the rheological model only two cases, Sindonga and Raemein watersheds, located in Mt. Woomyeon, Seoul could be used owing to accurate estimate of velocity from video recording during the occurrence of the event. In Dan-3D, the governing equations are formulated such that the basal rheological model mainly influences the velocity and the runout distance, while the volume affected by the growth rate controls the spreading. In all the debris flow events except the those in Mt. Woomyeon, no data regarding their velocity or spreading was available. Therefore, the velocity at the bends were calculated using the vortex equation and the rheological model was fitted using these estimated values. In view of this limitation, the results of the suitable rheological model selection were generalized using only the two events with actual measured data.

The Voellmy and frictional rheological model parameters were back-calibrated using the optimization code incorporated with the DAN-3D model. The code was used because a manual based trial-and-error method is time consuming, and has a limitation with regard to exploring the entire parameter space and possible non-identification of non-uniqueness existence. The optimization was based on the inverse model implemented in PEST, which minimizes the difference between the model and field observations.

The model output  $c$  as a function of the input parameters  $b$ , can be written as;

$$c = f(b) \quad (5.6)$$

The least square error function is used to measure the misfit between the model output and the field data as;

$$\phi = \sum_{i=1}^n w_i \times (c_i - o_i)^2 \quad (5.7)$$

where,  $\phi$  is the value of objective function,  $w_i$  is a user specified weight given to observation  $i$ ,  $c_i$  is the model simulated output and  $o_i$  is the observed data.

The fitness function is minimized via Gauss-Marquart-Levenberg algorithm using the observation values and the user specified initial guess for the parameters. The model trial runs over a given parameter space and determines the residuals and model sensitivities. This process was automated through a DAN-3D postprocessor which can interpret the Dan-3D output results and in turn calculate the residuals at the end of each run. The method determines the parameter values by fitting the following three outputs: velocity, landslide impact area, and landslide deposit distribution. Fig.5.3 shows the general methodology adopted for calibration.

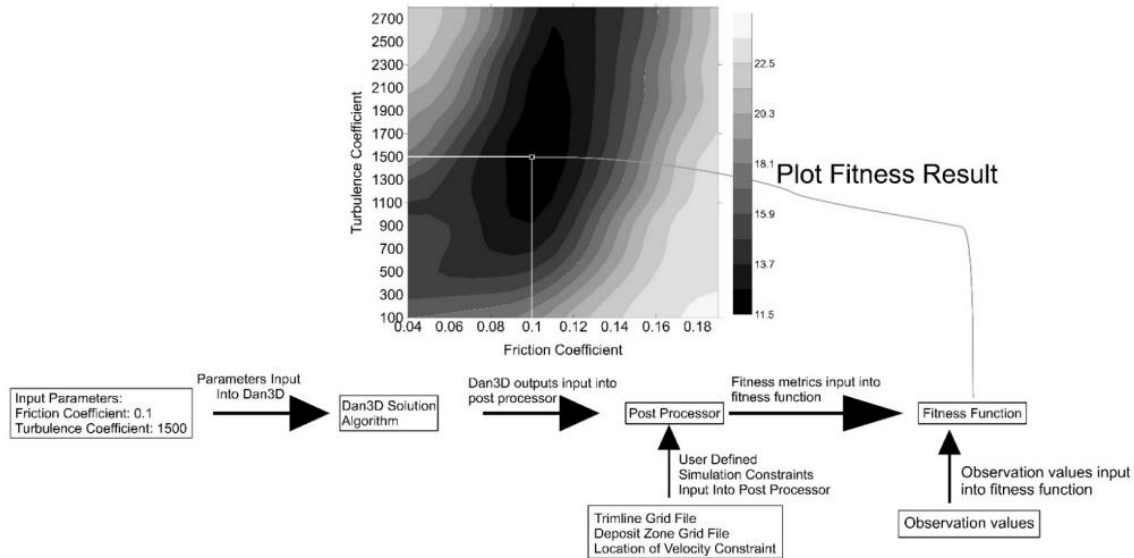


Fig. 5.4: Methodology for optimizing the rheological parameters (Aaron et al., 2015)

Table 5.2 shows the calibrated values obtained for Sindonga and Raemian watershed events and the corresponding velocity and volumes through frictional and Voellmy rheology. The results shown in the Table 5.2 points towards frictional rheology being more suited for debris flow modelling not only because they best fit the velocity values but also because it is a one-parameter model.

Table 5.2. Fitted parameters to field observations (Lee, 2016)

	Raemian			Sindonga		
	Velocity	Thickness	Volume	Velocity	Thickness	Volume
Observation	28	3-5	46125	18	NA	26220
Bingham	27.2	3.95	45884	17.5	2.95	25813
Voellmy	25.1	4.0	46970	13.7	2.88	26687
Frictional	27.5	4.0	46550	18	3.03	26840

The back-calibration was conducted for all of these 30 cases in order to ascertain the bulk or apparent friction angle for frictional rheology. Table 5.3 shows the values of factors obtained using back-calibration of the 30 events (excluding Raemian event). The back analysis of Voellmy model in Sindonga site, Mt. Woomyeon, gives a velocity of 25.1 m/hr which is less than the real measured velocity of 28 m/hr. The Voellmy model has a physical basis which can be explained through the experiment conducted by Bagnold (1954). He showed that the shear stress and effective normal stress in a dense dispersion of grains in fluid, shearing under constant volume, depends on the square of shearing strain rate. As the velocity increases, grains in the shearing layer will begin interacting dynamically with each other and with the fluid to produce dispersive effective normal stress. As the velocity of the flow increases an increase in volume will be accompanied, which if under undrained condition (pore pressure diffusion is very slow), will result in decrease in pore pressure thereby increasing the friction. Thus, in case of flows which are completely fluidized, the Voellmy is not appropriate to be applied since in that scenario the effective normal stress is zero and the basal friction should be negligible. Thus, for completely liquefied flow-type landslides, the Voellmy rheology tends to underestimate the velocity.

#### 5.2.2.2 Database for bulk frictional angle prediction model

Profile curvature is defined as the curvature of the terrain in the direction of the slope. This factor induces centripetal acceleration to the flow, which alters the bed-normal stress and thus can affect the basal and internal stresses (Park, 2015; McDougall, 2006). Plan curvature is defined as the curvature perpendicular to the slope direction and considers the effect of confinement, i.e. a gully or an open channel, of the debris flow in the channel. Fine content implies the proportion of silt or the clay content in the soil, which according to a research by Wang and Sassa (2003), can affect the pore pressure ratio during the flow and thus is an important factor which can change the bulk frictional angle during the flow. Another factor  $D_{50}$  representing the median grain size distribution in the soil bed of the slope is also considered. Travel angle is a parameter defined as the ratio of elevation difference between the starting point and the lowest point of deposition to the corresponding runout horizontal distance. It mainly indicates the mobility of a mass and in case of dry sand or broken rock it equals the angle of friction. A value of travel angle less than friction angle indicates the influence of pore pressure (Hungr and McDougall, 2006). Fig. 5.5 shows the frequency distribution for the above described independent factor values.

Table 5.3. Database of factors influencing bulk friction angle (Park,2015; Lee, 2016)

<b>Unit weight</b>	<b>Fine content</b>	<b>D<sub>50</sub></b>	<b>Travel angle</b>	<b>Plan</b>	<b>Profile</b>	<b>r<sub>u</sub></b>
1.492	2.757	1.314	0.29	-2.062	0.2	0.87
1.478	4.657	1.038	0.286	-5.602	2.272	0.86
1.459	2.321	1.961	0.49	-0.874	0.262	0.87
1.342	6.459	1.16	0.4	-4.487	1.324	0.89
1.161	1.686	0.957	0.255	1.434	0.08	0.9
1.507	6.781	1.357	0.225	-2.723	0.602	0.88
1.504	6.558	1.323	0.323	-4.21	0.134	0.95
1.509	6.957	1.37	0.296	-2.844	0.851	0.88
1.515	7.489	1.427	0.476	-5.179	0.706	0.88
1.513	7.294	1.413	0.344	-17.108	7.965	0.88
1.515	1.706	1.42	0.116	-3.089	0.729	0.91
1.514	1.831	1.411	0.275	-5.352	0.355	0.9
1.511	2.34	1.383	0.324	-4.193	0.956	0.92
1.579	4.864	0.644	0.386	-2.142	0.326	0.95
1.551	5.499	0.698	0.292	-3.695	0.955	1
1.479	2.743	1.128	0.389	-2.826	0.477	0.92
1.475	3.088	1.074	0.368	-0.793	0.284	0.89
1.467	3.198	1.003	0.348	-4.527	0.647	0.86
1.51	10.444	0.895	0.338	-1.407	0.237	0.85
1.448	4.19	1.054	0.183	-1.464	0.239	0.84
1.317	3.444	1.284	0.258	-4.036	0.766	0.88
1.447	2.363	1.245	0.279	-3.865	0.764	0.87
1.473	55.1	0.05	0.306	-4.276	0.837	0.88
1.265	28.8	0.2	0.526	-3.663	0.904	0.889
1.687	31.9	0.22	0.5	-2.434	0.568	0.97
1.687	31.9	0.22	0.536	-2.221	0.178	0.92
1.119	54.2	0.05	0.385	-6.51	0.644	0.89
1.687	31.9	0.22	0.422	-7.767	0.929	0.92
1.119	54.2	0.05	0.417	-6.135	0.863	0.86
1.616	30.9	0.42	0.306	-0.869	0.117	1

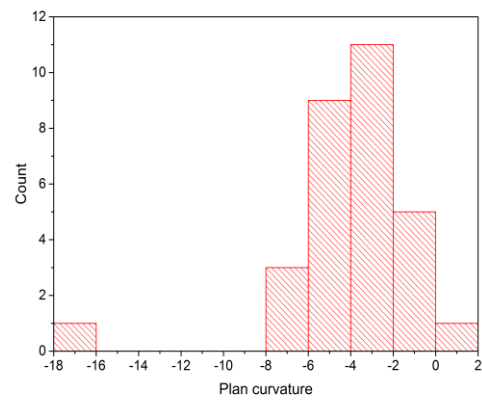
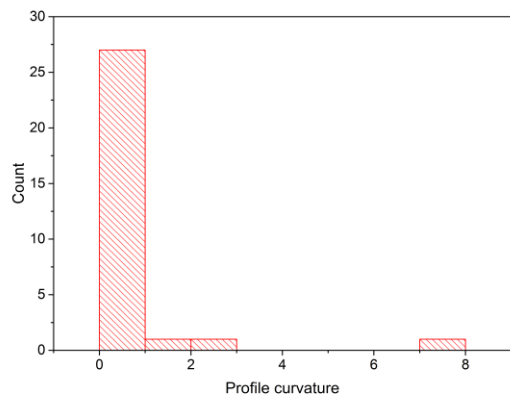
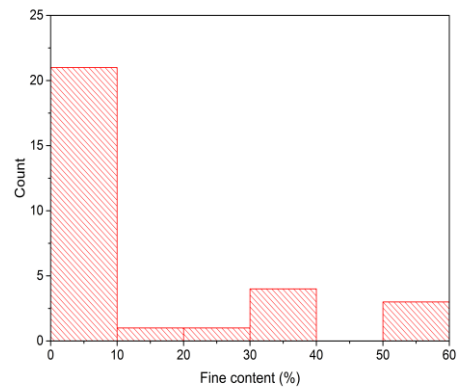
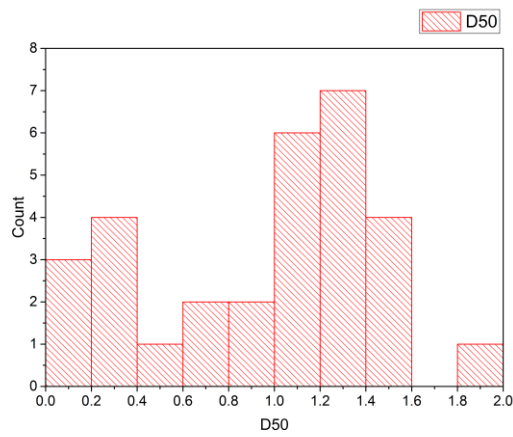
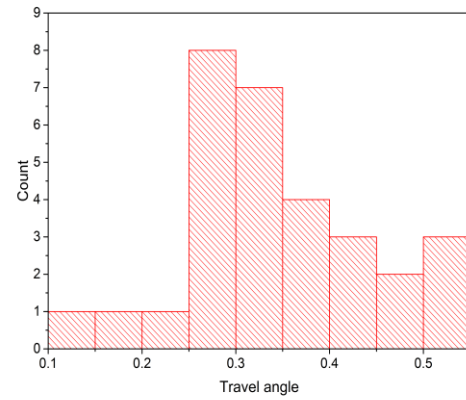
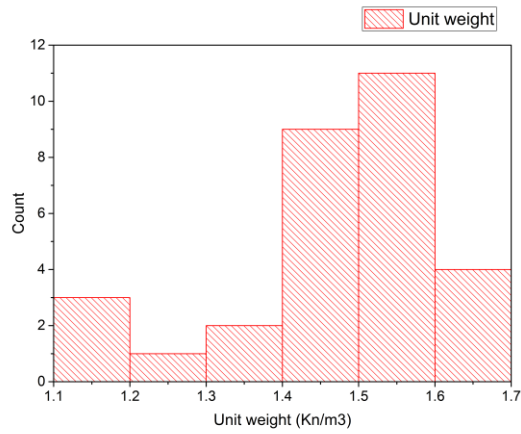


Fig. 5.5. Histogram for independent factors used for making the ANN model

### 5.2.2.3 ANN based predictive model

In this study an ANN model was used to consider the non-linear relationship existing among the independent and the dependent factors. The ANN modelling mainly consists of a combination of several layers, including the diverse neurons, the output value of a certain neuron is multiplied by a weight before inputting the value to the other neurons. A net is formed by adding all values, which are the multiplication of each weight and output value from the previous neurons, and then the output value to be used as input to the next neuron can be calculated through the activation function as shown in the equations below:

$$net = \sum_{i=1}^n W_i X_i \quad (5.8)$$

$$output = f(net - b) \quad (5.9)$$

where  $X_i$  is the input value to a certain neuron,  $W_i$  is the weight for the corresponding input value,  $b$  is the bias of each neuron, and  $f$  is the activation functions like step, sigmoid, tangent function etc. A multi-perceptron, consisting of an input layer, a hidden layer, and an output layer, are used for the ANN modelling since the usage of a single-layer perceptron is limited to linearly separable data sets. An error back-propagation learning algorithm is usually used in a multi-layer perceptron to determine the neural networks architecture. The difference between the output target value and the actual value is reduced through modulations of the weights and bias.

The ANN model was constructed using Matlab distributes of 90%, 5%, and 5% of the total 30 data among the training, testing and validation dataset, respectively. The training was conducted using the Levenberg-Marquardt (Marquardt, 1963) back propagation algorithm for different number of neurons in the hidden layer. After several trial and error for different combinations of parameters, the best model was obtained for four independent factors with 5 neurons. The four independent factors; unit weight, travel angle, fine content and  $D_{50}$ , gave the high model performance as shown in Fig. 5.6, with high R-square values of .93, 1 and 1 obtained for the training, validation and testing data, respectively. Fig. 5.7 a and b show the error histogram for the 3 datasets and the training stoppage based on the best validation performance value.



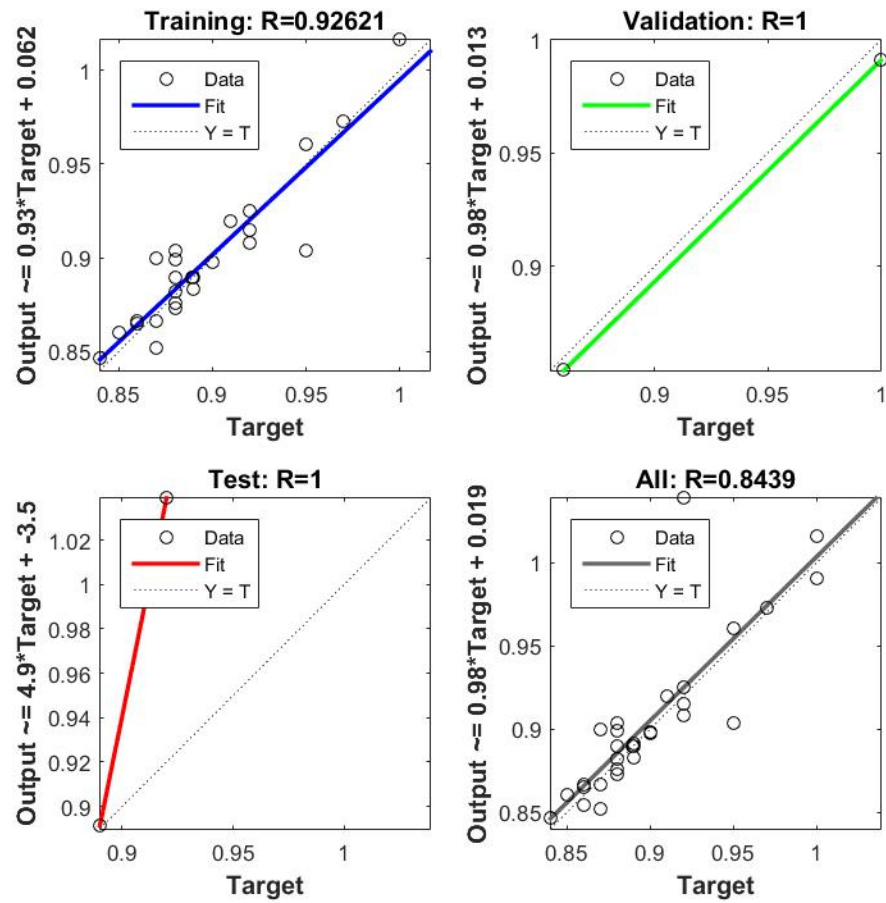
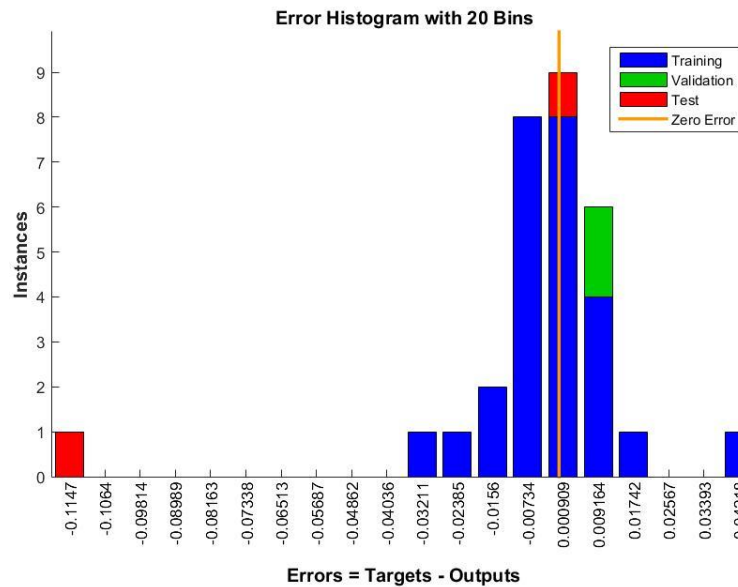


Fig.5.6. RMSE for training, testing and validation dataset



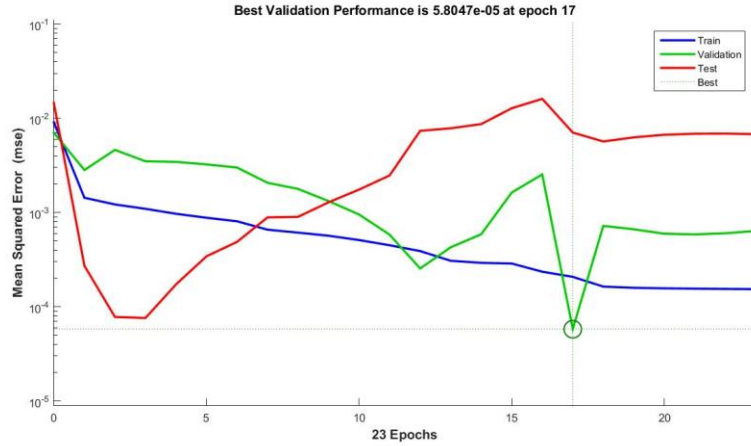


Fig.5.7. (a) Error histogram with 20 bins; (b) Training stoppage for best validation performance

### 5.2.3 Growth rate estimation for entrainment process

The final volume, run-out distance and spreading is mainly influenced by the amount of soil entrained during the debris flow runout. In Dan-3D, a simple erosion mechanism is implemented through a user defined value. The erosion is mainly by the growth rate parameter defined as:

$$E_s = \frac{\ln(V_f / V_o)}{L} \quad (5.10)$$

where,  $V_f$  is the final volume,  $V_o$  is the initial volume, and  $L$  is the approximate run out length

With objective of predictive modelling, the above parameters used in the determination of growth rate can be estimated as follows:

- 1) Final volume ( $V_f$ ) ( $m^3$ ): The final volume can be determined using the slope unit established for the watershed where there is a high debris flow occurrence potential. The soil depth map obtained from the Korea Forestry Research Institute can be used along with the approximate area calculated from the slope unit to estimate the total volume. An average value of depth over the entire slope unit can be used when calculating the final volume.
- 2) Initial volume ( $V_o$ ) ( $m^3$ ): The initial volume is estimated using the 3D seepage coupled limit equilibrium method as explained in section 5.2.1.

- 3) Run-out path length (m): The approximate distance travelled by the debris flow can be determined by inputting the total length of the slope unit from the initiation zone till the point where material exists for entrainment, which in a usual case is the end of mountain into the settlement area.

### **5.3 3-D based post-failure hazard assessment model for debris flow: DAN-3D**

In this section, the debris flow predictive modelling methodology comprising of the slope selection, run-out model, rheological models, growth rate estimation and finally application to a site is described.

Among the various number of existing physical based models as described earlier, we have selected DAN-3D (developed at the Department of Earth, Ocean and Atmospheric Sciences at the University of British Columbia UBC) for the predictive modelling of hazard. The reason for its selection is as follows:

- i) Rheological model choice
- ii) Constitutive model simplicity
- iii) Entrainment mechanism
- iv) User friendly GUI and visualization in GIS environment

Using the runout model a two-staged framework for estimating the components for debris flow hazard assessment at a site specific scale has been established. The first stage consists of the slope selection highly susceptible to debris flow using a mobilization criterion which then is processed in the next stage for runout assessment. The second stage is a bit more complex since it involves the estimation of input parameters for the DAN-3D analysis. There are three main input parameters in DAN-3D; i.e., initial volume, rheological model, and growth rate coefficient. The biggest challenge of using a physically based model in hazard assessment for EWS is the database establishment of the input parameters which are usually difficult to obtain. Thus, the second stage of the framework is more focused on database establishment and estimation method for the parameters used in runout modelling. Before discussing these methods in detail it is vital to understand the overall working of the model along with the influence of input parameters on the debris flow modelling.

The final continuum depth averaged based governing equations for mass and momentum are numerically solved through smooth particle hydrodynamics method.

The initial release volume inputted by the user is divided among finite number of reference mass columns centered at base as particle number density (equation 5.11) due to the incompressible shallow flow assumption of the working

governing equations.

$$f_i = \sum_{j=1}^N \frac{V_j}{h_j} f_j W_{ij} \quad (5.11)$$

The depth of the given initial mass is calculated through the definition of an interpolation function kernel, which is the backbone concept for SPH. The depth of interested particle is calculated through interpolation function as given by the equation below:

$$h_i = \sum_{j=1}^N V_j W_{ij} \quad (5.12)$$

The Lagrangian coordinate system (local coordinate system) for the particles is defined as; z direction is aligned with the local bed-normal direction and x direction is aligned with the local direction of motion. The distance between the reference columns, required for calculating the tangential strain is determined as:

$$s_{ij} = \sqrt{x_{ij}^2 + y_{ij}^2 + z_{ij}^2} \quad (5.13)$$

The equation (5.13) for calculating x and y components of depth is extended considering the irregular topographic surfaces through the equation:

$$\begin{aligned} \left( \frac{\partial h}{\partial x} \right)_i &= \sum_{j=1}^n V_j \left| \frac{\partial W}{\partial s} \right|_{ij} \frac{x_{ij}}{\sqrt{x_{ij}^2 + y_{ij}^2}} \\ \left( \frac{\partial h}{\partial y} \right)_i &= \sum_{j=1}^n V_j \left| \frac{\partial W}{\partial s} \right|_{ij} \frac{y_{ij}}{\sqrt{x_{ij}^2 + y_{ij}^2}} \end{aligned} \quad (5.14)$$

During the flow, the particles converging and diverging indicating the dilation and thinning mechanism are incorporated through the Rankine's earth pressure theory. Through plane strain assumption and ignoring the reorientation effect of the local reference frame under a small time step, the incremental tangential strain at a time step is:

$$\Delta \varepsilon(\theta) = \left( \frac{\Delta \varepsilon_x + \Delta \varepsilon_y}{2} \right)_i + \left( \frac{\Delta \varepsilon_x - \Delta \varepsilon_y}{2} \right)_i \cos 2\theta + \left( \frac{\Delta \gamma_{xy}}{2} \right)_i \sin 2\theta \quad (5.15)$$

where, the  $\varepsilon_{ij}$  between the two particles is  $\Delta \varepsilon_{ij} = \frac{s'_{ij} - s_{ij}}{s_{ij}}$  and the orientation is  $\theta_{ij} = \tan^{-1} \left( \frac{y_{ij}}{x_{ij}} \right)$

From the above equation it is clear that three equations are needed for the system to be determinate. However, if there are less than three neighboring particles or more than 3 neighboring particles (one smoothing length is used to determine if the particles are neighbors) then the system will be indeterminate or redundant, respectively. Therefore,

as a solution, only the principal increment tangential strains in the flow direction is considered while neglecting the transverse engineering strain. In the resulting system, for indeterminate condition the effect of strain is ignored while for redundant condition a two parameter least-square fitted as a line is used to estimate the  $\Delta\epsilon_x$  and  $\Delta\epsilon_y$ . Dan3D thus adopts an effective simple solution to a stress redistribution problem. The internal stress of flow-type landslides due to complex 3D deformations can have significant influence on the flow characteristics. In Dan-3D, assuming an elastic-plastic behavior, the initial stress coefficients  $k_x$  and  $k_y$  are assumed as 1 for a constant  $\phi$ . Decoupling the dynamic characteristics in x and y direction and assuming the internal stresses to vary linearly with depth, the tangential stress coefficients can be expressed as:

$$\begin{Bmatrix} k_x \\ k_y \end{Bmatrix} = \begin{Bmatrix} k'_x \\ k'_y \end{Bmatrix} + D \begin{Bmatrix} \Delta\epsilon_x \\ \Delta\epsilon_y \end{Bmatrix} \quad (5.16)$$

where D is the dimensionless stiffness coefficient.

Dan-3D can model entrainment process through an additional momentum flux term in the momentum balance equation. Flow-type landslides due to its rapid dynamics can entrain material along the path either through plowing or undrained loading of the bed. An initial small volume can be transformed to several times larger volume owing to erosion process as it is usually seen in all the debris flow events in the mountains of South Korea. The erosion mechanism is affected by the velocity, rheology and the bed characteristics. However, in DAN-3D a simple user defined model is incorporated through a concept of erosion velocity and growth rate.

The removal of mass by the flow not only adds to the volume but also reduces the velocity through generation of velocity-dependent inertial resistance in addition to the basal shear resistance considering the inelastic collision mechanism. This velocity dependent inertial resistance arising due to solid collisions, fluid thrust, and friction is implicitly considered in the governing equation during back analysis of the rheological parameters for determining the bulk basal shear resistance term. Thus, rheology, which influences the flow velocity, does not affect the erosion mechanism in DAN-3D. However, an implicit effect of increase in flow velocity on erosion is can be seen through the erosion velocity, which is incorporated in to the momentum balance equation through a user defined semi-empirical parameter called the growth rate ( $E_s$ ). It is defined as the depth of bed eroded in normal direction per unit flow depth and unit displacement and is a displacement-dependent erosion rate instead of velocity-dependent. The erosion rate and growth rate are related as:

$$E_t = E_s \times h \times v_x \quad (5.17)$$

## 5.4 Application to Raemian slope unit, Mt. Woomyeon, Seoul

### 5.4.1 Site-specific initial volume estimation

The Raemian slope (Fig. 5.8) for analyzing the debris flow hazard was selected based on the methodology detailed in the previous sections. The topography needed for the analysis was extracted using the spatial analyst tool in ArcGIS 10.1 extending between  $37^{\circ}27'17''$ – $37^{\circ}28'23''$  N latitude and  $127^{\circ}0'24''$ – $127^{\circ}0'30''$  E longitude, with the highest point 272 m above sea level. The soil profile, as seen in Fig. 5.9b, for the Raemian slope exhibits three main layers: a colluvium layer consisting of a poorly sorted sand and gravel mixture in a silty matrix up to 4 m thickness, a highly weathered rock layer with a thickness of 1 m, and a subsoil of stiff weathered bedrock of low permeability. The site investigation data in the Raemian watershed were obtained from the Korean Society of Civil Engineers (2012) and Korean Geotechnical Society (2011) reports. After the catastrophic event on 27 July, about 7 geotechnical investigation borehole were drilled in the site under consideration for collecting soil, hydrological and geological information. Locations of the sampling sites are shown in Fig. 5.9a. The hydraulic property of the soil in the site was characterized using the hydraulic conductivity and soil water characteristic curves as is seen in Fig. 5.10a and 5.10b. The SWCC was estimated for the sampled soils using the pressure plate extractor and filter paper method. The obtained data was fitted using the Van Genuchten formula and obtained a saturated and residual volumetric water content values of 0.5 and 0.18, respectively.

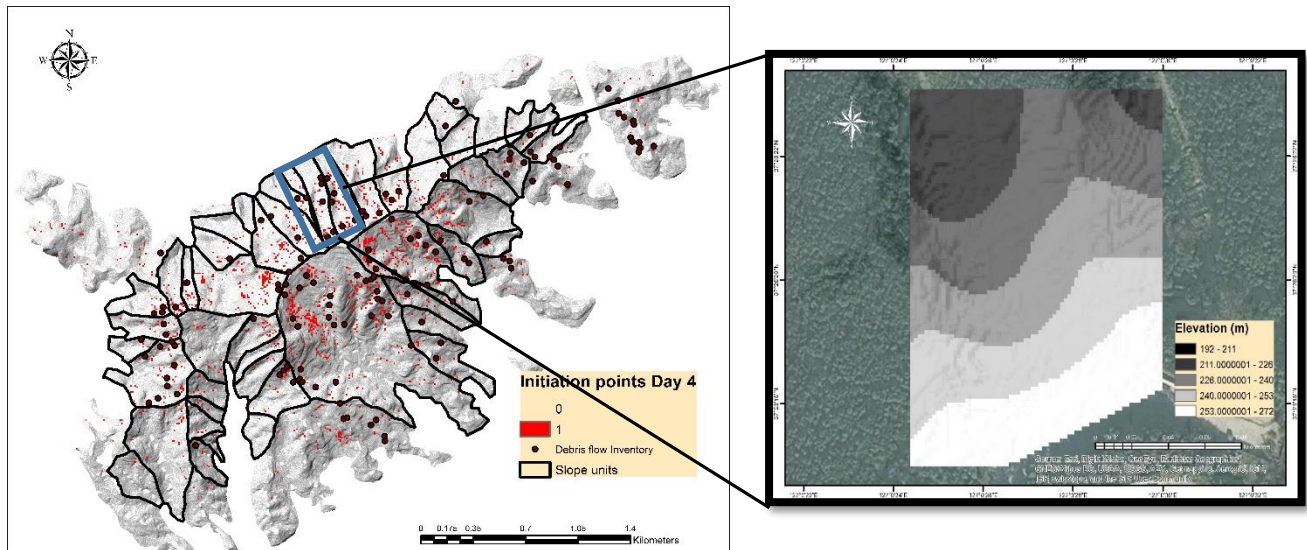


Fig. 5.8: Watershed selection for initial volume analysis

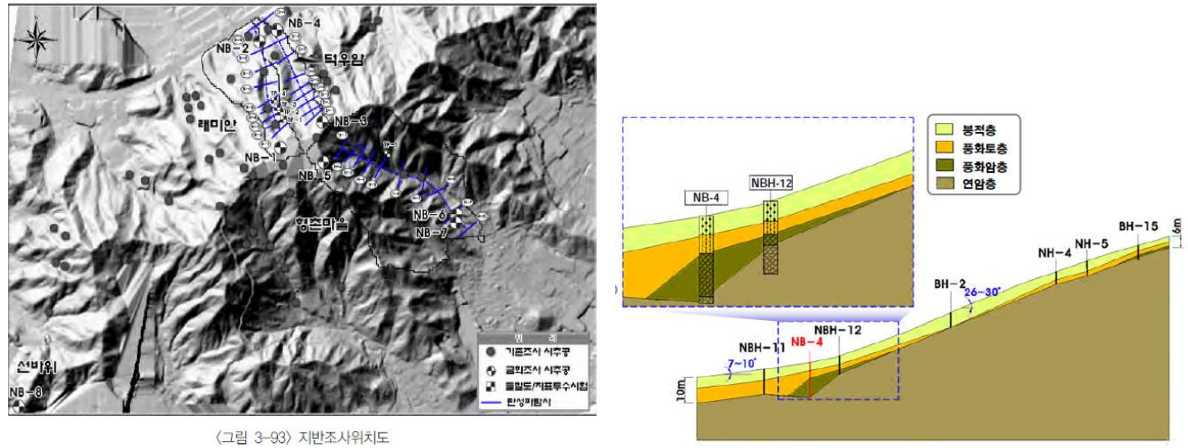


Fig 5.9: (a) Sampling locations, and (b) cross-section showing soil layers (KSCE report)

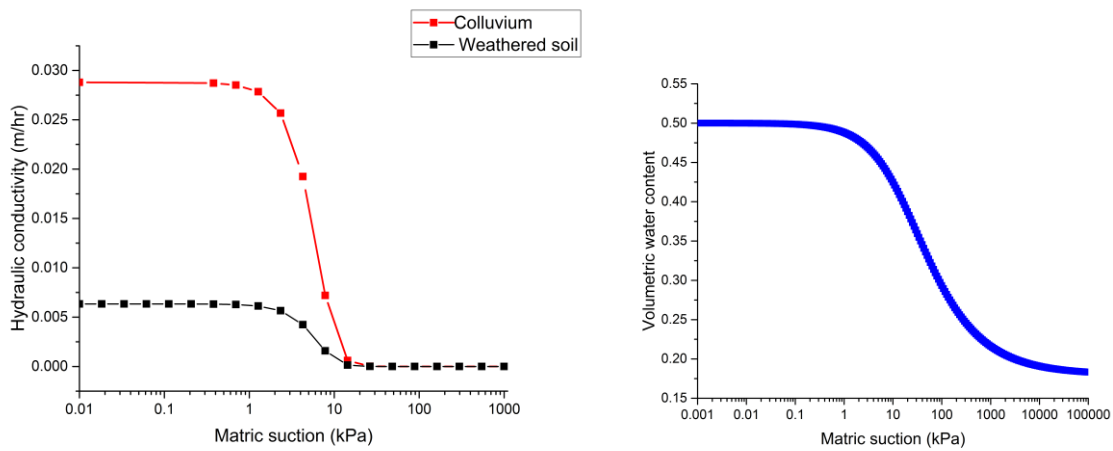


Fig 5.10: (a) Hydraulic conductivity for colluvium and weathered rock; (b) SWCC

The hydraulic conductivity of the soil was obtained through the constant head permeability test and the results for both the soil is shown in Fig. 5.10a. The hydraulic conductivity of the colluvium layer was one magnitude ( $10^1$ ) higher than that of the weathered rock layer. Also, the shear strength properties (cohesion and friction angle) obtained from the direct shear tests, given in Table 5.4, is lower for the colluvium layer in comparison that for the highly weathered rock.



Table 5.4: Soil hydraulic and strength characteristics

Parameters	Colluvium	Weathered
Ks (m/hr)	.0288	.006336
SWCC	0.5, 0.18	0.5, 0.18
Unit density (kN/m <sup>3</sup> )	18.5	19
Frictional angle	22.4	27.3
Cohesion (kPa)	18.1	12.8

The extreme rainfall event of 27 July, the application of ERI and landslide susceptibility in association with the mobilization criteria was used to chalk out the individual slope units for further site-specific debris low hazard assessment. For the predictive modelling of debris flow runout to be applied to Raemian watershed, the slope unit and initial volume estimation methodology was detailed in the previous chapter.

For assessing the most critical failure volume, at first 3D seepage analysis was conducted using the rainfall data given in Fig 5.11. The geometry shown in Fig 5.12 was meshed with about 15,669 triangular elements and 26,690 nodes.

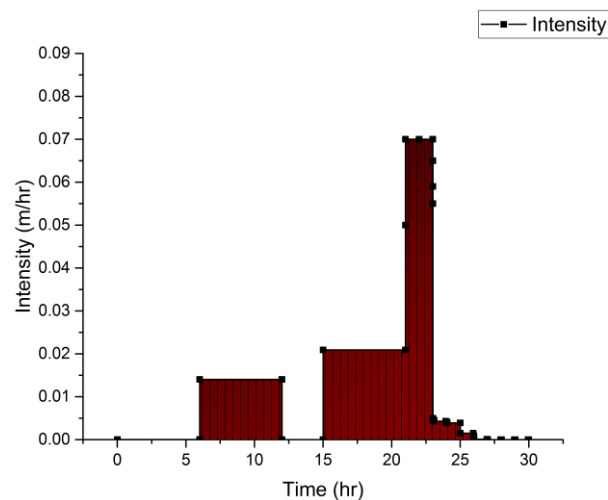


Fig 5.11: Rainfall pattern for initial volume estimation in Raemein slope

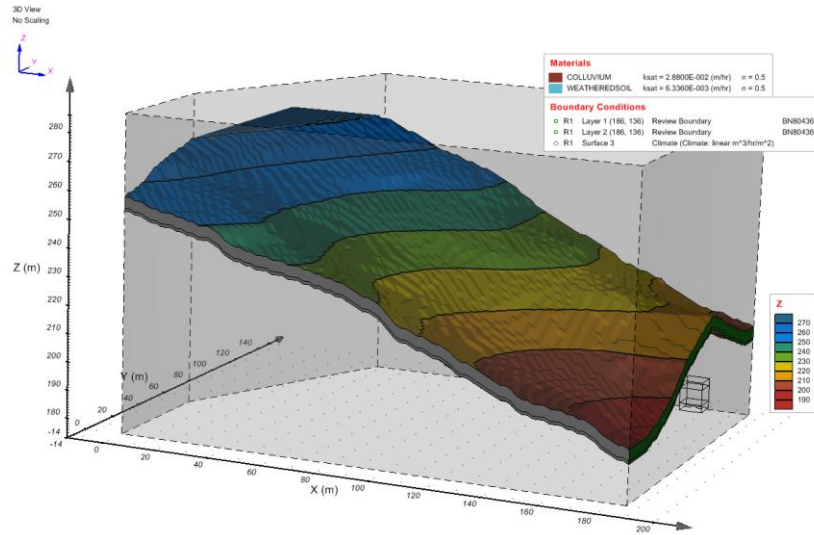


Fig 5.12: Numerical model used for initial volume estimation

The convergence of the model and the final results are highly dependent on the choice of the initial conditions and the boundary conditions. In this analysis, a boundary condition of zero flux implying, no flow normal to the boundary exists, was given at the upstream and both the sidewalls to create a flow in the downward direction. Also, at the base a review boundary condition was applied. The review boundary condition in SVFLUX behaves as follows: (1) If the pore water pressure is negative, then the boundary condition has zero flux; (2) As the saturation occurs and the positive pore water pressure (pwp) starts building up there will be a negative flux indicating an outward flow from the boundary. Finally, a flux boundary condition at the top surface using the rainfall profile indicated in Fig 5.12 is applied. In order to prevent any convergence issues a very small rainfall ( $10^{-5}$  m/hr) was applied during the periods of no rainfall. A field test monitoring the variation of matric suction on the Ramein slope indicated that during the dry period a suction between 60 and 80 kPa exists, however, a small amount of rainfall can rapidly decrease the suction value to a steady value of about 10 kPa and takes significant time to recover (Jeong et al., 2014). Thus, in the simulation an initial matric suction value of 5 kPa was applied.

Before analyzing the results, the normal flux values in Fig.5.13a, Fig.5.13b, Fig.5.13c, Fig.5.13d and Fig.5.13e needs to be discussed in order to ascertain the model behaves in accordance with the assigned boundary conditions. The bottom boundary in Fig.5.13a shows the flux to be zero except for the initial variation which is because the model is trying to converge for the given initial conditions. The graphs for the left, right and upstream boundaries also show zero normal flux with insignificantly small value of deviation at certain time steps. The Fig.5.13b showing the variation of normal flux with time for the downstream boundary indicates that the flow occurs only in the outward

direction and has a maximum flux of 7 m<sup>3</sup>/hr at the end of 25hr and remains constant until 30hr since there is no more rainfall occurring during this period.

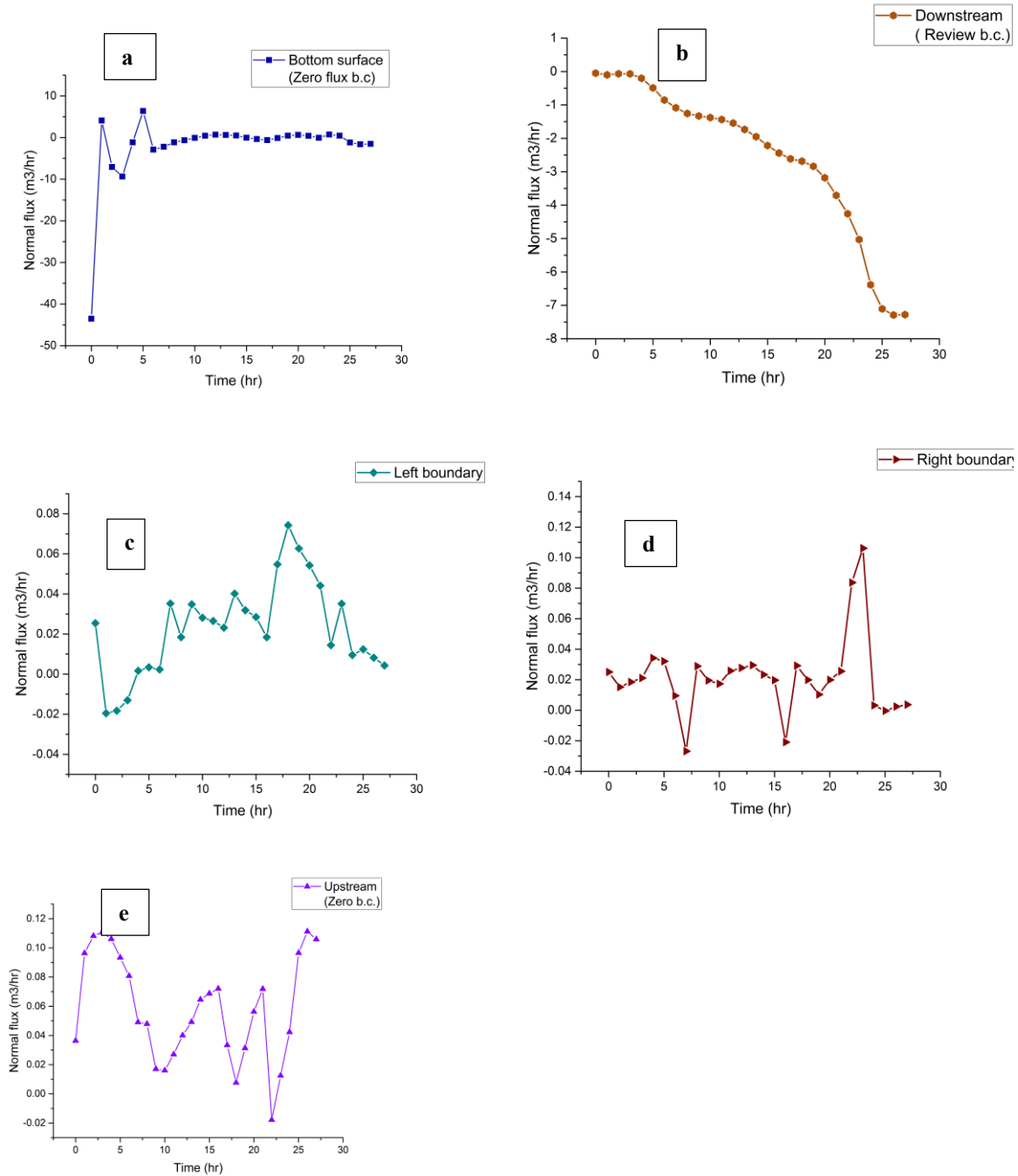
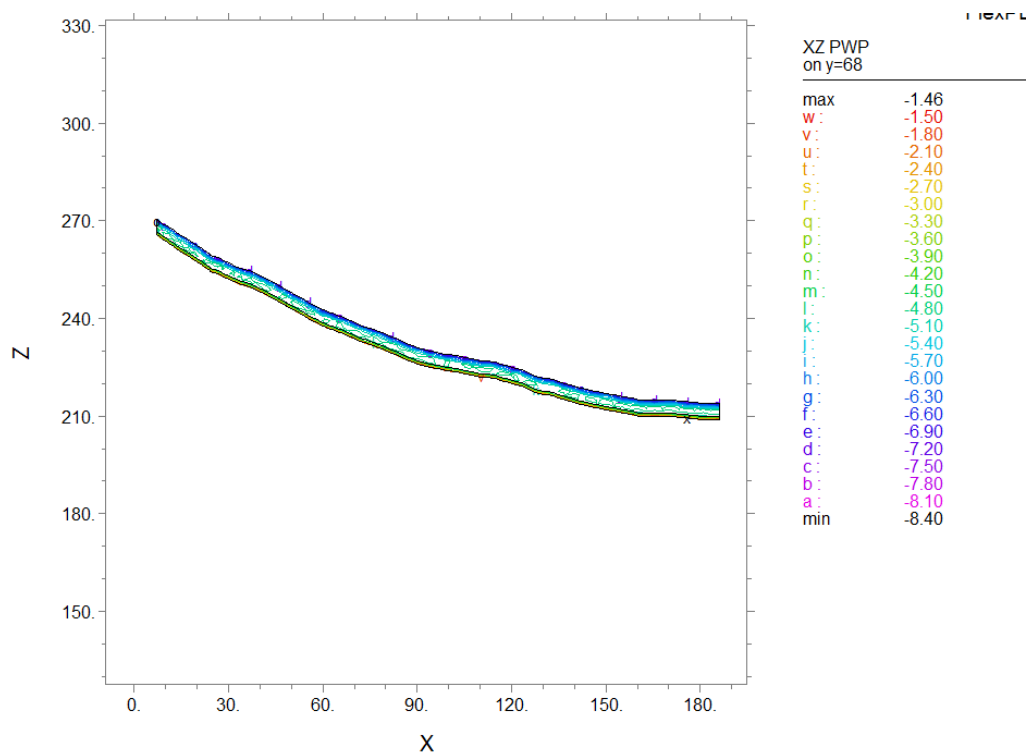
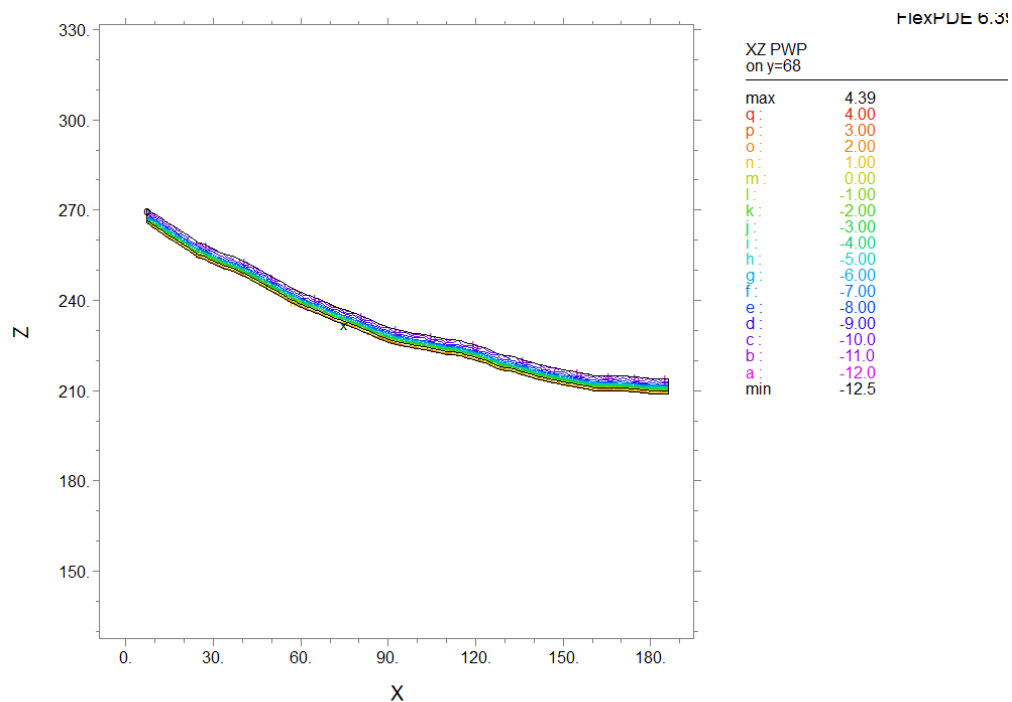


Fig. 5.13: (a) Bottom surface; (b) Downstream boundary; (c) Left boundary sidewall; (d) Right boundary sidewall; (e)

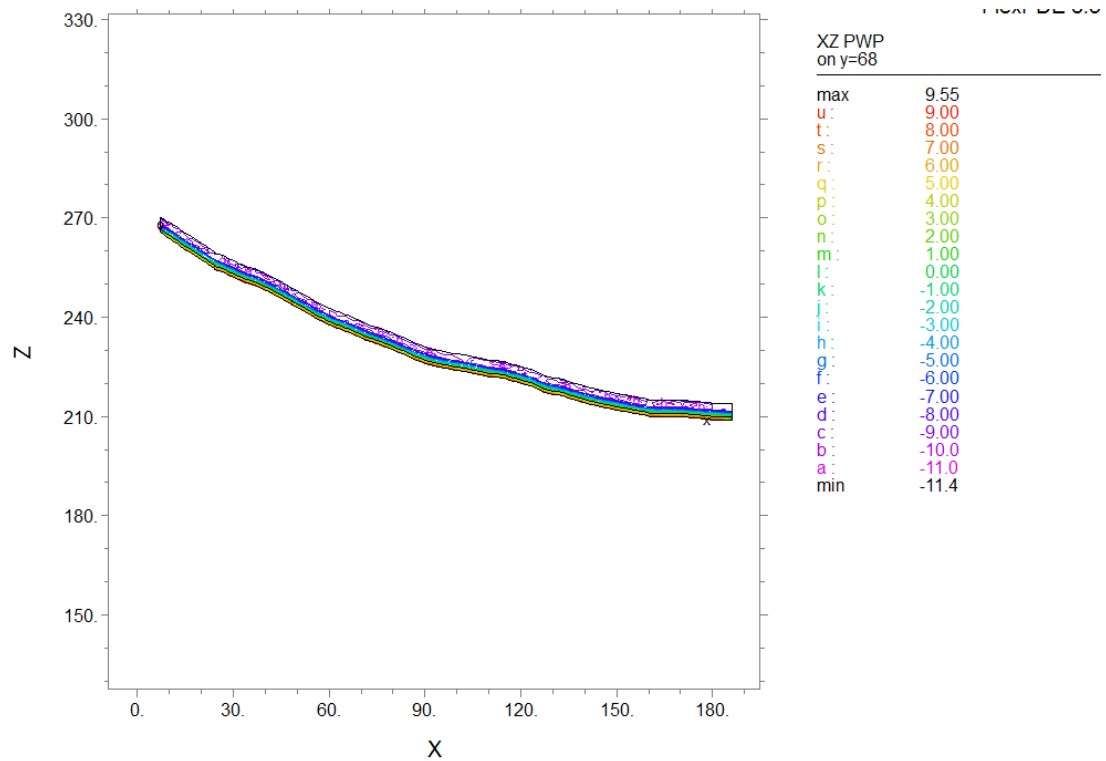
Upstream boundary



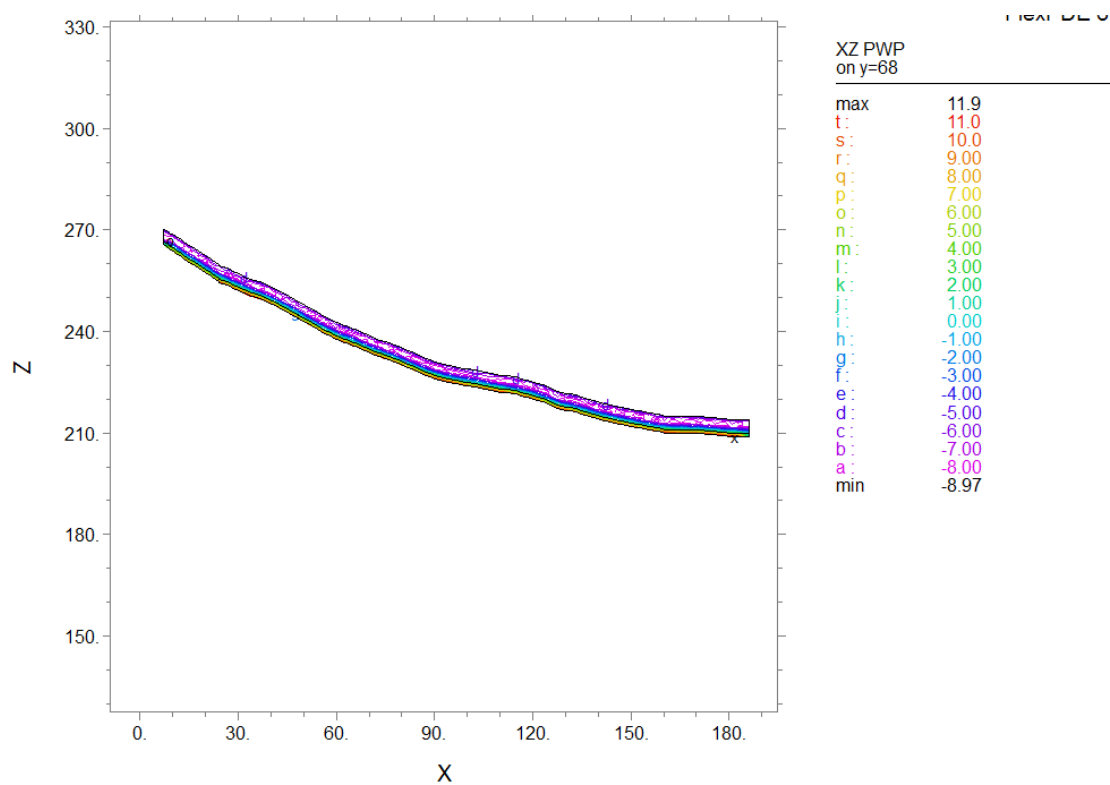
APR30TH\_BC\_PWP\_2: Cycle=0 Time= 0.0000 dt= 1.0000e-5 P2 Nodes=18521 Cells=10776 RMS Err= 1.  
Integral= -4507.979



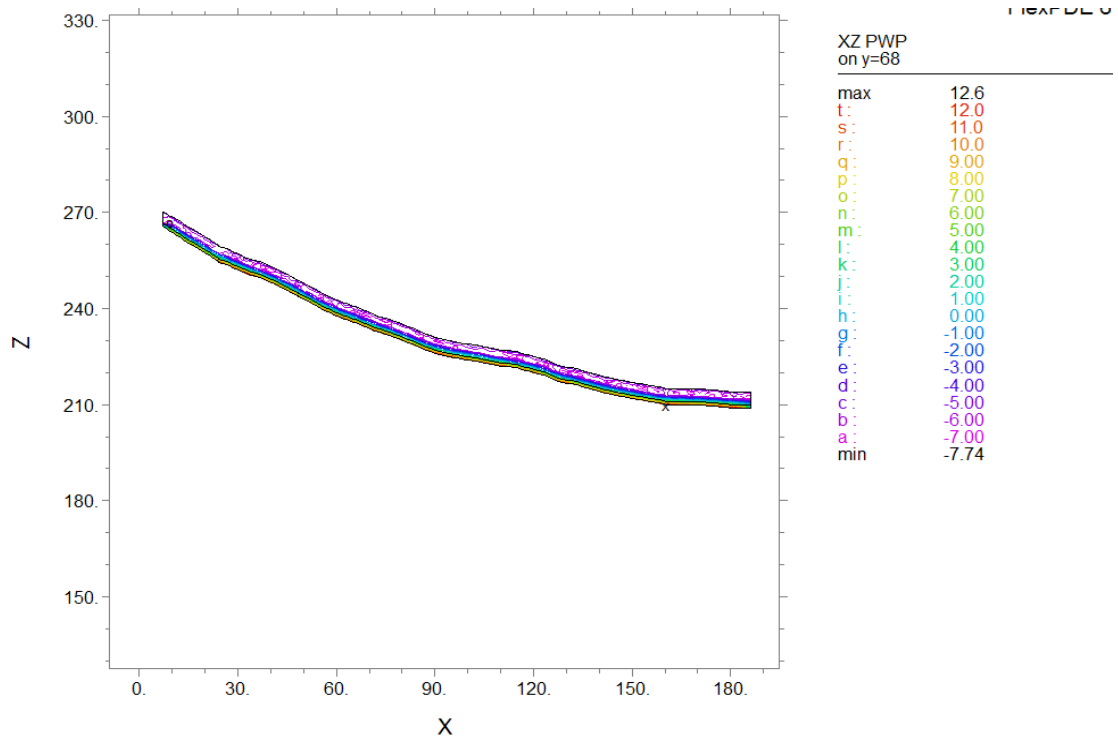
APR30TH\_BC\_PWP\_2: Cycle=123 Time= 4.4000 dt= 0.1000 P2 Nodes=18521 Cells=10776 RMS Err= 6.6e-5  
Integral= -4647.789



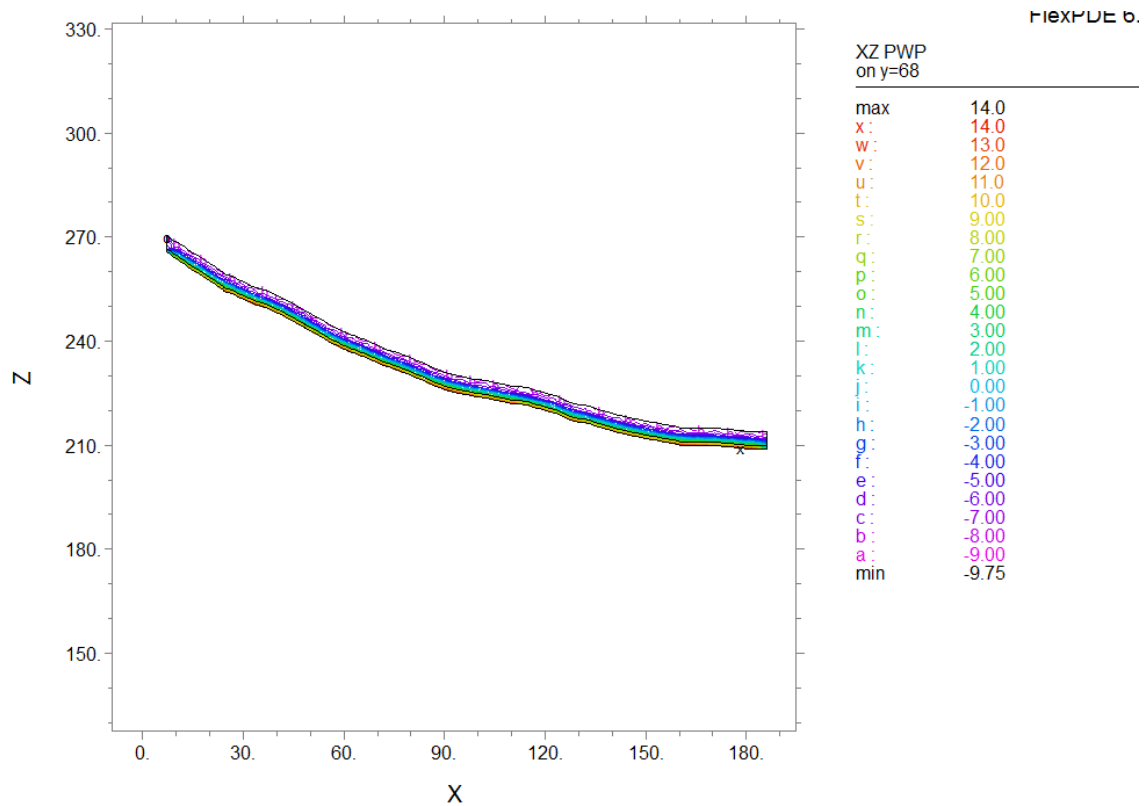
APR30TH\_BC\_PWP\_2: Cycle=156 Time= 6.6000 dt= 0.1000 P2 Nodes=18521 Cells=10776 RMS Err= 4.8e-5  
Integral= -3805.075



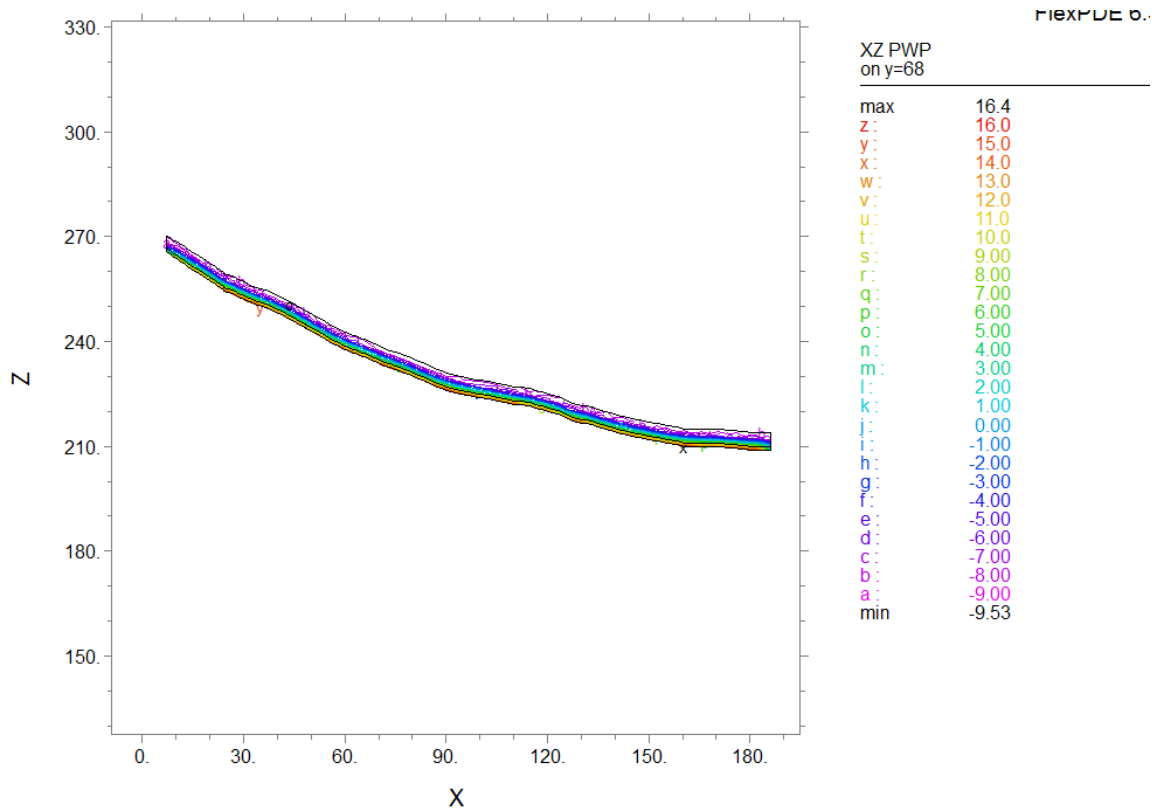
APR30TH\_BC\_PWP\_2: Cycle=178 Time= 8.8000 dt= 0.1000 P2 Nodes=18521 Cells=10776 RMS Err= 1.1e-4  
Integral= -2681.689



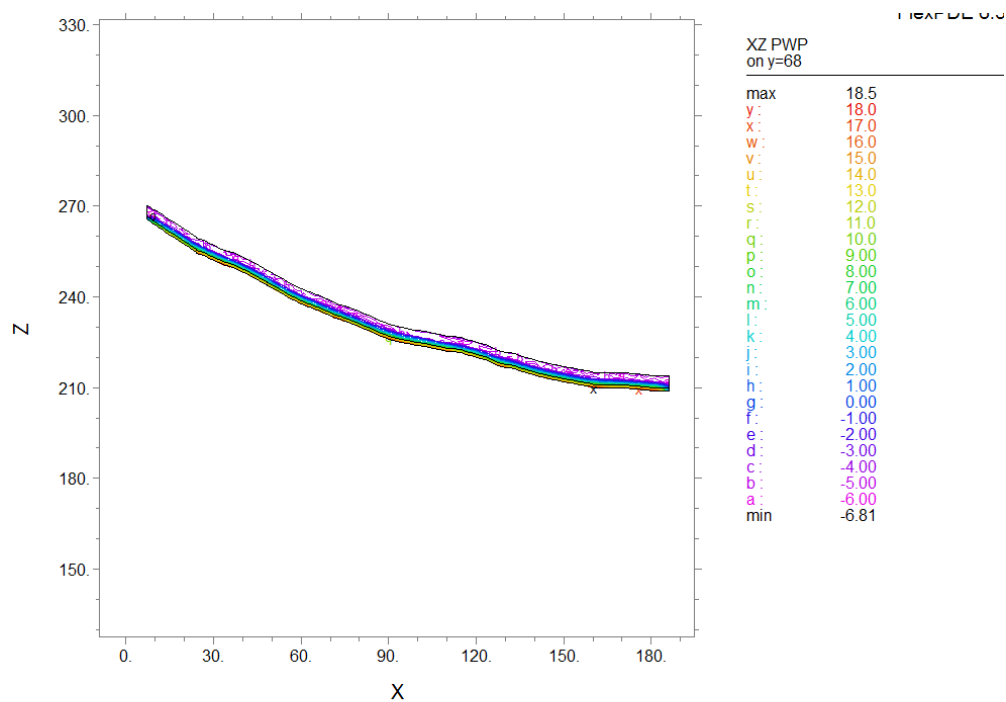
APR30TH\_BC\_PWP\_2: Cycle=200 Time= 11.000 dt= 0.1000 P2 Nodes=18521 Cells=10776 RMS Err= 1.e-4  
Integral= -1700.183



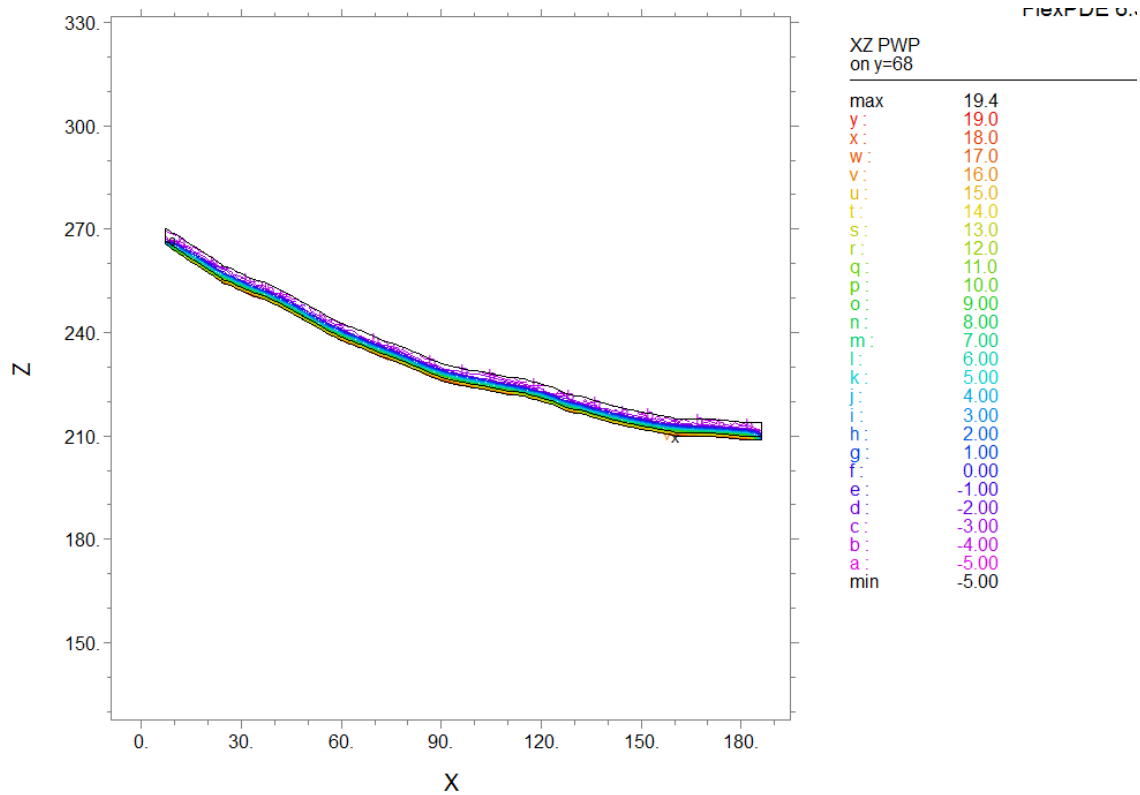
APR30TH\_BC\_PWP\_2: Cycle=233 Time= 13.200 dt= 0.1000 P2 Nodes=18521 Cells=10776 RMS Err= 9.9e-5  
Integral= -1182.056



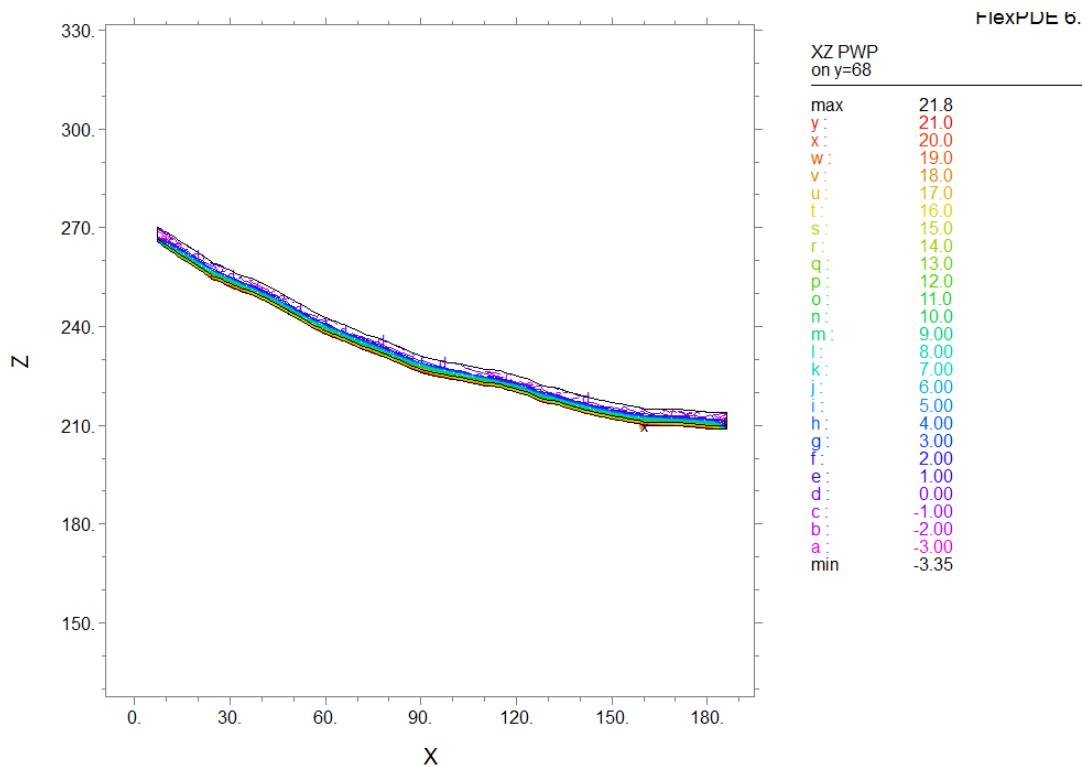
APR30TH\_BC\_PWP\_2: Cycle=258 Time= 15.400 dt= 0.1000 P2 Nodes=18521 Cells=10776 RMS Err= 8.5e-5  
Integral= -611.9513



APR30TH\_BC\_PWP\_2: Cycle=280 Time= 17.600 dt= 0.1000 P2 Nodes=18521 Cells=10776 RMS Err= 1.4e-4  
Integral= 907.8598



APR30TH\_BC\_PWP\_2: Cycle=302 Time= 19.800 dt= 0.1000 P2 Nodes=18521 Cells=10776 RMS Err= 1.6e-4  
Integral= 2414.550



APR30TH\_BC\_PWP\_2: Cycle=349 Time= 22.000 dt= 0.1000 P2 Nodes=18521 Cells=10776 RMS Err= 5.7e-5  
Integral= 4867.371



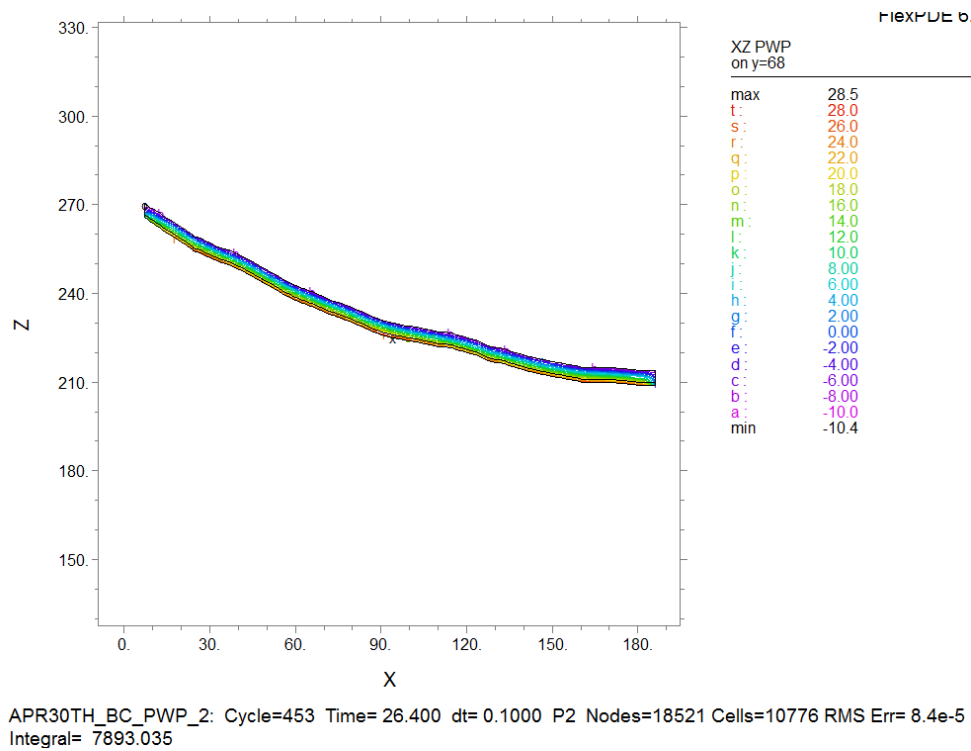
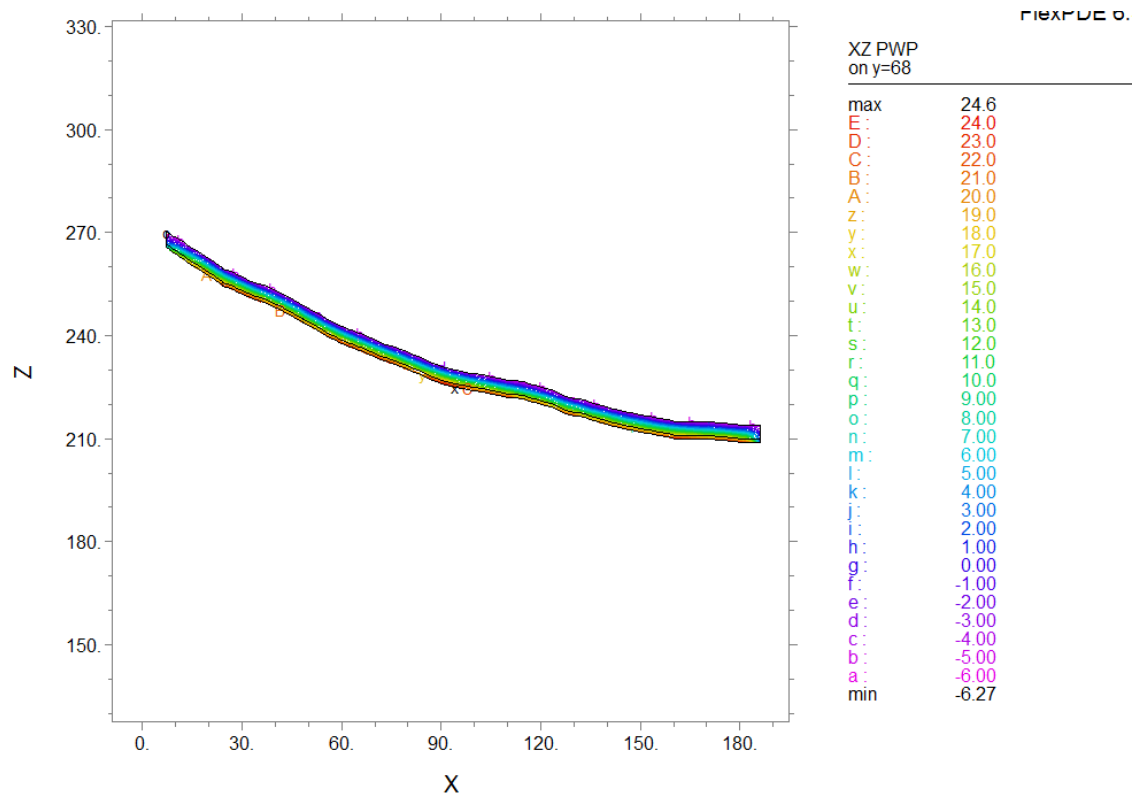
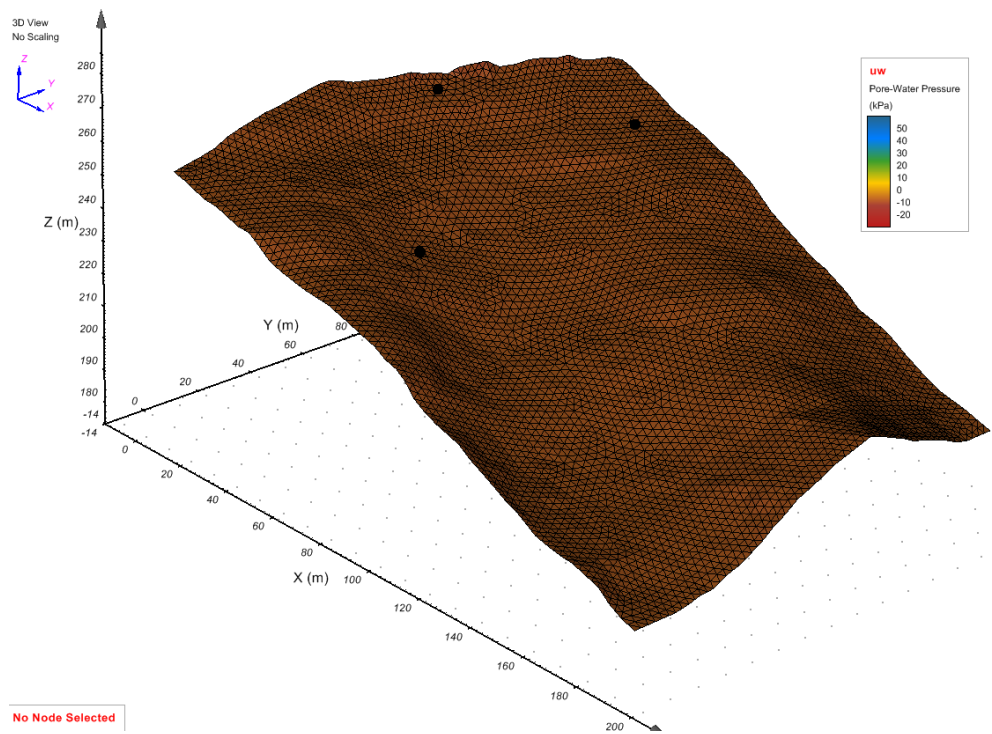
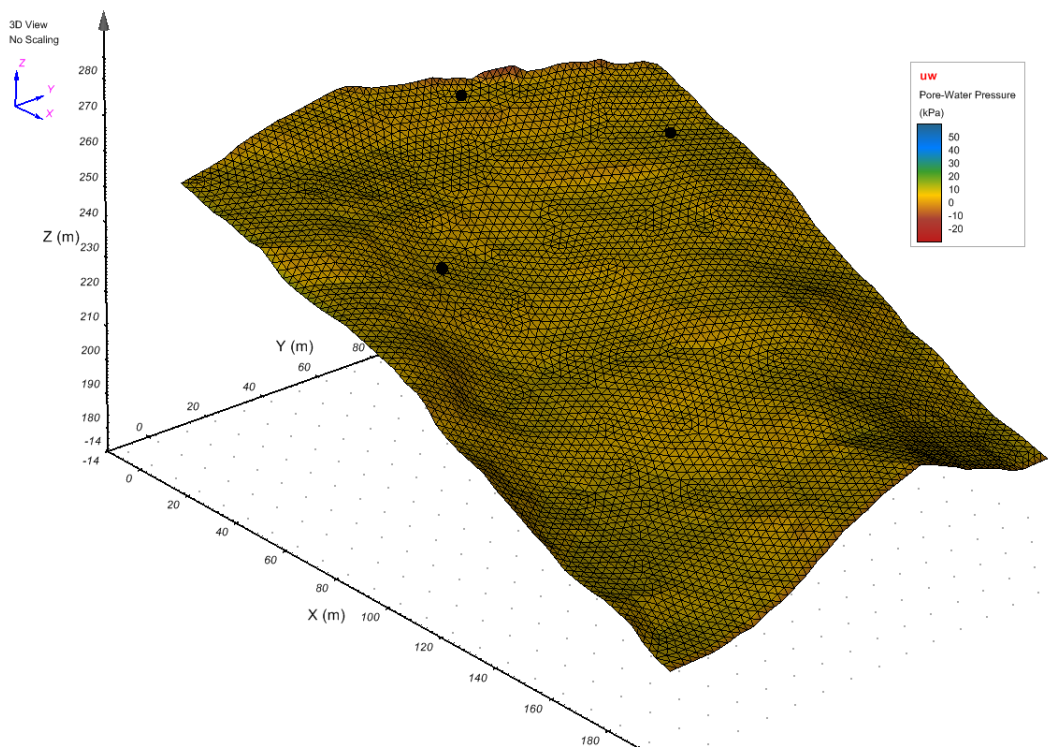


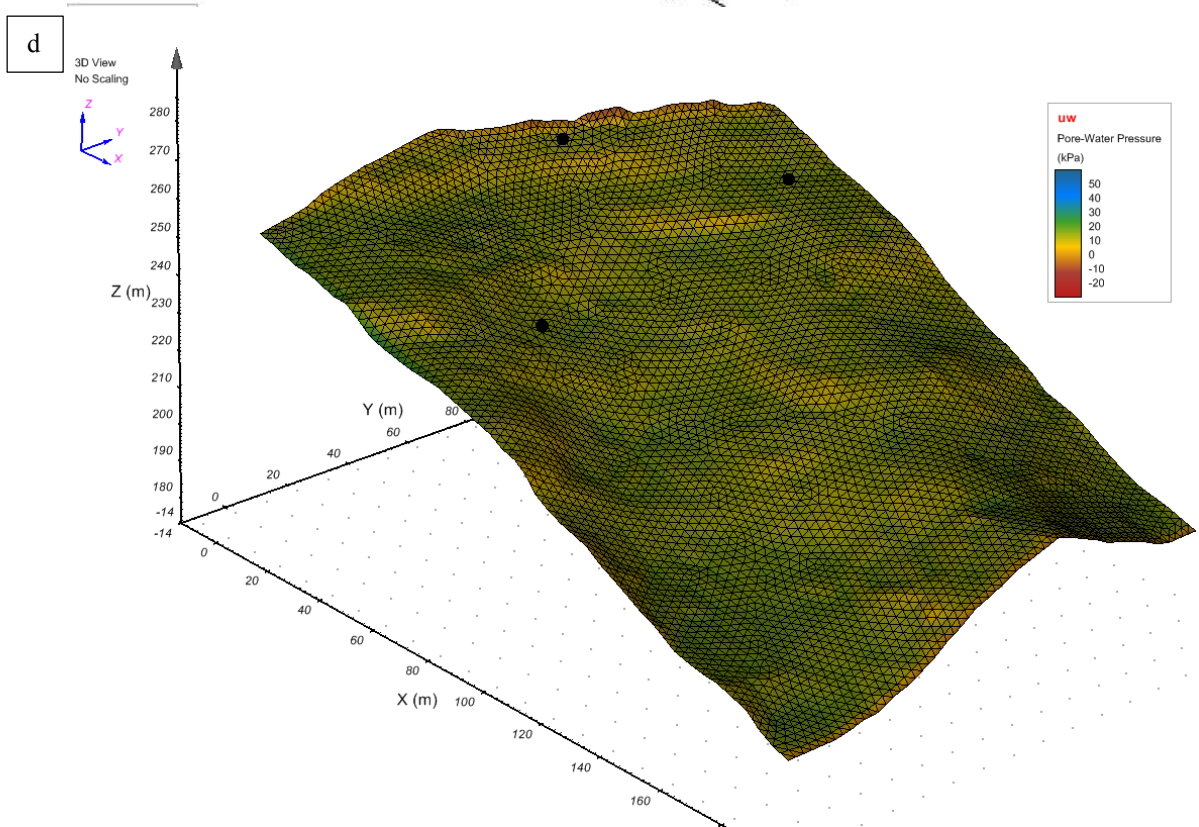
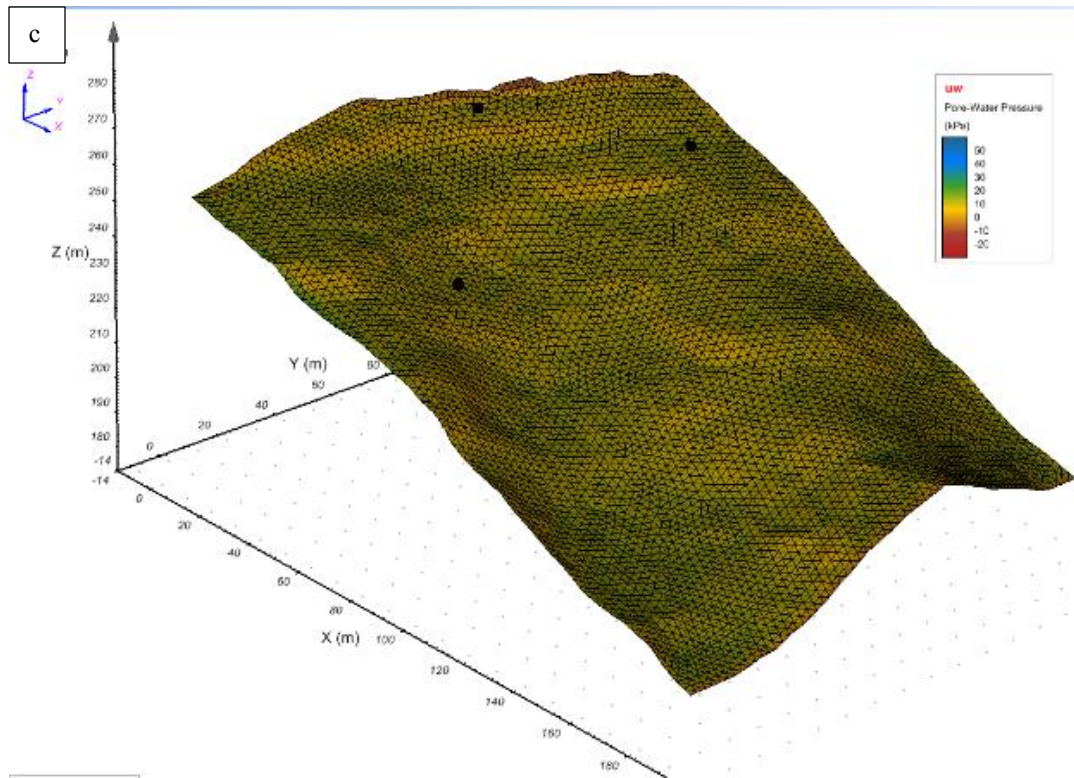
Fig 5.14: Pore-water pressure distribution corresponding to section Y=68m for time t=0 to 30 hr.

a

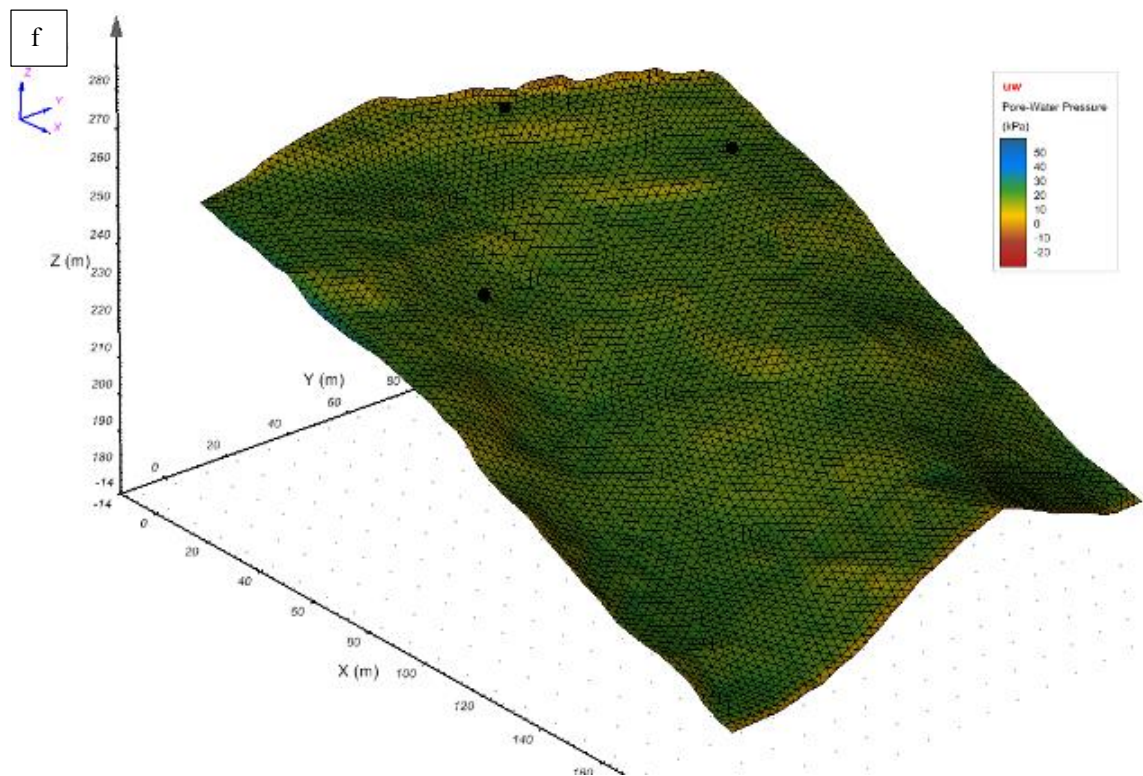
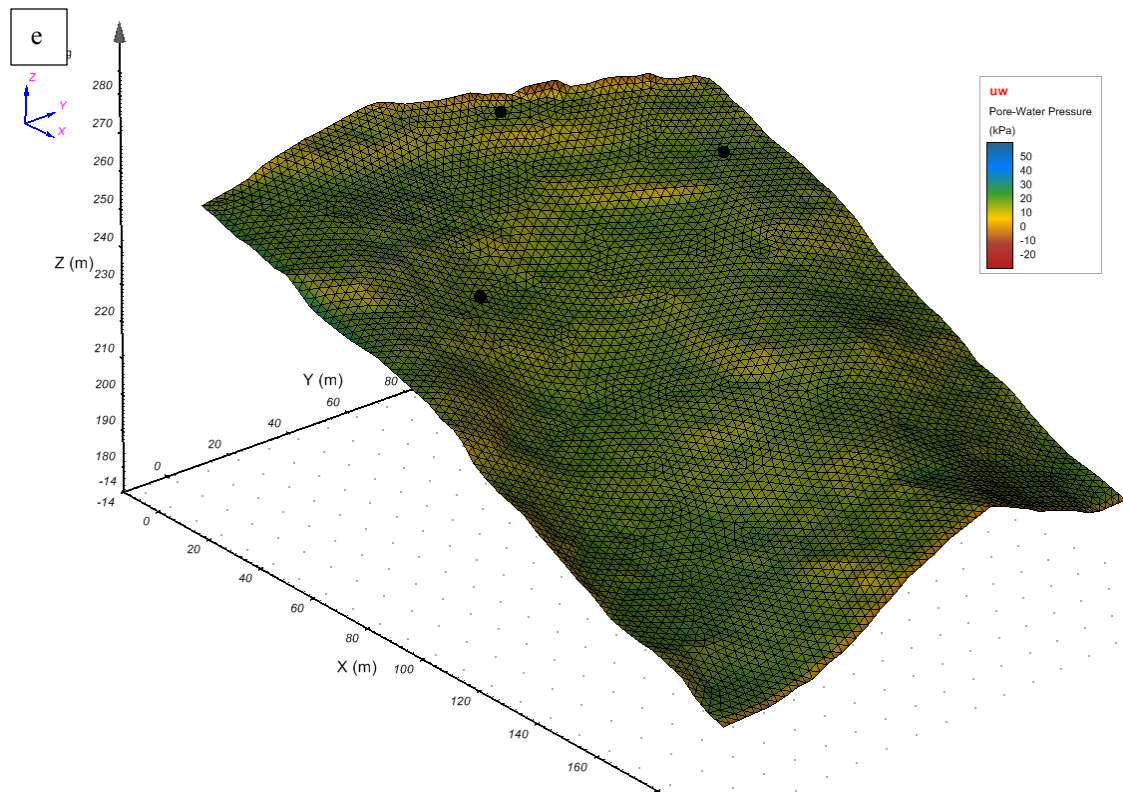


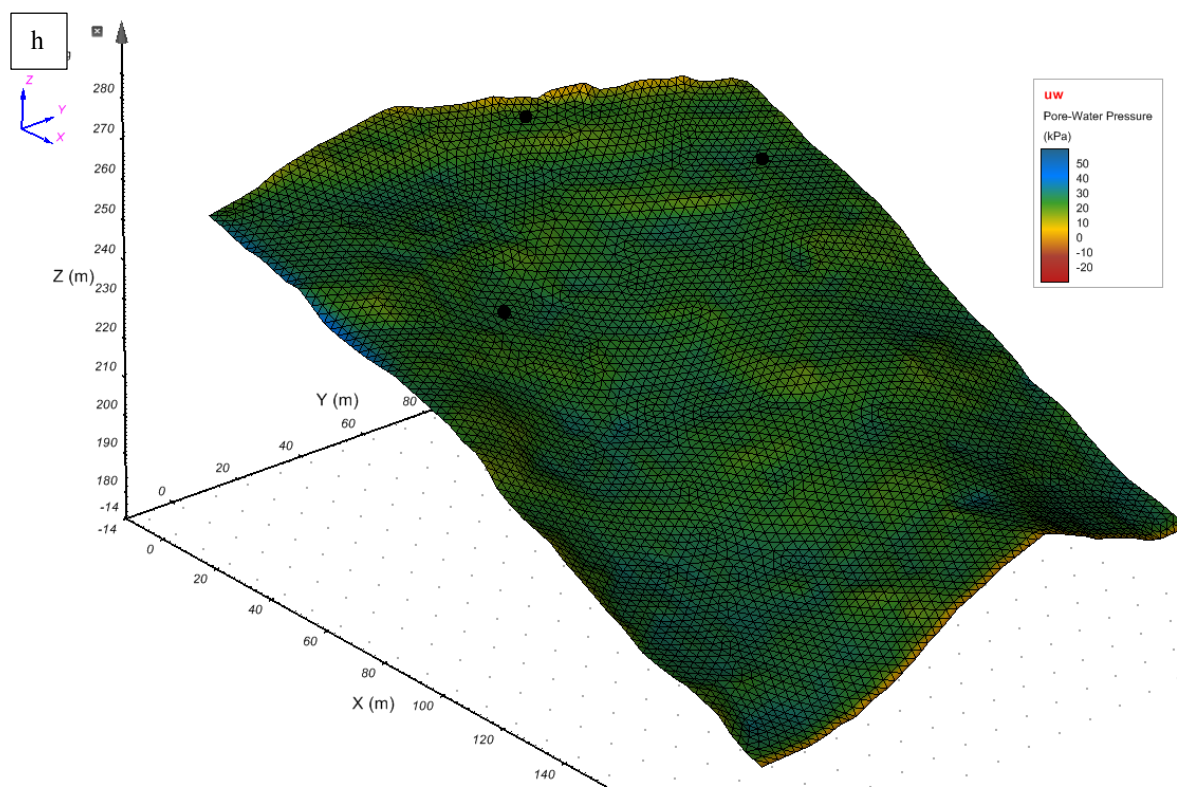
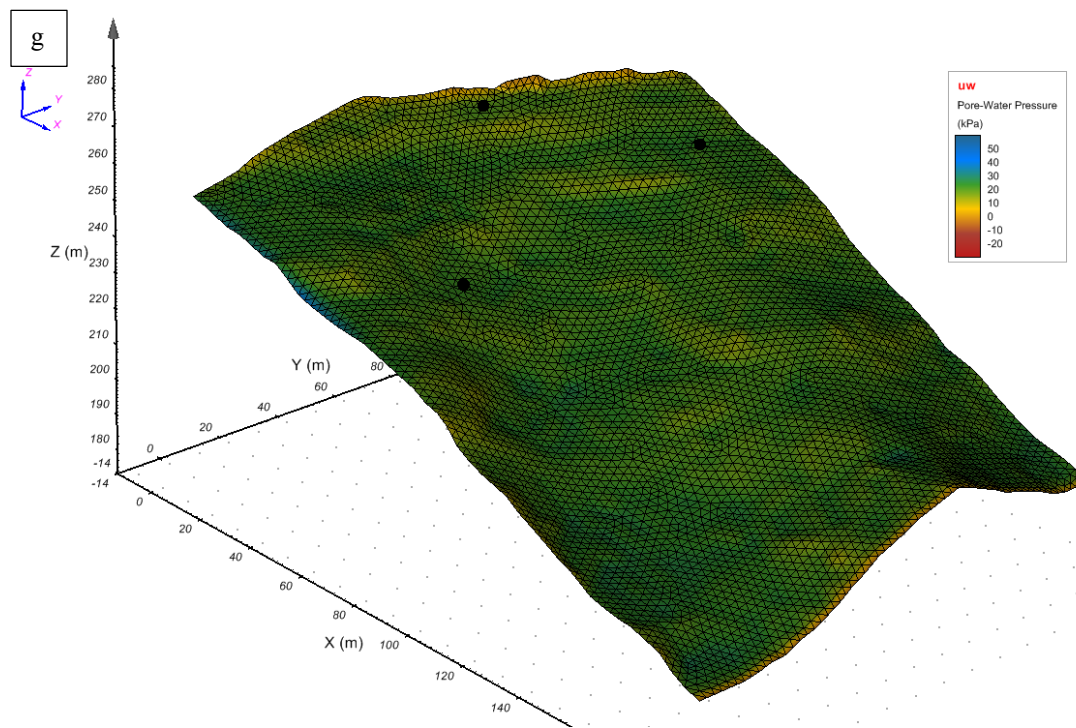
b













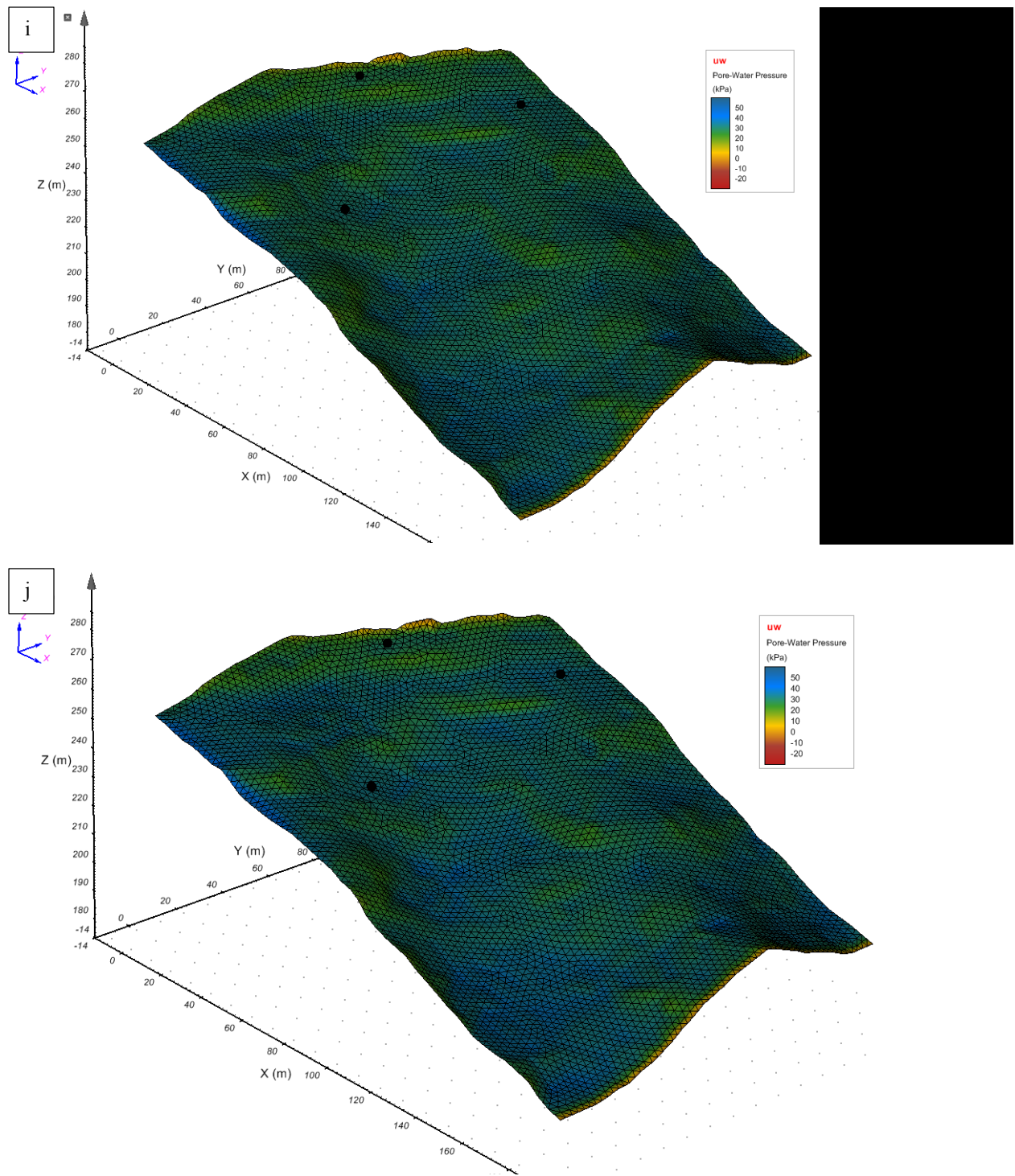
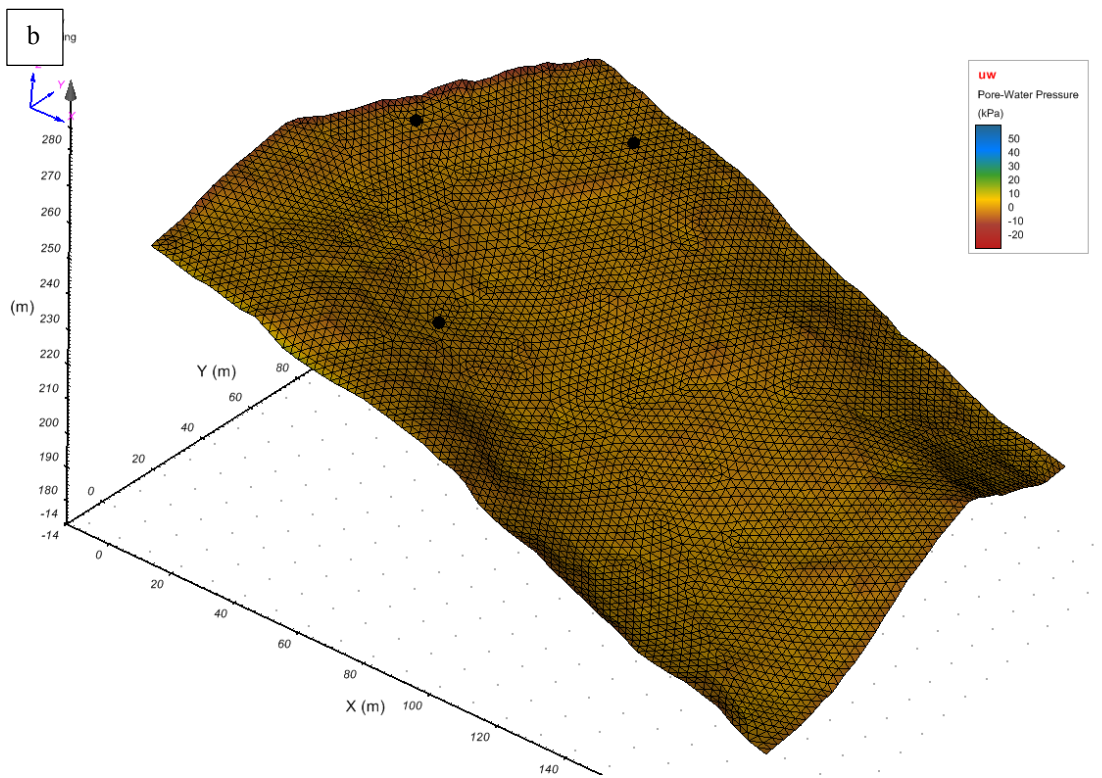
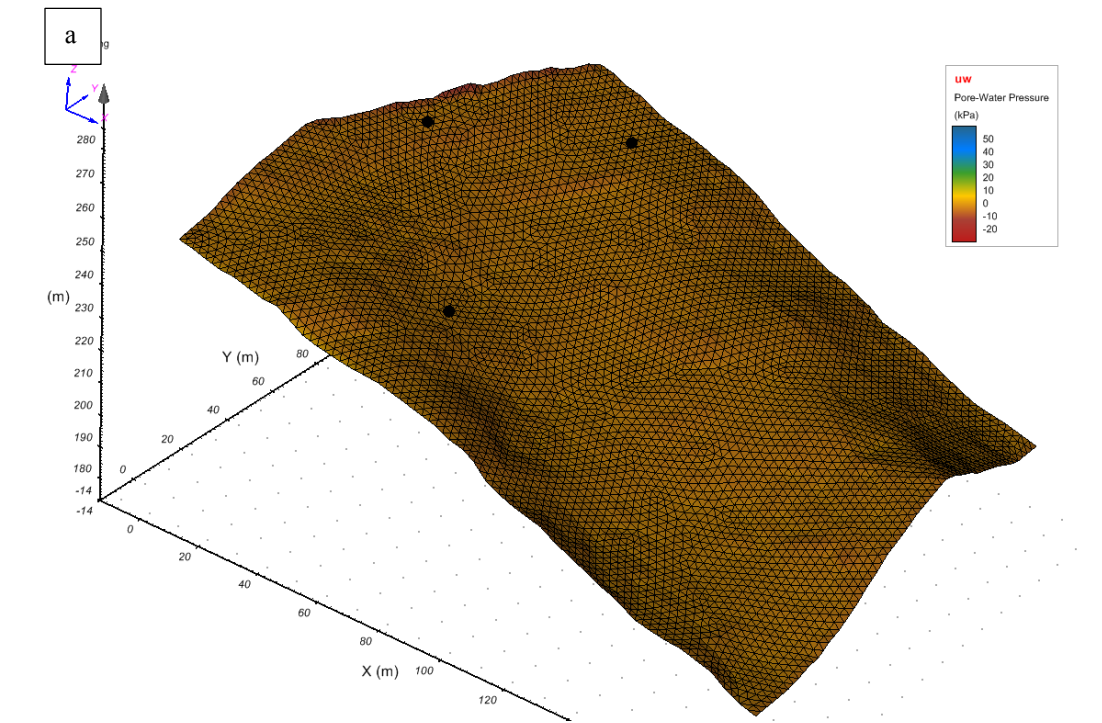
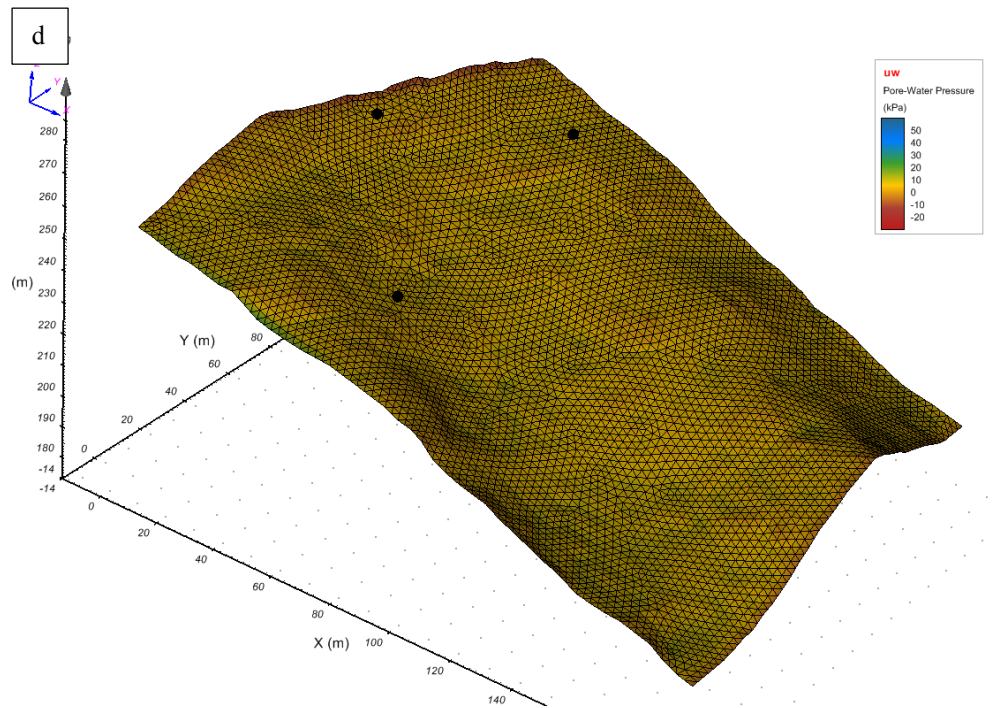
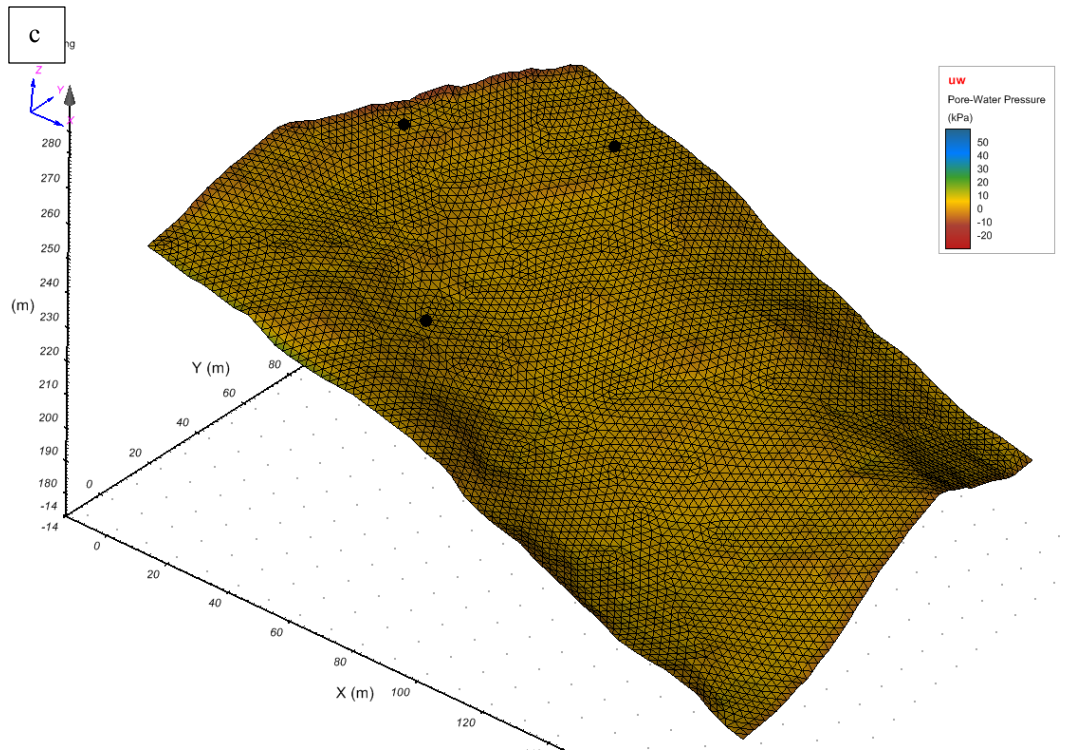
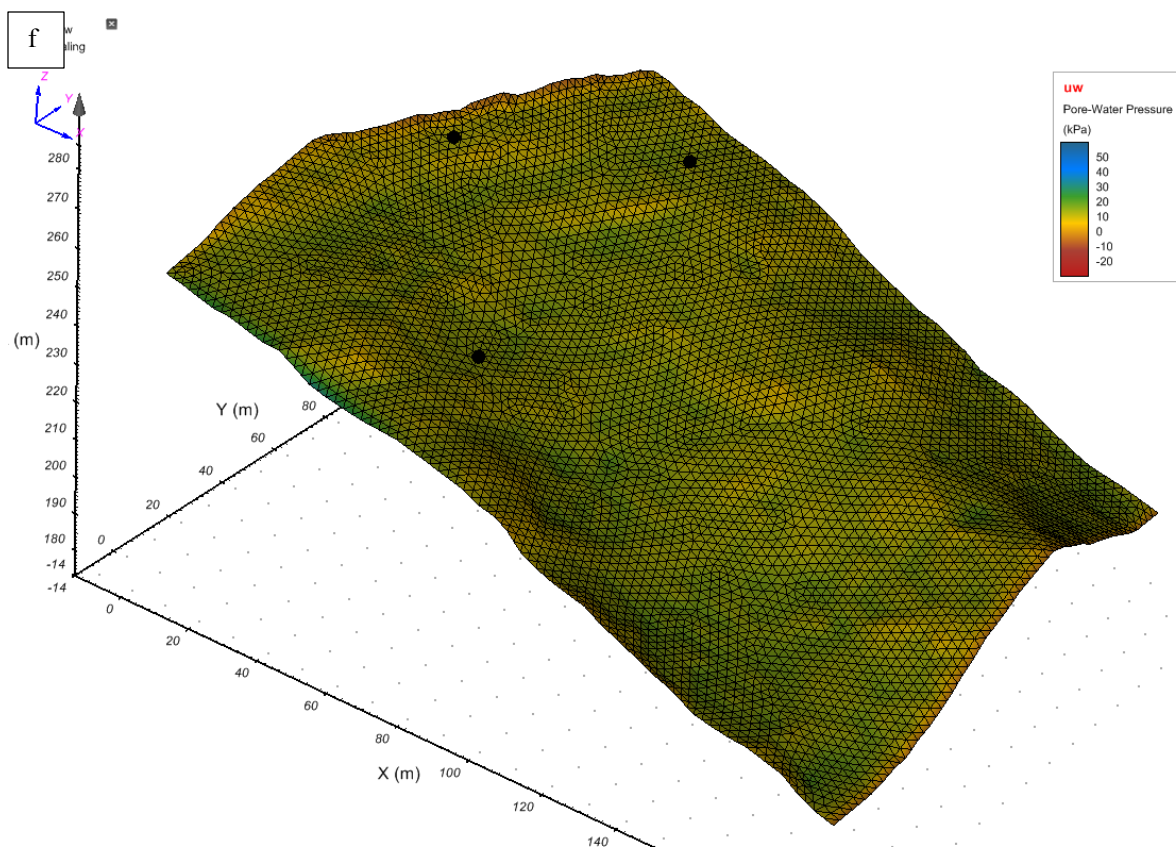
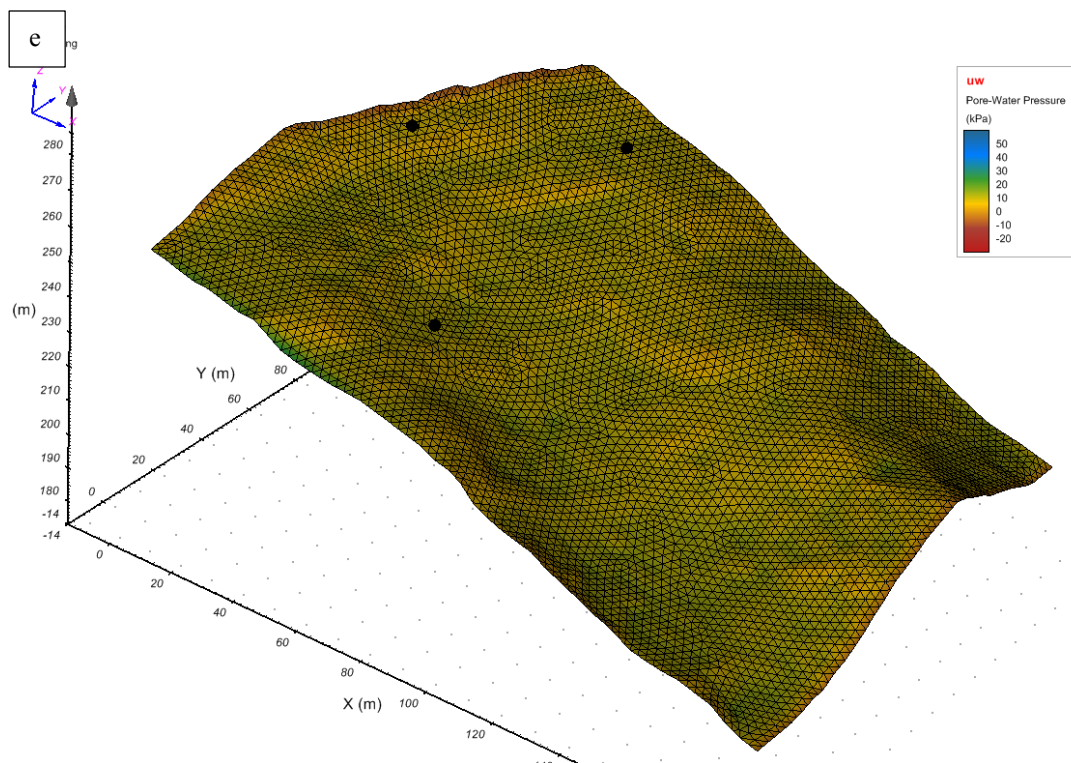


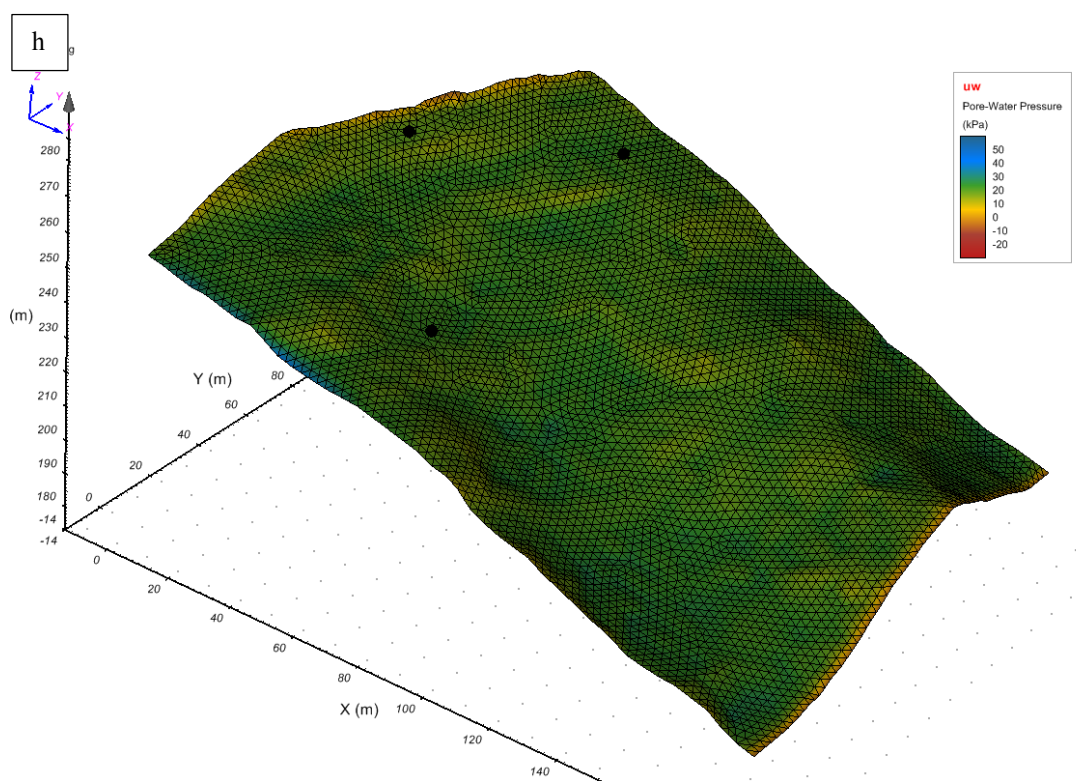
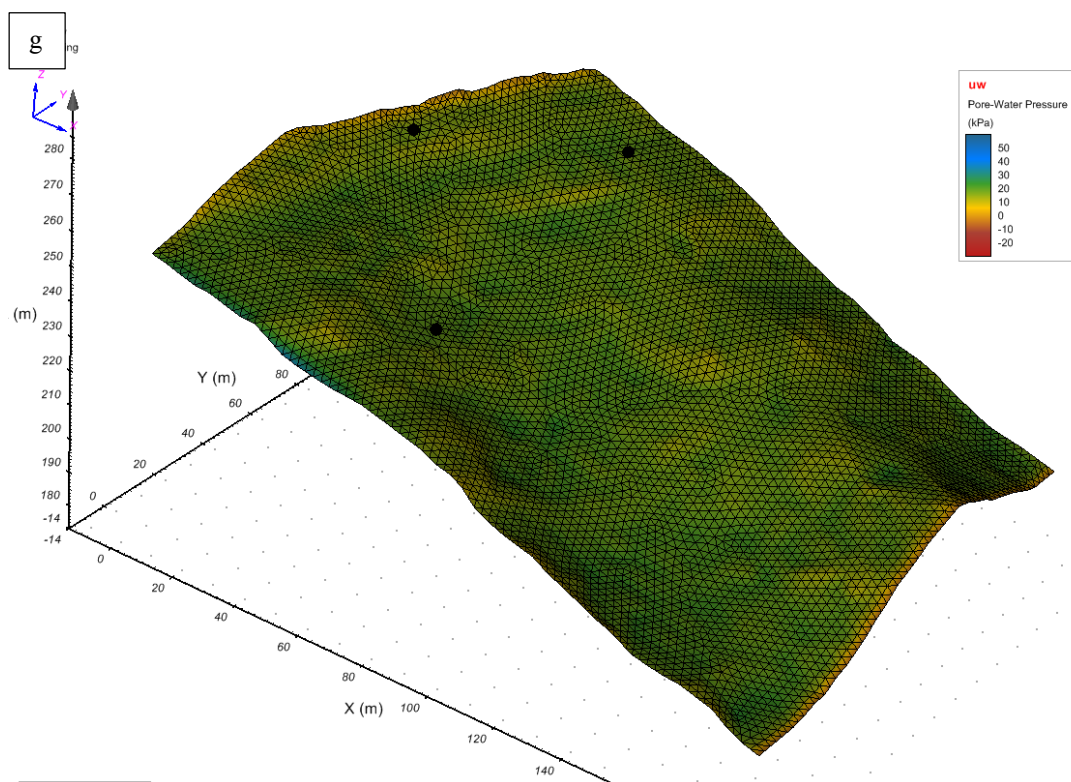
Fig 5.15: Spatial distribution of pwp on surface 1 (top of bedrock): (a) 0 hr ; (b) 7 hr ; (c) 12 hr ; (e) 15 hr; (d) 18 hr; (f) 21 hr; (g) 23 hr; (h) 25 hr; (i) 28 hr; (j) 30 hr













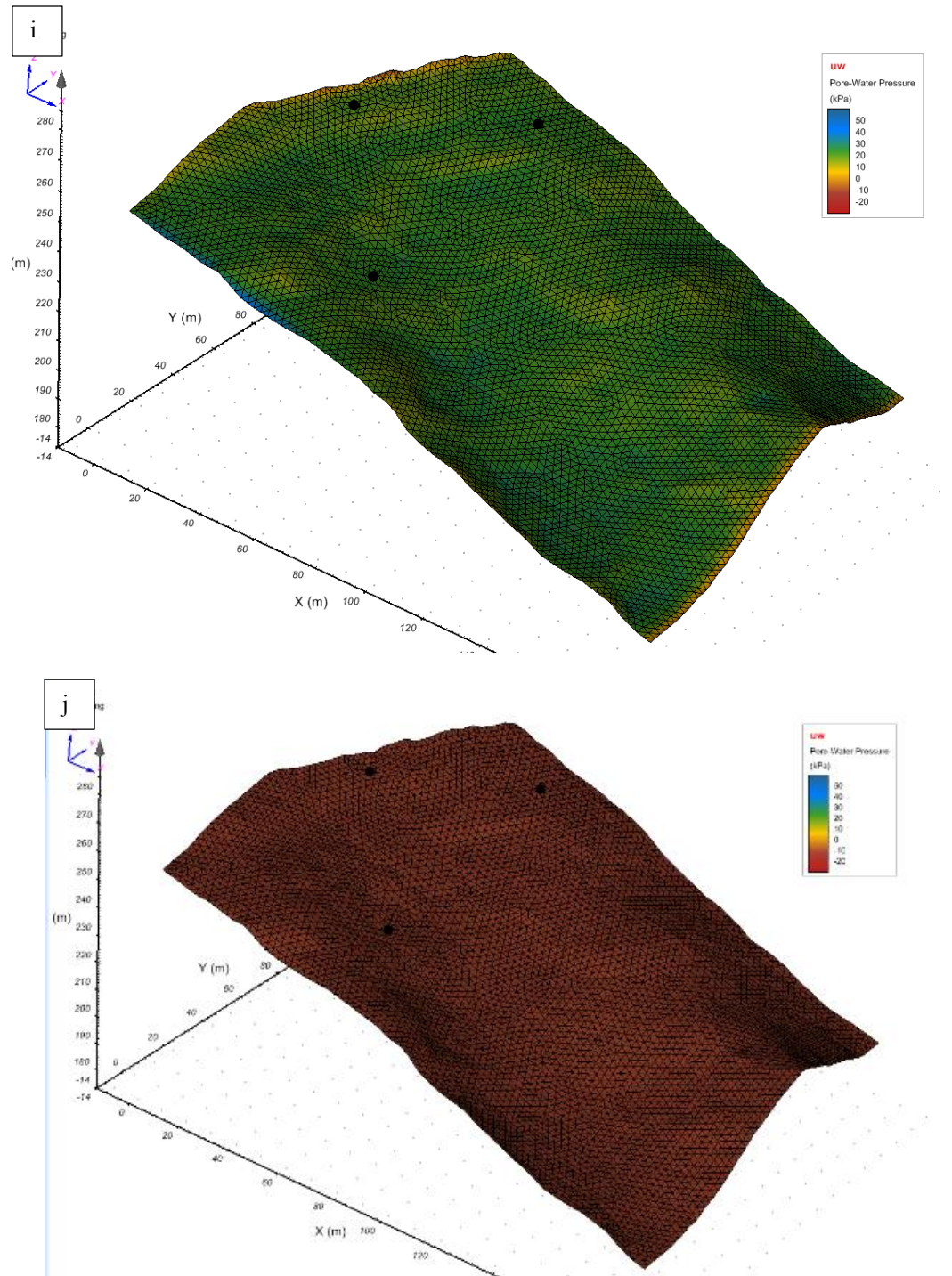


Fig 5.16: Spatial distribution of pwp on surface 2 (layer between colluvium and weathered rock): (a) 0 hr ; (b) 7 hr ; (c) 12 hr ; (e) 15 hr; (d) 18 hr; (f) 21 hr; (g) 23 hr; (h) 25 hr; (i) 28 hr; (j) 30 hr

Fig.5.14 shows the variation of pore water pressure for cross section at Y=68 m when the rainfall from period 0-30

hrs is applied. At time  $t=0$ , the top surface has initial matric suction value of 6 to 8 kPa, while the bottom has lower value around 1.5 kPa. Fig.5.15a and 5.16a shows that for both surfaces 1 and 2 there is not any significant spatial variation of matric suction, though the surface 2 exists at a higher matric suction value relative to surface 1 and is in correspondence to that seen in the field monitoring tests. As time progresses, though there is no significant rainfall, however the high permeability of the soil results in formation of an initial water table at approximately 20 to 40 cm from the bottom. At time  $t=8.8$  hrs, after the actual rainfall starts, the matric suction drops from a maximum value of 12.5 kPa (at time  $t=4.4$ ) to -8.97 and the positive pore water pressure builds up with maximum pore pressure at 11.9 kPa. The pore pressure variation on surface 1 (Fig.5.15b) and surface 2 (Fig.5.16b) indicates top most part near to the air force base to have lower pwp in comparison to the other area of the terrain due to the elevation effect. After a steady rainfall of .025 m/hr for 4hr starting from 15hrs, at 19.8hr the water table reaches about 1~1.6 m approximately, while the top surface is still unsaturated with maximum suction existing at 5 kPa. The peak of extreme rainfall at .07 m/hr occurred between 21 and 23 hrs during which the entire soil depth was saturated and pore water pressure reached about 25 kPa (at  $t=24.2$  hr). The Fig.5.15g and Fig.5.16g shows the spatial variation of pore water pressure at time 23 hrs at surface 1 and 2 respectively. The pore water pressure at some sections at right uppermost part has negative pore water pressure though significantly lower than that at previous time steps. The spatial pore-water pressure given in Fig. 5.17 for the upper most surface shows almost entire area having zero pore pressure at the end of 23 hr except the white portion at the top part and during the time ahead, the pore pressure at the top most surface significantly falls indicating the draining away of water.

The slope stability analysis was conducted using the pore water pressure condition at the end of 23 hrs. The critical slip surface is searched using the grid and tangent method. The general limit equilibrium method (GLE) was adopted to calculate the factor of safety (FOS) owing to its accuracy in comparison to the other methods implemented in the code and a half sine function was assumed for the interslice force. For the analysis, the vertical side resistance forces were also considered which parallels the direction of motion by adding shear resistance due to at-rest earth pressure. Fig.5.18 shows the critical slip surface value and location along with the other trial slip surfaces. The critical FOS for pore pressure at end of 23 hr is .907 and the total volume is about 2626.5 m<sup>3</sup> (Fig.5.18). The critical slip surface occurs almost near the location as that of real event, though the initial release volume was about 1827 m<sup>3</sup> (Jeong, 2014).

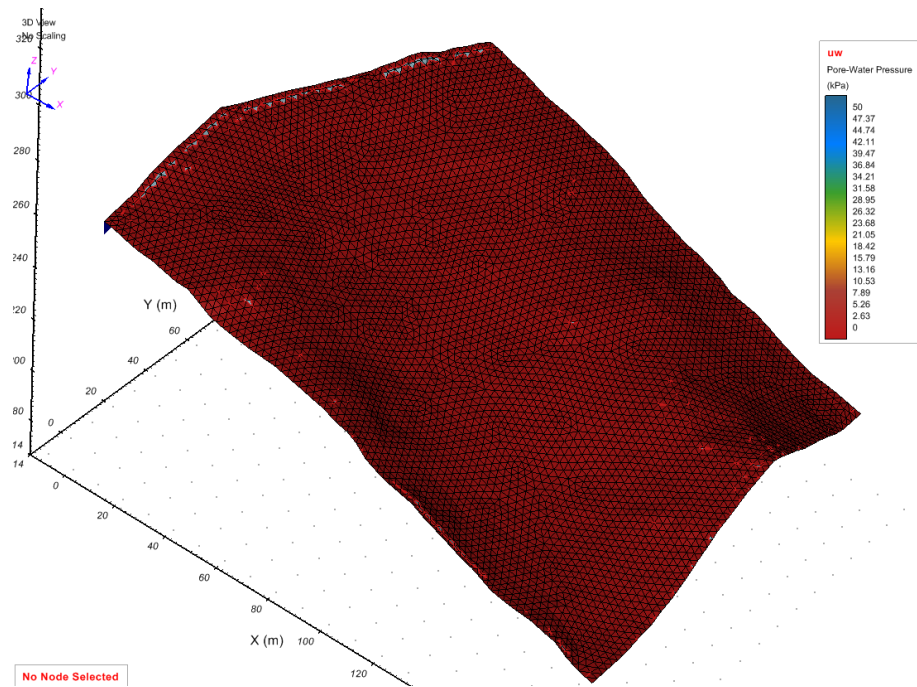


Fig 5.17: Spatial distribution of pwp on surface 3 (Top of colluvium layer) at time= 23 hr.

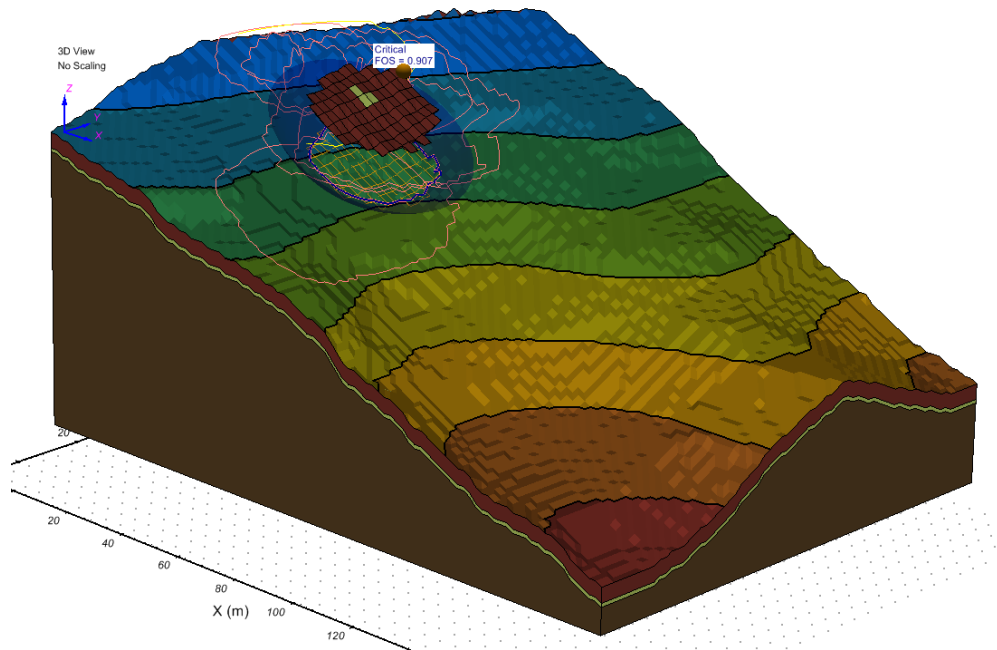


Fig 5.18: Critical slip surface at time t=23 hr.

### 5.4.2 Post-failure hazard assessment

The ANN model developed for the predictive estimation of bulk frictional angle was used in the Raemian watershed (section 5.2.2.2). Table 5.3 shows the independent factors and the estimated value of bulk frictional angle.

The final volume was calculated based on a conservative methodology of considering the entire area of the slope unit with the average soil depth. Fig. 2.3W shows the soil depth map for Mt. Woomyeon obtained from KFRI. The slope unit had an area of 79455.35 m<sup>2</sup> and from the soil depth map 0.71 m is selected as the soil depth as determined using ArcGIS 10.1. Thus, the final volume is approximately about 56413.3 m<sup>3</sup>. Also, the runout distance measured from the initiation area to the end of the slope unit using the COGO tool in ArcGIS 10.1 is about 619.34 m.

Thus the growth rate can be estimated as,

$$E_s = \frac{\ln(56413.3 / 2626.5)}{619.34} = .00495 \quad (5.18)$$

Table 5.5 shows the predicted parameters used for the debris flow run-out analysis in Raemian slope, Mt. Woomyeon, Seoul. The results show a lower predicted final volume than that observed in the field and hence for further analysis the soil depth information from the site investigation, shown in Fig.5.19b, is used.

Table 5.5. Predicted input factors for DAN-3D

Predicted input factors	Values
Initial release volume	2626.5
Bulk frictional angle ( $r_u$ )	0 (1)
Growth rate	.00495

The parameters of yield strength and viscosity were determined using rheometer test as explained in section 5.2.2.1. The Fig.5.19 shows different values of yield strength and viscosity for water contents between 60 % and 90% ( $C_v$  values between 0.4 and 0.1).

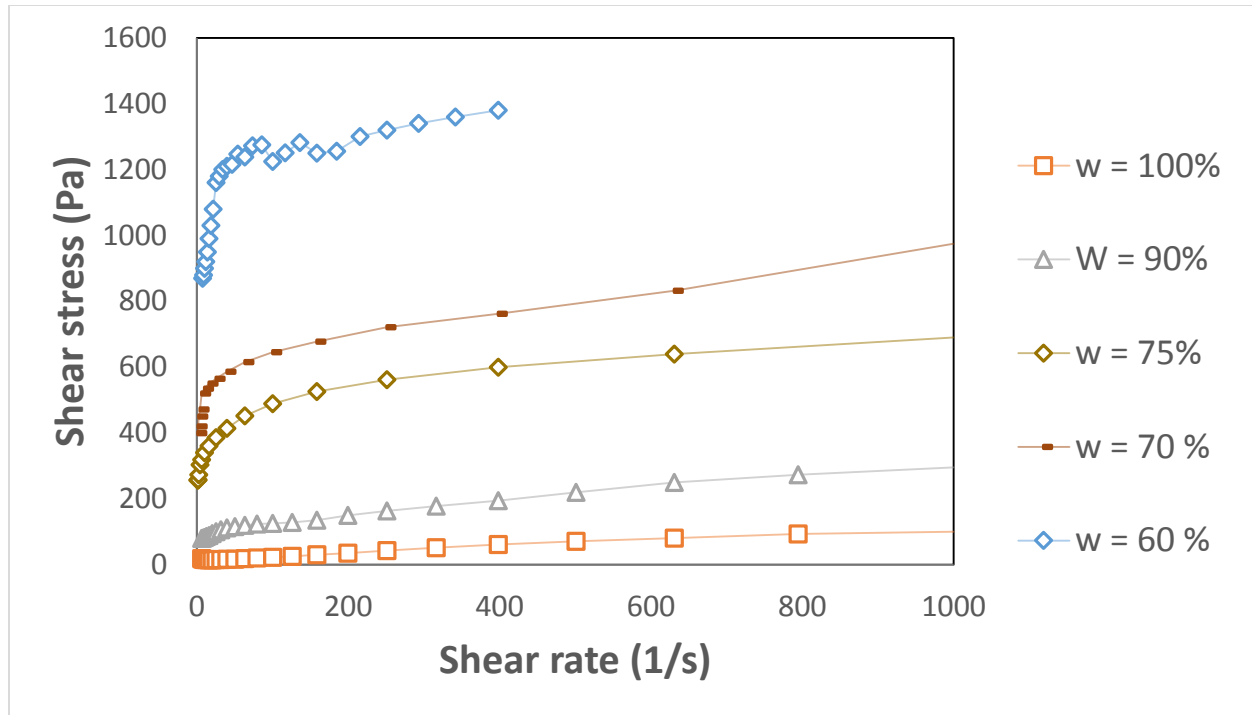


Fig. 5.19: Yield strength and viscosity for different water content in Raemein slope (Lee, 2016)

The fluidized flow has a very low yield strength and a general trend of decrease in yield strength and viscosity with the drop in  $C_v$  owing to the increase in water content is observed. The application of these values to DAN-3D model gave velocity values of 27.2 m/s, 26.4 m/s, 24.2 m/s, and 21.7 m/s corresponding to  $C_v$  values of 0.1, 0.2, 0.3, and 0.4, respectively.

The total volume of debris flow which reaches the road is around 41920 m<sup>3</sup> which is 9.12% less than that the actual volume. The less amount of volume mobilized can be assigned to the value of the erosion depth used in the model. The data from borehole in Fig. 5.9b shows the actual depth to be around 5 m at the top, which is almost 10 m towards the toe of the mountain as opposed to the 0.7 m used from the soil depth map. Considering the soil depth with an average value of 5 m would give us a conservative estimate of the volume of 52642.6 m<sup>3</sup> which is 14.13% larger than the field measured volume. Thus, the estimation of soil depth is extremely essential as it can affect the final volume, velocity and spreading based intensity values which in turn will influence the hazard levels for risk assessment. Fig. 5.20 showing the red boundary indicates the actual flow path and impact area of the debris flow, while the white and colored area shows that calculated using the model. The thickness of the fluidized landslide impacting the Raemian apartments is about 5 m i.e. about two floors shall be affected. Figure 5.21 shows that debris flow in Woomyeon mountain impacted more than 2 floors of buildings.



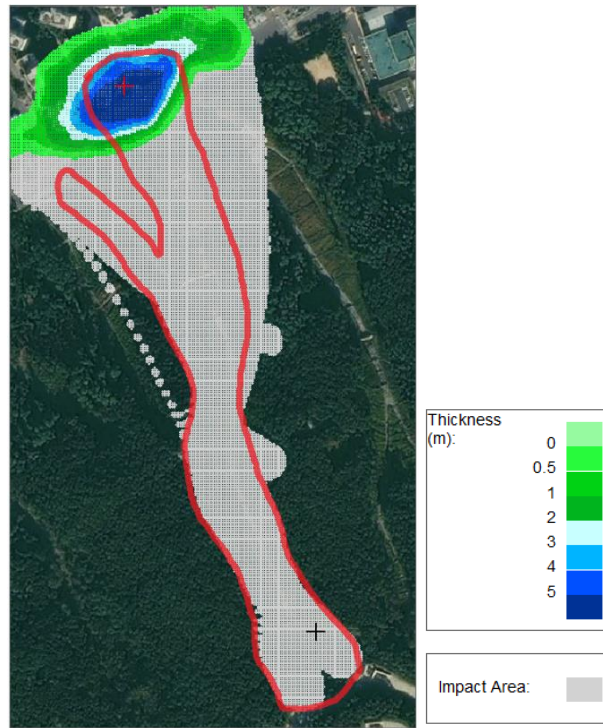


Fig. 5.20. Debris flow thickness and impact area



Fig. 5.21. Debris flow impact on buildings (Jang Seung-Yoon/ Getty images, Truth Leem/ Reuters)

In this analysis, at the deposition zone a rheology with higher bulk frictional angle was defined so as to bring the material to stop as in the real case due to the presence of obstructions like buildings, which otherwise would continue flowing until the maximum time of simulation is achieved. Table 5.6 indicates the maximum final velocity when the debris flow reaches the deposition zone as 27.5 m/s which is almost similar to that observed for the real event (28 m/s; video recording). Thus, the bulk frictional angle of  $0^\circ$  ( $r_u=1$ ) predicted by the ANN model corresponds to that observed in the field indicating that the flow was completely fluidized.

Table 5.6. Debris flow intensity parameters predicted using the model

<b>Intensity parameters</b>	<b>Model simulation</b>	<b>Field observation</b>
Volume (m <sup>3</sup> )	52642.6	46125
Velocity (m/s)	27.5	28
Run-out path	Follows the same path as observed in field	NA

Thus, the predictive debris flow runout conducted for Raemian slope gives a conservative estimate for the intensity parameters like the volume and spread out area while almost similar velocity value in comparison to the real event signifying that the database establishment methodology and the rheology selected are appropriate for the region.

However, the results are underestimated when using the soil depth values from the KFRI map and thus, users should be cautious when using them. It is recommended through research that depth be determined through site investigation in the slope-of-interest, before conducting the predictive analysis.

## Chapter 6. Conclusions and recommendations

### 6.1 Conclusions

The research attempts to develop and apply a framework for debris flow hazard analysis considering a real-time rainfall event through sequential sifting and scale reduction approach for integrating into the hazard component of the early warning system. For achieving the same, a new framework consisting of three new models along with a database establishment approach has been advanced. The results are summarized as below:

1. An attempt to shed light on the determination of the best subset of factors from numerous possible combinations using an objective general hybrid framework was done since most of the previous studies have focused on either using different supervised learning schemes with a fixed set of factors and selecting the best performance model or using filter models to generate a subset of relevant factors. When using the same dataset for creating a landslide susceptibility model through different learning algorithms or filter models, diverse factors will be selected each time and only using the set of relevant factors selected through initial screening does not always provide the best susceptibility model. Therefore, a two-stage hybrid algorithm was devised to select the optimal subset by first implementing a filter approach, using the Spearman's correlation, for the initial partitioning into relevant and irrelevant factors. The feedback-controlled scheme is further developed in two phases, the first of which is conducted to check for redundancy among the relevant subsets through backward substitution, and the latter is conducted through a forward search scheme, effectively screening for relevant features among the initially categorized irrelevant factors. The results showed that thirteen factors, namely, soil density, plan curvature, slope, SPI, STI, distance from stream, TRI, geology, soil depth, total curvature, elevation, TWI, and topography, are the most relevant factors for Mt. Woomyeon. The landslide susceptibility map developed using the hybrid model in comparison to that developed by the wrapper model gave the best performance, using a lower number of factors with a success rate and prediction rate AUC of 85% and 89%, respectively. The implemented scheme therefore provides a systematic approach to rank and select the relevant conditioning factor subsets, and the resulting high performing landslide susceptibility map can be used for hazard assessment by linking it with the temporal probability.

2. The existing methods to assess the landslide temporal component do not serve well in situations where the spatial

variation of landslides induced by extreme rainfall is observed due to the variability of soil properties and especially is critical when using real-time-based early warning systems, and when the landslide-hazard-level information is utilized at different tiers of decision-making. In this research, a simple statistical index coupling the rainfall and geotechnical factors to study evolution of the landslide hazard due to temporal variation of factors that trigger landslides was undertaken. The extreme rainfall index (ERI) was developed using four factors (continuous rainfall, 20-day antecedent rainfall, permeability, and storage capacity) and had high AUC values (89 and 97%, respectively) for the training and validation curves, indicating the good performance of the statistical index. The ERI was coupled with landslide susceptibility map to study the landslide hazard in Deokjeok-ri Creek for the extreme rainfall-induced landslide events in July 2006 using DHI. It was seen that the ERI values were quite low for the rainfall events prior to the extreme rainfall events starting on 11 July 2006, but increased almost 14-fold during the continuous rainfall (175 mm) on 12 July 2006, and reached the maximum value (0.99) for a CR of 467 mm on 15 July 2006. The entire study area prior to 12 July had very low DHI and was classified as low hazard. However, the extreme rainfall from 12 to 15 July reduced the percentage of cells in the low DHI level to 15.31%. About 48.86% of the cells in the region were reclassified as being under high hazard of landslides after the extreme rainfall of 202 mm on 15 July (formerly 20.59%), and an incremental trend towards transformation to instability was observed. This change in hazard areas accompanying the temporal variation of extreme rainfall, quantified using DHI, is useful in taking decisions with regard to dissemination of the early warning.

3. An index based approach was used to develop a criterion for debris flow mobilization to implicitly accommodate initiation mechanisms and be incorporated inexpensively into the EWS for spatial based sifting of debris flows from slides or other landslide types. In using Pearson's correlation analysis, four factors; Slope angle, profile curvature, SPI, and elevation with lower threshold values of 24°, -4 to +4, 4.0, and 60 m, respectively, were selected. The criterion was applied to Mt. Woomyeon and showed good predictability, thus indicating its discerning ability of debris flow from landslides. The criterion, however, gives a conservative estimate and can be improved in future by including slide data as well. The scale reduction for hazard assessment of debris flow caused by extreme rainfall was conducted through establishment of slope units incorporating the mobilization criterion. The Mt. Woomyeon, using the approach of combining the DEM and reverse DEM, was divided into 45 slope units. Among the current slope units in the Mt. Woomyeon, the Raemian slope unit was selected to predict the debris flow hazard since a well establish database of the field observations exists. The real event extreme rainfall scenario was applied to the terrain and a 3-D based

seepage analysis coupled with slope stability was conducted. It was seen that the failure occurred at 23 hours, when the rainfall had extremely high intensity of 70 mm/hr, owing to the high pore-water pressure generated in the entire soil depth. The 3-D limit equilibrium based analysis based on GLE method considering the vertical side forces gave a critical factor of safety of .44 for a landslide volume of 2626.5 m<sup>3</sup> which is about 43.76% higher than that observed in the field (1827 m<sup>3</sup>). It is always best to work using the conservative estimate owing to the uncertainties and spatial variabilities involved in the strength and hydraulic conductivity measurements, and also during the run-out assessment.

4. A predictive debris flow hazard assessment is conducted at a site-specific scale on the slope selected through the methodology detailed earlier. The reliability of the predictive modelling depends on the quality of the database used and hence, a framework is advanced for estimating the parameters used in the DAN-3D code for debris flow run-out modelling. At first, among the various rheological model the most suitable for the Korean conditions is selected, followed by estimation of the parameter for the same. In this study, frictional rheology was found to be the most suited and an ANN based model is used for the bulk frictional angle assessment. A method for estimation of growth rate, user controlled entrainment factor, was suggested. However, the use of soil depth from KFRI map was found to underestimate the predicted volume and therefore, site investigated soil depth values should preferably be used. The predictive modelling estimates the final volume of 52642.6 m<sup>3</sup>, a velocity of 27 m/s and about 5 m debris thickness concentrated near the Raemian apartment. Thus, a predictive modelling through scale reduction and sequential sifting for a given extreme rainfall event has been conducted in Mt. Woomyeon, Seoul.

## **6.2 Recommendations for further study**

- 1) The proposed framework along with the developed core technologies will be applied to mountainous region in Busan and the data from heavily instrumented slope will be helpful for site-specific analysis in the framework.
- 2) Mobilization criterion needs to be improved by considering both debris flow and slide events to reduce the false-positives. Hence, a methodology needs to be developed to distinguish debris flow from slides which can be extended to visual based mapping. Thus, a larger database can be created at lower cost as against site-investigation.
- 3) Further study is needed to develop run-out models considering effect of entrainment on the rheological property.

## References

- [1]. Aaron, J., Hungr, O., McDougall, S., 2015. Development of a systematic approach to calibrate equivalent fluid runout models. 12<sup>th</sup> International Symposium on Landslides, Napoli, Italy.
- [2]. Aleotti, P., 2004. A warning system for rainfall-induced shallow failures. *Eng. Geol.* 73(3-4), 247-265.
- [3]. Althuwaynee, O.F., Pradhan, B., Lee, S., 2012. Application of an evidential belief function model in landslide susceptibility mapping. *Comput. Geosci.* 44,120-135.
- [4]. Anagnosti, P.,1969. Three dimensional stability of fill dams. *Proceedings of the 7th International Conference on Soil Mechanics and Foundation Engineering, Mexico*, 2, pp. 275-280.
- [5]. Anderson, M., G., Lloyd, D., M.,1991. Using a combined slope hydrology-stability model to develop cut slope design charts. *Proc. Inst. Civ. Engineers* 91, 705-718.
- [6]. Ayalew, L., Yamagishi, H., 2005. The application of GIS-based logistic regression for landslide susceptibility mapping in the Kakuda-Yahiko Mountains, Central Japan. *Geomorphology* 65, 15-31.
- [7]. Bachmann, L., Yamagishi, H., 2005. The application of GIS-based logistic regression for landslide susceptibility mapping in the Kakuda-Yahiko Mountains, Central Japan. *Geomorphology* 65, 15-31.
- [8]. Bachmann, D., Bouissou, S., Chemenda, A., 2004. Influence of weathering and pre-existing large scale fractures on gravitational slope failure: insights from 3-D physical modelling. *Nat. Hazards Earth Syst. Sci.* 4,711-717.
- [9]. Bagnold, R. A., 1954. Experiments on a gravity-free dispersion of large solid spheres in a Newtonian fluid under shear, *Proc. R. Soc. London, Ser. A* 225, 49–63.
- [10]. Ballabio, C., Sterlacchini, S., 2012. Support vector machines for landslide susceptibility mapping: The Staffora River Basin case study, Italy. *Mathem. Geosci.* 44 (1), 47–70.
- [11]. Baum, R., L., Godt, J., W., Savage, W., Z., 2010. Estimating the timing and location of shallow rainfall induced landslides using a model for transient, unsaturated infiltration. *Journal of Geophysical Research*, 115. F03013
- [12]. Blahut, J., Horton, P., Sterlacchini, S., Jaboyedoff, M.,2010. Debris flow hazard modelling on medium scale: Valtellina di Tirano, Italy, *Nat. Hazards Earth Syst. Sci.*, 10, 2379–2390, doi:10.5194/nhess-10-2379-2010.
- [13]. Bromhead, E., N., Ibsen, M.-L., Papanastassiou, Zemichael, A., A.,2002. Three-dimensional stability analysis of a coastal landslide at Hanover Point, Isle of Wight. *Quarterly Journal of Engineering Geology and Hydrogeology* 35, 79-88.
- [14]. Campbell, C., S., Brennan, C., E., 1985.Computer simulation of granular shear flow. *J.Fluid Mech.* 151, 167-188.
- [15]. Campbell, C., S., 1990. Rapid granular flows. *Annu. Rev. Fluid Mech.* 22,57–92
- [16]. Castellanos, E.A., Van Westen, C.J., 2007. Qualitative landslide susceptibility assessment by multicriteria analysis: a case study from San Antonio del Sur, Guantanamo, Cuba. *Geomorphology* 94(3–4), 453–466.
- [17]. Carrara A., Cardinali, M., Detti, R., Guzzetti, F., Pasqui, V., Reichenbach, P., 1991. GIS Techniques and Statistical Models in Evaluating Landslide Hazard. *Earth Surface Processes and Landforms* (16), 427-445.
- [18]. Chauhan, S., Sharma, M., Arora, M.K., Gupta, N.K., 2010. Landslide Susceptibility Zonation through ratings derived from Artificial Neural Network. *International Journal of Applied Earth Observation and Geoinformation* 12, 340–350.

- [19]. Chen, C.-Y., Yu, F., -C., 2011. Morphometric analysis of debris flows and their source areas using GIS. *Geomorphology* 129, 387-397.
- [20]. Cheng, Y., Yip, C., 2007. Three-Dimensional Asymmetrical Slope Stability Analysis Extension of Bishop's, Janbu's, and Morgenstern-Price's Techniques. *J. Geotech. Geoenviron. Eng.*, 10.1061/(ASCE)1090-0241(2007)133:12(1544), 1544-1555.
- [21]. Choi, Y. J., 2004. Trends on temperature and precipitation extreme events in Korea. *J. Korean Geogr. Soc.* 39, 711-721 (in Korean).
- [22]. Chu, J., Lo, S. C. R., Lee, I. K., 1993. Instability of Granular Soils under Strain Path Testing. *Journal of Geotechnical Engineering*, 119(5), 874-892.
- [23]. Chu, J. & Leong, W. K., 2001. Pre-failure strain softening and pre-failure instability of sand: a comparative study. *Geotechnique*, 51(4), 311-321.
- [24]. Chung, C.F., Fabbri, A.G., 2003. Validation of Spatial Prediction Models for Landslide Hazard Mapping. *Natural Hazards* 30 (3), 451-472.
- [25]. Chung, C.F., Fabbri, A.G., 2005. Systematic procedures of landslide hazard mapping for risk assessment using spatial prediction models. Glade, T., Anderson, M., Crozier, M., (Eds.), *Landslide Hazard and Risk*. John Wiley and Sons, New York.
- [26]. Chleborad, A.F., 2003. Preliminary evaluation of a precipitation threshold for anticipating the occurrence of landslides in the Seattle, Washington, area. U.S. Geological Survey Open-File Report 2003-463, 39.
- [27]. Chleborad, A. F., Baum, R. L., Godt, J. P., 2006. Rainfall thresholds for forecasting landslides in the Seattle, Washington, Area exceedence and probability. U.S. Geological Survey Open-File Report, 2006-1064.
- [28]. Cho, S.E., Lee, S.R., 2002. Evaluation of surficial stability for homogeneous slopes considering rainfall characteristics. *J. Geotech. Geoenviron. Eng.*, 128(9), 756-763.
- [29]. Coe, J.A., Michael, J.A., Crovelli, R.A., Savage, W.Z., 2000. Preliminary map showing landslide densities, mean recurrence intervals, and exceedance probabilities as determined from historic records, Seattle, Washington. U.S. Geological Survey Open-File Report 00-303.
- [30]. Conforti, M., Pascale, S., Robustelli, G., Sdao, F., 2014. Evaluation of prediction capability of the artificial neural networks for mapping landslide susceptibility in the Turbolo River catchment (northern Calabria, Italy). *Catena* 113, 236-250.
- [31]. Costanzo, D., Rotigliano, E., Irigaray, C., Jimenez-Peralvarez, J.D., Chacon, J., 2012. Factor selection in landslide susceptibility modelling on large scale following the gis matrix method: Application to the river Beiro basin (Spain). *Nat. Hazards Earth Syst. Sci.* 12, 327-340.
- [32]. Crovelli, R., A., 2000. Probability Models for Estimation of Number and Costs of Landslides. U.S. Geological Survey Open File Report 00-249, 23.
- [33]. Crozier, M., 1999. Prediction of rainfall-triggered landslides: a test of the Antecedent Water Status Model. *Earth Surface Processes and Landforms* 24(9), 825-833.
- [34]. Cui, P., 1992. Studies on condition and mechanism of debris flow initiation by means of experiment, *Journal of Chinese Science Bulletin*, 379, 759-763, 1992



- [35]. Cundall, P., A., Strack, P., D., L., 1979. A discrete numerical model for granular assemblies. *Geotechnique* 29, 47–65.
- [36]. Davies, K.W., Petersen, S.L., Johnson, D.D., Davis, D.B., Madsen, M.D., Zvirzdin, D.L., Bates, J.D., 2010. Estimating Juniper cover from national agriculture imagery program (NAIP) imagery and evaluating relationships between potential cover and environmental variables. *Rangeland Ecol. Manage.* 63(6), 630–637.
- [37]. Denlinger, R., Iverson, R., 2004. Granular avalanches across irregular three-dimensional terrain: 1. Theory and computation, *J. Geophys. Res.* 109, F01014.
- [38]. De Vita, P., 2000. Fenomeni di instabilit  delle coperture piroclastiche dei Monti Lattari, di Sarno e di Salerno (Campania) ed analisi degli eventi pluviometrici determinant, *Quaderni di Geologia Applicata*, 7-2.
- [39]. Devkota, K., Regmi, A., Pourghasemi, H., Yoshida, K., Pradhan, B., Ryu, I., Dhital, M., Althuwaynee, O.F., 2012. Landslide susceptibility mapping using certainty factor, index of entropy and logistic regression models in GIS and their comparison at Mugling–Narayanghat road section in Nepal Himalaya. *Nat. Hazards* 65(1), 135–165.
- [40]. Dietrich, W.E., Reiss, R., Hsu, M., Montgomery, D.R., 1995. A process-based model for colluvial soil depth and shallow landsliding using digital elevation data. *Hydrological Processes* 9, 383–400.
- [41]. Dikau, R., Weichselgartner, J., 2005. *Der unruhige Planet. Der Mensch und die Naturgewalten*. Primus, Darmstadt (In German).
- [42]. Dou, J., Tien Bui, D., Yunus, A.P., Jia, K., Song, X., Revhuag, I., Xia, H., Zhu, Z., 2015. Optimization of causative factors for landslide susceptibility evaluation using remote sensing and GIS data in parts of Niigata, Japan. *PLoS One* 10(7), e0133262.
- [43]. Eckersley, D., 1990. Instrumented laboratory flowslides. *Geotechnique*, 40, 489–502.
- [44]. Ellen, S., D., Fleming, R. W., 1987. Mobilization of debris flows from soil slips, San Francisco bay region, California, in: *Debris flows/avalanches: process, recognition, and mitigation*, (Eds) Costa, J. E. and Wieczorek, G. F., *Geological society of America Reviews in Engineering Geology*, 7, 31–40.
- [45]. Ercanoglu, M., Gokceoglu, C., 2001. Assessment of landslide susceptibility for a landslide-prone area (north of Yenice, NW Turkey) by fuzzy approach. *Environmental Geology* 41, 720–730.
- [46]. Ercanoglu, M., Gokceoglu, C., Van Asch, T.W.J., 2004. Landslide susceptibility zoning north of Yenice (NW Turkey) by multivariate statistical techniques. *Natural Hazards* 32, 1–23.
- [47]. Ermini, L., Catani, F., Casagli, N., 2005. Artificial neural networks applied to landslide susceptibility assessment. *Geomorphology* 66, 327–343.
- [48]. Fleming, R., Ellen, S., Albus, M., 1989. Transformation of dilative and contractive landslide debris into debris flows – an example from Marin County, California. *Engineering Geology*, 27, 201–223.
- [49]. Florinsky, I.V., 2012. The Dokuchaev hypothesis as a basis for predictive digital soil mapping. *Eurasian Soil Science* 45(4), 445–451.
- [50]. Fredlund, D., G., 1984. Analytical methods for slope stability analysis. State-of-the-art address, Fourth Int. Sym. On landslides, Toronto, Canada.

- [51]. Fredlund, D.G., Xing, A., 1994. Equations for the soil-water characteristic curve. *Can. Geotech. J.* 31(3), 521-532.
- [52]. Gabet, E., Mudd, S., 2006. The mobilization of debris flows from shallow landslides. *Geomorphology*, 74, 207-218.
- [53]. Garson, G.D., 1991. Interpreting neural-network connection weights, *AI Expert* 6 (4), 47-51.
- [54]. Ghosh, S., Van Westen, C.,J., Carranza, E.,J.,M., Jetten, V.G., Cardinali, M., Rossi, M., 2012. Generating event-based landslide maps in a data-scarce Himalayan environment for estimating temporal and magnitude probabilities.
- [55]. Gokceoglu, C., Aksoy, H., 1996. Landslide susceptibility mapping of the slopes in the residual soils of the Mengen region (Turkey) by deterministic stability analyses and image processing techniques, *Eng. Geol.* 44, 147–161.
- [56]. Govi, M., Mortara, G., Sorzana, P., F. Eventi idrologici e frane, *Geologia Applicata ed Idrogeologia*, XX, Part II, 359–375, 1985.
- [57]. Griswold, J., P., Iverson, R., M., 2008. Mobility statistics and automated hazard mapping for debris flows and rock avalanches. *U.S. Geol. Surv. Sci. Invest. Rep.* 2007-5276, 59 p.
- [58]. Guzzetti, F., Carrara, A., Cardinali, M., Reichenbach, P., 1999. Landslide hazard evaluation: a review of current techniques and their application in a multi-scale study, Central Italy. *Geomorphology* 31(1-4), 181-216.
- [59]. Guzzetti, F., Malamud, B.D., Turcotte, D.L., Reichenbach, P., 2002. Power- law correlations of landslide areas in Central Italy. *Earth and Planetary Science Letters* 195, 169-183.
- [60]. Guzzetti, F., Stark, C.P., Salvati, P., 2005. Evaluation of risk to the population posed by natural hazards in Italy. Hungr, O., Fell, R., Couture, R., Eberhardt, E., (Eds.) *Landslide risk management*. Taylor & Francis, London, 381-389.
- [61]. Guzzetti, F., Reichenbach, P., Ardizzone, F., Cardinali, M., Galli, M., 2006. Estimating the quality of landslide susceptibility models. *Geomorphology* 81(1–2), 166–184.
- [62]. Guzzetti, F., Peruccacci, S., Rossi, M., Stark, C.P., 2007. Rainfall thresholds for the initiation of landslides in central and southern Europe. *Meteorol Atmos Phys.* 98, 239-268.
- [63]. Guyon, I., Elisseeff, A. 2003. An introduction to variable and feature selection. *J. Mach. Learn. Res.*, 3, 1157-1182.
- [64]. Harp, E.L., Reid, M.R., Michael, J.A., 2004. Hazard Analysis of Landslides Triggered by Typhoon Chata'an on July 2, 2002, in Chuuk State, Federated States of Micronesia, *USGS Open-File Report 2004-1348* US Dept. of the Interior, Washington, DC.
- [65]. Heinimann, H. R., Holtenstein, K., Kienholz, H., Krummenhacher, B., and Mani, P., 1998. Methoden zur Analyse und Bewertung von Naturgefahren, *Umwelt-Materialien, Naturgefahren BUWAL*, 85, Bern, pp. 248.
- [66]. Heyerdahl, H., Harbitz, C.B., Domaas, U., Sandersen, F., Tronstad, K., Nowacki, F., Engen, A., Kjekstad, O., Devoli, G., Buezo, S.G., Diaz, M.R., Hernandez, W., 2003. Rainfall induced lahars in volcanic debris in Nicaragua and El Salvador: practical mitigation. In: *Proceedings of international conference on fast slope movements—prediction and prevention for risk mitigation, IC-FSM2003*, Naples. Patron Pub, 275-282.

- [67]. Hovland, H., J., 1977. Three-dimensional slope stability analysis method. *Journal of the Geotechnical Engineering Division* 103(9), 971-986.
- [68]. Huang, G.-B., Zhu, Q.-Y., Siew, C.-K., 2006. Extreme Learning Machine: Theory and Applications. *Neurocomputing* 70, 489-501.
- [69]. Hungr, O., Morgan G., C., Kellerhals, R., 1984. Quantitative analysis of debris torrent hazards for design of remedial measures. *Can. Geotech. J.* 21, 663–77.
- [70]. Hungr, O., Morgan, G.C., Vandine, D., F., D., R., Lister., 1987. Debris flow defenses in British Columbia. In *Debris Flows/ Avalanches: Process, Recognition, and Mitigation*, p. 201- 222. Ed. By J.E. Costa and G.F. Wieczorek, Boulder, Geological Society of America, *Reviews in Engineering Geology*, 7.
- [71]. Hungr, O., Salgado, F., M., Byrne, P., M., 1989. Evaluation of a three-dimensional method of slope stability analysis. *Canadian Geotechnical Journal* 26(4), 679-686.
- [72]. Hungr, O., 1995. A model for the runout analysis of rapid flow slides, debris flows, and avalanches. *Can. Geotech. J.* 32, 610–23.
- [73]. Hughes, G. F. 1968. On the Mean Accuracy of Statistical Pattern Recognizers. *IEEE Transactions on Information Theory*, IT-14:55-63.
- [74]. Hutchinson, J., N., 1986. A sliding-consolidation model for flow slides. *Can. Geotech. J.* 23, 115–26.
- [75]. Intrieri, E., Gigli, G., Mugnai, F., Fanti, R., Casagli, N., 2012. Design and implementation of a landslide early warning system, *Eng. Geol.*, 147–148, 124–136.
- [76]. Iverson, R.M., 1997. The physics of debris flows. *Rev. Geophys.* 35 (3), 245 – 296.
- [77]. Jaiswal, P., Van Westen, C.J., 2009. Estimating temporal probability for landslide initiation along transportation routes based on rainfall thresholds. *Geomorphology* 112, 96-105.
- [78]. Jakob, M., 2000. The impact of logging on landslide activity at Clayoquot Sound, British Columbia. *Catena* 38, 279–300.
- [79]. Jeong, G., -C., K., -S., Kim, Choo, C, -O, Kim, M., -L, 2011. Characteristics of landslides induced by a debris flow at different geology with emphasis on clay mineralogy in South Korea. *Natural Hazards* 59 (1), 347-365.
- [80]. Jeong, S., S., Kim, J., H., Kim, Y., M., Bae, D., H., 2014. Susceptibility assessment of landslides under extreme-rainfall events using hydro-geotechnical model: a case of Umyeonsan (Mt.), Korea. *Nat. Hazard Earth Syst. Sci. Discuss.* 2, 5575-5601.
- [81]. Johnson, A.M., Rodine, J.R., 1984. Debris flow. In *Slope Instability*, Brundsen D, Prior DB (Eds). Wiley: Chichester; 257–361.
- [82]. Jung, I.-W., Bae, D.-H., Kim, G., 2011. Recent trends of mean and extreme precipitation in Korea. *Int. J. Climatol.* 31, 359–370.
- [83]. Kavzoglu, T., Sahin, E.T., Colkesen, I., 2015. Selecting conditioning factors in shallow translational landslide susceptibility mapping using genetic algorithm. *Engineering Geology* 192, 101-112.
- [84]. Keaton, J.R., Anderson, L.R., Mathewson, C.C., 1988. Assessing debris flow hazards on alluvial fans in Davis County, Utah. In *Fragaszy, R. J. (Editor), Twenty-Fourth Annual Symposium on Engineering Geology and Soils*

Engineering, Pullman, Washington: Publications and Printing, Washington State University, Pullman, WA, 89-108.

- [85]. Kim, J., Jeong, S., Park, S., Sharma, J., 2004. Influence of rainfall-induced wetting on the stability of slopes in weathered soils. *Engineering Geology* 75(3-4), 251-262.
- [86]. Kim, S.K., Hong, W.P., Kim, Y.M., 1991. Prediction of rainfall triggered landslides in Korea. In: Bell, D.H. (Ed.), *Landslides*, Rotterdam: A.A. Balkema, vol. 2, 989-994.
- [87]. Kim, S.W., Lee, J.H., Chun, K.W., 2008. Recent increases in sediment disasters in response to climate change and land use, and the role of watershed management strategies in Korea. *International Journal of Erosion Control Engineering* 1(2), 44-53.
- [88]. Kimerling, A.J., Buckley, A.R., Muehrcke, P.C., Muehrcke, J.O., 2011. *Map use: Reading analysis interpretation*. Esri Press, 360.
- [89]. Kincal, C., Akgun, A., Koca, M. Y., 2009. Landslide susceptibility assessment in the Izmir (West Anatolia, Turkey) city center and its near vicinity by the logistic regression method. *Environmental Earth Sciences* 59, 745-756.
- [90]. Kira, K., Rendell, L., 1992. A practical approach to feature selection. *Proceedings of the Ninth International Conference on Machine Learning*, 249-256.
- [91]. Korean Geotechnical Society, 2011. Research contract report: addition and complement causes survey of Mt. Woomyeon landslide. (In Korean)
- [92]. Korean Society of Civil Engineers, 2012. Research contract report: causes survey and restoration work of Mt. Woomyeon landslide. (In Korean)
- [93]. Kotsiantis, S. B., 2011. Feature selection for machine learning classification problems: a recent overview. *Artif. Intell. Rev.*
- [94]. Lade, P. V., 1993. Initiation of static instability in the submarine Nerlerk berm. *Canadian Geotechnical Journal*, 30(6), 895-904.
- [95]. Lam, L., and Fredlund, D.G. 1993. A general limit-equilibrium model for three-dimensional slope stability analysis. *Canadian Geotechnical Journal*, 30: 905-919.
- [96]. Lee, D.-H, 2016. Probabilistic analysis of rheological parameters for debris flow predictive modeling. M.S. thesis, KAIST.
- [97]. Lee, M.J., Choi, J.W., Oh, H.J., Won, J.S., Park, I., Lee, S., 2012. Ensemble-based landslide susceptibility maps in Jinbu area. *Korea Environ. Earth. Sci.* 67(1), 23-37.
- [98]. Lee, S.J., Lee, S.R., Kim, Y.S., 2003. An Approach to Estimate Unsaturated Shear Strength Using Artificial Neural Network and Hyperbolic Formulation. *Computers and Geotechnics* 30(3), 489-503.
- [99]. Leong, W.K., Chu, J., Teh, C.I. 2000: Liquefaction and instability of a granular fill material. *Geotechnical Testing Journal* 23, 178-192.
- [100]. Lim, T.T., Rahardjo, H., Chang, M.F., Fredlund, D.G., 1996. Effect of rainfall on matric suctions in a residual soil slope. *Canadian Geotechnical Journal*, 33(4), 618-628.

- [101].Lips, E.W., Wieczorek, G.F., 1990. Recurrence of debris flows on an alluvial fan in central Utah, *in* French, R.H., ed., *Hydraulics/Hydrology of Arid Lands (HAL)*. Proceedings of the International Symposium: American Society of Civil Engineers, 555-560.
- [102].Maharaj, R.J., 1993. Landslide processes and landslide susceptibility analysis from an upland watershed: a case study from St. Andrew, Jamaica, West Indies. *Engineering Geology* 34, 53-79.
- [103].Major, J. J., Pierson, T., C., 1992. Debris flow rheology: Experimental analysis of fine-grained slurries, *Water Resour. Res.* 28, 841–857.
- [104].Marjanovic, M., Kovacevic, M., Bajat, B., Vozenić, V., 2011. Landslide susceptibility assessment using SVM machine learning algorithm. *Eng. Geol.* 123(3), 225–234.
- [105].Marquardt, D., W., 1963. An Algorithm for Least Squares Estimation of Nonlinear Parameters. *J. Soc. Ind. Appl. Math.* 11, 431-441.
- [106].McDougall, S., 2006. A new continuum dynamic model for the analysis of extremely rapid landslide motion across complex 3d terrain. Ph.D. Thesis, University of British Columbia.
- [107].McDougall, S., Boulton, N., Hungr, O., Stead, D., Schwab, J., 2006. The Zymoetz River landslide, British Columbia, Canada; description and dynamic analysis of a rock slide debris flow. *Landslides* 3, 195.
- [108].Mckenna, J.P., Santi, P.M., Amblad, X., Negri, J., 2011. Effect of soil-engineering properties on the failure mode of shallow failure. *Landslides* 3(1), 215-228.
- [109].Medina-Cetina, Z., Nadim, F., 2008. Stochastic design of an early warning system, *Georisk: Assessment and Management of Risk for Engineered Systems and Geohazards*, 2, 223–236.
- [110].Mergili, M., Marchesini, I., Rossi, M., Guzzetti, F., Fellin, W., 2014. Spatially distributed three-dimensional slope stability modelling in a raster GIS, *Geomorphology* 206, 178–195.
- [111].Micheletti, N., Foresti, L., Robert, S., Leuenberger, M., Pedrazzini, A., Jaboyedoff, M., Kanevski, M., 2014. Machine learning feature selection methods for landslide susceptibility mapping. *Math Geosci* 46, 33-57.
- [112].Miha, V., Curk, T., 2006. ROC Curve, Lift Chart and Calibration plot. *Metodoloski Zvezki* 3(1), 89-108.
- [113].Miller, D., J., 1995. Coupling GIS with physical models to assess deep-seated landslide hazards. *Environ. Engng Geosc.*, 1, 263-276.
- [114].Miller, D., J., Sias., 1998. Deciphering large landslides: linking hydrological, groundwater and slope stability models through GIS. *Hydrological Processes*, 12, 923-941.
- [115].Montgomery, D., R., Dietrich, W., E., 1994. A physically-based model for topographic control on shallow landsliding. *Water Resources Research* 30 (4), 1153-1171.
- [116].Moore, I., Burch, G., 1986. Physical basis of the length-slope factor in the Universal Soil Loss Equation. *Soil Society of America Journal* 50, 1294 – 1298.
- [117].Moore, I. D., Grayson, R. B., Ladson, A. R., 1991. Digital Terrain Modelling: A Review of Hydrological, Geomorphological and Biological Applications. *Hydrological Processes* 5(1), 3-30.
- [118].Oh, H.-J., Pradhan, B., 2011. Application of a neuro-fuzzy model to landslide-susceptibility mapping for shallow landslides in a tropical hilly area. *Comput. Geosci.* 37(9), 1264–1276.

- [119].Pachauri, A.K., Pant, M., 1992. Landslide hazard mapping based on geological attributes. *Engineering Geology* 32, 81–100.
- [120].Pack, R., T., Tarboton, D., G., Goodwin, C., N., 1998. The SINMAP approach to terrain stability mapping. In D.P. Moore & O. Hungr (eds.), *Proceedings, Eighth International Congress of the International Association for Engineering Geology and the Environment*. Vancouver, Canada, September 21-25, 1998, 1157- 1165.
- [121].Park, D.W., Nikhil, N.V., Lee, S.R., 2013.Landslide and debris flow susceptibility zonation using TRIGRS for the 2011 Seoul landslide event. *Nat. Hazards Earth Syst. Sci.*13, 2833-2849.
- [122].Park, J.Y., 2015. A statistical entrainment growth rate estimation model for debris-flow runout prediction. M.S. thesis, KAIST.
- [123].Park, I., Lee, S., 2014. Spatial prediction of landslide susceptibility using a decision tree approach: a case study of the Pyeongchang area, Korea. *International Journal of Remote Sensing* 35 (16), 6089-6112.
- [124].Park, S.K., Lee, E., 2007.Synoptic features of orographically enhanced heavy rainfall on the east coast of Korea associated with Typhoon Rosa (2002). *Geophysical Research Letters* 34(2),L02803.
- [125].Pastor,M., Blanc,T., Haddad,B., Dremptec,V., MilaSanchez,M., Dutto,P., Stickle, M.,M., Mira,P., Merodo J.A.F., 2014. Depth Averaged Models for Fast Landslide Propagation: Mathematical, Rheological and Numerical Aspects. *Archives of Computational Methods in Engineering* 22(1), 1-38.
- [126].Perla, R., Cheng,T.,T., McClung,D.,M.,1980. A two parameter model of snow avalanche motion. *Journal of Glaciology* 26(94), 197-208.
- [127].Pike, R.J., Wilson, S.E., 1971. Elevation-Relief Ratio, Hypsometric Integral, and Geomorphic Area-Altitude Analysis. *Geol. Soc. Amer. Bull.* 82(4), 1079-1084.
- [128].Pourghasemi, H.R., Pradhan, B., Gokceoglu, C., 2012a. Application of fuzzy logic and analytical hierarchy process (AHP) to landslide susceptibility mapping at Haraz watershed, Iran. *Nat. Hazards* 63(2), 965–996.
- [129].Pourghasemi, H.R., Pradhan, B., Gokceoglu, C., 2012b. Remote sensing data derived parameters and its use in landslide susceptibility assessment using Shannon’s entropy and GIS. *AEROTECH IV-2012. Appl. Mech. Mater.* 225, 486–491.
- [130].Pradhan, A.M.S., Kim, Y.T, 2014. Relative effect method of landslide susceptibility zonation in weathered granite soil: a case study in Deokjeok-ri Creek, South Korea. *Natural hazard* 72, 1189-1217.
- [131].Pradhan, B., Lee, S., Buchroithner, M.F., 2010. A GIS-based back-propagation neural network model and its cross-application and validation for landslide susceptibility analyses. *Comput. Environ. Urban. Syst.* 34(3), 216–235.
- [132].Reid, M.,E., Christian, S.,B., Brien, D.,L., Henderson, S.,T., 2015.Scoops3D—Software to analyze 3D slope stability throughout a digital landscape:, U.S. Geological Survey *Techniques and Methods*, book 14, chap. A1, 218 p.
- [133].Rickenmann, D., Zimmermann, M., 1993. The 1987 debris flows in Switzerland: Documentation and analysis. *Geomorphology*, 8,175-189.
- [134].Riley, S. J., DeGloria, S. D., Elliot, R., 1999. A terrain ruggedness index that quantifies topographic heterogeneity, *Intermountain Journal of Sciences* 5 (1-4), 23-27.

- [135].Salciarini, D., Godt, J. W., Savage, W. Z., Baum, R. L., Conversini, P., 2008. Modeling landslide recurrence in Seattle, Washington, USA. *Eng. Geol.* 102, 227-237.
- [136].Santacana, N., Baeza, B., Corominas, J., Paz, A. D., Marturia, J., 2003. A GIS-Based Multivariate Statistical Analysis for Shallow Landslide Susceptibility Mapping in La Pobla de Lillet Area ( Eastern Pyreness, Spain) *Natural Hazards* 30, 281-295.
- [137].Sasitharan, S., Robertson, P. K., Sego, D. C., Morgenstern, N. R., 1993. Collapse behavior of sand. *Canadian Geotechnical Journal*, 30(4), 569-577.
- [138].Sassa, K., 1984. The mechanism starting liquefied landslides and debris flows, *Proc. 4th Int. Symposium on Landslides*, Toronto (Canada), 2, 349-354.
- [139].Seed, H.B., Seed, R.B., Schlosser, F., Blondeau, F., Juran, I., 1988. The Landslide at the Port of Nice on October 16, 1979. University of California, College of Engineering, Report No. UCB/EERC-88/10.
- [140].Seok, Y., Lee, S.R., Kim, Y.T., Gyu-Hyun, G., 2015. Estimation of saturated hydraulic conductivity of Korean weathered granite soils using regression analysis. *Geomechanics and Engineering* 9(1), 101-113.
- [141].Sezer, E.A., Pradhan, B., Gokceoglu, C., 2011. Manifestation of an adaptive neuro-fuzzy model on landslide susceptibility mapping Klang valley, Malaysia. *Expert Syst. Applicat.* 38(7), 8208–8219.
- [142].Stark, T. D., Eid, H. T., 1998. Performance of three-dimensional slope stability methods in practice. *J. Geotech. Geoenviron. Eng.*, 124(11), 1049-1060.
- [143].Takahashi T. (1981): Estimation of potential debris flows and their hazardous zones: Soft countermeasures for a disaster. *J. Natural Disaster Science*, 3(1), pp. 57–89.
- [144].Tang, J., Alelyani, S., Liu, H., 2014. Feature Selection for Classification: A Review. In: Aggarawal, C.C. (Ed.), *Data classification: Algorithms and Applications*. CRC press, Newyork, pp. 37-58.
- [145].Teufelsbauer, H., Wang, Y., Pudasaini, S.P., Borja, R.I., Wu, W., 2011. DEM simulation of impact force exerted by granular flow on rigid structures. *Acta Geotechnica* 6(3), 119–133. doi:10.1007/s11440-011-0140-9.
- [146].Tien Bui, D., Pradhan, B., Lofman, O., Revhaug, I., Dick, O.B., 2012. Landslide susceptibility mapping at Hoa Binh province (Vietnam) using an adaptive neuro-fuzzy inference system and GIS. *Comput. Geosci.* 45, 199–211.
- [147].Tien Bui, D., Pradhan, B., Lofman, O., Revhaug, I., Dick, O.B., 2013. Regional prediction of landslide hazard using probability analysis of intense rainfall in the Hoa Binh province, Vietnam. *Natural Hazards* 66 (2), 707-730.
- [148].UNISDR (United Nations International Strategy For Disaster Reduction), 2006. The International Early Warning Programme – The four elements of effective early warning systems – Brochure, Platform for the Promotion of Early Warning (PPEW), 4 pp., available at: <http://www.unisdr.org/2006/ppew/iewp/IEWP-brochure.pdf>.
- [149].Van Den Eeckhaut, M., Reichenbach, P., Guzzetti, F., Rossi, M., Poesen, J., 2009. Combined landslide inventory and susceptibility assessment based on different mapping units: an example from the Flemish Ardennes, Belgium. *Natural Hazards and Earth System Sciences* 9, 507-521.



- [150].Van Den Eeckhaut, M., Vanwalleggem, T., Poesen, J., Govers, G., Verstraeten, G., Vandekerckhove, L., 2006. Prediction of landslide susceptibility using rare events logistic regression: a case-study in the Flemish Ardennes, Belgium. *Geomorphology* 76, 392-410.
- [151].Van Den Eeckhaut, M., Reichenbach, P., Guzzetti, F., Rossi, M., Poesen, J., 2009. Combined landslide inventory and susceptibility assessment based on different mapping units: an example from the Flemish Ardennes, Belgium. *Natural Hazards and Earth System Sciences* 9, 507-521.
- [152].Van Westen, C.J., Van Asch, T.W.J., Soeters, R., 2006. Landslide hazard and risk zonation-why is it still so difficult? *Bull. Eng. Geol. Env.* 65, 167-184.
- [153].Varnes, D.J., 1984. Landslide hazard zonation: A review of principles and practice. IAEG Monograph, UNESCO, 59.
- [154].Wang, G., Sassa, K., 2003. Pore pressure generation and movement of rainfall- induced landslides: effects of grain size and fine particle content. *Engineering geology* 69, 109-125.
- [155].Wilson, J.P., Gallant, J.C. (Eds.), 2000. *Terrain analysis: principles and applications*, Wiley, New York.
- [156].Wu, W., Sidle, R., C., 1995. A distributed slope stability model for steep forested basins. *Water Resources Research* 31,2097–2110.
- [157].Yao, X., Tham, L.G., Dai, F.C., 2008. Landslide susceptibility mapping based on support vector machine: a case study on natural slopes of Hong Kong, China. *Geomorphology* 101(4), 572–582.
- [158].Yeon, Y.K., Han, J.G., Ryu, K.H., 2010. Landslide susceptibility mapping in Injae, Korea, using a decision tree. *Eng. Geol.* 116(3–4), 274–283.
- [159].Yesilnacar, E., Topal, T., 2005. Landslide susceptibility mapping: A comparison of logistic regression and neural networks methods in a medium scale study, Hendek region (Turkey). *Eng. Geology*, 79, 251–266.
- [160].Yilmaz, I., 2010. Comparison of landslide susceptibility mapping methodologies for Koyulhisar, Turkey: conditional probability, logistic regression, artificial neural networks, and support vector machine. *Environ. Earth Sci.* 61(4), 821–836.
- [161].Youden W.J., 1950. Index for rating diagnostic tests. *Cancer* 3, 32-35.
- [162].Xie, M., Esaki, T., Cai, M., 2006. GIS-based implementation of three-dimensional limit equilibrium approach of slope stability. *Journal of Geotechnical and GeoEnvironmental Engineering* 132, 656-660.
- [163].Xie, M. W., Esaki, T., Zhou, G. Y., and Mitani, Y. ,2003. Geographic information systems-based three-dimensional critical slope stability analysis and landslide hazard assessment. *J Geotech Geoenviron*, 129(12), 1109-1118.
- [164].Xu. Z., Jin, R., Lyu, M.R., King, I., 2010. Discriminative semi-supervised feature selection via manifold regularization. *IEEE Trans. Neural Networks* 21, 1303-1308.
- [165].Xu, C., Dai, F., Xu, X., Lee, Y.H., 2012. GIS-based support vector machine modeling of earthquake-triggered landslide susceptibility in the Jianjiang River watershed, China. *Geomorphology* 145-146, 70-80.
- [166].Zare, M., Pourghasemi, H. R., Vafakhah, M., Pradhan, B., 2012. Landslide susceptibility mapping at Vaz Watershed (Iran) using an artificial neural network model: A comparison between multilayer perceptron (MLP) and radial basic function (RBF) algorithms. *Arab J. Geosci.* 6, 2873-2888.

- [167].Zhu, A.X., Wang, R.X., Qiao, J.P., Qin, C.Z., Chen, Y.B., Liu, J., Du, F., Zhu. T.X., 2014. An expert knowledge-based approach to landslide susceptibility mapping using GIS and fuzzy logic. *Geomorphology* 214, 128-138.

# Curriculum Vitae

Name               Nikhil N.V.  
D.O. B             March 6<sup>th</sup>, 1986  
Contact            E-Mail: [nikil@gmail.com](mailto:nikil@gmail.com)

---

## EDUCATION

2016               **Ph.D.** KAIST, South Korea  
2011               **M.S.** in Structural and Geotechnical Engineering, Griffith University, Australia  
                      **M.S.** in Geotechnical Engineering, KAIST, Korea  
2007               **B.E.** in Civil Engineering, College of Engineering Goa, India

---

## WORK EXPERIENCE

June 2011-Feb 2009      Design Engineer  
                              Madhav Kamat and Associates  
                              Structural consulting Engineers, Goa, India  
  
Sept 2011 - June 2016    Research/Teaching Assistant  
                              Department of Civil and Environmental Engineering, KAIST, Korea  
  
March 2016-continuing    Teaching Assistant for Scientific writing course  
                              College of Liberal Arts and Convergence Science

---

## PUBLICATIONS

### *Journal Papers (SCI):*

1. **Nikhil N.V.**, S.R. Lee, A.M.S Pradhan, Y.-T. Kim, S.H. Kang, D.H. Lee, “A new approach to temporal assessment using ERI for extreme rainfall-induced landslide hazard”. Engineering Geology (Under revision).
2. **Nikhil N.V.**, S.R. Lee (2016), “A hybrid feature selection algorithm integrating an extreme learning machine for landslide susceptibility modeling of Mt. Woomyeon, South Korea”. Geomorphology 263, 50-70.
3. S.H. Kang, S.R. Lee, **Nikhil N.V.**, J.Y. Park, D.H Lee (2016), “Development and Application of Initiation Criterion for Debris Flows at a Regional Scale using Topographic Indices”. Catena (Under review after 1<sup>st</sup> revision).

4. D. W. Park, S. R. Lee, **Nikhil, N. V.**, S.H. Kang, J.Y. Park (2016), "Coupled model for simulation of landslides and debris flows at local scale". *Natural Hazards* 81 (3), 1653-1682.
5. G.H Go, S.R. Lee, **Nikhil N.V.**, Seok Yoon (2015), "A new performance evaluation algorithm for horizontal GCHPs (ground coupled heat pump systems) that considers rainfall infiltration". *Energy* 83, 766-777.
6. D. W. Park, S. R. Lee, **Nikhil, N. V.**, S. Yoon and G. H. Go (2013). "Quantitative assessment of landslide susceptibility on a regional scale using geotechnical databases developed from GIS-based maps". *Disaster Advances* 7(5), 26-38.
7. D. W. Park, **Nikhil, N. V.**, S. R. Lee (2013). "Landslide and debris flow susceptibility zonation using TRIGRS for the 2011 Seoul landslide event". *Natural Hazards and Earth System Sciences* 13, 2833-2849.

***Journal papers (Non-SCI and to be submitted):***

1. Nikhil N.V., D.H. Lee, S.R. Lee, J.Y. Park, A. Jordan, O. Hungr (2016), "Landslide initiation and run out modelling under extreme rainfall in South Korea" (To be submitted).
2. D. W. Park, S. R. Lee, **Nikhil, N. V.**, S. H. Kang, J. Y. Park (2013), "Debris flow hazard zonation by probabilistic analysis (Mt. Woomyeon, Seoul, Korea)". *International Journal of Innovative Research in Science, Engineering and Technology* 2(6), 2381-2390.
3. S.H. Kang, S.R. Lee, **Nikhil N.V.**, J.Y. Park (2015), "Analysis of Differences in Geomorphological Characteristics on Initiation of Landslides and Debris Flows". *J. Korean Soc. Hazard Mitig.* 15 (2), 249-258.

***Conference proceedings:***

1. **Nikhil N.V.**, S.R. Lee, J.Y. park, D.H Lee (2015), "A coupled hydro-mechanical mobilization analysis for extreme rainfall induced debris flow" COUPLED PROBLEMS 2015, San Servolo Island, Venice, Italy.
2. D.H. Lee, S.R. Lee, **Nikhil N.V.**, J.Y. Park (2015), "Modelling debris flow runout patterns on a local slope for 2011 Seoul event using DAN-3D", ICCES'15, Reno, NV, USA.
3. **Nikhil N.V.**, S.R. Lee, J.Y. Park, S.H. Kang (2014), "Triggering and mobilization of debris flow due to extreme rainfall: A case study in Korean peninsula" Sixth International Conference on Engineering Failure Analysis, Lisbon, Portugal.
4. J.Y. Park, S.R. Lee, **Nikhil N.V.**, S.H. Kang (2014), "Calibration-based assessment of debris flow hazard on a local slope for 2013 Yeosu event using Dan-3D" The Twenty-Seventh KKHTCNN symposium on Civil Engineering 2014, Shanghai, China.
5. S.R. Lee, **Nikhil N.V.**, S.H. Kang, J.Y. Park (2014), "Extreme rainfall induced debris flow prediction: Hazard analysis accommodating post event topographic changes in Mt. Woomyeon, South Korea" IDRC Davos 2014, Davos, Swiss
6. **Nikhil N. V.**, S. R. Lee, D. W. Park, S. H. Kang and J. Y. Park (2014). "GIS based regional susceptibility model for debris flow initiation in Woomyeon Mountain, South Korea". *Proceedings of World Landslide Forum* 3, 2-6 June 2014, Beijing.

7. D. W. Park, **Nikhil, N. V.**, S. R. Lee (2013). “Application of Landslide and Debris flow Coupled Model at Regional Scale”. *Proceedings of the 26th KKHTCNN symposium on Civil Engineering*, NUS, Singapore.
  8. D. W. Park, S. R. Lee, **Nikhil, N. V.**, S. H. Kang (2013). “Assessment of debris flow susceptibility of 2011 Woomyeon mountain landslide”. *Proceedings of the ICL Northeast Asia Network Symposium*, Seoul, Korea.
  9. **Nikhil N. V.**, S. R. Lee, D. W. Park (2013). “Landslide induced debris flow susceptibility mapping using extreme rainfall index”. *Proceedings of 9th International Workshop on ANCRiSST 2013*, July, Ulsan, Korea.
  10. **Nikhil N. V.**, S. R. Lee, D. W. Park (2013). “Coupled analysis for hazard modeling of debris flow due to extreme rainfall”. *Proceedings of ICCCGE*, 26-27 Dec 2013, Phuket.
  11. S. H. Kang, S. R. Lee, D. W. Park, **Nikhil N. V.** (2013). “Analysis of debris flow events occurred in Korea in 2013 using Extreme Rainfall Index (ERI)”. *Proceedings of the Korean Society of Civil Engineers*, Jeongseon, Korea.
  12. **Nikhil N.V.**, S. R. Lee (2012). “Suction stress based 1-D slope stability analysis for Korean granite weathered soil slopes” The 25th KKCNN Symposium on Civil Engineering, Busan, Korea, pp. 429-432.
- 

#### MISCELLANEOUS

- 1) Selected for 1<sup>st</sup> LARAM–ASIA “**Landslide Risk Assessment and Mitigation**” course 2011.
  - 2) Awarded Griffith university student exchange program scholarship to KAIST, South Korea, 2010.
  - 3) Invitation for membership to **Golden Key International Honor Society**, Griffith University Australia Chapter, 2010.
-